UNIVERSITY OF OKLAHOMA

GRADUATE COLLEGE

VIRUS-SELECTED OSTEOGENESIS-INDUCING PEPTIDES FOR ENHANCED BONE REGENERATION IN 3D PRINTED TITANIUM ALLOY IMPLANTS

A DISSERTATION SUBMITTED TO THE GRADUATE FACULTY

In partial fulfillment of the requirements for the

Degree of

DOCTOR OF PHILOSOPHY

By

KEGAN SUNDERLAND

Norman, Oklahoma

2018

Downloaded from SHAREOK. Persistent Handle URL: https://hdl.handle.net/11244/316302

VIRUS-SELECTED OSTEOGENESIS-INDUCING PEPTIDES FOR ENHANCED BONE REGENERATION IN 3D PRINTED TITANIUM ALLOY IMPLANTS

A DISERTATION APPROVED FOR THE

DEPARTMENT OF CHEMISTRY AND BIOCHEMISTRY

BY

Dr. Chuanbin Mao, Chair

Dr. Ann West

Dr. Christina Bourne

Dr. Daniel Glatzhofer

Dr. Scott Russell

© Copyright by KEGAN SUNDERLAND 2018

All Rights Reserved.

Acknowledgements

Words alone cannot express what it means to pursue and complete a PhD. It is akin to a grand adventure for which one must fight to keep the inner spark of insatiable curiosity aflame against the torrent of hardships, great loss, politics, exploitations, finances, and failures which relentlessly hammer away at a PhD student. After being immersed in such a world for so long it is only my ties to those closest to me which have grounded me and kept my spark from going out in the ever-encroaching darkness. They remind me that life should be joyous and achieving a work-life balance is more important than prestige. I am reminded that integrity, empathy, and humbleness are the true measures of greatness for without these, one is truly alone.

First and foremost, I would like to thank my family for their unyielding support during my PhD studies. They above all have kept me grounded. They provided what a PhD student needs the most. An escape to the real world and swift aid in times of dire need. I would like to give a special thanks to my mother and father for all the times they have pushed me to succeed and develop my skills in all aspects of life. These skills have translated to make me well-rounded, independent, and responsible. I also would like to thank my five brothers, Toby, Preston, Jeremy, Ryan, and Coleton as well as the Zikmund family for providing work-life balance and joyous adventures without which I most certainly would not have had the fortitude to continue my PhD.

I would also like to sincerely thank my advisor, Dr. Chuanbin Mao. He has worked tirelessly with everyone in his lab during my PhD. I'd like to say that somehow, he's found the 25th hour in a 24-hour day. He has greatly improved my writing skills and helped me publish many manuscripts. If not for his continued support, I would not have been as successful during my time here. We have worked closely together on many highly interdisciplinary projects which have broadened both my interests and abilities. He has also given me a great deal of freedom in selecting the direction of projects I was interested in for which I am very thankful.

Additionally, I cannot give enough praise and credit to the positive role my lab members have had during my PhD. They are both essential sources for troubleshooting experiments and dear friends. I would like to give a special thanks to Dr. Binrui Cao, Dr. Penghe Qiu, and Dr. Aron Roxin who have served as secondary advisors to me during my PhD. I would also like to give special thanks to Mengmeng Zhai, James Cho, Ningyun Zhou, Xuewei Qu, Lin Wang, and Wen Yang for all their help troubleshooting experiments or doing animal surgeries with me.

Lastly, I would like to thank my committee members, many collaborators, dear friends, and those whom I have consulted with for their expert advice during the PhD. Together everyone has been an integral part of the success of my PhD projects.

Table of Contents

Acknowledgements……iv

List of Tables……x

List of Figures……xi

List of Abbreviations……xv

Abstract……xviii

Chapter 1: Introduction……1

1.1 Viruses as a material in nanomedicine……1

1.1.2 Structures of different viruses……3

1.1.3 Biological properties of different viruses……7

1.1.3.1. Chemical stability of different viruses……7

1.1.3.2. Monodispersity……9

1.1.3.3. Biocompatibility……10

1.2 Phages……12

1.2.1 History and classification of phages……12

1.2.2 Life cycles of phages: temperate vs. professionally lytic……15

1.3 Virus-derived peptides for biomedical applications……23

1.3.1 Viral Libraries……37

1.3.2 Selecting Targeting Peptides by Virus-peptide Display……39

1.3.3 Virus-derived tissue regenerative peptides……42

1.3.4 M13 Phage assemblies for tissue regeneration……43

1.4 3D printing for tissue regeneration……44

1.4.1 Materials Used in Biomedical 3D Printing……45

1.4.2 Vascularized bone regenerative 3D printing……46

Chapter 2: Development and discovery of peptides capable of binding and detecting bone morphogenic protein receptors……49

2.1 Introduction……49

2.1.1 Phage display for identifying receptor-targeting peptides……51

2.1.2 Development of BMP-mimicking peptides.……52

2.2 Materials and Experiments……..……...56

2.2.1 Materials……..…….56

2.2.2 Negative selection of plastic or poly-L-lysine binders….56

2.2.3 Immobilization of target……..…….57

2.2.4 Selection procedure……...……..57

2.2.5 Titering……..……..……..59

2.2.6 Amplification of phage library……..60

2.2.7 DNA sequencing to determine peptides……..…..61

2.2.8 Enzyme-linked immune sorbent assay for receptor binding……..62

2.2.9 Live cell binding through immunofluorescence……64

2.3 Results and Discussion……..…….……65

2.3.1 Sequencing results and frequency of peptides……..….65

2.3.2 Relic peptide analysis……..……..69

2.3.3 Relative binding strengths of selected peptides and live cell binding of peptides to hMSCs……70

2.4 Conclusion……..……..73

Chapter 3: Generating a genetically engineered virus displaying newly discovered differentiation peptides and assembling it into a precise nanostructured film to control stem cell differentiation into osteoblasts…….……..…74

3.1 Introduction……..……74

3.1.1 Genetic manipulation of M13 phages……...74

3.1.2 Phage films……..……75

3.1.3 Osteoblast markers……..…75

3.2 Materials and Experiments……..……..76

3.2.1 Materials……..…….....76

3.2.2 M13 Phage Display……..77

3.2.2.1 Preparation of M13 plasmid vector……79

3.2.2.2 PCR reaction (Preparation of insert fragments)……...80

3.2.2.3 PCR products purification and digestion……...80

3.2.2.4 Preparation of TG1 competent cells……..……80

3.2.2.5 Ligation reaction……...…81

3.2.2.6 Transfection of DNA into competent E. coli TG1 cells ($CaCl_2$ method)……..……...….81

3.2.2.7 Confirmation of recombinant phagemid…….85

3.2.3 Amplification of genetically engineered M13 phage……85

3.2.4 Generation of phage films ……..…87

3.2.5 Characterization of M13 phage (AFM and TEM)…….88

3.2.6 Characterizing phage film morphology…….88

3.2.7 Cell proliferation on phage films…….....88

3.2.8 Immunofluorescence of osteoblast marker proteins…...89

3.2.9 Calcium Nodule Staining…….……90

3.2.10 qPCR of osteoblast marker genes…….……..90

3.3 Results and Discussion……..……91

3.3.1 Sequencing results of phage display…….……..91

3.3.2 M13 phage morphology images…….……..…….93

3.3.3 Organized ridge groove structure of phage films……94

3.3.4 Phage films support hMSC growth and proliferation…..98

3.3.5 Peptide-phage induced differentiation of hMSCs demonstrated by osteoblast marker proteins……..100

3.3.6 Peptide-phage induced hMSC calcium deposits……..100

3.3.7 Peptide-phage induced genetic upregulation of osteoblast marker genes…….……..…….……...…..104

3.4 Conclusion……..……106

Chapter 4: Elucidating the signaling pathway mechanism of newly discovered osteogenic peptides……107

4.1 Introduction: Bone regeneration signaling pathways……..……108

4.2 Materials and Experiments……..……111

4.2.1 Materials……..…….....111

4.2.2 Immunofluorescence of osteoblast signaling pathway marker proteins…….111

4.2.3 Selective inhibition effects on peptide signaling pathways……113

4.3 Results and Discussion……..……115

4.3.1 Synergistic activations of osteoblast differentiation pathways by osteogenic peptide phage films. ……..115

4.3.2 Inhibition of differentiation pathways……..116

4.4 Conclusion……..……125

Chapter 5: Development of hybrid bone regenerative materials: A combination of 3D printing, phage display, and freeze casting……131

5.1 Introduction……..……..…131

5.1.1 Personalized 3D printed bone regenerative scaffolds..131

5.1.2 Freeze casting organized bone-mimetic lamellar structures……...…133

5.2 Materials and Experiments……..……133

5.2.1 Materials……..……...134

5.2.2 3D printing titanium alloy……...…134

5.2.3 Creating a double-sided freeze casting machine……..134

5.2.4 HAP nanorod synthesis, TEM imaging of HAP, and powder X-Ray diffraction of HAP**…..**……..135

5.2.5 Generating bone mimetic lamellar structures of combination of phage, hydroxyapatite, and collagen through freeze casting, cross linking, and sintering processes..…….....136

5.2.6 Freeze casting M13 phages onto 3D printed titanium..138

5.2.7 Scanning electron microscopy, EDS, and cell attachment to scaffolds…….……139

5.2.8 Mechanical strength testing……..……..……139

5.2.9 Generating a rat radial bone defect model……..…141

5.2.10 Preparation and fixation of harvested bone defect tissues……141

5.2.11 Hematoxylin and Eosin tissue Staining…..……142

5.2.12 Von Kossa tissue Staining…...……143

5.3 Results and Discussion……..……143

5.3.1 Freeze casting machine performance……143

5.3.2 Hydroxyapatite powder X-Ray diffraction and TEM confirms synthesis of HAP nanorods……148

5.3.3 Just Phage and phage + hydroxyapatite characterization after freeze casting……..……..……..149

5.3.4 A combination of 3D printing, freeze casting, and growth factor mimetics to tune the microenvironment of implants….153

5.3.5 Mechanical strength properties of titanium-phage hybrid scaffolds show ideal bone-like properties in vivo ……..…158

5.3.6 Histological staining shows tissue and calcium deposits in scaffolds……..….160

5.4 Conclusion……..……163

References……..……...165

Appendix……204

List of Copyrights and Permissions…..……..……..….204

IACUC Approval……..…….210

Supplemental Data……..….211

List of Tables

Table 1. Various structures and applications of phages in nanomedicine

Table 2. Examples of Virus-derived Peptides in Clinical Trials for Humans

Table 3. Pathogen-targeting peptides derived from virus libraries

Table 4. Summary of human cell-targeting peptides derived from virus libraries

Table 5. Summary of tissue-targeting peptides derived from virus libraries in preclinical or clinical trials

Table 6. The DNA FASTA sequences corresponding to peptides obtained through biopanning on BMPR1A.

Table 7. The DNA FASTA sequences corresponding to peptides obtained through biopanning on BMPR2.

Table 8. The peptide sequences, the peptide structures, the primers used to display the peptides on pVIII of M13 bacteriophage, the restriction sites for the primers, and the net charge of each peptide.

Table 9. The DNA sequencing results for displaying the indicated peptides on the pVIII coat protein of M13 phages.

Table 10. Biodegradable freeze casting recipes.

Table 11. ANOVA statistical significance report corresponding to the ELISA data.

Table 12. ANOVA details for alamar blue cell proliferation data.

List of Figures

Figure 1. Viruses as a material in biomedical applications.

Figure 2. Overview of the various structures of viruses commonly used in material applications.

Figure 3. Phage display on M13 and T7 phages.

Figure 4. In vivo phage biopanning concept.

Figure 5. Summary of the process of biopanning.

Figure 6. Summary of 3D printed tissue examples for biomedical applications.

Figure 7. Summary of overall research plan.

Figure 8. Frequency of peptide sequencing results from biopanning on (A) BMPR1A and (B) BMPR2.

Figure 9. The peptides discovered through biopanning were compared to BMP2 using RELIC/MATCH.

Figure 10. Evaluation of the BMPR-binding peptides in binding BMPRs.

Figure 11. Generation of the insertion fragment for phage display.

Figure 12. Insertion of M13KO7 phage RF DNA into the PeCan49 phagemid display vector.

Figure 13. The morphology of M13 phages.

Figure 14. Osteogenic differentiation of hMSCs on phage films.

Figure 15. hMSC cell proliferation on the phage films.

Figure 16. Calcium (red) nodule staining (14 days).

Figure 17. Calcium (red) nodule staining (26 days).

Figure 18. Osteogenic differentiation of hMSCs on phage films after 14 days.

Figure 19. Several prominent signaling pathways for osteogenesis are shown.

Figure 20. Immunofluorescence showing signaling (green) among osteogenic pathways.

Figure 21. The effects of inhibiting Smad 1/5/8 (BMP pathway) and Hes1 (Notch pathway) on Gli1 (Hedgehog pathway) protein levels.

Figure 22. The effects of inhibiting Smad 1/5/8 (BMP pathway) and Hes1 (Notch pathway) on Hes1 (Notch pathway) protein levels.

Figure 23. The effects of inhibiting Smad 1/5/8 (BMP pathway) and Hes1 (Notch pathway) on Smad 1/5/8 (BMP pathway) protein levels.

Figure 24. The possible signaling pathway targets of the osteogenic peptides and phage films. The pathways have been greatly simplified to show the known points affected by the peptides or film topography.

Figure 25. In vitro work summary of the use of phages displaying BMPR-binding peptides to induce the differentiation of hMSCs into osteoblast cells.

Figure 26. Double Sided Freeze Casting rates for the top cold finger (top) and bottom cold finger (bottom).

Figure 27. An overlay of the top and bottom cold fingers freeze casting rates.

Figure 28. Temperature rates of the top (blue) and bottom (red) cold fingers in the double-sided freeze casting setup.

Figure 29. The temperature drop rate of a single-sided freeze casting system is shown.

Figure 30. Hydroxyapatite $Ca_5(PO_4)_3(OH)$ nanorods.

Figure 31. M13 phage scaffolds arranged through freeze casting and imaged by SEM.

Figure 32. Freeze-casted HAP.

Figure 33. Freeze casted HAP which has been sintered.

Figure 34. 3D printed titanium scaffolds.

Figure 35. 3D printed titanium scaffold coating results.

Figure 36. The mechanical properties of implanted scaffolds.

Figure 37. Top down view of a section of each cylindrical-shaped implant condition stained with H&E after being implanted 4 weeks.

Figure 38. Von Kossa stains of 4-week implants in rat radial defect bone models viewed from the top down of the cylindrical scaffolds.

List of Abbreviations

Abbreviation	Full name (alphabetically sorted)
AAV	Adeno-associated viruses
ALP	Alkaline phosphatase
ABTS	Azino-bis(3-ethylbenzothiazole sulfonic acid) diammonium salt
Phage	Bacteriophages
BMP	Bone morphogenic protein
BMPR1A	Bone morphogenic protein receptor type 1A
BMPR2	Bone morphogenic protein receptor type 2
BSA	Bovine serum albumin
Xgal	5-Bromo-4- chloro-3-indolyl-β-D-galactoside
CRISPR/Cas	Clusters of regularly interspaced short palindromic repeat and associated genes system
COL	Collagen type 1A
CAD	Computer-aided design
CCMV	Cowpea chlorotic mottle virus
CPMV	Cowpea mosaic virus
DNA	Deoxyribonucleic acid
dNTP	Deoxynucleoside triphosphate
DMSO	Dimethyl sulfoxide
DTT	Dithiothreitol
ddH_2O	Double distilled water
dsDNA	Double-stranded deoxyribonucleic acid
EDS	Energy-dispersive X-ray spectroscopy
EDC	1-ethyl-3-(3 dimethylaminopropyl) carbodiimide hydrochloride
EDTA	Ethylenediaminetetraacetic acid
ECM	Extracellular matrix
HCl	Hydrochloric acid
HAP	Hydroxyapatite
hMSCs	Human mesenchymal stem cells
IPTG	Isopropyl-β-D-thiogalactoside
LB	Luria broth
mRNA	Messenger ribonucleic acid
1D	One-dimensional
OCN	Osteocalcin
OPN	Osteopontin
PBS	Phosphate buffered saline
PCR	Polymerase chain reaction
qPCR	Quantitative polymerase chain reaction
PEG	Polyethylene glycol–8000
RNA	Ribonucleic acid
SEM	Scanning electron microscopy
SLM	Selective laser melting
ssDNA	Single-stranded deoxyribonucleic acid

NaCl	Sodium chloride
STL	Stereo Lithography
TMV	Tobacco mosaic virus
TBS	Tris-buffered saline
TBST	Tris-buffered saline + 0.1% v/v Tween-20
TEM	Transmission electron microscopy
2D	Two-dimensional
UV	Ultraviolet

Abstract

Bone morphogenetic proteins (BMPs) are part of the transforming growth factor-β superfamily and function as key regulators of cellular growth, differentiation, and tissue formation. While recombinant BMPs can be used to induce osteoblast differentiation, they are expensive to produce. In contrast, peptides can be efficiently produced in massive quantities through phage display. It would therefore be highly valuable to develop short peptides capable of mimicking BMPs which could be displayed on human-safe M13 phage. I have discovered the short, 12-mer peptide sequences TAKYLPMRPGPL, VHVPLHRGAVSA, SGTQDSMVGWNK, and RDYHPRDHTATW through a selective process called biopanning (patented). These 12-mer peptides have been shown to bind the BMP receptors on live cells by immunofluorescence and bind the BMP receptors in an ELISA when genetically displayed on the p3 coat protein of M13 bacteriophage. The peptides were then genetically displayed on the p8 coat protein of M13 bacteriophage. The p8 coat protein can have up to ~2700 copies of the peptide instead of just 5 available copies on the p3 coat protein. These newly engineered phages were incorporated into phage films having aligned ridge groove surface topographies which are arranged in a way that the p8 coat protein is exposed. Human mesenchymal stem cells (hMSCs) cultured on these films demonstrated varying levels of differentiation according to the peptide displayed as well as the concentration of the peptide. Differentiation of the hMSCs into osteoblasts was confirmed by immunofluorescence and qPCR of the osteoblast marker proteins and genes respectively for osteopontin, osteocalcin, and collagen

type 1a. Additionally, calcium deposition was observed to be exceptionally high for hMSCs cultured with the phage films compared to a leading company product, osteogenic media from Lonza. The mechanism of osteoblast differentiation for the two best peptides, VHVPLHRGAVSA and SGTQDSMVGWNK has also been determined through studying key target points as well as inhibition studies among the major osteogenic signaling pathways: BMP, Hedgehog, Wnt/β-Catenin, and Notch. These peptides follow two pathways, the Hedgehog and the BMP pathways independently. Additionally, the ridge groove 3D structure of the phage film contributes largely to differentiation through the Notch signaling pathway. The peptides displayed on phages were then directionally aligned on 3D printed porous titanium scaffolds using a double-sided freeze casting method. These scaffolds have Young's moduli and maximum strength not significantly different from natural bone before and after implantation demonstrating no degradation. Upon implantation of the peptide displaying phage-coated titanium implants in a rat radial bone defect model, bone regeneration was observed through Micro-CT, Von Kossa Staining, and H&E staining. Furthermore, the peptide-coated scaffolds showed greater bone regeneration around and within the scaffolds. The success of this work establishes a new technique whereby growth factor mimetic peptides can be discovered and used to coat implantable materials for tissue regeneration.

Chapter 1: Introduction

1.1 Viruses as a material in nanomedicine

Viruses come in a large variety of structures and properties which make them very useful for forming specialized structures in materials.[1-7] For example, M13 bacteriophages are filamentous in structure and can exhibit liquid crystalline properties which allow them to be arranged by a pulling force into ordered structures upon drying.[8-9] Even quasi-ordered 3D nano-bundles can be made from M13 bacteriophages.[10] Tobacco mosaic virus (TMV) is considered a rod-like virus or tubular structure.[11] Due to its tubular structure, it is naturally useful in nanotube assemblies, but is also useful in a variety of other applications.[11-15] Additionally, other viruses have icosahedral shapes such as with cowpea chlorotic mottle virus (CCMV).[16] CCMV has 180 identical coat proteins which assemble into a capsid having a triangulation number of T=3.[16] A special property of CCMV is that it can disassemble and reassemble based on the pH and ionic strength of its surrounding environment. This can be highly useful for drug encapsulation strategies.[16-17] In general, the various structures and properties of the many viruses play a key role in their applications as will be demonstrated. Several of these applications are illustrated in Figure 1.

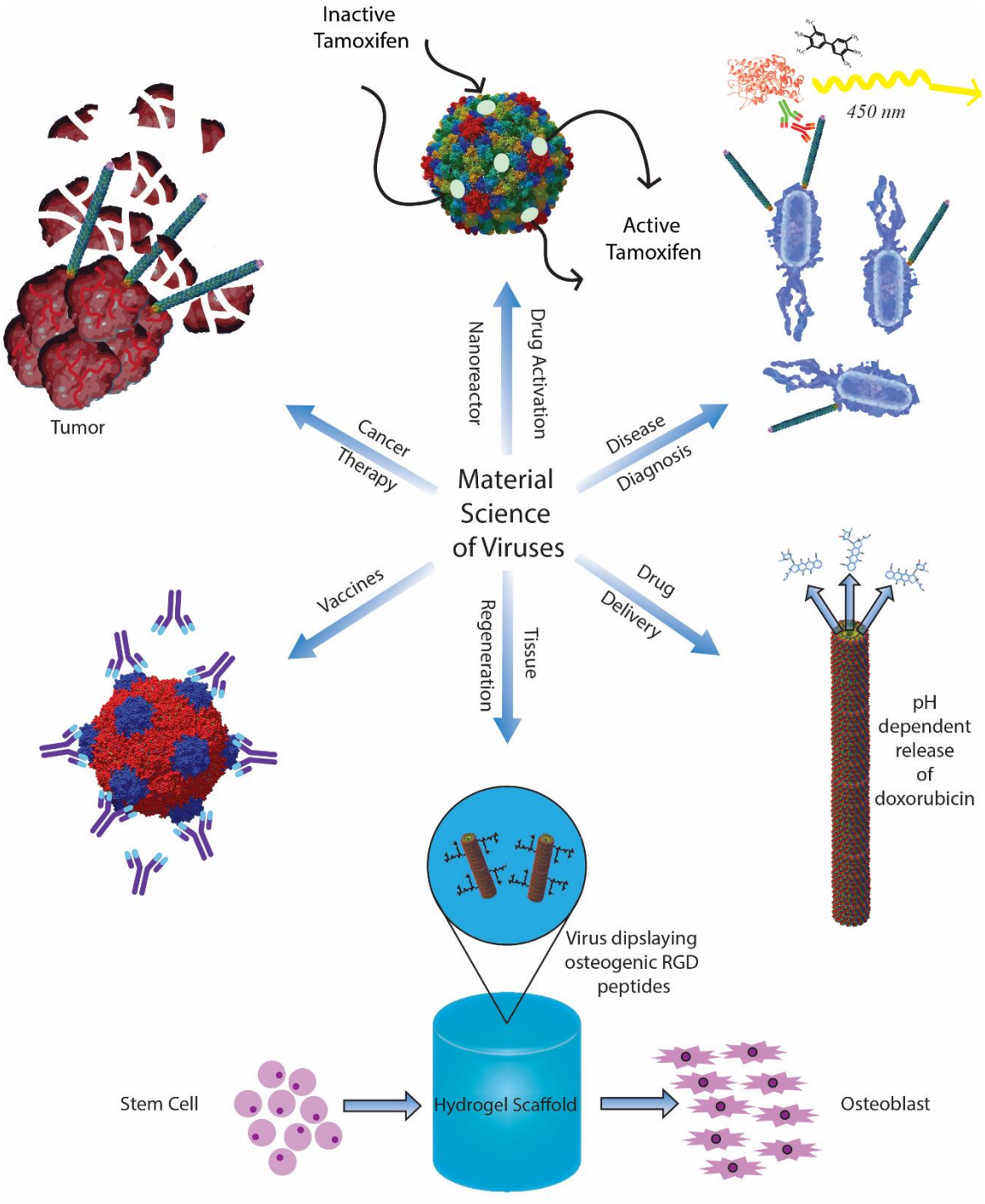


Figure 1. Viruses as a material in biomedical applications. Virus materials can be used in a number of applications such as vaccines, cancer therapy,

drug activation nanoreactors, disease diagnosis, drug delivery, and tissue regeneration.

1.2.2 Structures of different viruses

Several viruses' shapes and sizes are shown in Figure 2. The shape and size of each virus plays an important role in its applications. For example, if the application was to make nanotubes, a tubular-shaped virus such as TMV would be a good template but an icosahedral shaped CCMV would be a poor choice.[18] Additionally, shape and size can have major impacts for *in vivo* biomaterials. For example, even virus-like particles assembled from the same TMV coat protein can have significantly different circulation and clearance rates *in vivo* by varying their size and shape.[19]

M13 phage is a filamentous virus measuring roughly 9300 *Å* in length but having a diameter of just 65 Å.[20] The M13 virion contains roughly 6407 bases of circular single-stranded DNA encased in its coat proteins.[20-22] Of the coat proteins of M13 phage, the pVIII is the major coat protein having roughly 2700 copies helically arranged to form the filamentous structure of M13 phage.[23]Additional surface proteins include pIII, pVI, pVII, and pIX.[22-24]

MS2 phage is an icosahedral virus with a capsid made primarily of 180 copies of a coat protein shell.[25] Inside the shell is a single stranded RNA molecule. Each of MS2 phage's coat protein subunits come together to form a lattice having a triangulation number of *T=3*. This triangulation number is important as it describes the lattice of the major coat protein structure and structures often dictate the use of the virus in nanomaterials. The capsid has a diameter of 275 *Å*.[25]

P22 phage contains a double stranded DNA (dsDNA) with ~40 kilobases encapsulated by copies of a single capsid protein, gp5.[26-27] The icosahedral capsid has a triangulation number of *T=7*. The P22 procapsid undergoes several morphogenesis steps to reach the mature P22 capsid stage including the attachment of a tail spike on the final, infectious form. The diameter of P22 phage is 700 Å.[26]

TMV is a rod like or tubular shaped virus.[28] TMV is 3000 Å long and has a diameter of 180 Å. The central hole of the tubular shaped virus measures 40 Å in diameter.[28] The outer capsid is made up of around 2130 identical capsid protein subunits. Each subunit has a molecular weight of 17,500 and comes together to make a right-handed helix. The helix has a pitch of 23 *Å* consisting of 49 subunits in 3 turns.[28] The TMV RNA genome is made up of roughly 6400 single stranded, linear bases.[29]

The CCMV structure consists of 180 identical capsid proteins arranged into an icosahedral shell having a *T=3* quasi-symmetry.[30] The capsid measures 286 *Å* across (diameter) and encapsulates single stranded positive-sense RNA molecules.[30]

The grapevine fanleaf virus capsid consists of 60 identical coat proteins arranged in a pseudo *T=3* symmetry.[31-32] The icosahedral grapevine fanleaf viral structure measures 30 *nm* in diameter.[31] The capsid contains a bipartite positive-sense RNA genome.[31-32]

The cowpea mosaic virus (CPMV) capsid has a diameter of roughly 300 Å.[33] CPMV has a pseudo *T=3* surface lattice.[33] The capsid consists of both L and S protein subunits. The capsid encapsulates one RNA of length

5889 (RNA1) nucleotides and another having a length of 3481 nucleotides (RNA2).[33]

T7 phage is an icosahedral shaped virus with a short, noncontractile tail.[34] The capsid of T7 phage measures 60 to 61 nm in diameter.[34] T7 phages contain a 40 kilobase genome. The tail of T7 phages includes six fibers which are trimers of the gp17 protein.[34]

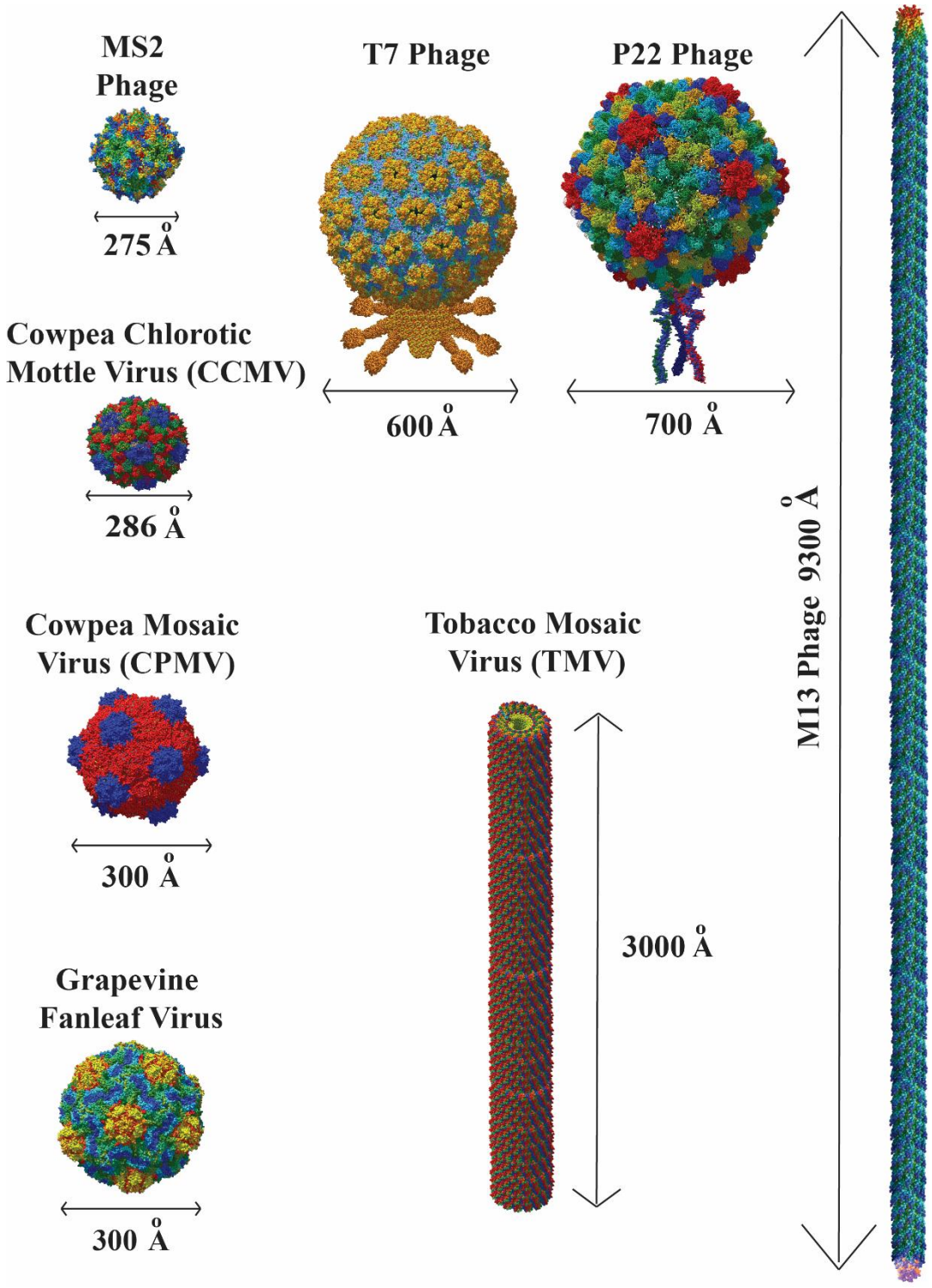


Figure 2. Overview of the various structures of viruses commonly used in material applications. All images were generated using data from the RCSB PDB.

1.1.3 Biological properties of different viruses

1.1.3.1. Chemical stability of different viruses

The stability of viruses is an essential feature for their use as nanomaterials. Their inherent stability arises as a property of their structural organizations. To gain a better understanding of virus stabilities, first information about the viruses' physical and geometric properties must be studied.[35] The arrangement of the molecules making up a virus' structure can be studied by electron microscopy or X-ray analysis. Once the viral structure is established, physicochemical observations can be done to study the assembly and disassembly of the virus. Lastly, by combining the study of physicochemical, chemical, and structural studies, more in depth information can be determined in regards to the specific noncovalent bonding which holds the virus together.[35]

TMV is a highly stable virus. Purified samples of TMV can be kept on a laboratory shelf for decades yet remain infectious.[35] However, as with other viruses, the ribonucleic acid (RNA) within the TMV can be destroyed by a ribonuclease or heat inactivation.[35] TMV does stay infectious even after being exposed to temperatures as high as 90 °C for 10 minutes.[36] TMV is also highly resilient and stable for years in water. TMV even exhibits some stability in polar organic solvents such as methanol (stable 24 hours) or acetone (stable 3 hours).[36] This stability in a variety of solvents can be very useful for chemical surface modifications. Within the intact TMV, the protein-protein and protein-RNA interactions account for the inherent stability of

TMV.[35] TMV is considered to be an ideal system for studying viruses as it is more stable than many other viruses.[35-36]

M13 phage is another highly stable virus.[37] For example, M13 phages can withstand pelleting in a centrifuge, vigorous pipetting, and repeated freeze thawing cycles without losing any appreciable amount of infectivity.[38] M13 phages are also not susceptible to osmotic shock even upon dilutions from 4 *M* NaCl into distilled water.[38] M13 phages can survive drying, and are resistant to denaturation by temperature. After being subjected to a temperature of 85 °C for 30 minutes, the infectivity of M13 phage only drops 10-fold.[38]

T7 phages which are commonly used for displaying functional peptides or creating peptide libraries are also considerably stable. T7 phages can survive being in 5 M NaCl.[39] T7 phages can also survive in 4 *M* urea, 2 *M* guanidine-HCl, and 100 *mM* Dithiothreitol (DTT).[39] T7 phages can survive a large pH range too (pH 4 to 10) which can make them an ideal virus to use in material applications. However, T7 phages can be rendered non-infectious with bleach or ultraviolet light.[39]

However, being highly stable, while desirable for many applications, is not always preferred. For example, CCMV virions have some interesting stability characteristics which can be exploited.[40-41] While not considerably stable compared to other viruses, the wild type CCMV (with viral RNA intact) is known to be stable between a pH range of 3 to 6.[42] CCMV is also stable under low ionic strength ($I \sim 0.1$ *M*). An interesting property of CCMV is that it disassembles at high ionic strengths ($I \sim 1$ *M*) at a pH above 7.[42] In addition, the virus swells in size up to 10% when the ionic strength is low

(I < 0.1 M) at a pH above 7.[42] A useful property for drug loading in CCMV is that the capsid proteins can be disassembled below a pH of 5 with an ionic strength between 0.1-0.2 *M* and then be reassembled by adjusting the conditions.[42] The reassembled viruses will still have the same shape and morphology as the wild type CCMV, but they will be devoid of RNA.[42-43] However, if the CCMV is then used under physiological conditions additional stabilization techniques should be considered.[44] Thus, it is important to consider the context of what application will be done with a virus when looking at its stability. Sometimes, very stable viruses such as M13 phage or TMV are ideal, but other times, encapsulation and reassembly strategies are far easier with less stable viruses such as CCMV. This will be an important concept to keep in mind when considering the applications of each virus.

1.1.3.2. Monodispersity

The monodispersity (not aggregated together) of viruses in a variety of solvents is highly important. In terms of dosages for medical applications, this is a necessity. In terms of consistently making well-ordered nanomaterial structures, this is also an important characteristic to have. While it has been discussed that viruses can be highly stable under a variety of conditions, they can also remain well dispersed and dissolved in a variety of solvents. For example, TMV can be dissolved in water, phosphate buffer, methanol, Dimethyl sulfoxide (DMSO) (80%), ethylammonium mesylate, and propylammonium mesylate.[35] As another example, M13 phages are also stable and capable of being dissolved (in a monodisperse way) in some organic solvents.[37] Lastly, the viruses discussed naturally dissolve in aqueous environments, making viruses a good material for consistent,

uniformly distributing applications.[45-46] Such applications could range from creating even distributions of phage films, having consistent dosages to patients, and creating highly ordered electrodes for batteries.

1.1.3.3. Biocompatibility

The biocompatibility of virus-based materials is of great importance for medical applications. If a virus is to be used *in vivo*, how the immune system reacts as well as the fate of the virus should be known to avoid potential unintended side effects. The viruses described in Figure 2 do not infect humans, but they can still elicit an immune response *in vivo.* Sometimes, as with virus-based vaccines, this is an intended consequence.[47] However, with other applications such as drug delivery, unintended immune responses are not ideal. It is known that viruses which do not naturally infect humans still illicit an immune response.[48] Some viruses which do not infect humans such as bacteriophage phi X 174 are well established in terms of our immune response to them.[48] However, not all of the viruses discussed in this review have been evaluated with such depth in humans. Still, several studies have been completed in animal models which have demonstrated a number of these viruses to be biocompatible.[7, 49] For example, Pratik Singh et al. evaluated the biocompatibility of CPMV and found it to be a safe, non-toxic material for *in vivo* use.[50] CPMV was found to have a rapid clearance from plasma (20 minutes in a mouse model). After just 30 minutes almost all of the CPMV particles were trapped in the liver with some also in the spleen. No toxicity was detectable even at doses of 100 *mg* per kg body weight. However, elevated B lymphocyte levels were present on the first day of virus

administration, but they did subside quickly.[50] Another virus used in many material applications is CCMV. Coleen R Kaiser et al. have evaluated the biocompatibility of this virus in mice.[51] A broad distribution among most tissues and organs was found. CCMV was also rapidly excreted (within 24 hours) and had no long-term persistence among tissues or organs. Additionally, no overt toxicity was observed after a single injection.[51] M13 phages have also been evaluated.[52] The half-life of wild type M13 phages in plasma (of C57BI/6 mice) was found to be 4.5 hours. M13 phages primarily ended in the spleen and liver indicating uptake by the reticuloendothelial system.[52] TMV is another virus that has been evaluated for biocompatibility by Michael A. Bruckman et al. in Balb/c mice.[19] The rod-shaped TMV particles were found to be cleared by macrophages in the liver and spleen, eventually ending up co-localizing in B-cell follicles. The TMV particles were then cleared from the liver and spleen within days. No changes in histology were observed and no blood clotting or hemolysis occurred thus demonstrating the biocompatibility of TMV.[19] Additionally, TMV has been coated in stealth proteins to study the effect on circulations time.[53] MS2 phages have also been studied in terms of biodistribution by Jacob M. Hooker et al. in Sprague–Dawley rats.[54] MS2 phages cleared from the blood rapidly. It was demonstrated that less than 0.01% ID/g of [^{18}F] fluorobenzaldehyde (chelated to MS2 phages) remained in the blood 3 hours post-injection. MS2 phage particles primarily accumulated in the liver and spleen after 3 hours.[54] With the amount of work done to evaluate the biocompatibility of several of these viruses, it is clear that viruses have the potential to be very good biomaterials. However, the limited data for

biocompatibility in humans is one issue that will need to be addressed in the future. Studies should also be done on longer term responses to multiple injections of viruses. Additionally, it is now understood that there is a widely diverse set of bacteria which symbiotically exist in the human gut.[55] There will be a need to understand what effects introducing new viruses will have on this natural system. For example, will introducing a new virus upset the balance of bacteria? This is an essential question to answer as the field moves forward.

1.2 Phages

1.2.1 History and classification of phages

One century ago, on September 3, 1917, Félix d'Hérelle announced he had “isolated an invisible microbe endowed with an antagonistic property against the bacillus of Shiga”.[56] He called these antagonists “bacteriophages” (phages). Since this discovery, phages have been employed for several uses. For example, lytic phages were widely used as an antibacterial agent until the invention of antibiotics seemingly appeared to make them obsolete.[57-58] However, with the development of antibiotic resistant bacteria, medical professionals around the world have resorted to employing lytic phages to treat common and antibiotic resistant bacterial infections.[59] In spite of their immunogenicity, phages have been reported to elicit only a mild immune response, which gives promise to their potential use in humans.[59] In fact, phage therapeutics is currently a very vibrant area especially in the context of the new clusters of regularly interspaced short palindromic repeat and associated genes (CRISPR/Cas) system and its ability to provide

selective pressure for antibiotic sensitive bacteria.[60-65] Specifically, bacteria actively using the CRISPR/Cas system to fight off some phage infections have been shown to lose their antibiotic resistance.[60-65] Indeed, even large scale human clinical trials have been completed or are underway such as the phagoburn (phase I-II clinical trials) project funded by the European Union under the 7th framework program for research and development.[58, 66-67] The phagoburn project focuses on treating infections caused by burn wounds with professionally lytic phages, and is a large scale clinical trial utilizing phages in medicine.

With the development of nanobiotechnology since 2000, using both lytic and temperate phages as biological nanoparticles have begun to fulfil a new role in nanomedicine. Precision medicine, ultrasensitive disease diagnosis, and targeted disease treatment in particular, have been greatly advanced by the emerging research with phages.[68] At the forefront of these advancements are intricate systems in which the natural biology of phages is utilized in addition to enhancements via genetic engineering. Such integrated systems make it possible, for example, to invent new highly sensitive ways to detect diseases as well as create biomaterials that are a hybrid of genetically engineered phages and inorganic materials for targeted disease treatment. They also allow for precision targeting in drug and gene delivery because they can be genetically engineered to bear targeting molecules or be used as a platform for identifying targeting molecules. This precision targeting is particularly useful for diseases such as cancer in which standard methods of treatment impact far more than their intended target, causing severe side effects.

The lack of medicinal use of phages in the US and UK to date has been attributed to a lack of acceptance by the mainstream scientific and medical authorities due to a lack of data from the Eastern European practitioners meeting Western standards for medical efficacy safety.[59]However, with present day increasing resistance to antibiotics and the pressing need for precision medicine, phages have become a versatile and extraordinary tool in nanomedicine. With promising new therapies available and the completion of several clinical trials, phage therapy has now been developed into a commercially viable technology. With this development, companies such as Pherecydes Pharma (based in the United Kingdom and France) have been leading the way to a new era of phage therapeutics.

The versatility of phages in nanomedicine in regard to precision targeting, self-assembled biomaterials, and many more techniques is in large part due to the natural biology and structure of phages. From a biological perspective, phages are a virus that specifically infect bacteria. They are classified taxonomically into families, but due to the rapid changes in the established taxonomies from year to year, the most current existing taxonomical families should be referenced according to the international committee on taxonomy of viruses.[59, 69] Each family is assorted according to the structure of their capsids encompassing their genomes, the chemical and structural composition of their genomes (linear, circular, double, or single stranded, DNA or RNA), and the mechanism of mRNA production.[59]In terms of making use of phage biology, there are several reviews encompassing phage display[70-78] and bacterial biosensing[79-80]. Phage display is useful for finding peptide ligands that can specifically bind to disease associated receptors and

microenvironments.[59, 81] Additionally, nanotechnology often employs the use of phage morphologies such as the naturally occurring filamentous structure of M13 phages.

1.2.2 Life cycles of phages: temperate vs. professionally lytic

Phages exist in various shapes and sizes from long rod-like filaments to more compact shapes with much shorter tails. A few representative phages are shown in Table 1. Despite their many differences, two broad categories, professionally lytic or temperate phages are sufficient to briefly understand phages (Table 1).[82] In essence, professionally lytic phages break open and kill the host bacteria when they infect bacteria to get amplified and then leave the bacteria. However, temperate phages do not kill the host bacteria when they infect the host bacteria; instead, they only use the host bacteria as a factory to be amplified and finally get secreted from the host. Additionally, it should be noted that some phages share qualities from both categories. For example, the term professionally lytic refers in particular to the predominant lifestyle of being lytic but that does not mean that this phage type cannot have phages capable of having temperate qualities.[82] For example, the temperate phage called lambda is one such phage. Infection by Lambda phage begins when the phage attaches to the host cell and injects its DNA into the cell. From here, the phage either enters the lytic or lysogenic cycle.[83] If followed, the lytic cycle involves the immediate replication of the phage DNA by bacterial machinery. The DNA templates are then used for production of phage proteins, which are assembled into phage particles. When phage particles build up, the cell undergoes lysis and is broken into fragments.[84]The phages are then released and begin infecting additional bacteria.

Upon viral DNA entry into the bacteria cell, the phage DNA may also enter the lysogenic cycle. In the lysogenic cycle, viral DNA integrates into the host genome through recombination, producing a prophage. Although a less common path, the lysogenic pathway can be followed when conditions are unfavorable for bacterial cell replication. Thus, this phage can also have temperate qualities. The prophage is then replicated each time the bacterial cell replicates. In lambda phage, to prevent a phage from being cut out of the genome and entering the lytic cycle, the lambda repressor is synthesized from the transcribed cI gene product and occupies the O_R1 and O_R2 sites.[85-87] This represses the cro gene. If conditions make cell death likely, the repressor protein is cleaved in half by recA (from the cell's distress response to DNA damage) and the cro gene is derepressed.[85, 88]The cro protein is created and occupies the O_R3 site, turning off transcription of the cI gene.[85] This allows the prophage to be cut out of the host genome and enter the lytic cycle.

Professionally lytic phage types are generally composed of a head and flexible tail, but lack the long filamentous shape shared by most temperate phages. These phages primarily resort to lysing the host cells during the infection cycle and some key examples of professionally lytic phages include T1-T7 phages.[82] These phages are often used in phage-based antibacterial strategies. An example of a professionally lytic phage is T7 phage. T7 phage is a member of the *Podoviridae* family and has an icosahedral head with a short tail. When T7 phages infect cells, several internal capsid proteins get ejected into the host cell wall and assemble an ejectosome allowing for the translocation of DNA from the T7 viral capsid into the cell.[89] The viral DNA immediately begins a process in which a set of proteins necessary for

replicating the phage DNA are transcribed and translated from the viral DNA template. This results in several copies of the viral DNA being made.[89] Next, a second set of proteins are made and assemble into the various structural components of the phages. Lastly, while the assembly process is taking place, lysozyme is produced. The lysozyme will lyse the host's cell wall and allow for the release of the mature viruses.[90] This whole process is actually quite fast and depending on the fitness of the phages; It can take just a matter of minutes to complete.[91] Therefore, professionally lytic phages have gained a lot of attention in antibacterial applications.

The temperate inoviruses are filamentous phages including the Ff, M13, f1, fd, Ike, and N1 phages.[59] So far, filamentous phages have found more applications in templating nanomaterials synthesis than professionally lytic phages, probably because filamentous phages tend to be used to template nanowires synthesis and self-assemble into higher-order structures. Filamentous temperate phages can be pictured as a long flexible nanofiber composed of five structural capsid proteins, which encase a relatively large circular single strand of DNA.[23, 92]One example includes wild-type M13 (Table 1), which measures ~9300 *Å* long, but has a diameter of only 65 *Å.*[20]The M13 virion consists of ~6407 bases of circular single-stranded DNA (ssDNA) in its genome, but longer genomes generate longer phages.[20-22]Although there are five different proteins, the majority of a filamentous phage is coated by ~2700 copies of a protein encoded by a single gene called pVIII,[23] which is helically arranged to form a filament tube.[92]This is the protein that is often modified for desirable characteristics in the lab, and the filamentous temperate phages can serve as a highly structured nanomaterial. The ends of filamentous phages

are composed of minor coat proteins. One end is composed of five copies of the proteins pIII and pVI, while the opposite end displays five copies of the proteins pVII and pIX.[22-24]The filamentous structure and major coat proteins are what makes these phages capable of creating many self-assembled nanostructures as well as develop excellent targeting abilities.

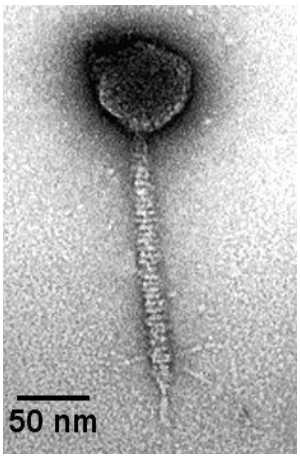
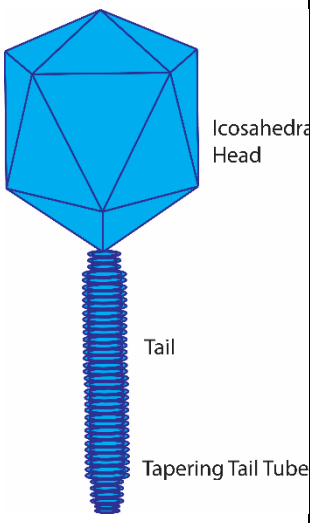
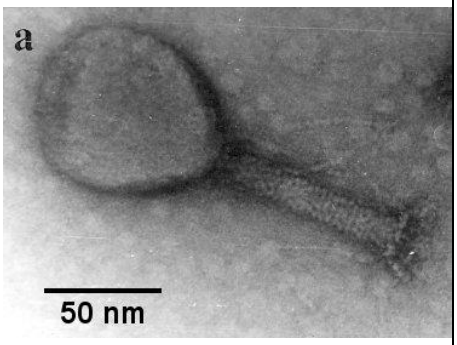
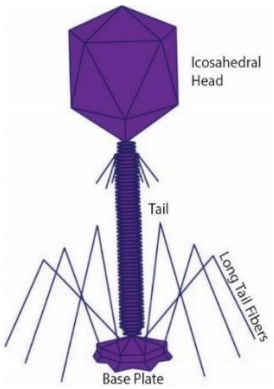
Unlike professionally lytic phages, filamentous phages are secreted from bacteria without bacterial cell lysis.[23, 92]Filamentous phages infecting *Escherichia coli* are among the most productive phages and can produce titers of up to 10^{13} phages per milliliter of culture.[92]The infection cycle begins when the minor coat protein at the tip, pIII, utilizes its N2 domain to bind to the F-pilus on the surface of a bacteria cell.[93] The F-pilus will then retract, pulling the phage closer to the surface of the bacterium.[20, 93-94]Next, it is thought that the N1 domain of pIII binds to the TolAIII domain on the highly conserved inner membrane complex, TolQRA.[92-93] Interaction of the C domain of pIII with the TolQRA complex or some conformational rearrangement of the C domain of pIII then exposes the hydrophobic C-terminal helix of pIII, allowing insertion of the helix into the inner membrane.[92]Finally, the phage ssDNA is injected into the cytoplasm, where it can either begin replicating (episomal) or integrate into the host's chromosome (temperate).[92] If the ssDNA goes the temperate route, it becomes a substrate for XerCD recombinase, which will bind to the forked hairpin loop termed AttP[92] and integrate the viral DNA into the bacterial genome through site-specific recombination at the dif site located between the chromosomal DNA and a previously inserted satellite phage such as RS1φ or TLCφ.[95]This process is called lysogenization. After integration into the chromosome, there may come a time when it is beneficial for the virus to

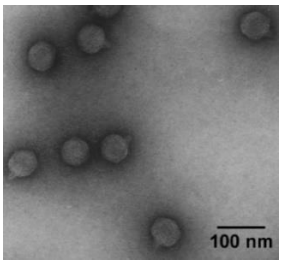
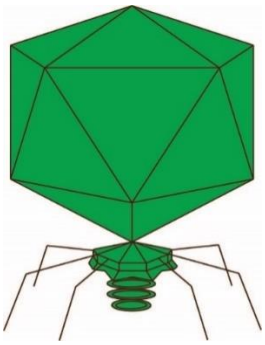
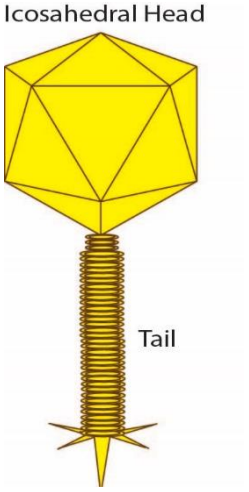
undergo induction. Such an event could occur if the cell undergoes damage as shown in experiments using UV light or Mitomycin C, which will incite a cellular SOS response in which LexA is degraded.[92]This results in P_A promoter transcription, which will eventually lead to the releasing of the recirularized old ssDNA, which is a combination of the satellite and prophage between the two origins of replication. It is important to note the resulting replicon is not the same as the one initially integrated into the chromosome.[92]The ssDNA can then replicate by the episomal path.

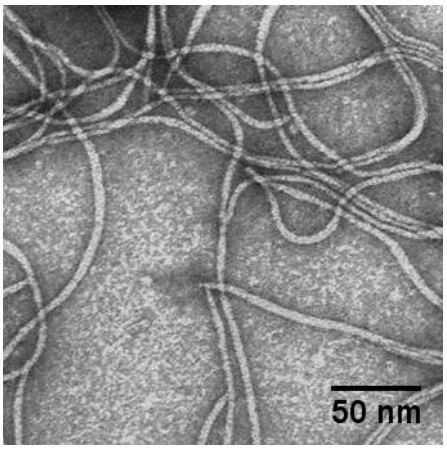
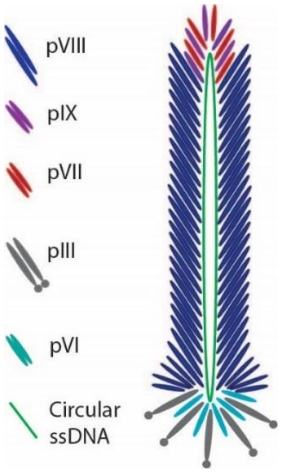
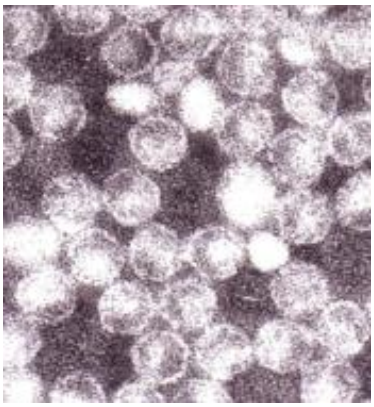
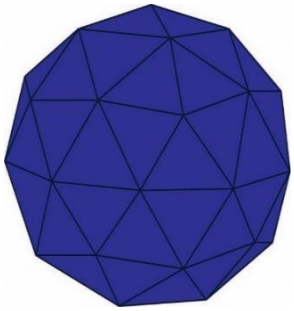
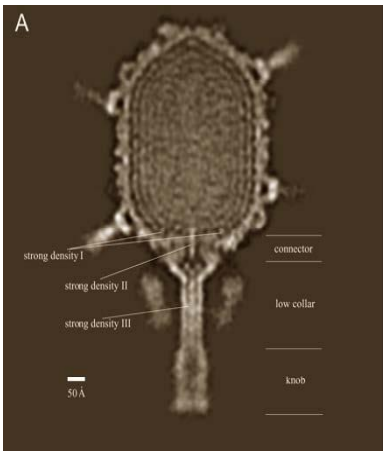
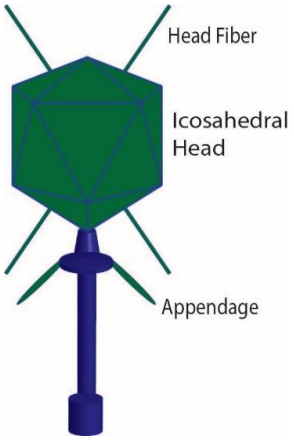
Negative strand synthesis of the ssDNA is carried out by bacterial RNA polymerase, which will first generate an RNA primer that is subsequently released from the template ssDNA.[96] Bacterial DNA polymerase III then creates a replica of the negative strand based on the RNA primer sequence. The positive strand synthesis is then initiated by the non-structural phage protein pII. Supercoiling occurs on the double-stranded DNA (dsDNA), which forms a stem-loop structure that allows a nick in the positive strand of the dsDNA to be created at the origin of replication.[92]Rolling circle replication then completes the new copy of viral DNA.[97] The copies of the replicative form of viral DNA then serve as a template to produce the non-structural phage proteins pII, pV, and pX to help with packaging of the substrate and genome replication.[20, 92]Non-structural proteins pI, pIV, and pXI are also created from the replicative form using bacterial cell machinery and form a transport complex spanning the outer and inner membrane of the bacteria cell. The phage structural proteins pVII, pIX, pVIII, pVI, and pIII are then inserted into the membrane for latter assembly into the phage virion.[24, 92] The positive strands of viral DNA are then coated by dimers of the ssDNA binding protein,

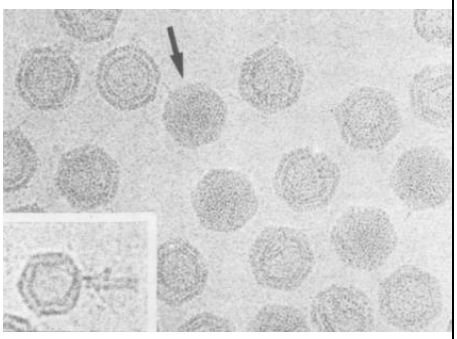
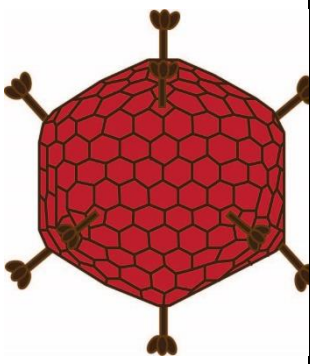
pV, and transported to the cell membrane for packaging by the transport complex and assembled into the exported virion form of the phages.[20, 92]

Table 1. Various structures and applications of phages in nanomedicine (Reproduced with permission from John Wiley and Sons)

Type of Phage	Electron micrograph image	Schematic	Common Applications
λ Phage (temperate)	 **Electron micrograph of a lambda phage negatively stained with 2% uranyl acetate.[98]**		Delivery of plasmid DNA into cells without cytotoxicity and in a concentration-dependent manner to mammalian cells.[99]
T4 Phage (professionally lytic)	 **TEM image of** a **T4 phage.[100]**		Food preservation[101] and antibiotics[102]. Magnetically-assisted impedimetric detection of bacteria.[103]Phage-based DNA and protein packaging, expression, and display systems.[104] T4 phage is also implemented in DNA delivery for potential vaccines.[105]

T7 Phage (professionally lytic)	 **Electron micrograph of negatively stained T7 phages.[106]**		Detection of protein markers through real-time immuno-PCR.[107] Detection of viral infections.[108] Rapid detection of *E. Coli* in drinking water supplies.[109] Naked eye counting of miRNA for disease diagnosis.[110]
Podovirus P22 (professionally lytic)	 **Podovirus P22 of *Salmonella typhimurium* at X 297,000 magnification.[111]**	Similar to T7.	Used in the assembly of CdS nanocrystals for enhanced photoactivity in tissue imaging.[112]
Siphovirus ɣ (professionally lytic)	 **Siphovirus ɣ of *B. anthracis* at X 297,000 magnification.[111]**		Used for the identification of B. anthracis, the etiologic agent of anthrax.[111]

M13 and *fd*Phages (temperate)	 **TEM image of M13 phage[113]**		Widely used for self-assembled nanostructures such as nanowires[114] and functionalized SWNTs[115]. Also prominent in targeted drug delivery, cancer treatments, and imaging. [116-117] Filamentous phages have also been implemented in siRNA delivery for gene therapy[118] and tissue regeneration[119-120]
Levivirus MS2 (professionally lytic)	 **Levivirus MS2 of *E. coli* at *X* 297,000 magnification.[111]**	 **Genome free schematic of mtMS2 phage particle.**	Used for multifunctional drug delivery vessels and tissue imaging.[121-123]
Φ29 Phages (professionally lytic)	 **CryoEM map of a Φ29 phage. High densities are white and low densities are black. The various proteins and DNA are labeled.[124]**		Development of a DNA packaging nanomotor associated with developing hybrid bio-nanostructures.[125]

PRD1 Phages (professionally lytic)	 **Cryo-electron micrographs of wild-type PRD1 phages mixed with a preparation of susI packaging mutant at 2 *μm* underfocus. The arrow points to a DNA filled phage particle and the inset shows a particle which has lost its DNA and formed a tail from the membrane.[126]**		Antibiotic studies involving the loss of antibiotic resistance in bacteria harboring an RP4 plasmid.[127]

1.3 Virus-derived peptides for biomedical applications

The proper diagnosis and treatment of illnesses is of vital importance worldwide. For example, cancer is a major cause of human death worldwide.[128] In the United States, ~25% of deaths are caused by cancer. There were a projected 1,660,290 new cancer cases and 580,350 deaths in 2013.[129] In China, according to the National Death Survey conducted by the Ministry of Health, cancer is currently the second leading cause of death due to increasing cancer mortality rates in the past years.[130] However, cancer patients are just one of many disease groups that can benefit from swift diagnoses and targeted treatments. Pathogens are another major cause of death. More than 9 million pathogen related illness diagnoses are due to foodborne pathogens in the United States alone.[131] Bacterial pathogens such as *Salmonella enterica* and *Listeria monocytogenes* alone account for $3.3 billion and $2.6 billion in medical costs a year in the United States, and this only scratches the surface. It is estimated that just 14 foodborne pathogens account for $14 billion a year in medical costs for the United States.[132] Among

other pathogens, fungal infections such as those caused by *Candida albicans* and *Paracoccidioidesbrasiliensis,* can also be devastating. It is estimated that the most common fungal diseases in humans affect ~1.7 billion (or roughly 25%) of the general worldwide population. Despite the current availability of antifungal drugs, invasive fungal infections often have mortality rates exceeding 50%.[132] Additionally, viral diseases such as *orthopoxviruses* (*cowpox* and *monkeypox*) infections, avian influenza A, and parasitic illnesses such as malaria or schistosomiasis are also devastating.[133-137] Hence, there is an overwhelming need for disease detection and therapeutics. These techniques must be both more effective than currently lacking techniques and cost-effective so that they may be used more widely around the world. This section will describe cutting edge techniques for disease detection and therapeutics centered around the development of short organism-binding peptide sequences developed through virus-peptide display technology.

Over the past decades, researchers have put forth a huge effort and investment towards developing affinity agents, including antibodies, proteins, peptides and nucleic acids.[138-146] The use of peptides now has an ever expanding role with unexpected applications and has even been implicated in virus communication to name just one unique role.[147] For example, it has been shown that phages can communicate with each other to make a group decision in regards to their life cycle using a peptide.[147] It would be of great importance to discover whether or not more dangerous viruses react in a similar manner. Among these applications, peptides possess several advantages in biomedical applications.[148-153] First, peptides can be easily obtained by chemical synthesis with a high yield and low cost. Second, due to

their small molecular weight, peptides (~10 amino acids long) can enter cells and penetrate tissue easily, be cleared in the blood rapidly, are quickly metabolized, and have a low immunogenic nature. Another advantage is that peptides do not need to be produced in animals or with cells which makes them more ethical as well as economical than antibody development techniques.[153] These advantages make peptides very appealing for biomedical applications, such as molecular imaging, disease diagnosis, and therapy.

Organism-targeting peptides, which can selectively bind to a specific type of organism with high affinity, have been derived from several different origins. One way to discover organism-targeting peptides is to use peptides that are ligands for specific cell-surface receptors. A good example of this is RGD (Arg-Gly-Asp) and its derivatives.[154-158] RGD is also one of the first tumor-homing peptides which was discovered by randomly synthesizing portions of the amino acid sequence from fibronectin.[159-160] RGD shows a high selectivity and strong affinity to the integrins that are highly expressed on the surface of some kinds of cells such as cancer cells and is useful in a number of applications.[161-164] This method of identifying peptides is based on guessing and checking, which can be very cumbersome for larger peptide sequences. Therefore, more efficient methods have gained interest. Some of the most effective strategies for discovering novel targeting peptides are evolutionary screening virus-peptide display techniques.[165-167] For example, through biopanning with phage, the well-known RGD motif has been rediscovered by Wadih Arap et al. where it is part of a longer sequence, CDCRGDCFC.[168] This has become a famous sequence now called RGD-4C.[168-170] Despite the massive potential

impact of such treatments worldwide, this topic of combining biopanning with peptide-based treatments is relatively new and upcoming and has thus not yet received much attention. Table 2 gives a few examples of human clinical trials involving virus-derived peptides. Additionally, an overview of the available virus-derived peptides can be found in Table 3 (pathogen targeting), Table 4 (human cell-targeting), and Table 5 (tissue-targeting).

Table 2. Examples of Virus-derived Peptides in Clinical Trials for Humans

Status / Year	Study Title	Brief Description	Condition	Virus Type Used to Discover Peptides	Reference
Recruiting Participants as of November, 2016	Electro-Phage and Colorimetric Aptamer Sensors for Clinical Staging and Monitoring of Bladder Cancer	This study seeks to identify a molecular fingerprint (peptide) capable of detecting recurrent bladder cancer using phage display technology.	Bladder Cancer	Phage display library.	[169]
Not yet recruiting as of July, 2016	Peptide-drug-conjugates for Personalized, Targeted Therapy of Chronic Lymphocytic Leukemia	Phage libraries will be used to isolate phages specifically internalized by chronic lymphocytic leukemia cells taken from newly diagnosed and untreated patients. Following treatment options will then be tailored to the specific patients' results in terms of binding peptides isolated from each patients' individualized biopanning study.	Chronic Lymphocytic Leukemia	Phage display library to be used.	[169]
Study is ongoing as of April, 2014	Gluten-free Diet in Gluten-genetically Predisposed Subjects	The gluten dependent humoral immune response will be measured by means of phage display libraries before and after 12 months of a gluten-free diet. This study seeks to demonstrate the mucosal gluten-dependent response in relation to a gluten-free diet. It will also evaluate the targeting specificity of a double staining	Celiac disease	Phage display library to be used.	[169]

		technique for detecting IgA antitransglutaminase mucosal deposits utilizing antibody fragments developed through phage display.			
Study Completed, 2002	Steps toward mapping the human vasculature by phage display	This study was carried out on a 48-year-old male Caucasian patient with the intention of mapping the human vasculature system in terms of finding homing peptides for all tissue targets.	Not intended for just one condition but to create a molecular targeting map for the human vasculature system usable for future clinical applications.	M13 phage CX7C library	[171]
Study Completed, October 2015 (It should be noted that there are a large number of clinical trials using this virus derived peptide. This is just one example.)	Study of AMG-386 in Combination With Paclitaxel and Carboplatin in Subjects With Ovarian Cancer	Trebananib (AMG-386) is a peptibody discovered through phage display which blocks the interaction between angiopoietin-1 and angiopoietin-2. Blocking this interaction reduces angiogenesis and therefore the growth of tumors. This study evaluated a combined treatment using AMG-386 with paclitaxel and carboplatin as a treatment for stages II-IV of epithelial ovarian, primary peritoneal, and fallopian tube cancers.	Stages II-IV of epithelial ovarian, primary peritoneal, and fallopian tube cancers.	Three filamentous phage libraries were used called TN8-IX, TN12-I, and Linear ($1.0x10^{10}$ independent transformants)	[169, 172]

Study Completed February, 2015	DNX-2401 (Formerly Known as Delta-24-RGD-4C) for Recurrent Malignant Gliomas	The phage library derived sequence CDCRGDCFC (often called DNX-2401 or 24-RGD-4C) homes to multiple tumor types (including carcinoma, sarcoma, and melanoma). This study was to determine the highest tolerable dosage and to determine the effect of the peptide on tumors.	Brain tumors	Phage library	[168-169]

Table 3. Pathogen-targeting peptides derived from virus libraries

	Pathogen	Viral Library // Virus type	Targeting peptide sequence	Applications	Ref.
Parasite	Rhipicephalus (Boophilus) microplus (cattle tick)	fUSE5/15-mer // M13 phage	RNLWPGDLRWVGWH, RLGPLHFLNAWGHDH	Potential targeted chemotherapy / vaccination strategies	[173]
	Plasmodium, (the causative agent of malaria)	XCX_8CX // M13 phage	PCQRAIFQSICN	Inhibited *Plasmodium* invasion of salivary gland and midgut epithelia to prevent malaria	[174]
	Schistosoma japonicum schistosomula	Ph.D.-12 // M13 phage	YSGLQDSSLRLR	Exhibited potent schistosomicidal activity *in vitro*. Also a possible drug carrier.	[175]

	Leishmania major	Hexapeptide Library // M13 phage	MAAKYN	Inhibits *L. major* growth kinetics *in vitro,* and reduces cutaneous lesions	[176]
Yeast / Fungus	*Candida albicans*	Ph.D. 12 // M13 phage	ELMAVPVPLPPA, SEYTSQLIFTAT, SEFSYIVIDTSL, ELTAILVSPAPL, ELNAQHIMEPKY, ELIPMLIMQSTS, EDYSTIMKTLAH, STPKSPHSVASH, AVQHNPTHPFYP	Rapid, highly specific diagnosis of *Candida albicans infection*	[177]
	Candida albicans disease biomarker (antisecreted aspartyl proteinase 2 IgG antibody)	Antibody M13 phage display library // M13 phage	VKYTS	Highly sensitive diagnosis and detection of *Candida albicans infection (indirectly by looking for the immune response)*	[178-179]
	Paracoccidioidesbrasiliensis	CX7C // M13 phage	CGSYGFNAC	Selectively kills only virulent *Paracoccidioidesbrasiliensis*	[180]

				yeasts to treat Paracoccidioidomycosis	
Virus	*Avian influenza A H5N1*	VHH Library // M13 phage	AAGPLSWYAHEFLEYSGHEYNY, TEHRGFDDNDYVLPALGARAANY, AAPPLPDCYSGSWSPFTDEYNY	Diagnosis of H5N1 infection	[181]
	Avian influenza A H7N2	VHH library // M13 phage	See reference for full length sequences.	Diagnosis of H7N2 infection	[182]
	orthopoxviruses	Ph.D. 12 // M13 phage	TADKLLYGLFKS	Orthopoxvirus detection	[183]
Bacteria	*Klebsiella pneumoniae*	Naïve human single chain fragment variable // M13 phage	See reference. Sequences not provided.	*Klebsiella pneumoniae* antibody therapeutics and vaccines	[184]
	Listeria monocytogenes	VHH library // M13 phage	AARRGPGTSVLSDDYDY, ATTRTPRVRLPTESREYTY	Detection and diagnosis of the foodborne pathogen *Listeria monocytogenes*	[185]
	Salmonella	PhD-12 // M13 phage	NRPDSAQFWLHH	Rapid *Salmonella* testing	[186]
	E. coli and P. aeruginosa	PhD-12 // M13 phage	RLLFRKIRRLKR	Bactericidal activity against *E. coli* and *P. aeruginosa*	[187]
	Staphylococcus aureus	Ph.D.-12 // M13 phage	VPHNPGLISLQG	Detection and diagnosis of *Staphylococcus aureus* infection	[187]

	Mycobacterium leprae	Ph.D.-12 // M13 phage	LEQCQES, LEQCQES	Diagnosis and potential vaccine for Leprocy	[188]
	Mycobacterium tuberculosis	Ph.D.-7 // M13 phage	WHLPLSL	Diagnosis of tuberculosis	[189]

Table 4. Summary of human cell-targeting peptides derived from virus libraries					
	Organism / Cell type	Viral library	Targeting peptide sequence	Applications	Ref.
Cancer cells	Human breast carcinoma SKBR-3	f8/8 landscape // M13 phage	VSSTQDFP	SKBR-3 breast cancer cells internalization	[190]
	Basal cell adhesion molecule (BCAM) and laminin subunit alpha 5 (LAMA5) of human colorectal cancer cells	Ph.D. 7 // M13 phage	ASGLLSLTSTLY, SSSLTLKVTSALSRDG	Impairs adhesion of KRAS-mutant colorectal cancer cells to endothelial cells	[191]
	Esophageal cancer cells	Ph.D.-12 // M13 phage	RALAHPRDHPDL, ATCSMLLSRNEA	Early screening of esophageal cancer	[192]
	PPC-1 human prostate carcinoma cell	T7 library // T7 phage library	(R/K)XX(R/K)	PPC-1 human prostate carcinoma cell targeting	[193]
	PC3 human prostate cancer cells *in vitro* and *in vivo*	Ph.D.-12 // M13 phage	KQFSALPFNFYT	Targeted delivery of doxorubicin to prostate cancer cells	[194]
	Colon cancer cell line SW480	Ph.D. 7 // M13 phage	VHLGYAT	Imaging	[195]
	U87MG malignant glial cell line	Ph.D. 12 // M13 Phage	VTWTPQAWFQWV	Drug delivery	[196]
	Hepatocellular carcinoma cell line BEL-7402	Ph.D. 12 // M13 phage	AGKGTPSLETTP	Drug delivery	[197]
	Cervical carcinoma	CX9C // M13 phage	C(R/Q)L/RT(G/N)XXG(A/V)GC	Drug delivery	[198]
	Human colorectal cell line WiDr	Ph.D. 12 // M13 phage	HEWSYLAPYPWF	Gene delivery	[199-200]
	Neuroblastoma, and breast cancer cell	Ph.D. 12 // M13 phage	VPWMEPAYQRFL	Imaging	[201-202]

	Acute myeloid leukemia cells	X_7 AAV2 // adeno-associated virus 2	NQVGSWS	Acute myeloid leukemia gene therapy	[203]
	HO-8910 ovarian cancer cells	Ph.D.-7 // M13 phage	NPMIRRQ	Potential ovarian cancer diagnosis tool	[204]
	Human gastric adenocarcinoma cancer cells	Ph.D. 12 // M13 phage	ETAPLSTMLSPY	Peptide can bind to the surface of gastric adenocarcinoma cancer cells and reverse their multidrug resistance.	[205]
			IHKDKNAPSLVP	High affinity and specificity binding to gastric adenocarcinoma cancer cells.	[206]
	HO-8910 ovarian cancer cells Promiscuous ligand targeting of Lung and pancreatic cancer cells	Ph.D.-C7C // M13 phage	SWQIGGN	Control of ovarian cancer cell migration, viability, invasion, and adhesion capacity	[207]
		F8/9 // M13 phage	GSLEEVSTL, GEFDELMTM	Promiscuous ligand targeting of lung and pancreatic cancer cells for targeted doxorubicin delivery	[208]
Stem cells	Primate embryonic stem cells	Ph.D. 12 // M13 phage	APWHLSSQYSRT	Imaging	[209]
	Human mesenchymal stem cells	Ph.D. 7 // M13 phage	EPLQLKM	Recruitment of hMSCs	[210]
	Human pluripotent stem cell-derived progenitor cell lines	Ph.D. 12 // M13 phage	EWLFEFPTPVDA DWIATWPDAVRS	Cell isolation	[211]
	Adult neural stem cell surface	Ph.D. 7 // M13 phage	KLPGWSG	Enhanced neural stem cell neuronal	[212]

	receptors (one or more)			differentiation *in vitro*	
	Human embryonic progenitor cell line W10	Ph.D. 12 // M13 phage	DWLWSFAPNVDT	Imaging	[213]

Table 5. Summary of tissue-targeting peptides derived from virus libraries in preclinical or clinical trials

	Tissue Type	Viral Library	Targeting peptide sequence	Applications	Ref.
Tumor tissues	MDA-MB-435 breast carcinoma xenografts	CX_7C // T7 phage	CGNKRTRGC	MDA-MB-435 breast carcinoma xenografts targeting	[214]
	p32-expressing breast tumors	CX7C // T7 phage	CKRGARSTC	Drug delivery to p32-expressing breast tumors	[215]
	Gastric tumor tissues	Ph.D. 12 // M13 phage	AADNAKTKSFPV	Imaging	[216]
	Bladder tumor tissues	CX_7C T7 // T7 phage	CSNRDARRC	Imaging	[217]
		Ph.D.-C7C // M13 phage	CSSPIGRHC	Imaging	[145]
	Vasculature of human gastric cancer	Ph.D.-C7C // M13 phage	CGNSNPKSC	Imaging	[218]
	Human lung adenocarcinoma	CX_7C // M13 phage	CAKATCPAC	Imaging	[219]
		CX_7C // M13 phage	LYANSPF	Imaging	[220]

Other tissues	Brown adipose tissue	A mixture of cyclic CX_7C and CX_8C // M13 phage	CPATAERPC	Imaging	[221]
	Normal breast tissue	CX_7C // T7 phage	CPGPEGAGC	Breast tissue targeting	[222]
	Ischemic stroke tissue	CX_7C // phage T7	CLEVSRKNC	Imaging	[223]
	Endothelium of the pulmonary vasculature	X_7 AAV2 // adeno-associated virus 2	ESGHGYF	Gene delivery	[224]
	Tympanic membrane transport to middle ear tissue	Ph.D-12 // M13 phage	SADSTKTTHLTL	Targeted transportation across the tympanic membrane to the middle ear for patients infected with Otitis media	[225]
	Brain microvasculature endothelial cell tissue	Heptapeptide AAV2 // adeno-associated virus 2	NRGTEWD	Targeted gene therapy vector able to ameliorate severe cerebrovascular pathology of incontinentiapigmenti	[226]
	Central nervous system and other tissues including brain, spinal cord, muscle, pancreas, and lung tissues	AAV capsid library // adeno-associated virus 1	VDFAVNTEGVYSEPRPIGTRYLTRNL	Targeted gene therapy for the central nervous system and other tissues including brain, spinal cord, muscle, pancreas, and lung tissues	[227]
	Human bone marrow	CX7C M13 phage	GGG, GFS,	These peptide motifs were	[171]

		display library	LWS, ARL, FGG, GVL, SGT	isolated from a human patient *in vivo* to map potential targets of the vasculature system.	
	Human fat tissue		EGG, LLV, LSP, EGR, FGV		
	Human prostate tissue		AGG, EGR, GER, GVL		
	Human skin		GRR, GGH, GTV, ARL, FGG, FGV, SGT		

1.3.1 Viral Libraries

Virus-peptide libraries are a mixture of millions of virus particles where each virus displays a unique and random set of peptides. There are two major types of viral libraries, one based on non-lytic or lytic bacteriophages (phages) and another based on adeno-associated viruses (AAV). Filamentous fd and M13 phages, which are non-lytic bacteria-specific viruses (and very similar in structure and morphology to each other), are the most widely adopted phages in phage display techniques likely due to their commercial availability.[75, 228-230] They have a rod-like shape that is ~800 *nm* in length and ~6 *nm* in width (Figure 3).[231] The circular, single-stranded DNA genome is surrounded by a protein sheath consisting of ~2700 copies of one major coat protein (pVIII), and five copies of four minor coat proteins (pIII and pVI on one tip, pVII and pIX on the other tip).[232] These coat proteins are encoded by corresponding genes located in the DNA genome. Foreign DNA that encodes for foreign peptide expression can be inserted into the phage genome to display any desired peptides on the surface of the protein sheath.[166, 233-234] In other words, a foreign peptide can be fused to minor and/or major coat proteins to site-specifically display at the end and/or along the side wall of phage particles by DNA engineering methods. Lytic phages such as T7 phage have also become widely used.[39, 235-237] Since phage display was introduced by George P. Smith

in 1985 [238], this technique has proved to be one of the most powerful approaches for selecting affinity ligands, including cell/tissue and pathogen targeting peptides.[239] Nowadays, phage display has been further developed in combination with other techniques, such as microfluidics or better analysis software, to improve its selection efficiency.[193, 240-242] The most widely used phages for phage display are shown in Figure 3.

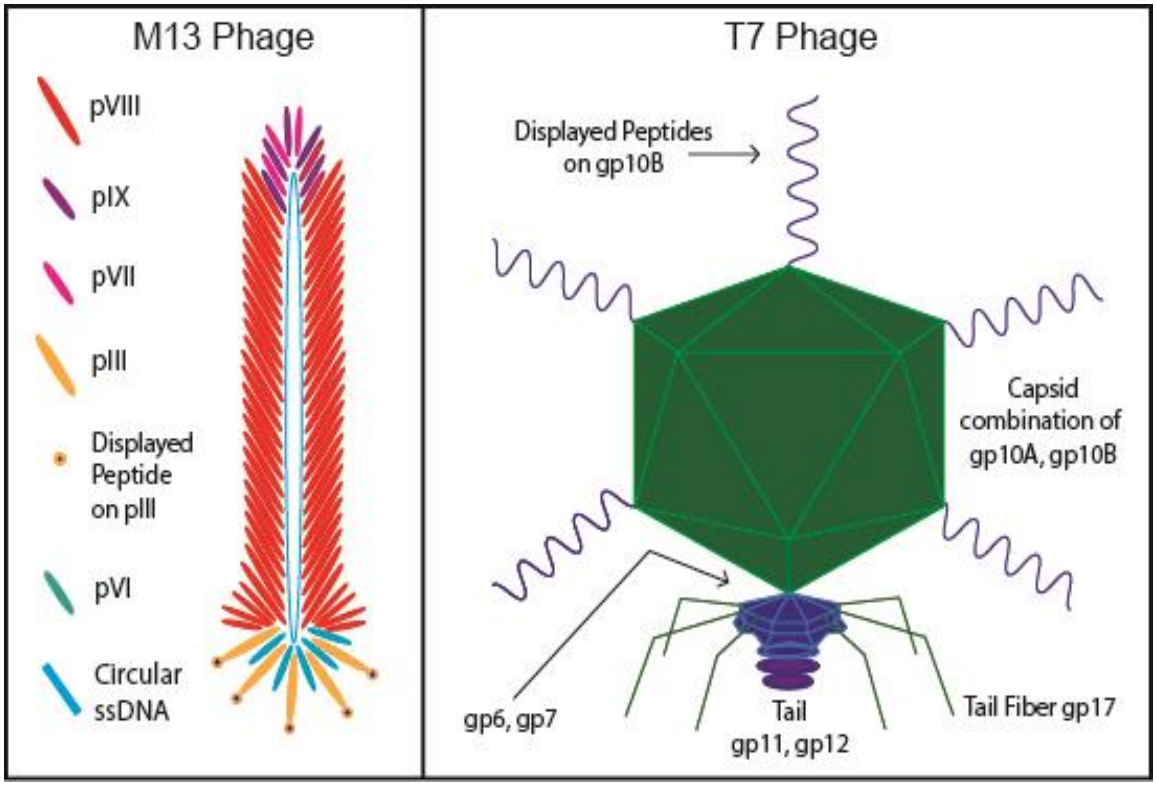


Figure 3. Phage display on M13 and T7 phages. For M13 phage, the 5 copies of pIII are usually utilized in phage libraries for biopanning. After a desired targeting sequence is obtained, that sequence may be genetically engineered into another M13 phage to be displayed on the much more plentiful pVIII. Biopanning is frequently done with pIII rather than pVIII for M13 phages. Stronger binding sequences will be obtained using only 5 copies of pIII vs using a large number of weak binding pVIII. For T7 phage, the capsid is

composed of 415 copies of the coat protein 10A and/or 10B. Through phage display, ~5-15 copies of the genetically engineered peptide sequence will be displayed on the C-terminus of capsid 10B.[243] (Reproduced with permission from American Chemical Society)

1.3.2 Selecting Targeting Peptides by Virus-peptide Display

Targeting peptides can be selected by allowing the aforementioned viral libraries to interact with the target organisms *in vitro, ex vivo,* or *in vivo*. In addition, biopanning can be more generally carried out on any target which does not have to be a biological target. The general procedure for biopanning is shown in Figure 5 while the *in vivo* procedure is shown in Figure 4. By using such a virus-peptide display technique, virus-derived peptides targeting pathogen (Table 2), human cells (Table 3) and tissues (Table 4) can be discovered and widely applied in human disease diagnosis and therapy.

Cell/tissue-targeting peptides can be selected from a phage library containing up to 10^9 phage clones, each clone displaying a unique and random peptide, through an evolutionary screening process called biopanning.[165, 233, 244-245] The general biopanning procedures for discovering cell/tissue-targeting peptides from a phage library are as follows.[190, 246-248] First, an input phage library containing billions of phage clones with randomly displayed peptides is incubated with target cells or tissues. Some phages bind to and/or internalize into target cells/tissues while others do not during incubation. Second, a washing buffer is used to remove the weakly bound and unbound phages from the cell/tissue surface. Third, the cell/tissue-targeting phages are eluted from the target cells/tissues using an elution buffer. Fourth,

the eluted cell/tissue-targeting phages are biologically amplified by infecting *E. coli* bacteria which are cultured and used to enrich the selected phages. The process from step one to step four is designated as one round of selection. The enriched library is considered as an output for the previous round. The enriched library is used as a new input for the next round of selection. After 3-5 rounds of selection, the foreign DNA insert-coding region in a phage genome is sequenced to determine the peptides that are expressed on the phages. The amount of rounds to use can be determined by sequencing each round and checking the diversity of peptides still present. A diversity of 20 peptides in which several are more frequent is best. This quantity helps avoid bias in selecting peptides which are better at amplifying rather than binding the target of interest. This is possible because the displayed peptides are genetically encoded by the phage genome (Figure 4).

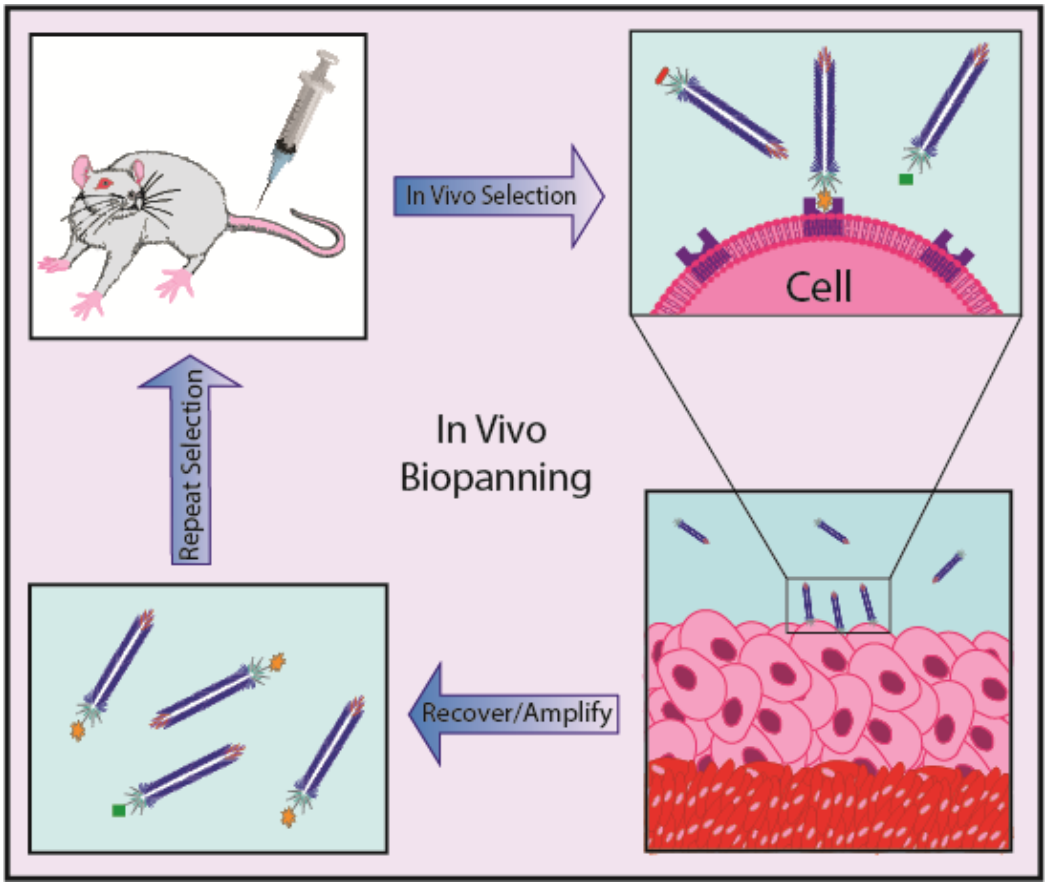


Figure 4. *In vivo* phage biopanning concept. A phage library displaying roughly one billion different combinations of peptides is injected into an animal model. Phages can migrate to their target organs, tissues, receptors, disease cells, etc. for which their peptides have the highest affinity. The phages are then recovered from the animal model by harvesting the desired target, such as a specific organ. The phages are then amplified and go through additional rounds of selection. After 3-4 rounds of selection, phages are sequenced to identify the high-affinity peptides achieved. (Reproduced with permission from American Chemical Society)

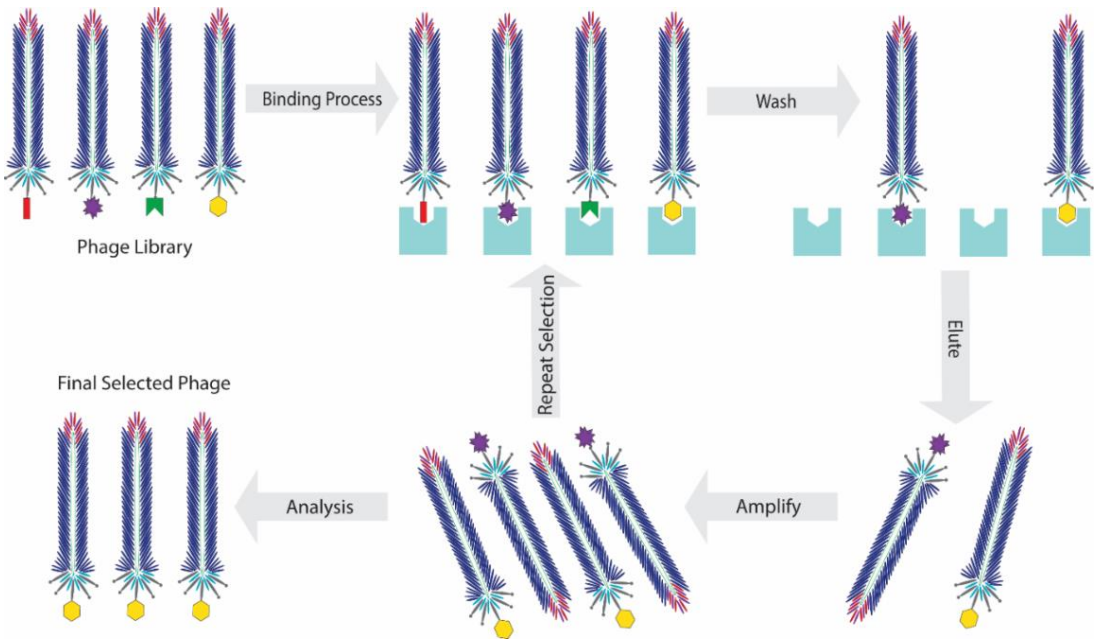


Figure 5. Summary of the process of biopanning. Briefly, a target ligand is immobilized on a surface. A bacteriophage library can then be washed over that surface (a negative selection for the surface without ligand should also be done first) after which only those phages displaying peptides that bind the target will stay bound. The surviving phages can then be released by

disrupting the interaction. Released phages can be amplified and the selection can be repeated, usually 3 to 4 times. At the end, phages can be titered and individual plaques can be picked to be sent for sequencing. The most frequently occurring peptides identified from sequencing are then presumed to be the best at binding the target ligand. (Reproduced with permission from John Wiley and Sons)

1.3.3 Virus-derived tissue regenerative peptides

The versatility of virus-derived peptides for diverse applications also extends to discovering new tissue regenerative peptides.[8, 249] For example, Caprini et al. developed a short peptide, KLPGWSG, which binds to neural stem cells and enhances differentiation toward the neuronal phenotype. The peptide was developed through biopanning with an M13 phage Ph.D. 7 library (New England Biolabs). The differentiation effects were characterized *via* rheometry and circular dichroism, atomic force microscopy, and assessing differentiation of cells in nanostructured hydrogels. Additionally, virus-based techniques can be used to better isolate the most effective peptides among known tissue regenerative peptides. For example, we displayed several osteoblast inducing peptides on M13 phages to test the effects of each peptide.[8] The comparison involved the peptides RGD, RGD/PHSRN (double displayed), ALKRQGRTLYGFGG (osteogenic growth peptide), and KIPKASSVPTELSAISTLYL (from bone morphogenic protein 2). By creating phage films out of these different genetically engineered M13 phages, these peptides were able to be compared side by side in a relatively easy and cheap manner. This was done by culturing stem cells on the different phage films. By comparing the results of quantitative real time PCR as well as the

immunofluorescence of marker genes and proteins respectively, the effectiveness of each peptide could be assessed. The results demonstrated that the peptides ALKRQGRTLYGFGG and KIPKASSVPTELSAISTLYL were the most effective at differentiating induced pluripotent stem cells into osteoblasts. While this technique is not the typical biopanning method, it demonstrates an alternative way to derive clinically relevant peptides from using viral techniques.

1.3.4 M13 Phage assemblies for tissue regeneration

There are also numerous examples of using M13 bacteriophages in other ways for tissue regeneration. One frequently used technique is to assemble bacteriophages into a phage film.[8] The nanotopography of the phage film can help induce the differentiation of stem cells into a desired mature cell type.[8] Additionally, genetically displaying peptides on the phage films allows for the activation of signaling pathways which further enhances differentiation.[8] Alternatively, the phage itself can be incorporated into scaffolds as a nanofiber.[158] When signaling peptides such as RGD are incorporated into these scaffolds (perhaps made from 3D printing or other methods), tissue regeneration has been shown to be enhanced.[158]

1.4 3D printing for tissue regeneration

The need for both tissue regeneration and organ transplants worldwide is staggering.[250-254] For some patients, it can be more beneficial to accept an organ such as a kidney from a donor with diabetes than it can be to remain on the waiting list for a lengthy time.[255] In addition, patients may have incompatibility issues with available donated organs creating more complications.[256] At the forefront of regenerative and replacement strategies to combat these issues is 3D printing.[257-259] In recent years, 3D printing has progressed to be capable of reproducing some of the most complex biological structures down to the cell niche.[260] For example, cardiovascular tissues, aortic valves, skin, bone, liver, brain, muscle, cartilage, kidney, ovary, tumor, and adipose tissues are all being worked on with novel 3D printing strategies.[261-272]There have been numerous of reviews which cover the technical aspects of 3D printing including software usage and the mechanical properties of 3D printers as well as the available materials to use in 3D printing.[273-277] Figure 6 shows some of the recent types of tissues which have been made using 3D printing.

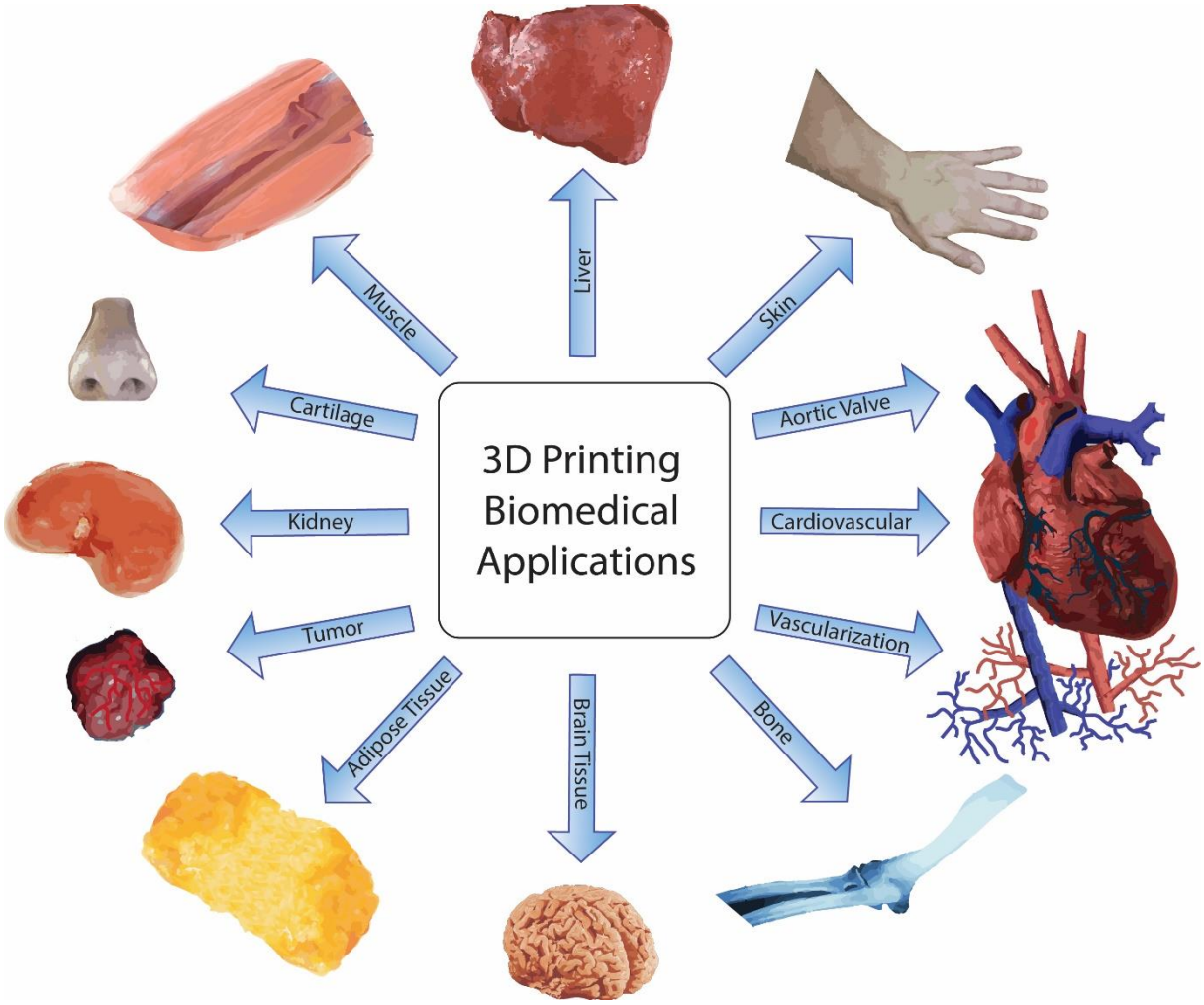


Figure 6. Summary of 3D printed tissue examples for biomedical applications. 3D printing can be used to fabricate skin tissue, aortic valves, cardiovascular tissue, bone, brain tissue, adipose tissue, tumors, kidneys, cartilage tissue, muscle tissue, livers, and promote vascularization in these printed constructs.

1.4.1 Materials Used in Biomedical 3D Printing

There is a nearly endless supply of options for materials to use in 3D printing. The material used depends on the application. For example, if 3D printing is only being used as a way of creating a model for presurgical planning

or mold for another application, cheap plastic materials such as polylactic acid or acrylonitrile butadiene styrene are often used.[278-280] For certain tissue regenerative strategies such as those dealing with bone, various inorganic materials such as $Ca_7MgSi_4O_{16}$ or titanium alloy (Ti-6Al-4V) have gained attention as well as others.[262, 281-282] When it comes to incorporating live cells into materials, hydrogels are the primary choice.[283-285] Some popular hydrogel options include the individual components or combinations of alginate[263-264, 270, 286-289], gelatin[263, 270, 288], chitosan[264], fibrinogen[270, 288], collagen[263, 265], methacrylated chondroitin sulfate[290], agarose[291], polyethylene glycol[283, 292-293], and hyaluronic acid[294-296]. Another bioink-hydrogel based option also exists which incorporates virus into a hydrogel.[297] This bioink, created by Doe-Young Lee and Hyeongjin et al. incorporated genetically modified M13 bacteriophages into a hydrogel.[297] By genetically altering the M13 bacteriophages to double display the GRGDS (from the famous RGD peptide sequence which can enhance osteoblast differentiation) and DDYD (which is a calcium-binding peptide) a virus-based bioink for bone tissue regeneration applications could be created.[297-299] In addition, 3D printing materials can incorporate antimicrobial drugs such as anti-microbial nitrofurantoin or 3D printing can be used to print the drug itself onto a substrate.[300-301] With so many material options available to use in 3D printing, it is important to consider the details of the desired application before choosing which materials to print with.

1.4.2 Vascularized bone regenerative 3D printing

The vascular system should not be thought of separately from all other tissues and organs. In fact, all 3D printing for tissue regeneration having scaffolds thicker than 100 µm (depending on cell type as some cells such as cartilage cells are more robust) must consider the vascularization of the tissue construct.[302] Without vascularization, nutrients, oxygen transport, and waste discharge are at the mercy of diffusion.[302-303] This is a major problem for cells. Most cells do not survive at distances greater than 200 *µm* from a blood vessel.[302] More sensitive cells such as islets show necrosis at just 100 *µm*.[302] Still, there are some more robust cells such as cartilage which can live up to 1 *mm* away from the nearest blood vessel.[302] To date, vascularization strategies in 3D printing have been a hot topic.[263, 303-309] One known strategy for organizing endothelial cells into microtubes which then form blood vessels is to include microchannels in the 3D material.[262, 310-311] For example, Wenjie Zhany, Chun Feng, and Guangzheng Yang et al. developed a 3D printing microchannel material having a hollow-pipe-packed structure containing silica, magnesium, and calcium ($Ca_7MgSi_4O_{16}$) as a bioceramic material.[262] The hollow struts could be 3D printed with an internal diameter of 500 *µm* and an external diameter of 1 *mm*. The material had a compressive strength of up to 26 *MPa*. The bioactive ions within the material had multiple purposes. Previous studies have demonstrated that silica ions can enhance vascular ingrowth as well as exhibit a capacity for osteogenic induction.[262, 312-313] The magnesium ions are considered to directly influence vascularization and bone regeneration.[262, 314] Thus, as one might expect, this material is an example of both vascularization

with 3D printing and bone tissue regeneration.[262] The hollow-pipe-packed structure was then seeded with rabbit bone mesenchymal stem cells and implanted into a rabbit radial bone defect model. The hollow-pipe-packed structure significantly promoted the rapid infiltration of the host's blood vessels. Additionally, they allowed for better delivery of stem cells and growth factors which enhanced tissue regeneration. Radiological and histological findings in the rabbit radial bone defect model further showed that the 3D printing construct could enhance early vascularization as well as long-term bone regeneration. This work demonstrates just one of the many unique ideas currently being used in 3D printing for improving vascularization. This will continue to be an important and exciting field of study in the years to come.

Chapter 2: Development and discovery of peptides capable of binding and detecting bone morphogenic protein receptors

2.1 Introduction

Growth factors are abundant in human bodies, such as bone morphogenic proteins (BMPs), insulin-like growth factors (IGFs), and vascular endothelial growth factor (VEGF).[315-317] They are important in organ development and tissue regeneration. They are proved to be capable of inducing stem cell differentiation. For example, BMP2 and VEGF can induce hMSCs to differentiation into osteoblasts[318-319]; IGF-I can induce quiescent neural stem cells to differentiation into neurons.[320] Growth factors are normally produced by recombinant protein engineering or purified from animals making them expensive or immunogenic. For instance, recombinant BMP-2 costs about $3,500 for 1 mg. In addition, the growth factors are usually large proteins. They are added to the tissue regeneration scaffolds by either mechanical mixing or chemical conjugation with the scaffolds. However, to conjugate a growth factor with a scaffold relies on a tedious and complicated procedure and may render the growth factor not functional due to the blocking of some functional domains.[321] Procedures such as amine coupling for growth factors (e.g., BMP-2) have been used, but these procedures also do not control the orientation of immobilized protein.[322] The immobilization strategy can also influence the rate of growth factors release.[321] Problems can also arise when growth factors such as BMP-2 leak outside of target areas and cause unwanted side effects as was the case in spinal patients.[323] With short functional peptides,

greater control over the orientation and access of the peptides to targets can be achieved during the immobilization process. This may help alleviate some of the issues involved with using full proteins. Thus, there is a pressing need for a cheaper and simpler substitute for a growth factor to be used in regenerative medicine.

Short peptides have various advantages in biomedicine compared to proteins.[324-330] Peptides can be easily synthesized in high yields, high purities, and at low costs. Short functional peptides such as the ones made of about ten amino acids are much cheaper and simpler than proteins (e.g., 396 amino acids constituting human BMP-2). More importantly, they are much less immunogenic than growth factors isolated from other sources and produced in a recombinant way.[330] For example, leakage of BMP-2 from the intended location in spinal patients has caused 35 out of 151 patients (23.2%) to experience adverse side effects such as hematoma, difficulty swallowing, breathing problems, or dramatic swelling.[331] These effects are likely due to diffusion of BMP-2 outside of the intended surgical location.[323, 331] Since growth factors function by binding to their receptors on the cells, we propose to search for growth factor-like short peptides that can bind to the same receptors by using BMPs as model growth factors.

BMPs are one member of the transforming growth factor-beta (TGF-β) superfamily and participate in bone extracellular matrix (ECM) development.[332-336] Among different BMPs, BMP-2 was found to induce osteogenic differentiation of stem cells[337] and promote bone formation.[338] BMP-2 forms

dimers, which bind to type I and type II BMP receptors (BMPR1A and BMPRII) on the cell surface to initiate osteogenic differentiation. BMP-2 signals go through heteromeric complexes of transmembrane receptors (BMPR1A and BMPR2[332-336,339]). Upon activation of these receptors by BMPs, a Smad signaling pathway is triggered, resulting in the phosphorylation of R-Smads (Smad1/5/8). After the phosphorylation is finished, R-Smads are dissociated from the receptor and then complexed with Smad4. The complex enters the nucleus of the stem cells, activating their osteogenic differentiation.[340] Since BMPs bind and recognize two types of BMP receptors (BMPR1A and BMPR2) to trigger the osteogenic differentiation, we employed phage display to identify BMPR1A and BMPR2-binding peptide domains. Our hypothesis is that BMP receptor-binding peptides may potentially mimic BMPs in inducing osteogenic differentiation since BMPs bind the same receptors to perform the desired functions.

2.1.1 Phage display for identifying receptor-targeting peptides.

M13 phage is a human-safe natural biopolymer nanofiber composed of ~3000 highly ordered copies of the major coat protein (p8, made of 50 amino acids) surrounding a circular ssDNA.[341-342] M13 phages have received a BSL-1 risk assessment rating in relation to human health.[343] The DNA encodes coat proteins including p8 on the major coat (i.e., side wall) and four other structural proteins at the two tips (called minor coats) such as p3. By inserting DNA encoding peptides into the genes of the coat proteins, the peptides are themselves displayed on the outer surface of the phage at the tips by genetic

fusion to minor coat proteins (e.g., p3 display) or along the length by genetic fusion to major coat protein p8 (p8 display). Thus, a library made of billions of phage clones with each clone displaying a unique foreign peptide sequence can be constructed.[342] Currently, there are two major types of peptide libraries: (1) a p3-displayed phage library where each peptide is displayed at the p3 tip through fusion to 5 copies of p3, and (2) a p8-displayed phage library where each peptide is displayed along the side wall through fusion to every copy of p8. The p3-displayed phage library has been used to identify a peptide sequence that can specifically recognize and bind to a target (e.g., a protein[344], a cell[345], or a crystal[346]) through biopanning. In this chapter, I will use the widely used p3-displayed phage library[346-347] as a pool of peptide candidates to screen the peptides that can target and bind the extracellular domain of bone morphogenic protein (BMP) receptors (BMPR1A and BMPR2).

2.1.2 Development of BMP-mimicking peptides.

BMPs belong to the transforming growth factor-beta superfamily and were discovered in bone extracellular matrix (ECM). Among different BMPs, BMP-2 was found to be able to induce osteogenic differentiation of stem cells[337] and promote the formation and regeneration of bone.[338] BMP-2 forms dimers, which function by binding to type I and type II bone morphogenic protein receptors on the cell surface to initiate osteogenic differentiation. Although the precise receptor-binding region in BMP-2 is still unknown, there has been some general understanding of the role of BMP-2 in osteogenic differentiation of cells. BMP-2 signals go through heteromeric complexes of transmembrane Serine/Threonine

kinase receptors[339]: BMPR1A and BMPR2,[332-336] which then propagate signals to the Smad pathway. Binding of BMP-2 to its receptor complex results in the phosphorylation of R-Smads (Receptor-Regulated Smads): Smad1, Smad5 and Smad8 molecules. Once phosphorylated, R-Smads dissociate from the receptor, form a complex with the Co-Smad called Smad4, and enter the nucleus to activate the transcription of specific genes involved in the osteoblast differentiation.[340] There have been limited studies on the effect of domains of BMP-2 on osteogenic differentiation, and some domains were found to promote osteogenic differentiation.[338, 348] For example, the sequence corresponding to the domain (residues 73-92) of the BMP-2, KIPKASSVPTELSAISTLYL, can bind to a BMP-2-specific receptor, and elevate both alkaline phosphatase (ALP) activity and osteocalcin (OCN) mRNA in the murine mesenchymal cell line.[338] However, the reported work used either free synthetic peptides or peptides chemically immobilized on a material surface, which does not allow for an easy systematic study of the stem cell fate in response to single or dual peptides on the same surface. Moreover, the reported work does not recognize that two peptides, derived from BMPR1A- and BMPR2-binding domains from BMP-2, respectively, may act together to induce or promote the osteogenic differentiation. In addition, BMP-2 is an expensive growth factor. Thus, there is a need to identify one or two short peptide sequences derived from BMP-2 that can induce or promote the osteogenic differentiation. Phage display can identify BMPR1A and BMPR2 binding peptide domains. Namely, BMPs bind and recognize BMP receptors (BMPR1A and BMPR2) to trigger the osteogenic differentiation. Hence, BMP

receptor-binding peptides may potentially mimic BMPs in inducing osteogenic differentiation. Short peptides possess several advantages in biomedical applications compared to proteins.[324-330] Peptides can be easily synthesized in high yields, high purities, and at low costs. Compared to proteins, small molecular weight peptides (~2000 *Da*) can enter cells and penetrate tissue efficiently and have a lower immunogenicity.[330] Peptides also do not need to be produced in animals overcoming burdensome manufacturing conditions as well as ethical issues.[329-330] Therefore, in this chapter, I utilized phage display techniques to discover possible BMP mimetic peptides.

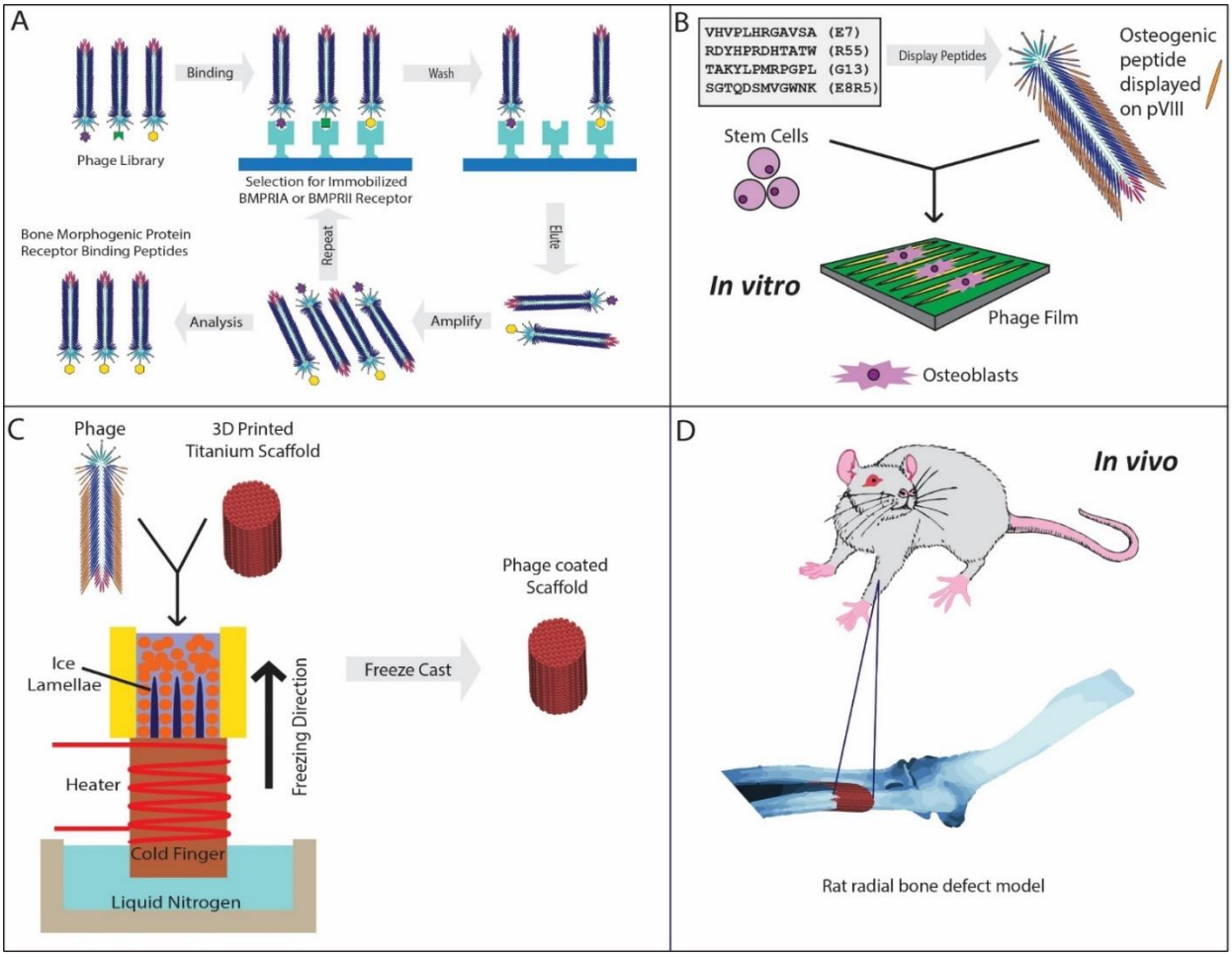


Figure 7. Summary of overall research plan. (A) Peptides capable of binding the receptors BMPR1A and BMPR2 were selected through biopanning. (Chapter 2) (B) Osteogenic peptides were genetically displayed on M13 phage and incorporated into phage films for the differentiation of hMSCs into osteoblasts. (Chapter 3 and 4) (C) Freeze casting was used to coat 3D printed titanium implants with lamellar engineered phage fibers triggering both biophysical and biochemical cues for bone regeneration. (Chapter 5) (D) A rat radial bone defect model was completed to study bone regeneration using the phage-titanium hybrid scaffolds. (Chapter 5)

2.2 Materials and Experiments

2.2.1 Materials

Agarose**,** Anti-M13 Bacteriophage Coat Protein g8p antibody [RL-ph2] (ab9225 from Abcam), azino-bis(3-ethylbenzothiazole sulfonic acid) diammonium salt (Sigma, cat. # A-1888) ,BMPR1A-Fc (G&P Biosciences), BMPR2-Fc (G&P Biosciences), Bovine Serum Albumin,5-Bromo-4- chloro-3-indolyl-β-D-galactoside (Xgal), Corning® BioCoat™ Poly-D-Lysine Multiwell and Assay Plates (Thomas Scientific), dimethyl formamide,E. coli host strain ER2738 (New England Biolabs), Glycine-HCl, Goat-anti mouse AF-488 (Abcam), isopropyl-β-D-thiogalactoside (IPTG), Ethanol (Sigma-Aldrich), Human Mesenchymal Stem Cells (Lonza),Luria Broth Medium,Mesenchymal stem cell growth mediaBulletKit (PT-3238 & PT-4105) (Lonza),mouse anti-g3p (p8) IgG, Ph.D.™-12 Phage Display Peptide Library Kit (New England Biolabs), phosphate buffered saline,polyethylene glycol–8000 (PEG), PureBlu™ Hoechst 33342 Nuclear Staining Dye #1351304 (BioRad), Sodium Azide, Sodium Bicarbonate,Sodium Chloride, Tetracycline, 3,3',5,5'-Tetramethylbenzidine, Tris-HCl.

2.2.2 Negative selection of plastic binders

The Ph.D.™-12 phage library (New England Biolabs) was diluted in tris-buffered saline mixed with Tween-20 (TBS + 0.1% *v/v* Tween-20 and abbreviated TBST) for a final concentration of 2 x 10^{11} phage in 1 *mL* of TBST. The diluted library was then pipetted onto one of the wells of a 12-well poly-L-

lysine plate followed by rocking the plate gently for 60 minutes at room temperature. Next, the supernatant containing phages which did not bind to either the plate or poly-L-lysine were collected. This supernatant served as the starting phage library for subsequent binding selections. The phages which stuck to the plate were discarded.

2.2.3 Immobilization of target

This procedure is only applicable if the charge of the desired protein to be immobilized is negative. Check the isoelectric point (pI) value for your protein before proceeding. When the pH > pI, a protein has a net negative charge. This procedure was written for 12-well plates coated in poly-L-lysine (positively charged). Adjust volumes appropriately if you are using a different size plate. Separate solutions of pI=5.72 BMPR1A-Fc (G&P Biosciences) and pI=5.90 BMPR2-Fc (G&P Biosciences) were prepared at 80 *μg/mL* in Tris-buffered saline (pH 7.5). In separate wells and on separate poly-L-lysine coated 12-well plates, 0.3 *mL* of each solution of receptor was added. The solutions of BMPR1A-Fc and BMPR2-Fc were swirled around the plate surface until the entire surface was wet. The plates were then incubated overnight at 4 degrees Celsius with gentle agitation in a humidified container (a sealed plastic box with damp paper towels). Each individual receptor was now immobilized.

2.2.4 Selection procedure

The following selection procedure is based off of the direct coating procedure outlined in the Ph.D.™-12 Phage Display Libraries instructional

manual (New England Biolabs) with some alterations. This procedure was carried out after immobilizing the targets BMPR1A-Fc and BMPR2-Fc in a 12-well poly-L-lysine coated plate. A stock solution of tetracycline was prepared (20 *mg / ml* in 1:1 ethanol:water). The coating solution containing the target receptors was poured off followed by firmly slapping the plates face down on a clean paper towel. Each well was then filled with blocking buffer (0.1 *M* $NaHCO_3$ (pH 8.6), 5 *mg / mL* BSA, 0.02% NaN_3. Filter sterilize, store at 4°C) and incubated for 1 hour at 4°C. The blocking solution was then poured off followed by firmly slapping the plates down against a clean paper towel. Each plate was washed rapidly 6 times with Tris-buffered saline mixed with Tween-20 (TBS + 0.1% *v/v* Tween-20). The plate was slapped against a clean paper towel each time. 1 *mL* of the phage library created from the negative selection process was then pipetted onto each of the target coated wells. The plates were then rocked gently at room temperature for 60 minutes. The non-binding phages were then discarded by pouring off the supernatant and slapping the plate face-down on a clean paper towel. The plate was then washed 10 times with TBST followed by slapping the plate face-down on a clean paper towel each time (a clean section of paper towel was used each time to prevent cross-contamination). The bound phages were then eluted by incubating with a nonspecific disruption buffer (0.2 *M* Glycine-HCl (pH 2.2), 1 *mg/ mL* bovine serum albumin (BSA) for 15 minutes. The eluate (immersed in the disruption buffer) was then pipetted into a microcentrifuge tube followed by neutralization with 150 *µL* of 1 *M* Tris-HCl (pH 9.1). A small portion (~1 *µL*) of this eluate could be titered and sequenced if

desired (see titering section). The rest of the eluate was amplified (see amplification of phage library section). Once amplified, the eluate was also tittered to determine the concentration of amplified phages by counting the blue plaques in titering (as described below). The amplified library was diluted to contain $2x10^{11}$ phages in 1 *mL* of TBS (as little as 10^9 plaque forming units per mL can be used). A second poly-L-lysine 12-well plate was then coated with the target receptors to allow for a second round of biopanning. A second round of biopanning was carried out doing the same steps except that the Tween-20 concentration in the wash steps was raised to 0.5% (*v/v*). The eluate from the second round was then amplified, titered and used in an additional 3rd round of panning on newly receptor coated plates. 0.5% Tween was again used in the washing steps for the 3rd round. After the 3rd round of panning, the eluate was titered. Blue plaques from the titering were picked and incubated in 10 *mL* of luria broth overnight. The cultures were then mixed with an equal amount of 50% glycerol in water and stored at -80°C or sent on ice for sequencing.

2.2.5 Titering

The *E. coli* strain ER2738 was inoculated into 10 *mL* of luria broth and tetracycline (final concentration of 12 *µg/mL* tetracycline). The phages contain a gene which provides *E. coli* resistance to tetracycline when infected. The culture was incubated at 37 °C with vigorous shaking. This culture was grown to an early log phase of growth (optical density at 600 *nm* was between 0.01-0.05). The top agar was melted in the microwave and 3 *mL* was transferred to a sterile culture tube. One of these tubes was prepared for each corresponding

phage dilution. The phage dilutions of the amplified panning eluate were typically from 10^8-10^{10} *pfu* and they were 10^1-10^4 *pfu* for unamplified eluate. The early log phase E. coli culture was then dispensed into separate 200 *µL* microcentrifuge tubes (one for each phage dilution). The cultures were then inoculated with 10 *µL* of phage solution for each individual dilution. The inoculated culture was allowed to incubate at room temperature for 1-5 minutes. The infected cells were then transferred one infection at a time to the culture tubes containing 45°*C* Top Agar. The tubes were vortexed briefly and immediately poured onto prewarmed LB/IPTG/Xgal plates prepared according to the Ph.D.™-12 Phage Display Libraries instructional manual (New England Biolabs). The plates were gently tilted to pread the top agar out evenly. The plates were then allowed to cool for 5 minutes at room temperature, inverted, and incubated overnight at 37°*C*. On the next day, the blue plaques could be counted or picked for sequencing. For plates that had roughly 100 plaques, the plaques were counted and the number of plaques was multiplied by the dilution factor to get the plaque forming units per 10 *µL*.

2.2.6 Amplification of phage library

The E. coli strain ER2738 was inoculated into 20 *mL* of luria broth medium in a 250 *mL* Erlenmeyer flask. The culture was incubated at 37 °C with vigorous shaking. The eluate not used for titering from the previous round of selection (depending on which round was last completed) was added to the 20 *mL* ER2738 culture during the early-log phase of growth (optical density at 600 *nm* was between 0.01-0.05). The culture was then incubated for 4.5 hours at

37°C with vigorous shaking. The culture was then transferred to a centrifuge tube and spun for 10 minutes at 12,000 *g* at a temperature of 4°*C*. The supernatant was then transferred to a new tube and re-spun. The upper 80% of the supernatant was then transferred to a new tube and mixed with 1/6 volume 20% PEG/2.5 *M* NaCl. The phages were then allowed to precipitate out at 4°*C* overnight (or a minimum of 2 hours). The PEG precipitated phages were then centrifuged at 12,000 g for 15 minutes at 4°*C*. The supernatant was discarded and the tube was re-spun briefly. Any residual supernatant was removed with a pipette. The phage pellet was then visible as a very small white finger print like smear on the side of the tube. The pellet was then resuspended in 1 *mL* of TBS. The resuspended phages were then centrifuged at 14,000 *rmp* for 5 minutes at 4°*C* to remove any residual cells. The supernatant was then transferred to a new microcentrifuge tube followed by reprecipitation in 1/6 volume 20% PEG/2.5 *M* NaCl. The solution was incubated on ice for 60 minutes. The solution was then microcentrifuged on a table top centrifuge at 14,000 *rpm* for 10 minutes at 4°*C*. The supernatant was again discarded, and the tube was spun briefly followed by removal of any additional supernatant. The pellet was then resuspended in 200 *µL* of TBS. The phage solution was then re-spun for 1 minute to remove any insoluble material. The supernatant was transferred to a fresh tube. This solution was considered the amplified eluate.

2.2.7 DNA sequencing to determine peptides

Blue plaques from the titering were picked and incubated in 10 *mL* of luria broth overnight. The cultures were then mixed with an equal amount of 50% glycerol in water and stored at -80°*C* or sent on ice for sequencing. Those samples sent for sequencing were sent to MCLAB Molecular Cloning Laboratories. The pIII coat protein gene for M13 phage was sequenced. The resulting chromatogram files containing the sequencing data were analyzed using FinchTV software. The peptide sequences could be determined according to the Ph.D.™-12 Phage Display Libraries instructional manual (New England Biolabs). An example of processing the data is shown in Table 6.

2.2.8 Enzyme-linked immune sorbent assay for receptor binding

A blocking buffer (0.1 *M* $NaHCO_3$ (pH 8.6), 5 *mg/mL* BSA, filter sterilized, and stored at 4°C) was prepared. TBS (50 *mM* Tris-HCl (pH 7.5), 150 *mM* NaCl, autoclaved, stored at room temperature) was prepared. Separate solutions of the target receptors were then made. For BMPR1A, a 10 *µg/mL*stock solution was made. For BMPR2, a 10 *µg/mL* solution was also made. Four separate wells for each different peptide bearing phage group (which will be added after the wells are coated in receptors) were then coated with one of the receptors. The coating was done by adding 100 *µL* of the BMPR1A or BMPR2 solutions to wells of a 96-well plate followed by swirling until the surface was completely wet. The plates were then allowed to incubate overnight at 4 °*C* with gentle agitation in a humidified container (a plastic box lined with damp paper towels). Any excess target solution was then removed, and the plate was slapped face-down on a clean paper towel. The wells of the

plate were then blocked with 200 *μL* of blocking buffer for 1 hour at room temperature. An additional row of uncoated wells was also blocked to serve as a background signal control. The blocking buffer was then removed from each plate followed by 5 washes with 200 *μL* of TBST. Each time the plate was slapped against a clean section of paper towel face-down. In a separately prepared blocked plate, serial dilutions of the phages in 200 *μL* of TBST were prepared. After a brief pilot test, it should be noted that using 10^{10} *phage / mL* was determined to work best (lowest concentration needed to still differentiate between conditions), but other higher concentrations of virus also worked consistently. Therefore, 100 *μL* of 10^{10} *phage / mL* was pipetted (with a multichannel pipettor) to each row of target-coated wells as well as the rows without target. The mixtures were incubated at room temperature for 1.5 hours with agitation. The wells were then emptied and washed 5 times with 200 *μL* of TBST. Next, 100 *μL* of mouse anti-g3p (p8) IgG was added to every well followed by incubation at room temperature for 1 hour. The wells were then washed 5 times with 200 *μL* of TBST. Then, 100 *μL* of anti-mouse IgG conjugated with HRP (diluted in TBST + 5% BSA) was added to every well followed by incubation for 1 hour. The wells were emptied followed by 5 more washes with 200 *μL* of TBST. Then, 100 *μL* of freshly prepared 3,3',5,5'-Tetramethylbenzidine (TMB) was added to each well and the absorbance at 370 *nm* and 652 *nm* was monitored for 1 hour using an ELISA plate reader. After 1 hour, the substrate reaction was stopped using equal volumes (100 *μL*) of 1 *M* HCl. The absorbance at 450 *nm* for each well was then measured.

2.2.9 Live cell binding through immunofluorescence

Human mesenchymal stem cells (hMSCs) were grown to roughly 60% confluence in a 48-well tissue culture plate according to the company Lonza's culturing protocols. Phages (each type having a different peptide displayed on the pIII coat protein which were previously isolated through biopanning) were then filtered (0.2 *μm* syringe filter) and subjected to 1 hour of ultraviolet (UV) light for disinfection. The hMSCs were then blocked with 0.5% BSA (dissolved in cell media) for 1 hour. The cell media for the hMSCs was then replaced with 1 *mL* of new cell media having of concentration of 10^{12} *phages / mL* followed by incubation for 6 hours at 37 degrees Celsius. Next, the plates were washed once with 400 *μL* of phosphate buffered saline (PBS) at a pH of 7.4. The hMSCs were then incubated with Anti-M13 Bacteriophage Coat Protein g8p antibody [RL-ph2] (ab9225) at a 1:1000 dilution in cell media (200 *μL* per well). The wells were then washed again with PBS (400 *μL* per wash). Next, the hMSCs were incubated with the fluorescent secondary antibody, Goat-anti mouse AF-488 (Abcam) for 1 hour (1 *ug/mL* final concentration of antibody in media). The wells were then washed again with PBS (400 *μL* per wash). A Hoechst nuclear stain was used to stain the nuclei (PureBlu™ Hoechst 33342 Nuclear Staining Dye #1351304 from BioRad) according to the company's protocol. Cell Mask™ Orange Plasma Membrane Stain was used to stain membranes (CellMask™ Orange Plasma Membrane Stain Catalog number: C10045 from Thermo Fisher Scientific) according to the company's

protocol. The phages binding to the cells were then imaged on a Nikon Eclipse Ti fluorescent microscope.

2.3 Results and Discussion

2.3.1 Sequencing results and frequency of peptides

Upon sequencing the phages which remained after biopanning on the receptors BMPR1A and BMPR2, the DNA sequences were converted into peptide sequences for the peptide insert region of the DNA. The resulting frequencies and sequences are shown in Figure 8. Each tick mark on the frequency axis represents a plaque picked from biopanning which was sequenced. For the receptor BMPR1A, the most frequently obtained peptide was TAKYLPMRPGPL followed by other promising peptides. For the receptor BMPR2, RDYHPRDHTATW was the most frequent peptide. While a higher frequency may indicate better binding to the receptors, it can also represent a preference in the ability of a phage to replicate during the amplification steps. Therefore, frequency alone is not a reliable indicator of the best peptides to select. Knowing this, both the highest frequency peptides and peptides which showed more unique sequences were selected for further tests. The sequencing results of those peptides later shown to have more promise are given in Table 6 and Table 7.

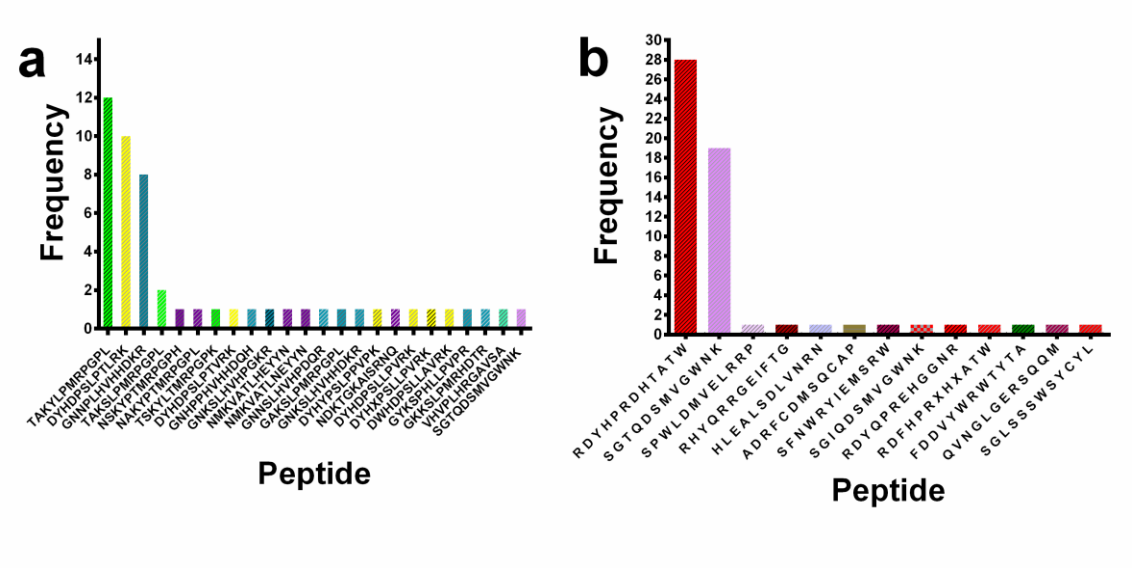


Figure 8. Frequency of peptide sequencing results from biopanning on (a) BMPR1A and (b) BMPR2. This figure shows the diversity of peptide sequences obtained through biopanning as well as the highest frequency peptides.

Table 6. The DNA FASTA sequences corresponding to peptides obtained through biopanning on BMPR1A. For those peptides with multiple frequencies of occurring only one example is shown. Only sequences later found to be relevant for bone regeneration are shown.

Peptide	FASTA DNA Sequence for M13 phage pIII coat protein
TAKYLPMRPGPL	>G13_96glll_E02 Reverse Complement NGTTANNGTNNTCTGCNTNANTGAATGTNGGTNTCCTAAATCTCAACTGA TGANTNTTNTNCCTGTNANNAATNTGNNNNNTTANTTCGTTTTATTAACG TAGATTTTTCTTCCCAACGTCCTGACTGGTATAAATGANCCAGTTTCTTA AAATCGCATAAGGTAATTCACAATGATTAAAGTTGAAATTAAACCCATCT CAAGCCCAATTTACTACTCGTTCTGGTGTTTCTCGTCAGGGCAAGCCTTA TTCACTGAATGAGCAGCTTTGTTACGTTGATTTGGGTAATGAATATCCGG TTCTTGTCAAGATTACTCTTGATGAAGGTCAGCCAGCCTATGCGCCTGGT CTGTACACCGTTCATCTGTCCTCTTTCAAAGTTGGTCAGTTCGGTTCCCT TATGATTGACCGTCTGCGCCTCGTTCCGGCTAAGTAACATGGAGCAGGTC GCGGATTTCGACACAATTTATCAGGCGATGATACAAATCTCCGTTGTACT TTGTTTCGCGCTTGGTATAATCGCTGGGGGTCAAAGATGAGTGTTTTAGT GTATTCTTTTGCCTCTTTCGTTTTAGGTTGGTGCCTTCGTAGTGGCATTA CGTATTTTACCCGTTTAATGGAAACTTCCTCATGAAAAAGTCTTTAGTCC TCAAAGCCTCTGTAGCCGTTGCTACCCTCGTTCCGATGCTGTCTTTCGCT GCTGAGGGTGACGATCCCGCAAAAGCGGCCTTTAACTCCCTGCAAGCCTC AGCGACCGAATATATCGGTTATGCGTGGGCGATGGTTGTTGTCATTGTCG GCGCAACTATCGGTATCAAGCTGTTTAAGAAATTCACCTCGAAAGCAAGC TGATAAACCGATACAATTAAAGGCTCCTTTTGGAGCCTTTTTTTTGGAGA TTTTCAACGTGAAAAAATTATTATTCGCAATTCCTTTAGTGGTACCTTTC

	TATTCTCACTCTACTGCGAAGTATCTGCCTATGCGTCCTGGGCCGCTTGG TGGAGGTTCGGCCGAAACTGTTGAAAGTTGTTTAGCAAAATCCCATACAG AAAANTCATTTACTAACGTCTGNNANNCNNNNNNNNN
VHVPLHRGAVSA	>E7_96glll_C09 Reverse Complement NTNCCNTTTNGGNNNTNNNNTATNNTGCNNTANTGAATGNGGNNTNCCTN NNNTCTNNNTGANNATCTTNTACCTGTAANTAATGTTNNNNNAGTTCGTT TTATNAACGTAGATTTTTCTTCCCAACGTTCCTGACTGGTATAATGANCC AGTTCTTAAATCGCATAAAGGTAATTCACAATGATTAAAGTTGAAATTTA AACCCATCTCAAGCCCAATTTACTACTCGTTCTGGTGTTTCTCGTCAGGG CAAGCCTTATTCACTGAATGAGCAGCTTTGTTACGTTGATTTGGGTAATG AATATCCGGTTCTTGTCAAGATTACTCTTGATGAAGGTCAGCCAGCCTAT GCGCCTGGTCTGTACACCGTTCATCTGTCCTCTTTCAAAGTTGGTCAGTT CGGTTCCCTTATGATTGACCGTCTGCGCCTCGTTCCGGCTAAGTAACATG GAGCAGGTCGCGGATTTCGACACAATTTATCAGGCGATGATACAAATCTC CGTTGTACTTTGTTTCGCGCTTGGTATAATCGCTGGGGGTCAAAGATGAG TGTTTTAGTGTATTCTTTTGCCTCTTTCGTTTTAGGTTGGTGCCTTCGTA GTGGCATTACGTATTTTACCCGTTTAATGGAAACTTCCTCATGAAAAAGT CTTTAGTCCTCAAAGCCTCTGTAGCCGTTGCTACCCTCGTTCCGATGCTG TCTTTCGCTGCTGAGGGTGACGATCCCGCAAAAGCGGCCTTTAACTCCCT GCAAGCCTCAGCGACCGAATATATCGGTTATGCGTGGGCGATGGTTGTTG TCATTGTCGGCGCAACTATCGGTATCAAGCTGTTTAAGAAATTCACCTCG AAAGCAAGCTGATAAACCGATACAATTAAAGGCTCCTTTTGGAGCCTTTT TTTTGGAGATTTTCAACGTGAAAAAATTATTATTCGCAATTCCTTTAGTG GTACCTTTCTATTCTCACTCTGTTCATGTTCCGTTGCATAGGGGTGCGGT TTCGGCGGGTGGAGGTTCGGCCGAAACTGTTGAAAGTTGTTTAGCAAAAT CCCATNCAGAAAATNCNTTNNTAACGTCNGGAAANNNNNNNNNNNNNNN
SGTQDSMVGWNK (Appears in both biopanning targets)	>E8_96glll_D09 Reverse Complement NCGTAATTCCTTTTGGCNNTNANGTNTNCTGGCNTTANTGAATGTGGTAT CCTAAATCTCAACTGANGANNTTNTACCTGTAATAATGTNGNTCCNTAGT TCNNNTATNAACGTAGATTTTTCTTNCAACGTCCTGACTGGTATAATGAN CCAGTTCTTAAATCGCATAAGGTAATTCACAATGATTAAAGTTGAAATTA AACCATCTCAAGCCCAATTTACTACTCGTTCTGGTGTTTCTCGTCAGGGC AAGCCTTATTCACTGAATGAGCAGCTTTGTTACGTTGATTTGGGTAATGA ATATCCGGTTCTTGTCAAGATTACTCTTGATGAAGGTCAGCCAGCCTATG CGCCTGGTCTGTACACCGTTCATCTGTCCTCTTTCAAAGTTGGTCAGTTC GGTTCCCTTATGATTGACCGTCTGCGCCTCGTTCCGGCTAAGTAACATGG AGCAGGTCGCGGATTTCGACACAATTTATCAGGCGATGATACAAATCTCC GTTGTACTTTGTTTCGCGNNNNNGTATAATCGCTGGGGGTCAAAGATGAG TGTTTTAGTGTATTCTTTTGCCTCTTTCGTTTTAGGTTGGTGCCTTCGTA GTGGCATTACGTATTTTACCCGTTTAATGGAAACTTCCTCATGAAAAAGT CTTTAGTCCTCAAAGCCTCTGTAGCCGTTGCTACCCTCGTTCCGATGCTG TCTTTCGCTGCTGAGGGTGACGATCCCGCAAAAGCGGCCTTTAACTCCCT GCAAGCCTCAGCGACCGAATATATCGGTTATGCGTGGGCGATGGTTGTTG TCATTGTCGGCGCAACTATCGGTATCAAGCTGTTTAAGAAATTCACCTCG AAAGCAAGCTGATAAACCGATACAATTAAAGGCTCCTTTTGGAGCCTTTT TTTTGGAGATTTTCAACGTGAAAAAATTATTATTCGCAATTCCTTTAGTG GTACCTTTCTATTCTCACTCTTCTGGTACTTAGGATTCTATGGTTGGTTG GAATAAGGGTGGAGGTTCGGCCGAAACTGTTGAAAGTTGTTTAGCAAANN CCCNNNNNANAANNNTNNCNNNNTNNNNNN

Table 7. The DNA FASTA sequences corresponding to peptides obtained through biopanning on BMPR2. For those peptides with multiple frequencies of occurring only one example is shown. Only sequences later found to be relevant for bone regeneration are shown.

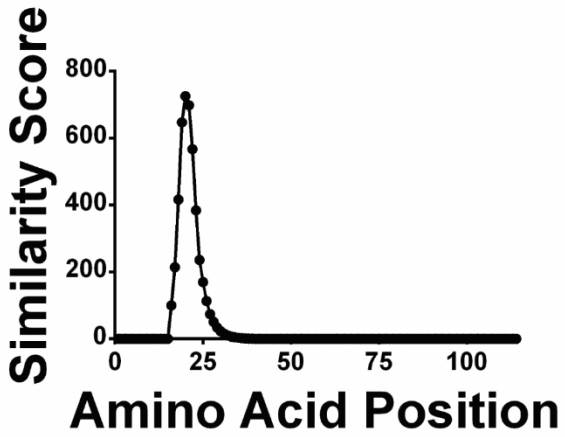
Peptide	FASTA DNA Sequence for M13 phage pIII coat protein
RDYHPRDHTATW	>R55_-_96III_G05_ FASTA Reverse Complement NNNNNNTTNNNNNNNTATNCNTNNNTNNGNAANGNNNNNNNNNAGTNTTG CTCTANNTANNCNNCGNNNNNNNNNNNNTNANGTANNTGCNTNNNNNAAT NNGTANTCCNTAAATCTCNACTGATGAATCTTTNTACCTGTAATAAANGT NGTTCCCGTTAGTTCGTTTTATTAACGTAGATTTTTTCTTCCCAACGTCC TGACTGGTATAATGANCCAGNTTCTTAAAATCGCATAAGGTAATTCACAA TGATTAAAGTTGAAATTAAACCATCTCAAGCCCAATTTACTACTCGTTCT GGTGTTTCTCGTCAGGGCAAGCCTTATTCACTGAATGAGCAGCTTTGTTA CGTTGATTTGGGTAATGAATATCCGGTTCTTGTCAAGATTACTCTTGATG AAGGTCAGCCAGCCTATGCGCCTGGTCTGTACACCGTTCATCTGTCCTCT TTCAAAGTTGGTCAGTTCGGTTCCCTTATGATTGACCGTCTGCGCCTCGT TCCGGCTAAGTAACATGGAGCAGGTCGCGGATTTCGACACAATTTATCAG GCGATGATACAAATCTCCGTTGTACTTTGTTTCGCGCTTGGTATAATCGC TGGGGGTCAAAGATGAGTGTTTTAGTGTATTCTTTTGCCTCTTTCGTTTT AGGTTGGTGCCTTCGTAGTGGCATTACGTATTTTACCCGTTTAATGGAAA CTTCCTCATGAAAAAGTCTTTAGTCCTCAAAGCCTCTGTAGCCGTTGCTA CCCTCGTTCCGATGCTGTCTTTCGCTGCTGAGGGTGACGATCCCGCAAAA GCGGCCTTTAACTCCCTGCAAGCCTCAGCGACCGAATATATCGGTTATGC GTGGGCGATGGTTGTTGTCATTGTCGGCGCAACTATCGGTATCAAGCTGT TTAAGAAATTCACCTCGAAAGCAAGCTGATAAACCGATACAATTAAAGGC TCCTTTTGGAGCCTTTTTTTTGGAGATTTTCAACGTGAAAAAATTATTAT TCGCAATTCCTTTAGTGGTACCTTTCTATTCTCACTCTCGGGATTATCAT CCTCGTGATCATACTGCTACTTGGGGTGGAGGTTCGGCCGAAACTGTTGA AAGTTGTTTAGCAAAATCCCATACAGAAAANTCATTACTAACGTCNGNAN NNNNNNNN
SGTQDSMVGWNK (Appears in both biopanning targets)	>R5_-_96III_E11 Reverse Complement NNNNNNNNNGNNTTTNNTNNGNNNNNNNNNNANNNGNNGNNNNNNANNNN NNNNNNCTTNNCTATNNCNTNGTAANNNCTTTNNNNNTNATGTATCTGNN TAGTTGAAATGTGGNNTCCTAAATCTCNACTGATGANTCTTCTACCTGTA AATAAATGTNGNNCCCGTAGTTCNNTNTATTAACGTAGATTTTTCTTCCC AACGTCCTGACTGGTATAATGANCCAGTTCTTAAAATCGCATAAGGTAAT TCACAATGATTAAAGTTGAAATTAAACCATCTCAAGCCCAATTTACTACT CGTTCTGGTGTTTCTCGTCAGGGCAAGCCTTATTCACTGAATGAGCAGCT TTGTTACGTTGATTTGGGTAATGAATATCCGGTTCTTGTCAAGATTACTC TTGATGAAGGTCAGCCAGCCTATGCGCCTGGTCTGTACACCGTTCATCTG TCCTCTTTCAAAGTTGGTCAGTTCGGTTCCCTTATGATTGACCGTCTGCG CCTCGTTCCGGCTAAGTAACATGGAGCAGGTCGCGGATTTCGACACAATT TATCAGGCGATGATACAAATCTCCGTTGTACTTTGTTTCGCGCTTGGTAT AATCGCTGGGGGTCAAAGATGAGTGTTTTAGTGTATTCTTTTGCCTCTTT CGTTTTAGGTTGGTGCCTTCGTAGTGGCATTACGTATTTTACCCGTTTAA TGGAAACTTCCTCATGAAAAAGTCTTTAGTCCTCAAAGCCTCTGTAGCCG TTGCTACCCTCGTTCCGATGCTGTCTTTCGCTGCTGAGGGTGACGATCCC GCAAAAGCGGCCTTTAACTCCCTGCAAGCCTCAGCGACCGAATATATCGG TTATGCGTGGGCGATGGTTGTTGTCATTGTCGGCGCAACTATCGGTATCA AGCTGTTTAAGAAATTCACCTCGAAAGCAAGCTGATAAACCGATACAATT AAAGGCTCCTTTTGGAGCCTTTTTTTTGGAGATTTTCAACGTGAAAAAAT TATTATTCGCAATTCCTTTAGTGGTACCTTTCTATTCTCACTCTTCTGGT

	ACTTAGGATTCTATGGTTGGTTGGAATAAGGGTGGAGGTTCGGCCGAAAC TGTTGAAAGTTGTTTAGCAAANTCCCATNCAGAAAATTCATTACTAACGT CNNNNNNNNNNNNNNN

2.3.2 Relic peptide analysis

Bone morphogenic protein 2 (BMP-2) is a popular and potent osteoblast inducer which naturally binds to the receptors BMPR1A and BMPR2. Due to the strategy of biopanning, it was expected that some peptides may resemble sequences in BMP-2. To test this option, the sequences were loaded into a program called RELIC. RELIC uses a scoring matrix to test similarity scores between peptide sequences. Typically, a score above 10 indicates a region of similarity.[344] Out of all of the peptides, the peptide SGTQDSMVGWNK demonstrated significant similarity to a region of BMP-2, LYVDFSDVGWND. This similarity may indicate that this region of BMP-2 has some yet unknown role in receptor binding or activation. The results of the RELIC analysis are shown in Figure 9.

a



b

```
QAKHKQRKRLKSSCKRHPLYVDFSDVGWNDWIVAPPGYHAFYCHGECPFP   50
                      SGTQDSMVGWNK

LADHLNSTNHAIVQTLVNSVNSKIPKACCVPTELSAISMLYLDENEKVVL   100

KNYQDMVVEGCGCR                                       150
```

Figure 9. The peptides discovered through biopanning were compared to BMP2 at each amino acid position (a) using a bioinformatics program (RELIC/MATCH). (a-b) Similarity scores (a) and alignment (b) of the peptide SGTQDSMVGWNK to BMP2 demonstrated a high degree of similarity between the peptide SGTQDSMVGWNK and a region of BMP2. In (b), the peptide was aligned under the full sequence of BMP2.

2.3.3 Relative binding strengths of selected peptides and live cell binding of peptides to hMSCs

The peptides selected to be tested for relative binding strength in an ELISA are shown in Figure 10a and 10b. For the receptor BMPR1A, 3 statistically significant peptides emerged as the best binders. These peptides were VHVPLHRGAVSA, SGTQDSMVGWNK, and TAKYLPMRPGPL. For the receptor BMPR2, the sequences RDYHPRDHTATW and SGTQDSMVGWNK were statistically significant binders. The peptide SGTQDSMVGWNK was especially interesting because it showed up as a result of biopanning on both BMPR1A alone and BMPR2 alone. Additionally, live hMSC interactions with peptide-bearing phages were observed through immunofluorescence. Figure 10c shows that the phages (shown in green) for the sequences SGTQDSMVGWNK, RDYHPRDHTATW, and VHVPLHRGAVSA bind to what appears to be the same location as the outer membrane. The receptors are transmembrane receptors, and therefore it was expected that the binding would occur on the outer membrane as was observed. It is also not expected that the phages enter hMSCs because of their biology, so they are likely on the surface of the hMSCs.

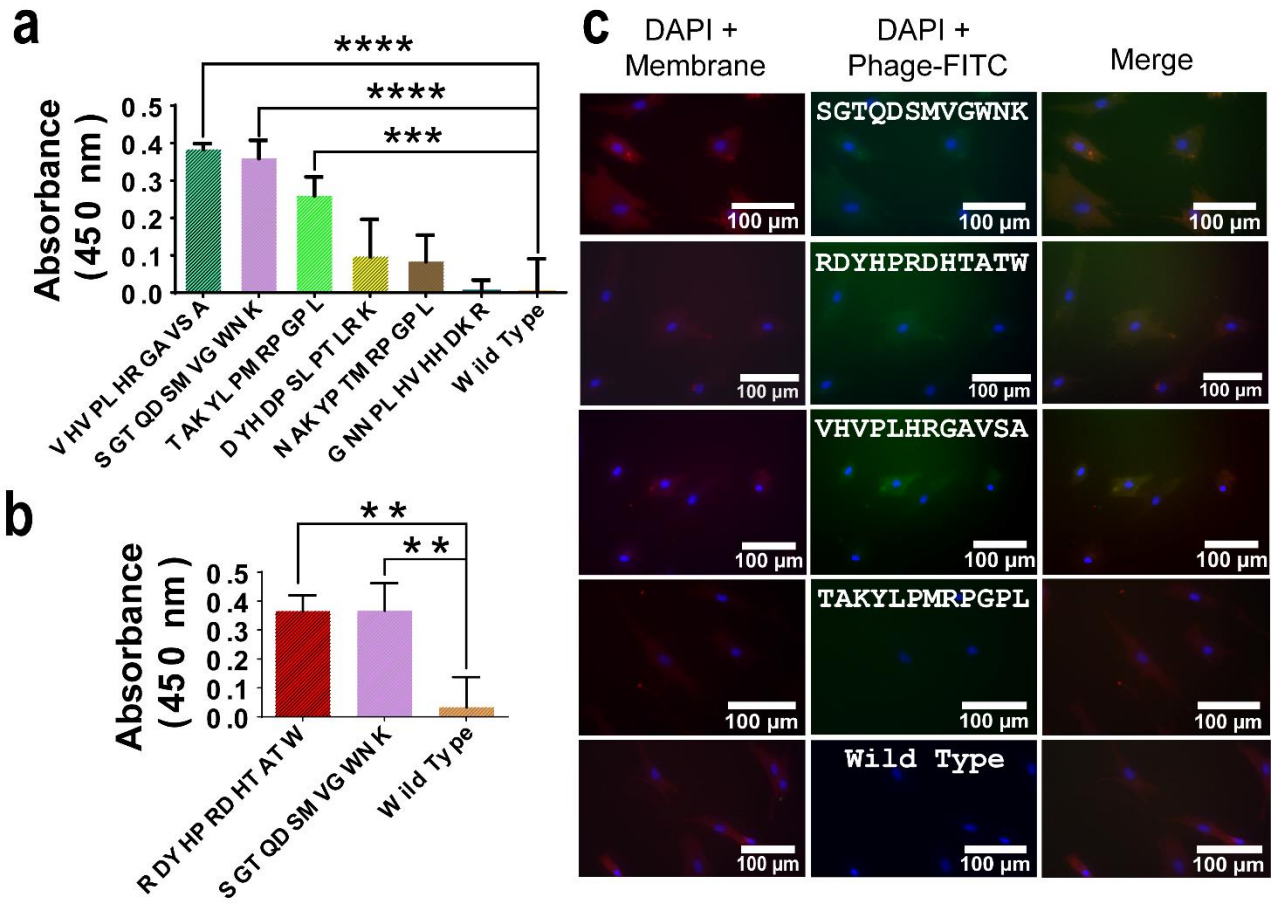


Figure 10. Evaluation of the BMPR-binding peptides in binding BMPRs. (a and b) Comparative ELISA test for binding of peptides to BMPR1A (a) and BMPR2 (b). The ELISA (n=4) was carried out using a phage concentration of $2x10^{12}$ *phage/mL*. The phage displayed the peptide indicated on its p3 coat protein. The primary antibody was mouse anti-g3p (p8) IgG. The secondary antibody was anti-mouse IgG conjugated with horseradish peroxidase (HRP). The substrate of the HRP, 3,3',5,5'-Tetramethylbenzidine, was detected at 450 *nm* after stopping the reaction with 1 *M* HCl. The data shows that the peptides VHVPLHRGAVSA, SGTQDSMVGWNK, TAKYLPMRPGPL, and RDYHPRDHTATW all bind the

receptors significantly better than wild type. (c) Fluorescence images of the peptides (displayed on p3 of phage) binding live hMSCs. In green, Primary: Mouse anti-g3p (p8) IgG; Secondary: Goat-anti mouse AF-488: IgG H and L. In red, Cell Mask^{TM} Orange Plasma Membrane Stain. Orange, overlay of red and green. The 4 best peptides determined by ELISA in (a) and (b), including 2 MPRR1A-binding peptides and 2 BMPR2-binding peptides, were chosen as indicated. Among these 4 peptides, the peptides SGTQDSMVGWNK, RDYHPRDHTATW, and VHVPLHRGAVSA showed the best binding images. All data represent the mean $\pm$ standard deviation (n=4, *, **, ***, and **** represent a P value not higher than 0.05, 0.01, 0.001, and 0.0001, respectively). This data shows that the peptides selected preferentially bind to their respective receptors.

2.4 Conclusion

In this chapter, I used a technique called biopanning to isolate M13 phages bearing peptides capable of binding to the receptors BMPR1A and BMPR2. These peptide-bearing phages were demonstrated to bind significantly better than a wild type phage control in ELISA tests. The peptides SGTQDSMVGWNK, RDYHPRDHTATW, and VHVPLHRGAVSA also demonstrated an ability to bind to some locations on the outer membrane (presumably on the BMPR1A and BMPR2 receptors) of live hMSCs. Additionally, a peptide matching and scoring system, RELIC identified that the peptide SGTQDSMVGWNK shows a high similarity with a previously uncharacterized region of BMP-2.

Chapter 3: Generating a genetically engineered virus displaying newly discovered differentiation peptides and assembling it into a precise nanostructured film to control stem cell differentiation into osteoblasts

3.1 Introduction

In the previous chapter, possible bone regenerative peptides were discovered. In this chapter, I will focus on techniques which were used to evaluate the ability of these peptides.

3.1.1 Genetic manipulation of M13 phages

Filamentous temperate M13 phages can be pictured as a long flexible nanofiber composed of five structural capsid proteins, which encase a relatively large circular single strand of DNA.[23, 92] Wild-type M13 phage measures ~9300 *Å* long, but has a diameter of only 65 *Å*.[20] The M13 virion consists of ~6407 bases of circular single-stranded DNA (ssDNA) in its genome, but longer genomes generate longer phages.[20-22] Although there are five different proteins, the majority of a filamentous phage is coated by ~2700 copies of a protein encoded by a single gene called pVIII,[23] which is helically arranged to form a filament tube.[92] This is the protein that is often modified for desirable characteristics and will be genetically modified in this work to provide more copies of the peptides selected in the previous chapter. The ends of filamentous phages are composed of minor coat proteins. One end is composed of five copies of the proteins pIII and pVI, while the opposite end displays five copies

of the proteins pVII and pIX.[22-24] The filamentous structure and major coat proteins are what makes these phages capable of creating many self-assembled nanostructures as well as develop excellent targeting abilities. By inserting DNA encoding peptides into the genes of the coat proteins, the peptides are themselves displayed on the outer surface of the phages at the tips by genetic fusion to minor coat proteins (e.g., pIII display) or along the length by genetic fusion to major coat protein pVIII (pVIII display).

3.1.2 Phage films

M13 bacteriophages have been implemented in a variety of organic synthesis strategies and organic biomaterials.[349-350] One of the major biomaterials made out of M13 phages is called phage film.[68, 351] Phage films consist of self-assembled layers of M13 phages that can come in a variety of nanotopographies depending on the preparation method.[8, 10, 352-355] Often times, the phages are naturally self-assembled into a ridge groove structure with the help of a pulling force.[8] However, due to the liquid crystalline properties of M13 bacteriophage, even more complex structures can be made.[10] A major benefit of phage films is that different peptides can be displayed on the phages without changing the structure of the film.[8] This allows for distinguishing the effects of different peptides in cellular differentiation assays.[8]

3.1.3 Osteoblast markers

Osteoblasts are essential for new bone formation. Osteoblasts are responsible for the synthesis and secretion of the majority of the proteins in the

bone extracellular matrix.[356] Osteoblast also induce mineralization of the extracellular matrix. Osteoblasts are derived from undifferentiated mesenchymal stem cells. These mesenchymal stem cells have the capacity to differentiate into osteoblasts, adipocytes, chondrocytes, and myoblasts.[356-357]There are several frequently used markers for identifying osteoblasts. Some common markers include alkaline phosphatase, type I collagen, osteopontin, bone sialoprotein, and osteocalcin.[356] However, the expression of these markers can vary over time. For example, alkaline phosphatase, bone sialoprotein, and collagen type 1a can be early indicators of osteoblast differentiation while osteocalcin is a late marker.[356]Osteopontin expression peaks twice during proliferation and can later peak again during the late stages of differentiation.[356] None of the genes mentioned which are involved in the extra cellular matrix mineralization are unique to osteoblasts or bone.[356] However, the coexpression of these genes is unique to osteoblasts.[356]Therefore, several of these markers and calcium mineralization were the focus of establishing osteoblast differentiation in this chapter.

3.2 Materials and Experiments

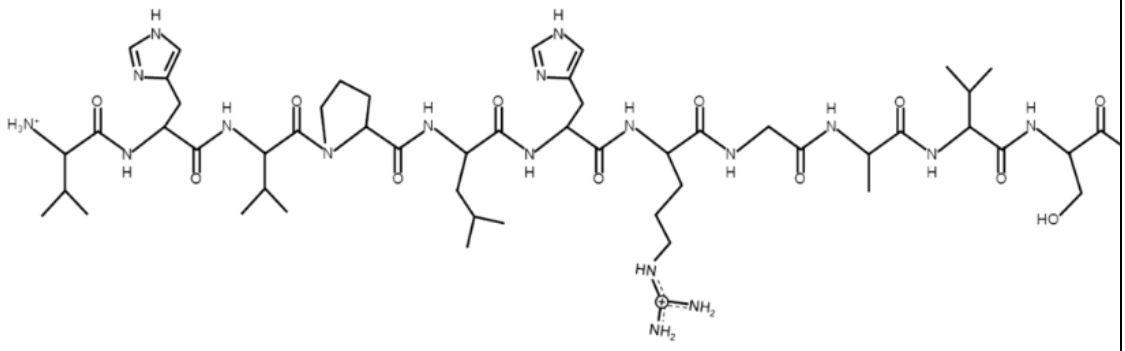
3.2.1 Materials

Acetic acid, agarose, alamarBlue® (Bio-Rad), Calcium Chloride, Chloramphenicol, deoxynucleosidetriphosphate, E. coli strain TG1, ER2738 bacteria (New England Biolabs), Ethylenediaminetetraacetic acid (EDTA), 5 × GC buffer, Glycerol,Goat Anti-Rabbit IgG H&L Alexa Fluor 555ab150078 (Abcam),Goat Anti-Mouse IgG H&L (Dylight 650) preadsorbed ab96882

(Abcam), hMSC Osteogenic BulletKit (Lonza),Hind III restriction enzyme (New England Biolabs),human collagen type 1A primer (GeneCopoeia), human GAPDH primer (GeneCopoeia), human osteocalcin primer (GeneCopoeia), human osteopontin primer (GeneCopoeia), Luria broth, M13KO7 phage (New England Biolabs), Mesenchymal stem cell growth medium BulletKit (Lonza), MiniOpticon Real Time PCR System (Bio-Rad), Nco I restriction enzyme (New England Biolabs),OCN [OC4-30] ab13418 (Abcam), Pfu 1U DNA polymerase, polyethylene glycol–8000,Power SYBR™ Green Cells-to-CT™ Kit (Thermo Fisher Scientific), QIAgen gel DNA extraction kit, QIAgen miniprep plasmid extraction kit, RbpAB to osteopontin ab8448 (Abcam),T4 ligase (Invitrogen), Tris base , XL_1 Blue E. Coli harboring the PeCan49 phagemid DNA for chloramphenicol resistance, uranyl acetate.

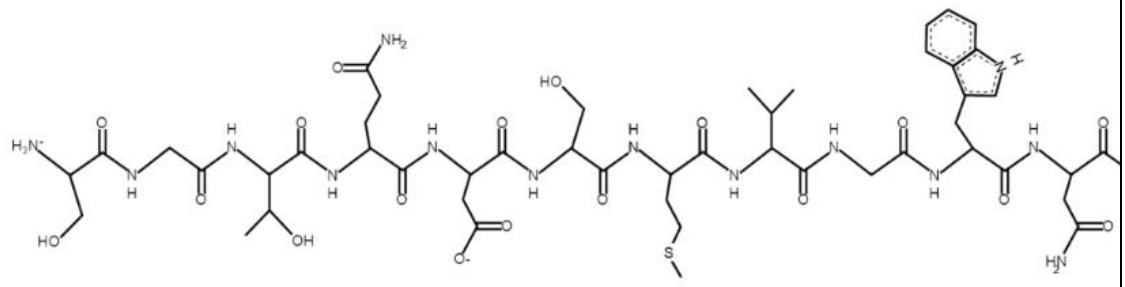
3.2.2 M13 Phage Display

Peptide: VHVPLHRGAVSA
Forward Primer (Primer 1 differs for each peptide) Nco 1 restriction site
5′-ATCCATGGCGGTTCATGTTCCGTTGCATAGGGGTGCGGTTTCGGCGGATCCCGCAAAAGCG-3′
Net charge: +1

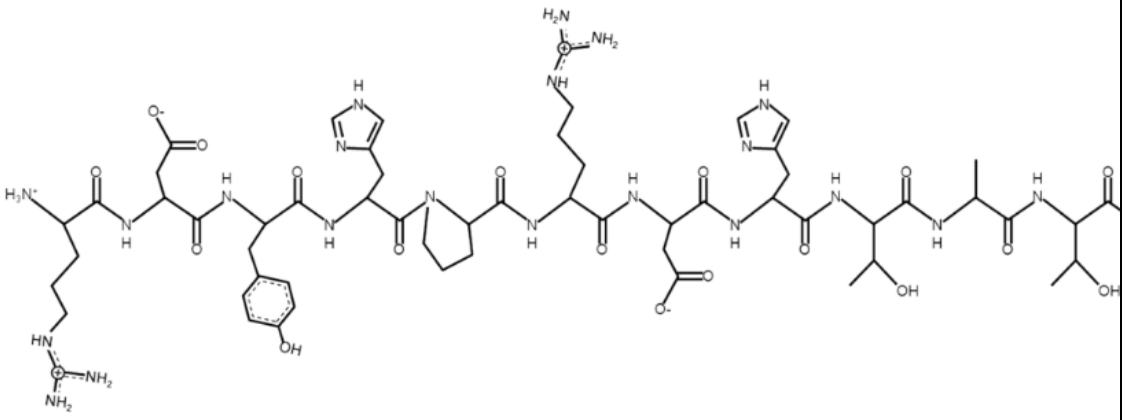


Peptide: SGTQDSMVGWNK
Forward Primer (Primer 1 differs for each peptide) Nco 1 restriction site
5′-ATCCATGGCGTCTGGTACTTAGGATTCTATGGTTGGTTGGAATAAGGATCCCGCAAAAGCG-3′

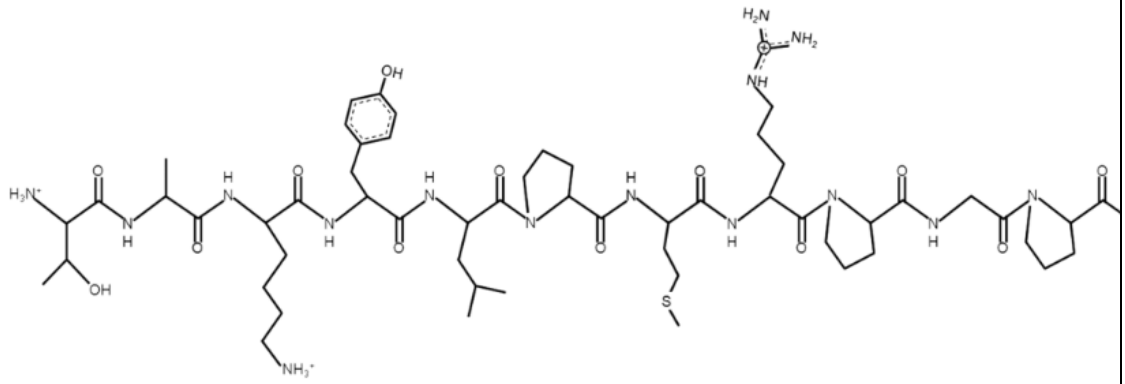
Net charge: 0



Peptide: RDYHPRDHTATW
Forward Primer (Primer 1 differs for each peptide) Nco 1 restriction site
5′-ATCCATGGCGCGGGATTATCATCCTCGTGATCATACTGCTACTTGGGATCCCGCAAAAGCG-3′
Net charge: 0



Peptide: TAKYLPMRPGPL
Forward Primer (Primer 1 differing for each peptide) Nco 1 restriction site
5′-ATCCATGGCGACTGCGAAGTATCTGCCTATGCGTCCTGGGCCGCTTGATCCCGCAAAAGCG-3′
Net charge: +2



Reverse Primer (Primer 2 is the same for all) Hind III restriction site 5′-GCAAGCTTTTATCAGCTTGCTTTCGAG-3′

Table 8. The peptide sequences, the peptide structures, the primers used to display the peptides on pVIII of M13 phage, the restriction sites for the primers, and the net charge of each peptide.

3.2.2.1 Preparation of M13 plasmid vector

A culture of XL_1 Blue *E. coli* harboring the PeCan49 phagemid DNA with chloramphenicol resistance was incubated at 37°*C* overnight on a LB plate (35 *μg / ml* chloramphenicol antibiotics). A well separated clone from the overnight culture was then inoculated into 3 *mL* of LB medium with the antibiotic chloramphenicol and incubated overnight at 250 rmp at 37°*C*. Phagemid DNA was then isolated and prepared with a QIAgen miniprep plasmid extraction kit, and the DNA was eluted with 50 *μL* of sterile double distilled water (ddH_2O)

Linear vector fragments were prepared by digesting the phagemid DNA from the separated clones with both the Nco I and Hind III restriction enzymes purchased from New England Biolabs. To accomplish this, a sterile micro-centrifuge tube had the following components: Phagemid DNA (5 *μL*), 10× New England Biolab buffer 2 (2 *μL*), Nco I 10 U (1 *μL*), Hind III 10 U (1 *μL*), and ddH2O 11 *μL* for a total of 20 *μL* of solution. The contents of the micro-centrifuge tube were then incubated for 2.5 hours at 37 °*C*.

After the digestion, the linear fragments were loaded into 1% agarose gel and isolated by electrophoresis in 1xTAE buffer (a mixture of Tris base, acetic

acid and EDTA). The linear DNA fragments were extracted from the agarose gel using a QIAgen gel DNA extraction kit. The DNA was then eluted with 20 *µL* of sterile ddH2O and kept at -20 °*C*.

3.2.2.2 PCR reaction (Preparation of insert fragments)

The polymerase chain reaction (PCR) was carried out in a sterile 200 *µL* micro-centrifuge tube using a Bio-RAD MJ MiniTM Personal Thermal Cycler. See Table 9 for primers. The reaction system consisted of M13KO7 phage RF DNA (2 µL) as the DNA template, primer 1 (1 *µL* at 50 pmol), primer 2 (1 *µL* at 50 *pmol*), 10 *mM* deoxynucleoside triphosphate (dNTP)(1 *µL*), 5 × GC buffer (10 *µL*), ddH_2O (35 *µL*), and Pfu 1U DNA polymerase (0.5 *µL*) under the PCR cycling conditions of 98 °C for 30 sec, 30 cycles (98 °*C* for 10 sec, 56 °*C* for 30 sec and 72 °*C* for 15 sec), and a last extension at 72 °*C* for 4 minutes. This process is outlined in Figure 11.

3.2.2.3 PCR products purification and digestion

PCR products were purified using a QIAgen PCR product purification kit. The DNA was eluted with 10 *µL* of sterile ddH2O. The purified DNA was then digested with both the Nco I and Hind III restriction enzymes in a sterile micro-centrifuge tube. Next, the micro-centrifuge tube was incubated for 2.5 hours at 37°*C*. After this digestion, the DNA fragments were loaded into 1% agarose gel and isolated by electrophoresis in 1 x TAE buffer. The digested fragment of DNA was removed from the agarose gel by gel extraction. The DNA was then eluted with 20 *µL* of sterile ddH_2O.

3.2.2.4 Preparation of TG1 competent cells

An overnight culture of E. coli strain TG1 was grown in a 125 *mL* sterile flask containing LB at 37 °C with vigorous shaking to an optical density of ~0.4 at 600 *nm*. The cells were then collected by centrifuging at 2500 rmp at a temperature of 4°C for 10 minutes. The cells were then re-suspended in 10 *mL* of cold sterile 100 *mM* $CaCl_2$. Next, the cells were kept on ice for 30 minutes and then collected by centrifuging. Cells were resuspended in 100 *mL* of $CaCl_2$ containing 15% glycerol. The competent cells were then stored at -80 °*C* until needed.

3.2.2.5 Ligation reaction

The ligation reaction was carried out by mixing the DNA vector fragment (phagemid) (0.020 pmol), insertion fragment from the PCR (0.060 *pmol*), 5 x ligation buffer (4 *µL*), T4 ligase from Invitrogen (2 *µL*), and ddH2O (8 *µL*). The reaction was incubated at 25 °*C* for 2 hours. This process is outlined in Figure 12.

3.2.2.6 Transfection of DNA into competent E. coli TG1 cells ($CaCl_2$ method)

In a sterile 1.5 mL Eppendorf tube, 100 *µL* of competent cells and 20 *µL* of ligation mixture was mixed. The mixture was held in ice water for 1 hour, 90 seconds at 42 °*C*, and then 2 minutes in ice water. Luria broth medium (1 *mL*) was added to the tube followed by incubation at 37 *ºC* for 1 hour in a shaking incubator. The transfected bacteria (200 *µL*) was then transferred onto a luria

broth plate containing chloramphenicol. The vector fragments without ligation were used as a control.

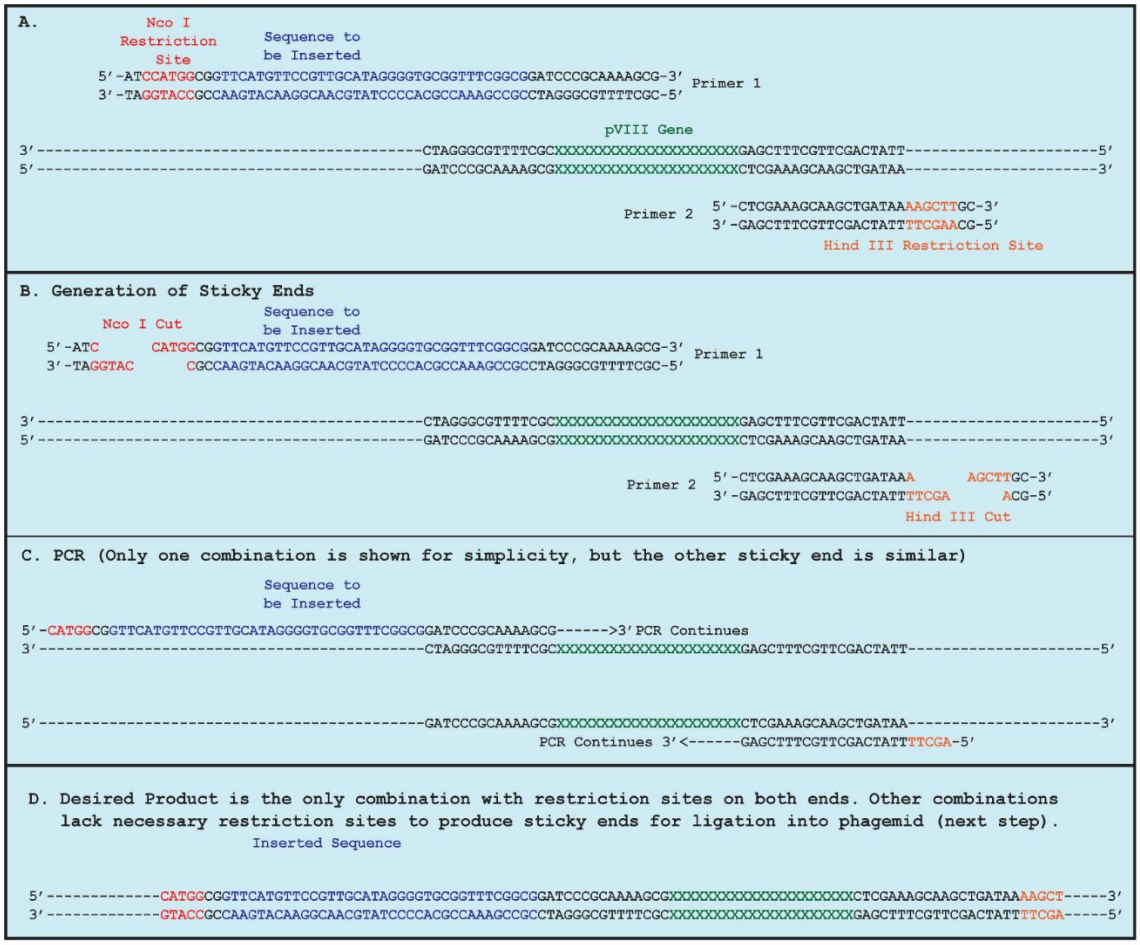


Figure 11. Generation of the insertion fragment for phage display. This example is for the peptide VHVPLHRGAVSA. (A) Primer 1 and primer 2 are digested with the restriction enzymes Nco I and Hind III respectively. T(B) The resulting sticky ends generated by the restriction enzymes. (C) PCR reaction and alignment of sticky ends to M13KO7 phage RF DNA. This process can create several options for products. (D) The desired end product is shown. This will be the only product which has both necessary restriction sites. These restriction sites get used later to generate new sticky ends and insert into the PeCan49 phagemid vector.

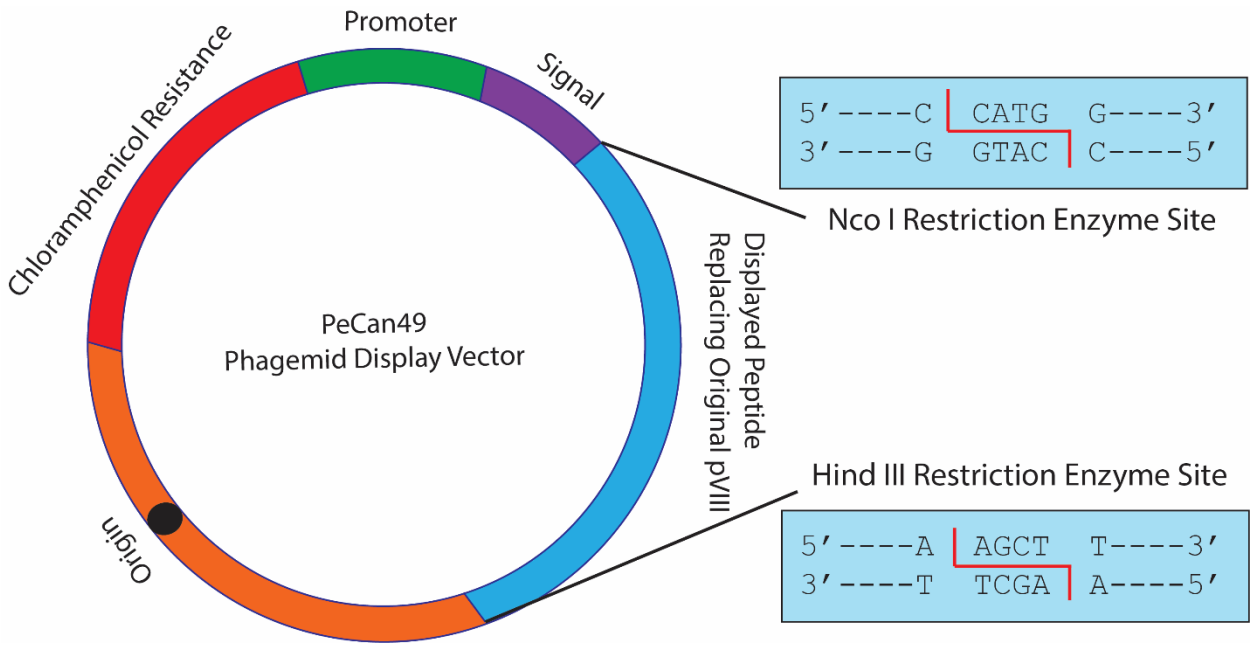


Figure 12. Insertion of M13KO7 phage RF DNA into the PeCan49 phagemid display vector. The final products from the PCR reactions on the M13KO7 RF DNA as well as the PeCan49 Phagemid Display Vector were cut by Nco I and Hind III to generate sticky ends. These sticky ends interact to insert the modified M13KO7 phage RF DNA harboring the sequence for the desired peptides into the PeCan49 Phagemid display vector. A T4 ligase is used to fully join the pieces. This leaves a PeCan49 phagemid vector harboring both chloramphenicol resistance and the desired gene for displaying peptides on the pVIII coat protein of M13 phage. The modified phagemids can then be used to transform the competent cells into cells which are both resistant to chloramphenicol and produce the desired engineered pVIII coat protein. When an M13KO7 helper phage is incubated with the transformed cells, many of the

pVIII coat proteins of the new phages will have the engineered pVIII coat protein.

3.2.2.7 Confirmation of recombinant phagemid

Individual colonies of bacteria were then inoculated into luria broth medium and amplified. The phagemid was purified from the amplified bacteria and sent for sequencing (MCLAB) to confirm the insertion fragment was added and the sequence did not have mutations. It should be noted that the cell line TG1 was very poor for amplifying phages but did harbor the correct plasmid sequence. Therefore, this method was repeated using ER2738 competent cells (sequenced again) and the amplification of phages was greatly improved.

3.2.3 Amplification of genetically engineered M13 phage

ER2738 (with recombinant plasmid) was inoculated into 5 *mL* of luria broth containing chloramphenicol (0.05 *mg/mL*). The culture was incubated at 37 °*C* at 200 rpm overnight.300 *uL* of overnight culture was mixed with 1200 *uL* of luria broth with 45 *uL* of helper phage (M13KO7). The mixture was incubated without shaking at 37 °*C* for 1 hour, then transferred to 30 *mL* of luria broth. The mixture was then shaken for 1 hour followed by the addition of 30 *uL* of chloramphenicol additional shaking for 3 more hours. The mixture was then transferred to 2.0 *L* of LB containing kanamycin (0.07 *mg/mL*) and IPTG (0.1 *mM*). The mixture was then incubated for 24 hours at 37 ºC with vigorous shaking. The mixture was then centrifuged at 8200 *g* for 50 minutes. The supernatant which contains the isolated phages after amplification was

transferred to a new container and mixed with 1/6 volume 20% PEG/2.5 *M* NaCl. The mixture was allowed to precipitate overnight at 4 ºC. Next, the mixture was centrifuged at 8200 *g* for 50 minutes at 4 *ºC*. The supernatant was discarded. The mixture was re-spun briefly followed by the removal of any residual supernatant. The pellet of phages was then resuspended in 10 *mL* of distilled water and transferred to a centrifuge tube. The mixture was then allowed to disperse more evenly over time by shaking it for 1 hour at room temperature (centrifugation can cause aggregation of phages). The mixture was then centrifuged at 7200 *rpm* for 50 minutes to remove any residual bacteria or other insoluble material. The supernatant was then transferred to a new tube and mixed with 1/6 volume 20% PEG/2.5 *M* NaCl. The mixture was then allowed to precipitate at 4 *ºC* overnight. Next the precipitated mixture was centrifuged at 7200 *rpm* for 50 minutes. The supernatant was discarded, and the pellet was resuspended in 1 *mL* of distilled water. The solution was transferred to a microcentrifuge tube followed by shaking for 1 hour at 200 *rpm* (or until the phage pellet fully dissolved). The solution was then centrifuged at 12,000 *rpm* on a table top centrifuge for 10 minutes to remove any insoluble material. The supernatant was transferred to a new tube and the optical density at 269 *nm* was measured to determine the concentration based on a proportionality concentration curve (optical density x $1x10^{14}$ = number of *phages / mL*). This process only works within the linear portion of the calibrated concentration curve (from 0.1 to 1.0 optical density). To further purify the phages, the phages were then transferred into dialysis tubing. Dialysis was

carried out in 5 L of distilled water with water changes every 3 hours for 9 hours. A final water change was allowed to go overnight. Next, the phages were transferred to vortex tubes and vortexed for 1 minute. The phages were then passed through a 0.2 *μm* filter. The concentration could then be re-measured using the same optical density procedure.

3.2.4 Generation of phage films

This procedure can be scaled for any size well plates or petri dish, but the volumes included are for 96-well tissue culture plates. For each film, 120 *μL* of poly-L-lysine was pipetted into a well of a tissue culture 96-well plate. The solution was allowed to incubate at room temperature for 30 minutes. The poly-L-lysine was pipetted out and saved in a clean container. The plates were allowed to completely dry in a sterile cell culture hood with the fan on. 100 µL of $1.5x10^{13}$ phage/mL was added to each well. The phage solution was allowed to incubate at room temperature for 30 minutes. The phages were transferred to a new clean container and the 96-well plate was dried in the hood again. 100 *μL* of the recycled poly-L-lysine solution was pipetted into each well and allowed to incubate at room temperature for 30 minutes. The poly-L-lysine solution was discarded, and the wells were allowed to completely dry again in the hood. 80 µL of the recycled phage solution was pipetted into each well. The coating was evenly spread across the wells. The solution was allowed to dry overnight in the hood. The films (with film structures verified in Figure 13) were exposed to UV light in a clean environment for 24 hours. The films were now complete. The

films were then soaked in cell medium overnight. The soaking medium was then discarded and new medium was used before seeding any cells.

3.2.5 Characterization of M13 phage (AFM and TEM)

M13 phages were characterized by atomic force microscopy (AFM) on a BIOSCOPE catalyst with ScanAsyst AFM (Bruker). The samples were prepared by pipetting 40 *μL* of $3x10^{12}$ *phages/mL* onto a glass slide followed by spin drying. The samples were imaged under 4 modes, height, inphase, peak force error, and quadrature.

For transmission electron microscopy (TEM), 10 μL of $1x10^{12}$ *phages/mL* were pipetted onto a formvar-coated TEM grid and allowed to soak for 3 minutes. The extra liquid was then wicked away from the grid using a piece of filter paper. 10 *μL* of 0.5% uranyl acetate at a pH of 4.5 was then added to the grid for 10 seconds. The extra uranyl acetate was then wicked away. The grid was then blown dry quickly with a hair dryer. Images were then taken on a Zeiss 10 TEM at a magnification of 6300.

3.2.6 Characterizing phage film morphology

Phage films were generated according to the described protocol. The phage films were then imaged using a Nikoneclipse Ti microscope under brightfield imaging. Additionally, the phage films were imaged using a BIOSCOPE catalyst with ScanAsyst AFM (Bruker) under 4 modes, height, inphase, peak force error, and quadrature.

3.2.7 Cell proliferation on phage films

hMSCs were seeded onto 96-well plate phage films (200 *μL* of $1x10^4$ *cells/mL*) and grown for 47 hours or 71 hours. Both stimulated and unstimulated controls were included. At the end of the indicated growth times, alamarBlue® (Bio-Rad) was added as 10% of the volume in the well mixed with cell media. The cultures were allowed to incubate 8 hours. The absorbance at 570 *nm* and 600 *nm* were then measured. The percent reduction of alamarBlue® was then calculated (higher percent reduction = more growth).

3.2.8 Immunofluorescence of osteoblast marker proteins

After culturing hMSCs on phage films for 26 days, the cells were fixed with 4% paraformaldehyde (10 minutes) and permeabilized with 0.2% Triton X-100 (2 minutes) at room temperature. 5 washes with PBS were done after each step. The cells were then blocked with 5% goat serum solution for 1 h followed by 5 washes with PBS. The osteogenic protein markers osteopontin (OPN), osteocalcin (OCN), and collagen type 1A (COL) were detected through immunofluorescence. OPN was detected with the primary antibody for OPN (RbpAB to osteopontin ab8448 from Abcam). The secondary antibody used was Goat Anti-Rabbit IgG H&L (Alexa Fluor 555) (ab150078) from Abcam (red). OCN was detected with the primary antibody for OCN [OC4-30] (ab13418) from Abcam). The secondary antibody used was Goat Anti-Mouse IgG H&L (Dylight 650) pre-adsorbed from abcam ab96882 (red). COL was detected using a primary antibody for COL (RbpAb to collagen 1 ab34710). The secondary antibody used was Goat Anti-Rabbit IgG H&L (Alexa Fluor 555) (ab150078) from abcam (red). Cell nuclei were stained by DAPI (blue) for

all samples, and actin was stained by phalloidin (green). The positive control was osteogenic media from Lonza ((hMSC Osteogenic Bullet Kit). All other samples were grown in basal media (MSCGM Bullet Kit (PT-3238 & PT-4105) from Lonza.

3.2.9 Calcium Nodule Staining

After 26 days of culturing hMSCs under differentiating conditions, the cell media was removed from the 6-well tissue culture plates. The plates were rinsed once with PBS. The cells were then fixed with 4% paraformaldehyde solution for 10 minutes. After fixation, the wells were rinsed twice with distilled water and the cells were stained with 2% Alizarin Red solution (pH 4.2) for 3 minutes. The wells were then rinsed 5 times with PBS, and the cells were imaged using bright field microscopy.

3.2.10 qPCR of osteoblast marker genes

hMSCs were seeded ($1x10^3$ cells per culture plate) on to phage films as well as relevant control plates. The cells were then cultured for 26 days. The cells then were processed with a Power SYBR™ Green Cells-to-CT™ Kit. The number of cells was adjusted to be $5x10^3$ cells per lysis reaction. All other parameters were kept the same as the manufacturer's protocol for this kit (Thermo Fisher Scientific). The gene expression of osteopontin, osteocalcin, and collagen type 1A were measured as a fold change normalized to the reference gene GAPDH and a negative control (basal media + cells but no phage) such that the baseline at zero-fold change represents the negative

control. For temperature cycling and measuring CT values, a MiniOpticon Real Time PCR System was used.

3.3 Results and Discussion

3.3.1 Sequencing results of phage display

On the first sequencing of phage plasmid in TG1 bacteria, the results came out with the correct inserts. However, the amplification of engineered phages was poor in this strain of bacteria. Generating large quantities of phages is essential to use as a biomaterial. Therefore, ER2738 competent cells were transfected with the plasmid instead. The sequencing results of this transfection are shown in Table 10. All sequences were incorporated as desired.

Table 9. The DNA sequencing results for displaying the indicated peptides on the pVIII coat protein of M13 phages. The highlighted region represents the inserted DNA sequence which corresponds to the indicated peptide. The genetically engineered plasmids are in ER2738 bacteria.

Peptide	FASTA from sequencing corresponding to the pVIII coat protein plasmid for M13 bacteriophage (insert highlighted in yellow).
VHVPLHRGAVSA	>E7B1_RevP_C10 Reverse Complement NNNCCNNCTGGNATNNNNCNGNNNNCNNNNNNTNNNNNNGCTNNCCTGCN CTAATGNNNNNNNNNNNTTTNNGATNNTNTCTGNNNAGNNNCCCATCNNC AGTNTTATTTNNNCCATGAAGNCGGNTACGCGACTGGGCGTGGGAGCATC TGGTCGCATTGGGTCACCAGCAAAATCGCGCTGTTAGCGGNNCCANTTAA GTTCTGTCTCGGCGCGTCTGCGTCTGGCTGGCTGGCATAAATATCTCACT CGCAATCAAATTCAGCCGATAGCGGAACGGGAAGGCGACTGGAGTGCCAT GTCCGGTTTTCAACAAACCATGCAAATGCTGAATGAGGGCATCGTTCCCA CTGCGATGCTGGTTGCCAACGATCAGATGGCGCTGGGCGCAATGCGCGCC

	ATTACCGAGTCCGGGCTGCGCGTTGGTGCGGACATCTCGGTAGTGGGATA CGACGATACCGAAGACAGCTCATGTTATATCCCGCCGTTAACCACCATCA AACAGGATTTTCGCCTGCTGGGGCAAACCAGCGTGGACCGCTTGCTGCAA CTCTCTCAGGGCCAGGCGGTGAAGGGCAATCAGCTGTTGCCCGTCTCACT GGTGAAAAGAAAAACCACCCTGGCGCCCAATACGCAAACCGCCTCTCCCC GCGCGTTGGCCGATTCATTAATGCAGCTGGCACGACAGGTTTCCCGACTG GAAAGCGGGCAGTGAGCGGTACCCGATAAAAGCGGCTTCCTGACAGGAGG CCGTTTTGTTTTGCAGCCCACCTCAACGCAATTAATGTGAGTTAGCTCAC TCATTAGGCACCCCAGGCTTTACACTTTATGCTTCCGGCTCGTATGTTGT GTGGAATTGTGAGCGGATAACAATTTCACACAGGAAACAGCTATGACCAT GATTACGAATTTCTAGAGAAGGAGATATACATATGAAATCCCTATTGCCT ACGGCAGCCGCTGGATTGTTATTACTCGCGGCCCAGCCGGCCATGGCGGT TCATGTTCCGTTGCATAGGGGTGCGGTTTCGGCGGATCCCGCAAAAGCGG CCTTTAACTCCCTGCAAGCCTCAGCGACCGAATATATCGGTTATGCGTGG GCGATGGTTGTTGTCATNGTCGGCGCAACTATCGGTNNCAAGNGTNGANN NNNN
SGTQDSMVGWNK	>E8R5B1_RevP_A10 Reverse Complement NNNNNNNCTNGANNCNNTTNNNNNTNNTCNNTGGANNGNNNNGNANNNNT NNNNTGNNNGCNNNCCNTNNCNNNTANNNNNNNNNNNTNATTTNNTTGAT NTNNNCTNNNAGNACNCCCATCNNNAGTNTTANTTTTNTCCCATNAAGAC GGGTACGCGACTGGGCGTGGAGCATCTGGTCGCATTNGGGTCNCCAGCAA ATCGCGCTGNTTAGCGGNNCCATTAAGTTCTGTCTCGGGCGCGTCTGCGT CTGGCTGGCTNGNATAAATATCTCACTCGCAATCAAATTCAGCCGATAGC GGAACGGGAAGGCGACTGGAGTGCCATGTCCGGTTTTCAACAAACCATGC AAATGCTGAATGAGGGCATCGTTCCCACTGCGATGCTGGTTGCCAACGAT CAGATGGCGCTGGGCGCAATGCGCGCCATTACCGAGTCCGGGCTGCGCGT TGGTGCGGACATCTCGGTAGTGGGATACGACGATACCGAAGACAGCTCAT GTTATATCCCGCCGTTAACCACCATCAAACAGGATTTTCGCCTGCTGGGG CAAACCAGCGTGGACCGCTTGCTGCAACTCTCTCAGGGCCAGGCGGTGAA GGGCAATCAGCTGTTGCCCGTCTCACTGGTGAAAAGAAAAACCACCCTGG CGCCCAATACGCAAACCGCCTCTCCCCGCGCGTTGGCCGATTCATTAATG CAGCTGGCACGACAGGTTTCCCGACTGGAAAGCGGGCAGTGAGCGGTACC CGATAAAAGCGGCTTCCTGACAGGAGGCCGTTTTGTTTTGCAGCCCACCT CAACGCAATTAATGTGAGTTAGCTCACTCATTAGGCACCCCAGGCTTTAC ACTTTATGCTTCCGGCTCGTATGTTGTGTGGAATTGTGAGCGGATAACAA TTTCACACAGGAAACAGCTATGACCATGATTACGAATTTCTAGAGAAGGA GATATACATATGAAATCCCTATTGCCTACGGCAGCCGCTGGATTGTTATT ACTCGCGGCCCAGCCGGCCATGGCGTCTGGTACTTAGGATTCTATGGTTG GTTGGAATAAGGATCCCGCAAAAGCGGCCTTTAACTCCCTGCAAGCCTCA GCGACCGAATATATCGGTTATGCGTGGGCGATGGTTGTTGTCNNNNCGGC GCNNNNNNN
TAKYLPMRPGPL	>G13B2_RevP_H10 Reverse Complement NCNNNNNGNNATTGNNNNANGATNNNNNNNCTNNNGAAGCNNNNNNNNNA ATNNNNCNNNNNNNNANTTNNTGATNTTNTCTGNNCNAGACNCCCATNNNN AGTANTNATTTNNNNATGAAAGACNGTACGCGACTGGNNNGTGGAGCATC TGGTCGCATTNGGGTCNCCAGCAAATCGCGCTNTTAGCGNNNCCANTNAA NTTCTGTCTCGGGCGCGTCTGCGTCTGGCTGGCTGGCATAAATATCTCAC TCGCAATCAAATTCAGCCGATAGCGGAACGGGAAGGCGACTGGAGTGCCA TGTCCGGTTTTCAACAAACCATGCAAATGCTGAATGAGGGCATCGTTCCC

	ACTGCGATGCTGGTTGCCAACGATCAGATGGCGCTGGGCGCAATGCGCGC CATTACCGAGTCCGGGCTGCGCGTTGGTGCGGACATCTCGGTAGTGGGAT ACGACGATACCGAAGACAGCTCATGTTATATCCCGCCGTTAACCACCATC AAACAGGATTTTCGCCTGCTGGGGCAAACCAGCGTGGACCGCTTGCTGCA ACTCTCTCAGGGCCAGGCGGTGAAGGGCAATCAGCTGTTGCCCGTCTCAC TGGTGAAAAGAAAAACCACCCTGGCGCCCAATACGCAAACCGCCTCTCCC CGCGCGTTGGCCGATTCATTAATGCAGCTGGCACGACAGGTTTCCCGACT GGAAAGCGGGCAGTGAGCGGTACCCGATAAAAGCGGCTTCCTGACAGGAG GCCGTTTTGTTTTGCAGCCCACCTCAACGCAATTAATGTGAGTTAGCTCA CTCATTAGGCACCCCAGGCTTTACACTTTATGCTTCCGGCTCGTATGTTG TGTGGAATTGTGAGCGGATAACAATTTCACACAGGAAACAGCTATGACCA TGATTACGAATTTCTAGAGAAGGAGATATACATATGAAATCCCTATTGCC TACGGCAGCCGCTGGATTGTTATTACTCGCGGCCCAGCCGGCCATGGCGA CTGCGAAGTATCTGCCTATGCGTCCTGGGCCGCTTGATCCCGCAAAAGCG GCCTTTAACTCCCTGCAAGCCTCAGCGACCGAATATATCGGTTATGCGTG GGCGATGGTTGTTGTCATGTCGGCGCAACTATCGGNNCAAAGCNTTNANN NNNNCNNN
RDYHPRDHTATW	>R55B2_RevP_F10 Reverse Complement NNGGGAANTGNNNNNGGNNNGCNNNNNTNNNNNAGCNNCCTGNNNTAAAN NNNNNNNNNNNNTTTCNNNNATGNNTCTGNNNAGACNNCCCANCANNNAG TNNTNANNTTNNNNATGAAAGNNCGGTACGCGACTGGNNGTGGAGCATCT GGTCGCATTNGGGTCNCCAGCAAATCGCGCTGTTTAGCGGNCCCNTTAAA GTTTCTGTCTCGGCGCGTCTGCGTCTGGCTGGCTGGGCATAAATATCTCA CTCGCAATCAAATTCAGCCGATAGCGGAACGGGAAGGCGACTGGAGTGCC ATGTCCGGTTTTCANCAAACCATGCAAATGCTGAATGAGGGCATCGTTCC CACTGCGATGCTGGTTGCCAACGATCAGATGGCGCTGGGCGCAATGCGCG CCATTACCGAGTCCGGGCTGCGCGTTGGTGCGGACATCTCGGTAGTGGGA TACGACGATACCGAAGACAGCTCATGTTATATCCCGCCGTTAACCACCAT CAAACAGGATTTTCGCCTGCTGGGGCAAACCAGCGTGGACCGCTTGCTGC AACTCTCTCAGGGCCAGGCGGTGAAGGGCAATCAGCTGTTGCCCGTCTCA CTGGTGAAAAGAAAAACCACCCTGGCGCCCAATACGCAAACCGCCTCTCC CCGCGCGTTGGCCGATTCATTAATGCAGCTGGCACGACAGGTTTCCCGAC TGGAAAGCGGGCAGTGAGCGGTACCCGATAAAAGCGGCTTCCTGACAGGA GGCCGTTTTGTTTTGCAGCCCACCTCAACGCAATTAATGTGAGTTAGCTC ACTCATTAGGCACCCCAGGCTTTACACTTTATGCTTCCGGCTCGTATGTT GTGTGGAATTGTGAGCGGATAACAATTTCACACAGGAAACAGCTATGACC ATGATTACGAATTTCTAGAGAAGGAGATATACATATGAAATCCCTATTGC CTACGGCAGCCGCTGGATTGTTATTACTCGCGGCCCAGCCGGCCATGGCG CGGGATTATCATCCTCGTGATCATACTGCTACTTGGGATCCCGCAAAAGC GGCCTTTAACTCCCTGCAAGCCTCAGCGACCGAATATATCGGTTATGCGT GGGCGATGGTTGTTGTCATGTCGGCGCAACTATCGGTANCAAAGNCNNNN NNNNNNNNCC

3.3.2 M13 phage morphology images

The amplified M13 phages were imaged by AFM and TEM as shown in Figure 13. A single M13 phage measures ~1000 nm in length. A property frequently observed with M13 phage is a bundling effect. The bundling effect is the tendency for M13 phages to align themselves next to each other and can contribute to highly ordered structures as shown.

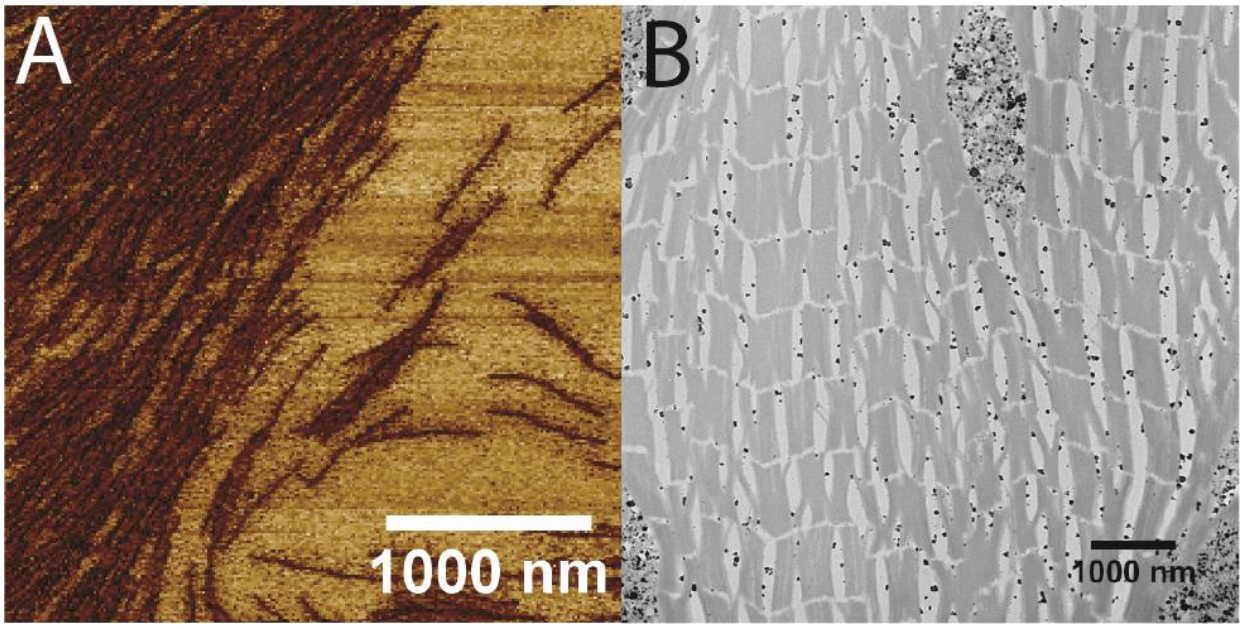


Figure 13. The morphology of M13 phages. (A) M13 phages imaged by AFM on a BIOSCOPE catalyst with Scan Asyst (Brunker). (B) M13 phages imaged by a Zeiss 10 transmission electron scope at a magnification of 6300. The phages were stained with 0.5% uranyl acetate.

3.3.3 Organized ridge groove structure of phage films

It is well known that M13 phages can self-assemble into ordered structures during liquid crystalline phase transitions.[353, 358-359] However, the consistency of these assembly strategies is far less than desirable as is often

the case with M13 phage film structures. Structural differences in films can cause differences in cellular differentiation which is problematic when comparing different peptides displayed on phages within a phage film. Due to repeatability issues, I developed a new protocol as described. This protocol involved alternating layers of M13 phages and poly-L-lysine for 2 layers of each. A major difference to reported protocols is that the M13 phages were both desalted and filtered through a 0.2 *μm* filter. This provided more clean and consistent structures as shown in Figure 14a-c. Also, in the final step the M13 phage solution was allowed to slowly dry overnight rather than pulling it off again. It was also very important to use fresh poly-L-lysine as well as good tissue culture plates. The resulting structures are highly organized and more repeatable (success 50% of the time on the entire plate, but large regions always had this structure even if the whole plate was not uniform). In addition, these phage films were highly durable supporting hMSC growth over the course of a month with no loss of structure. Additionally, hMSCs grown on these films align and stretch with the background structure of organized phages as shown in Figure 14b. Due to these properties, these films demonstrated some improvement over previously published methods.

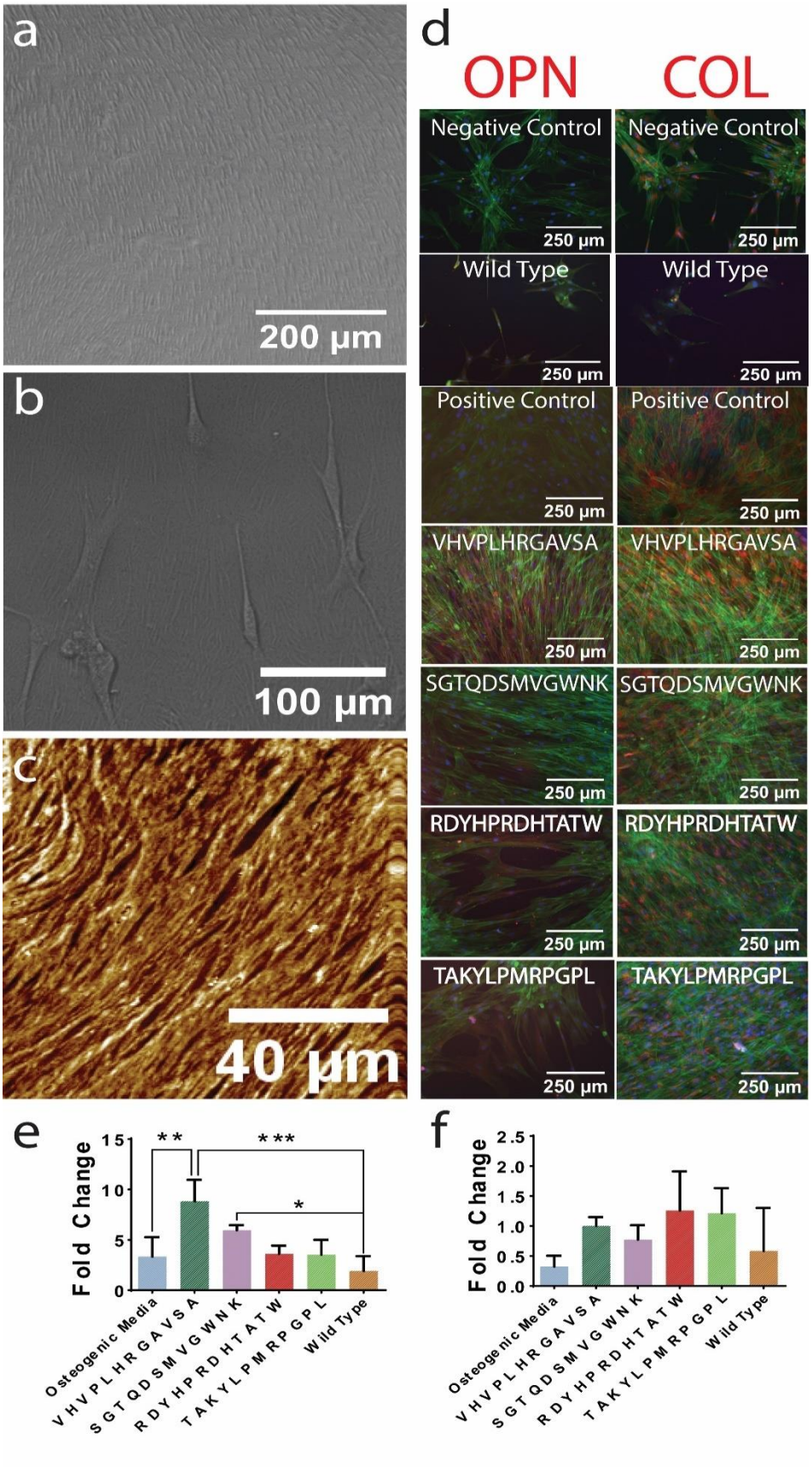

a
200 µm
b
100 µm
c
40 µm
d
OPN
COL
Negative Control
Wild Type
Positive Control
VHVPLHRGAVSA
SGTQDSMVGWNK
RDYHPRDHTATW
TAKYLPMRPGPL
250 µm
e
Fold Change
15
10
5
0
**
***
*
Osteogenic Media
VHVPLHRGAVSA
SGTQDSMVGWNK
RDYHPRDHTATW
TAKYLPMRPGPL
Wild Type
f
Fold Change
2.5
2.0
1.5
1.0
0.5
0.0
Osteogenic Media
VHVPLHRGAVSA
SGTQDSMVGWNK
RDYHPRDHTATW
TAKYLPMRPGPL
Wild Type

Figure 14. Osteogenic differentiation of hMSCs on phage films. (a-b) Phage film ridge groove morphology. Nikon microscope bright field image of representative phage film structure without cells (a) and with hMSCs (b). Large regions of aligned ridge groove structures can be seen in (a). hMSCs tend to bind and stretch along the direction of the phage film grooves (b). (c) Atomic force microscopy (AFM) images of the film, further demonstrating an aligned fiber-like ridge groove structure. The AFM image was made using the height input. (d) Immunofluorescence of osteogenic protein markers including osteopontin (OPN), and collagen type 1A (COL). OPN was detected with the primary antibody for OPN (RbpAB to osteopontin ab8448 from Abcam). The secondary antibody used was Goat Anti-Rabbit IgG H&L (Alexa Fluor 555) (ab150078) from Abcam (red). COL was detected using a primary antibody for COL (RbpAb to collagen 1 ab34710). The secondary antibody used was Goat Anti-Rabbit IgG H&L (Alexa Fluor 555) (ab150078) from abcam (red). Cell nuclei were stained by DAPI (blue) for all samples, and actin was stained by phalloidin (green). The positive control was osteogenic media from Lonza ((hMSC Osteogenic BulletKit). All other samples were grown in basal media (MSCGM BulletKit (PT-3238 & PT-4105) from Lonza. Peptides were displayed on M13 phages and developed into thin films for which the hMSCs were grown on for 26 days. This data shows that the phage films were able to upregulate the osteoblast marker protein, OPN. (e) Fold change ($2^{-\Delta\Delta Ct}$) for osteopontin (OPN) expression of hMSCs after 26 days of culturing on phage films displaying the indicated peptide or controls. The sequence VHVPLHRGAVSA appears to

be the best with a fold change better than the Lonza osteogenic media. The sequence SGTQDSMVGWNK appears to be second best with a significant advantage over the wild type, but no difference from the Lonza osteogenic media. (f) Collagen (COL) type 1A fold change expression (a control that should be the same for all samples) of hMSCs after 26 days of culturing on phage films displaying the indicated peptide or controls. The gene expression was normalized to GAPDH (a reference gene). All fold changes are relative to a negative control (basal media with no peptides or phage) which represents the baseline at zero-fold change. All data are expressed as the mean $\pm$ standard deviation (n=3, * $P \leq 0.05$, ** $P \leq 0.01$, *** $P \leq 0.001$). These data show that the aligned phage film structures (biophysical cue) could induce increased osteoblast gene expression as demonstrated by the upregulation of osteoblast genes in wild type films. Additionally, they show that the peptides VHVPLHRGAVSA and SGTQDSMGWNK further improved the differentiation of hMSCs into osteoblasts through a biochemical signaling route as they had a statistically significant advantage over wild type for OPN expression.

3.3.4 Phage films support hMSC growth and proliferation

The phage films did support stem cell growth and proliferation. However, hMSCs not exposed to phages did grow at a statistically significant ($P \leq 0.05$) faster rate within the first 47 and 71 hours. Slower cell proliferation on phage films is associated with osteoblast differentiation.[8] Over longer periods of time, the hMSCs on the phage films did proliferate to densely cover the entire plate as can be seen in Figure. 14. Over time, the percent reduction of alamar blue

did increase for both the positive control and the phage films demonstrating that the cells could survive and proliferate on these phage films (Figure 15).

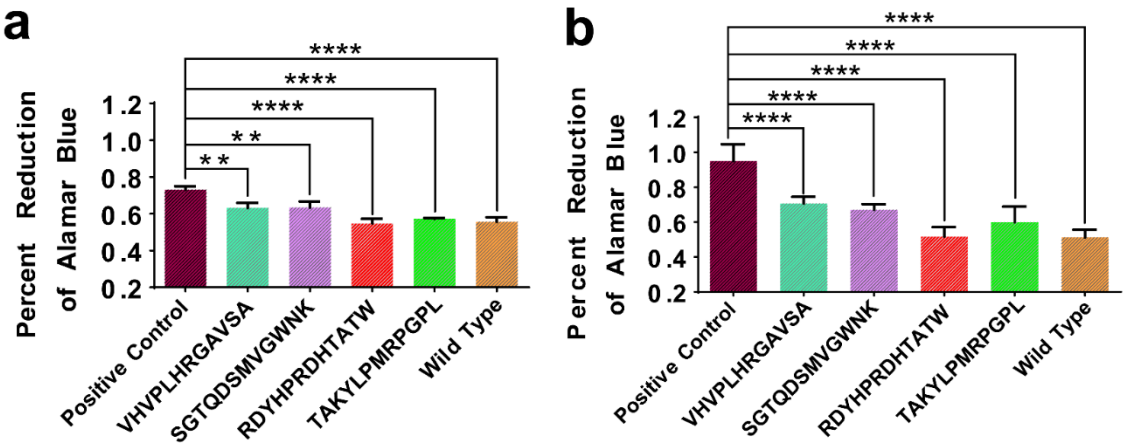


Figure 15. hMSC cell proliferation on the phage films. Proliferation was measured as the percent reduction of alamar blue. The hMSCs were grown for 47 h (a) or 71 h (b) before incubation with alamar blue and measurement of the absorbance at 570 nm and 600 nm. The percent reduction of alamar blue was then calculated (a higher percent reduction reflects more growth of the cells). The phage films did significantly lower cell proliferation, consistent with the earlier findings that a higher differentiation potential results in a lower proliferation potential of the stem cells. All data represent the mean $\pm$ standard deviation of n=3 (* $P \leq 0.05$, ** $P \leq 0.01$, *** $P \leq 0.001$). The positive control is hMSCs grown in basal medium with no phages.

Detailed ANOVA statistics for this data are given in Table 11.

3.3.5 Peptide-phage induced differentiation of hMSCs demonstrated by osteoblast marker proteins

The osteoblast marker protein osteopontin (OPN) was detected using immunofluorescence. Collagen type 1A (COL) was used as a control which shows the same level of expression (by eye) on each different peptide-bearing phage film. The results are shown in Figure 14. All peptides on phage films showed expression of osteopontin including the wild type phage film. This indicates that the highly ordered ridge groove structure of the phage films can induce osteoblast differentiation. Additionally, the peptide VHVPLHRGAVSA showed a qualitatively higher level of osteopontin protein expression than the other groups and a higher expression than the positive control (osteogenic media from Lonza). This data demonstrated that the phage films could induce osteogenesis, but it also showed a distinct advantage for the VHVPLHRGAVSA peptide sequence. The other sequences also showed differentiation but required more quantitative results rather than the qualitative immunofluorescence images which is later done using qPCR.

3.3.6 Peptide-phage induced hMSC calcium deposits

Calcium nodule staining was done using Alizarin red at 14 and 26 days as shown in Figure 16 and Figure 17 respectively. At 14 days, hMSCs on the phage films and those cultured in osteogenic media showed an increase in calcium deposits at similar levels. In this test, it was not possible to establish a difference between osteoblast induction through the topography of the phage films vs from the peptides used on each phage film. However, it does show that

each phage film after 14 days is able to induce calcium deposits on the level of the positive control which is a leading product for osteogenesis. At 26 days, a major difference between the negative control, phage film samples, and the osteogenic media was observed. All phage film, although indistinguishable from each other by this method, performed substantially better than the negative or positive control. This indicates that the hMSCs are depositing a mineralized matrix which is indicative of osteoblast when cultured on phage films. Additionally, the phage films may be an alternative to using osteogenic media as they performed better than the positive control.

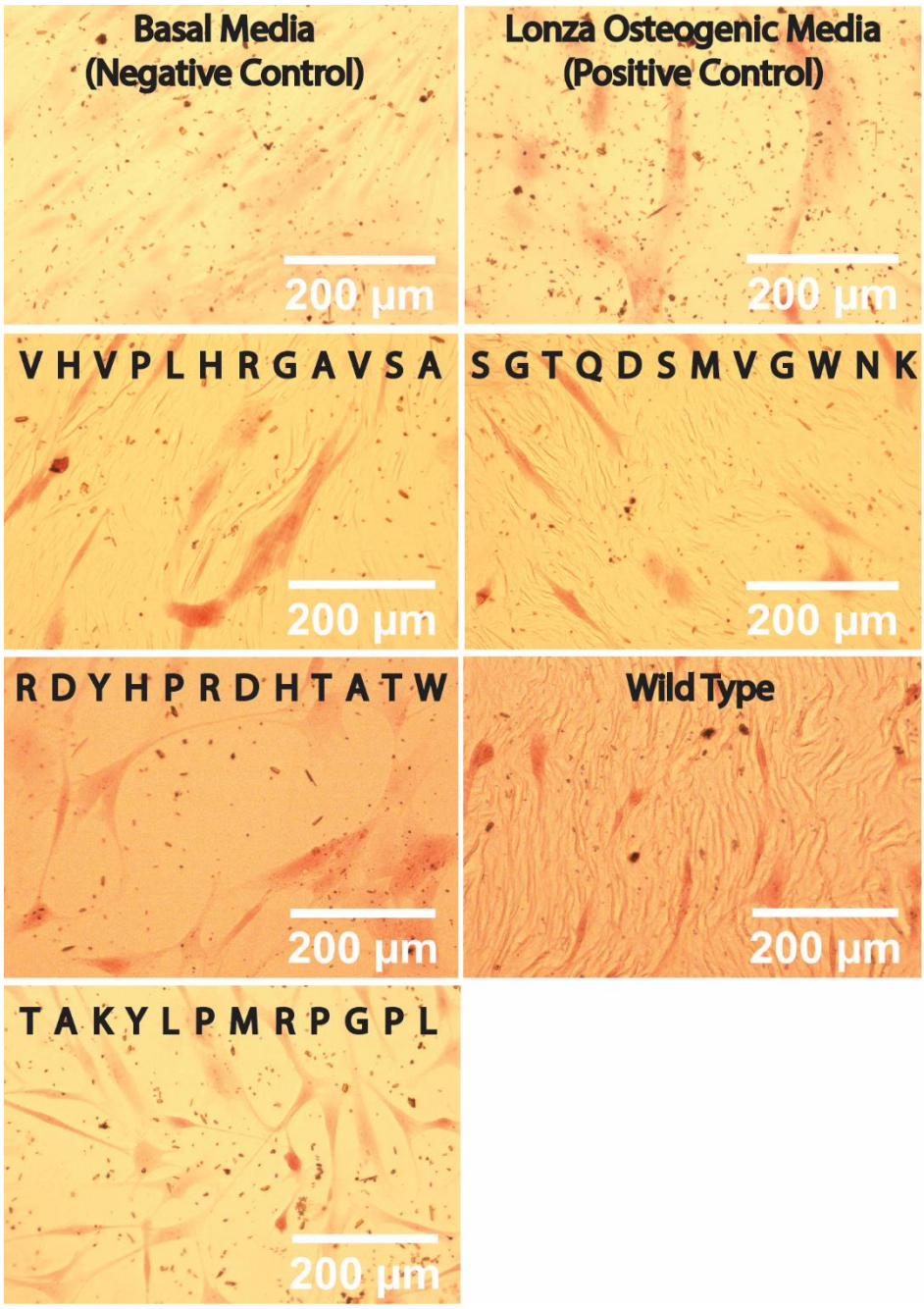


Figure 16. Calcium (red) nodule staining (14 days). Briefly, hMSCs were seeded onto either phage films having the indicated peptides or the indicated control groups. Calcium deposits were stained with Alizarin red after 14 days of culturing hMSCs on phage films.

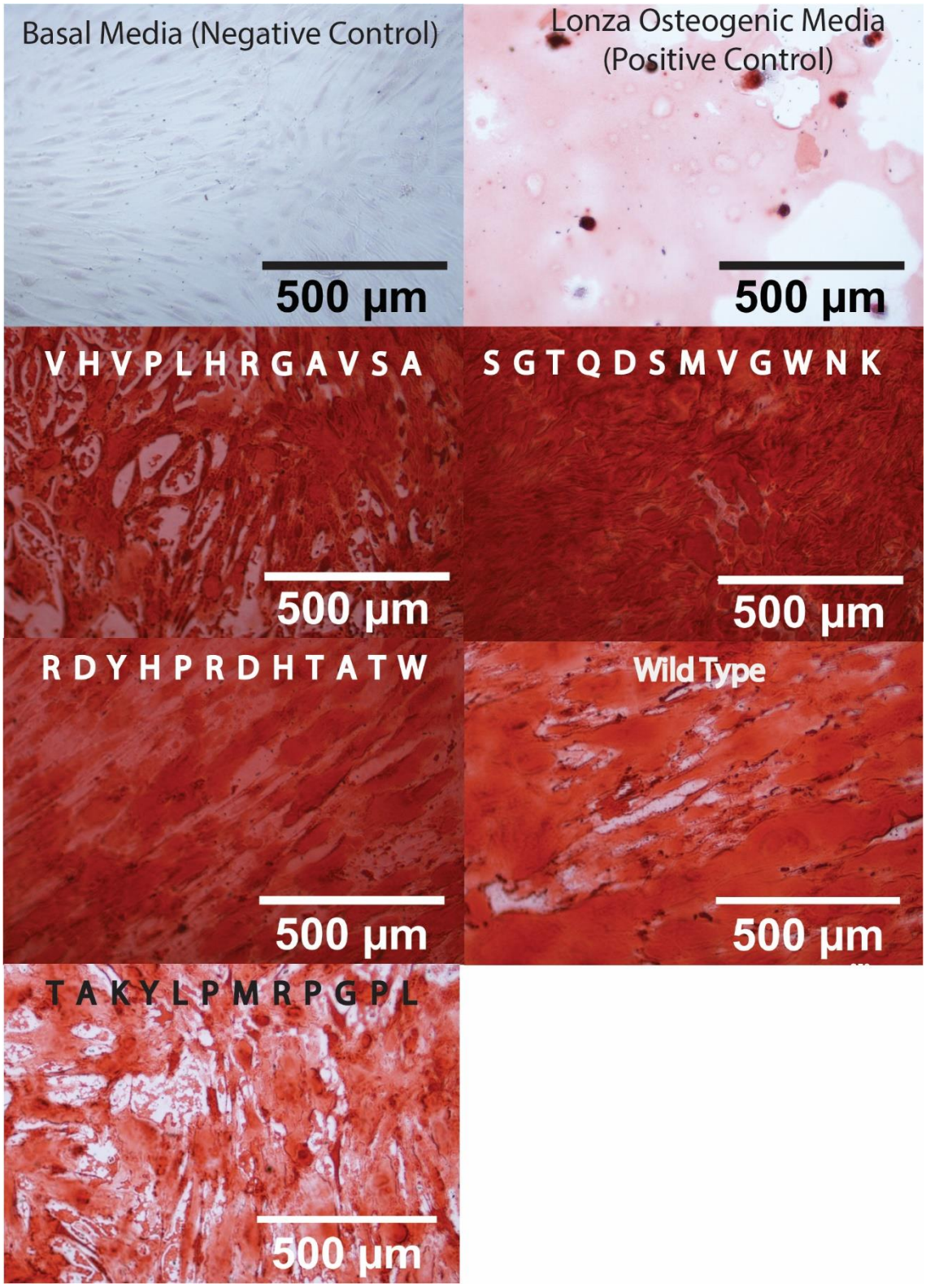

Basal Media (Negative Control)
500 µm
Lonza Osteogenic Media
(Positive Control)
500 µm
V H V P L H R G A V S A
500 µm
S G T Q D S M V G W N K
500 µm
R D Y H P R D H T A T W
500 µm
Wild Type
500 µm
T A K Y L P M R P G P L
500 µm

Figure 17. Calcium (red) nodule staining (26 days). Briefly, hMSCs were seeded onto either phage films having the indicated peptides or the indicated control groups. Calcium deposits were stained with Alizarin red after 26 days of culturing hMSCs on phage films.

3.3.7 Peptide-phage induced genetic upregulation of osteoblast marker genes

After the cells were cultured on the phage films in a basal media (non-osteogenic media) for 14 or 26 days, the BMPR1A-binding peptide (VHVPLHRGAVSA) and BMPR1A/BMPR2 dual-binding peptide (SGTQDSMVGWNK) showed significantly higher capability in inducing the osteogenic differentiation than the BMPR2-binding peptide (RDYHPRDHTATW) and other peptides. This result is demonstrated by qPCR and immunofluorescence imaging of the osteogenic specific marker (osteopontin, OPN) at the gene and protein level, respectively (Figure 14d-e and Figure 18). More importantly, VHVPLHRGAVSA was the strongest inducer and even better than the commercial osteogenic differentiation inducing media after 26 days while SGTQDSMVGWNK did not show statistical difference in osteogenic differentiation induction in comparison to the commercial media after 26 days. For the 14-day time point group, the early differentiation capabilities of osteogenic media and VHVPLHRGAVSA were not statistically different, suggesting that the advantages of VHVPLHRGAVSA over osteogenic media only become apparent over a longer period of time. For the non-osteogenic marker (Type 1 Collagen, COL), all groups including all peptide groups and the no peptide group (wild type

phage) as well as the commercial osteogenic differentiation media showed no statistical differences after 26 days (Figure 14f). For the 14-day COL groups, TAKYLPMRPGPL showed less gene expression than RDYHPRDHTATW and SGTQDSMVGWNK while all other groups were not statistically different (Figure 18b). All these data show that the BMPR1A-binding peptide (VHVPLHRGAVSA) and BMPR1A/BMPR2 dual-binding peptide (SGTQDSMVGWNK) are the best osteogenic peptides with the former even stronger than the commercial differentiation inducing media for longer time points. It should be noted that hMSCs were elongated on all phage films (Figure 14b), suggesting that the same topographical cue affected the cell morphology and differentiation similarly for all phage groups.

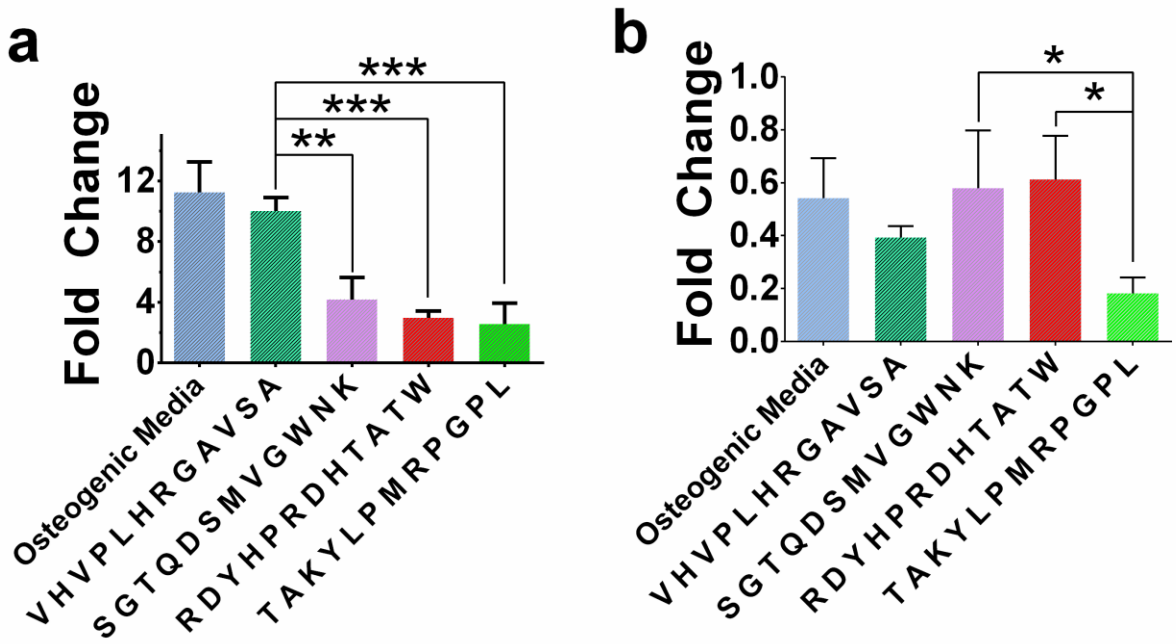


Figure 18. Osteogenic differentiation of hMSCs on phage films after 14 days. (a) Fold change ($2^{-\Delta\Delta Ct}$) for osteopontin (OPN) expression of hMSCs after 14

days of culturing on phage films displaying the indicated peptide or controls. The sequence VHVPLHRGAVSA appears to be the best with a fold change significantly better than the other peptides and no difference from the osteogenic media. (b) Collagen (COL) type 1A fold change expression of hMSCs after 14 days of culturing on phage films displaying the indicated peptide or controls. The peptides SGTQDSMVGWNK and RDYHPRDHTATW were upregulated relative to TAKYLPMRPGPL. All other conditions had no significant difference. All Gene expressions were normalized to the reference gene, GAPDH. All fold changes are relative to a negative control (basal media with no peptides or phage) which represents the baseline at zero-fold change. All data represent the mean $\pm$ standard deviation of n=3 (* $P \leq 0.05$, ** $P \leq 0.01$, *** $P \leq 0.001$). This data shows that VHVPLHRGAVSA is as good as osteogenic media for upregulating the osteoblast marker, OPN at 14 days.

3.4 Conclusion

The morphology of M13 phages was characterized by TEM and AFM. The M13 phages amplified were demonstrated to be filamentous in structure measuring ~1000 nm in length. The phages also demonstrated a self-assembly into highly ordered and aligned bundling structures brought about during a liquid crystalline phase transition. The natural ability of these phages to self-assemble into ordered structures was then used to develop a new, more reliable phage film generation strategy. This strategy produced highly organized phage films with an aligned ridge groove morphology. This morphology was shown to be a potent biophysical cue for osteoblast differentiation at a genetic level, protein

production level, and demonstrated large amounts of calcium deposition (greater than a leading company product). Novel possible osteogenesis inducing peptides discovered in Chapter 2 were then genetically displayed on the pVIII coat protein of M13 phages. When the peptide-bearing phage films were assembled, they allowed for a side-by-side comparison of the effects of each peptide on differentiation relative to the wild type phage control. The peptides, VHVPLHRGAVSA and SGTQDSMVGWNK demonstrated exceptional abilities to induce osteoblast differentiation as indicated by osteoblast marker proteins, marker genes, and calcium mineral deposits. In particular, the peptide VHVPLHRGAVSA displayed on a phage film demonstrated an ability to differentiate hMSCs better than a leading company product, osteogenic media from Lonza. This work demonstrated that these newly discovered peptides are in fact osteoblast differentiation inducing peptides. When these peptides are combined with the biophysical cue of a highly ordered phage film, they may be potent factors for increasing bone regeneration.

Chapter 4: Elucidating the signaling pathway mechanism of newly discovered osteogenic peptides

4.1 Introduction: Bone regeneration signaling pathways

Efficient bone regeneration involves a combination of factors such as biophysical and biochemical cues which act upon cellular signaling pathways. Deficiency in activating the correct signaling pathways can result in fracture non-unions during bone healing.[360] Conversely, the combined utilization of multiple osteogenic differentiation inducers which target multiple osteogenic differentiation pathways often results in enhanced bone repair.[360-362]The peptide-bearing phages developed in Chapters 2 and 3 were expected to provide both a biophysical cue due to their assembled, ordered structures as well as a biochemical cue due to the peptide displayed. The expectation due to the process of discovering these peptides is that they will signal through the BMP signaling pathway. As a reminder that process was done by biopanning against the receptors of BMP. However, until now, this presumption had not been studied. Additionally, no study has determined the signaling pathways wild type phage film structures trigger for osteoblast differentiation. Other than the BMP signaling pathway, there are alternate pathways which can induce osteogenesis. Some of the more prominent pathways include the Wnt/*β*-catenin, Notch, and Hedgehogs pathways.[363]Additionally, among all of these pathways, there are multiple routes which can be followed. For example, in the BMP pathway, signaling can proceed by either Smad depended (Smad 1/5/8) or independent processes (p38 MAPK). Several of the interactions among

these pathways are summarized in Figure 19. Though even more synergy among pathways exist than can be shown clearly in this figure, it should be noted that signaling is frequently synergetic and not isolated to any one pathway.[125]

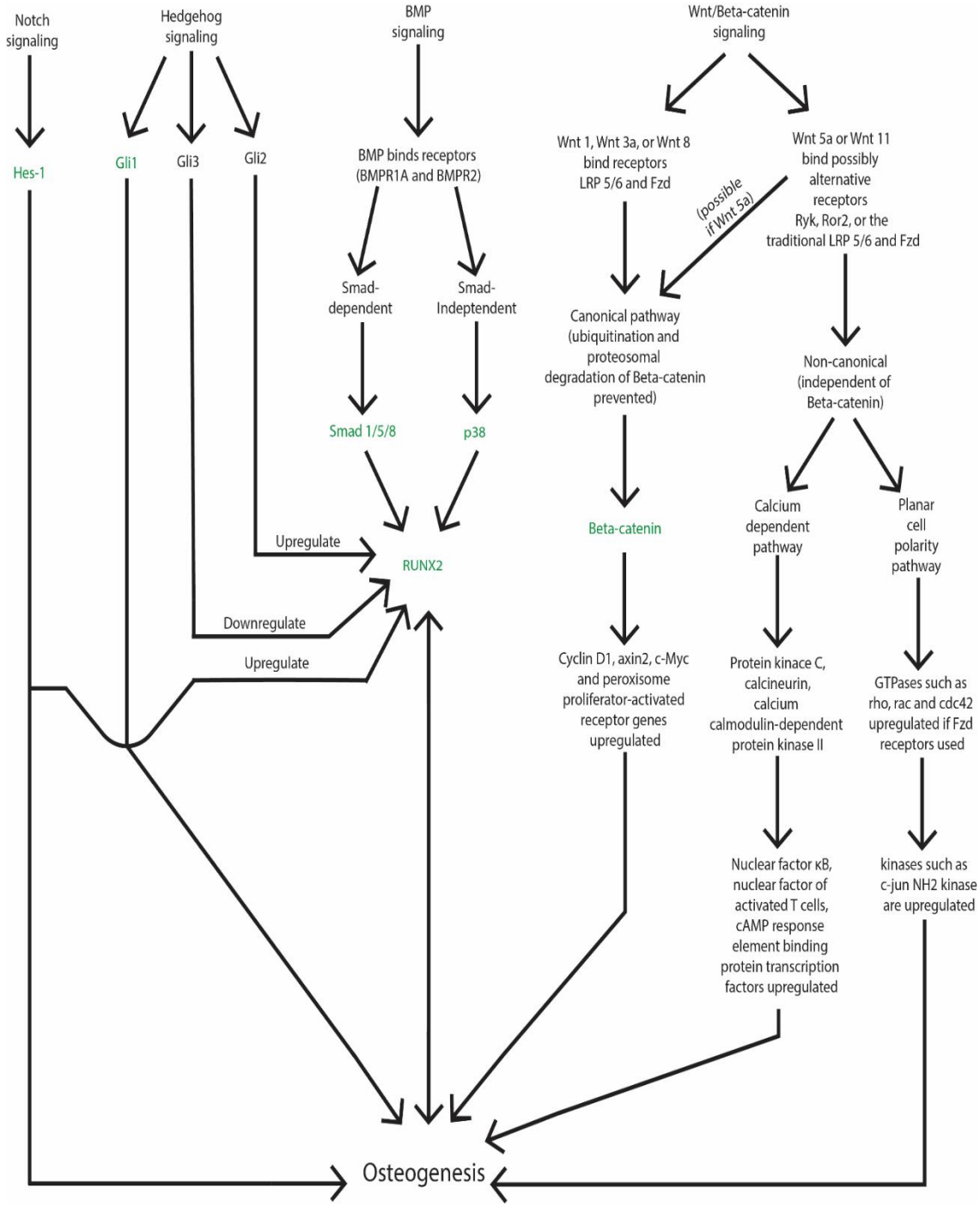


Figure 19. Several prominent signaling pathways for osteogenesis are shown. Key signaling steps within these pathways which were studied are highlighted in green. These are known transcription factors. This figure does not show every possible differentiation pathway or the details of every pathway, but it does

identify key targets in each pathway that indicate the pathway is active. This figure was assembled from information originating from many publications.[125, 362, 364-375]

4.2 Materials and Experiments

4.2.1 Materials

Anti-beta Catenin antibody (ab32572 from Abcam), Anti-Gli1 antibody (ab151796 from Abcam), Anti-Hes1 antibody (ab71559 from Abcam), Anti-p38 antibody (ab197348 from Abcam), Anti-RUNX2 antibody (ab23981 from Abcam), Anti-SMAD 1/5/8/9 antibody (ab13723 from Abcam), Bone morphogenic protein 2 (Prospec), Bovine serum albumin (Sigma Aldrich), Dexamethasone (Sigma Aldrich), Dorsomorphin (ab120843 from Abcam),Goat Anti-Rabbit IgG H&L (Alexa Fluor® 488 ab150077 from Abcam),Human Hes6 protein (ab132389 from Abcam), Human mesenchymal stem cells (Lonza), L-Ascorbic acid 2-phosphate sesquimagnesium salt hydrate (Sigma Aldrich),Mesenchymal stem cell basal medium for adipose, umbilical and bone marrow-derived MSCs (ATCC® PCS-500-030™), Mesenchymal stem cell growth kit for bone marrow-derived MSCs (ATCC® PCS-500-041™), Triton X-100 (Sigma Aldrich).

4.2.2 Immunofluorescence of osteoblast signaling pathway marker proteins

Phage films (or no film for controls) for each peptide sequence were prepared in 96-well plates according to the previously described protocol. The

plates were subjected to 12 hours of UV radiation and soaked in cell media in a cell incubator overnight prior to cell seeding. Next, 300 µL of $3.6x10^4$ *hMSCs / mL* were then seeded into each well for each condition tested (3 biological replicates were included for every condition). The cells were then grown for 14 days in hMSC basal media (Lonza) with regular media changes (every 2 days). For the BMP condition, 400 *ng/mL* of BMP-2 was incorporated into the medium. For the DAG condition, 10 *µM* concentrations of dexamethasone and 0.05 *mM* L-Ascorbic acid 2-phosphate sesquimagnesium salt hydrate were incorporated into the cell medium. For the DAG + BMP-2 condition, the components of the BMP and DAG conditions were combined. The cells were then fixed by incubating in 4% paraformaldehyde for 10 minutes. Following fixation, the cells were washed 5 times with PBS, permeabilized with 0.2% Triton X-100 (2 minutes), blocked with 5% bovine serum albumin solution for 1 hour, and washed 5 more times with PBS. The cells were then incubated with one of the following primary antibodies (diluted in PBS) for 12 hours: Anti-SMAD 1/5/8/9 antibody (ab13723) (10 *µg / mL*), Anti-p38 antibody (ab197348) (1:100 dilution), Anti-RUNX2 antibody (ab23981) (10 *µg / mL*), Anti-beta Catenin antibody [E247] (ab32572) (1:250 dilution), Anti-Hes1 antibody (ab71559) (1:200 dilution), Anti-Gli1 antibody (ab151796) (1:50 dilution). The cells were then washed 5 times with PBS. Each condition was then incubated with the secondary antibody, Goat Anti-Rabbit IgG H&L (Alexa Fluor® 488) (ab150077) (1:1000 dilution) for 2 hours. The cells were washed again 5 times with PBS. The cells were then stained by DAPI (Millipore Sigma) according to the

manufacturer's protocol followed by a final 5 washes with PBS. The cells were then imaged on a Nikon Eclipse Ti fluorescent microscope using the ∞ Ph1 lens. The following capture times were used for each condition: DAPI (4.4 seconds), SMAD 1/5/8/9 (10 seconds), RUNX2 (10 seconds), Hes1 (20 seconds), Gli1 (20 seconds), Beta-Catenin (6 seconds).

4.2.3 Selective inhibition effects on peptide signaling pathways

Phage films (or no film for controls) for each peptide were prepared in 96-well plates according to the previously described protocol. The plates were subjected to 12 hours of UV radiation and soaked in cell media in a cell incubator overnight prior to cell seeding. Next, 300 µL of $3.6x10^4$ *hMSCs / mL* were then seeded into each well for each condition tested. The cells were then grown in basal media (Lonza) for 14 days with regular media changes (every 2 days). For the BMP condition, 400 *ng/mL* of BMP was incorporated into the medium. For the DAG condition, 10 *µM* concentrations of dexamethasone and 0.05 *mM* L-Ascorbic acid 2-phosphate sesquimagnesium salt hydrate were incorporated into the cell medium. For the DAG + BMP-2 condition, the components of the BMP and DAG conditions were combined.

For inhibiting the BMP pathway, 1200 *nM* dorsomorphin was incorporated into the cell medium and prepared freshly for each media change as it is otherwise unstable. The dorsomorphin required the preparation of a concentrated stock solution in which dorsomorphin was dissolved in ethanol followed by sonication at 55 ℃ until dissolved. The stock was aliquoted into

smaller amounts stored at -20 ℃ which could be diluted in cell medium to use fresh on each media change. Dorsomorphin acts to inhibit the phosphorylation of Smad 1/5/8 by the BMP receptor complex causing a drop in Smad 1/5/8 mRNA and protein levels. For inhibiting the Notch pathway, Human Hes6 protein (3.92 *nM*) was mixed into each media change (purchased from Abcam). Hes6 inhibits Hes1 function and may also decrease Hes1 mRNA and protein levels.[376-377]

After 14 days of growth, the cells were fixed by incubating in 4% paraformaldehyde for 10 minutes. Following fixation, the cells were washed 5 times with PBS, permeabilized with 0.2% Triton X-100 (2 minutes), blocked with 5% bovine serum albumin solution for 1 hour, and washed 5 more times with PBS. The cells were then incubated with one of the following primary antibodies depending on the pathway being studied for 12 hours: Anti-SMAD 1/5/8/9 antibody (ab13723) (10 *μg/mL*), Anti-Hes1 antibody (ab71559) (1:200 dilution), Anti-Gli1 antibody (ab151796) (1:50 dilution). The cells were then washed 5 times with PBS. Each condition was then incubated with the secondary antibody, Goat Anti-Rabbit IgG H&L (Alexa Fluor® 488) (ab150077) (1:1000 dilution) for 2 hours. The cells were washed again 5 times with PBS. The cells were then stained by DAPI (Millipore Sigma) according to the manufacturer's protocol followed by a final 5 washes with PBS. The cells were then imaged on a Nikon Eclipse Ti fluorescent microscope using the ∞ Ph1 lens. The following capture times were used for each condition: DAPI (4.4 seconds), SMAD 1/5/8/9 (10 seconds), Hes1 (20 seconds), Gli1 (20 seconds).

4.3 Results and Discussion

4.3.1 Synergistic activations of osteoblast differentiation pathways by osteogenic peptide phage films.

The possible signaling pathways of the two strongest osteogenic inducing peptides, VHVPLHRGAVSA and SGTQDSMVGWNK, were further evaluated. To sort out the signaling, hMSCs were cultured on phage films bearing the peptides for 14 days and immunofluorescence imaging was done in parallel under exactly matching imaging conditions for markers of the osteogenic pathways including the Hedgehog (Gli 1 marker), Notch (Hes1 marker), BMP (Smad 1/5/8 or p38 MAPK markers), and Wnt (β-catenin marker) pathways as shown in Figure 20.[125, 362, 364-375, 378-390] For the BMP pathway, which goes through either Smad 1/5/8 or p38 MAPK, Smad 1/5/8 was upregulated for each of the peptide conditions while p38 MAPK was not. This indicates that the Smad 1/5/8 route is activated either directly and/or synergy exists between the Smad 1/5/8-mediated BMP pathway and another pathway. For the hedgehog pathway, Gli 1 was upregulated for the peptides VHVPLHRGAVSA, SGTQDSMVGWNK, and a combination of these 2 peptides. Gli1 upregulation by a combination of the two peptides was slightly more than that by each peptide alone. This indicates that each peptide upregulates this pathway, and using two peptides together synergistically upregulates it further. For the Notch pathway, all peptides on the phage films were upregulated equally relative to the basal condition. This indicates that the phage film topography, which is the same for all phage films, is likely a potent activator of

the Notch pathway. The Wnt pathway appeared to be the same for all conditions (with or without peptides) and thus was likely unaffected by the peptides we discovered.

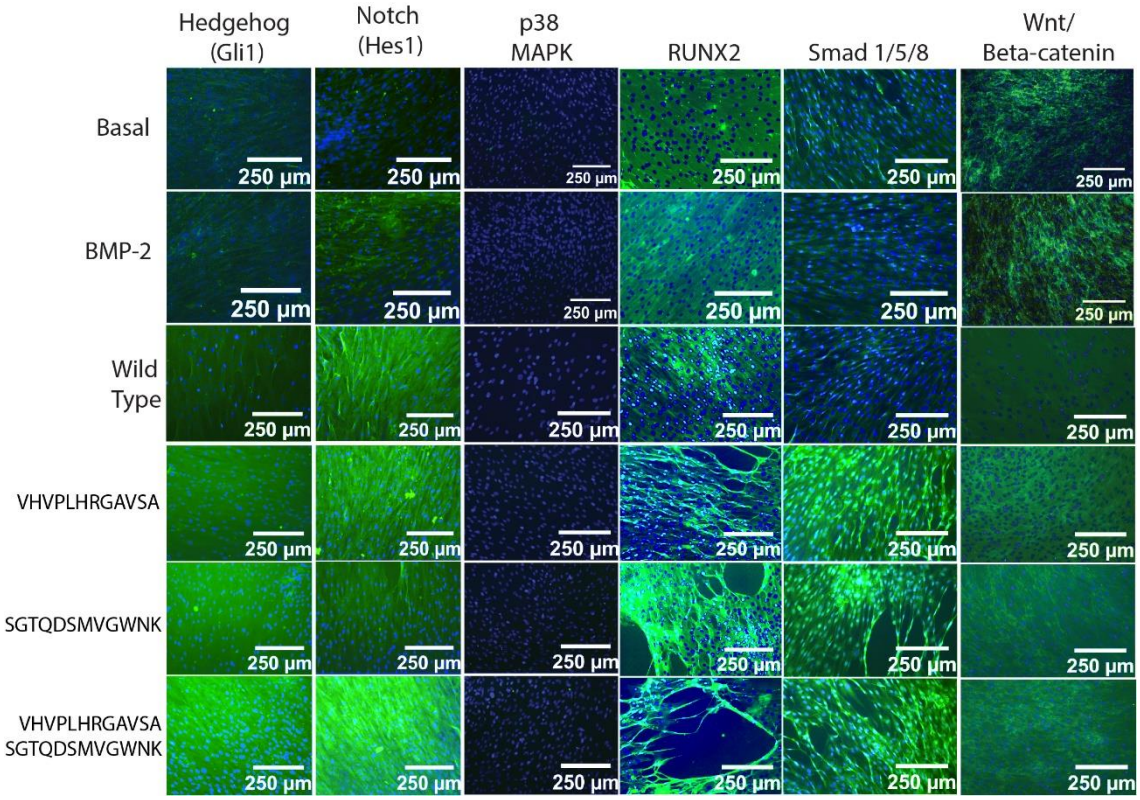


Figure 20. Immunofluorescence showing signaling (green) among osteogenic pathways. The peptide-based phage films have an advantage in Hedgehog (Gli1 marker) and BMP (Smad 1/5/8 marker) signaling. The phage film topography appears to have an advantage in Notch (Hes1) signaling.

4.3.2 Inhibition of differentiation pathways

To further clarify the impact of the peptides, VHVPLHRGAVSA and SGTQDSMVGWNK, on the upregulation of the BMP, Hedgehog, and Notch pathways, specific inhibitors were used to selectively disrupt one of the

pathways followed by observation of the impact on the other pathways (Figure 24, Figures 21-23). For all studies, hMSCs were seeded onto osteogenic-peptide bearing phage films or control conditions followed by culturing for 14 days. All studies were done in parallel using the same stocks of cells, inhibitors, and imaging conditions for optimal side-by-side comparison.

First, the Hedgehog pathway was examined while other pathways were inhibited (Figure 21). Dorsomorphin was used to inhibit the Smad 1/5/8 phosphorylation to effectively suppress the BMP pathway.[373] When the BMP pathway was inhibited, the Hedgehog pathway remained upregulated in all peptide conditions. Next, Hes6 was used to inhibit Hes1 function, and thus the Notch pathway was inhibited.[376-377] Suppression of the Notch pathway failed to affect the Hedgehog pathway, either. Therefore, the increased signaling caused by the peptides VHVPLHRGAVSA and SGTQDSMVGWNK in the Hedgehog pathway were independent of BMP and Notch signaling. This shows that the Hedgehog pathway is a key pathway for differentiating the hMSCs into osteoblasts using the peptides VHVPLHRGAVSA and SGTQDSMVGWNK.

It has already been shown in Figure 20 and Figure 23 that BMP signaling is upregulated by the peptides VHVPLHRGAVSA and SGTQDSMVGWNK. To further examine the signaling mechanism of this upregulation, the BMP pathway was examined while either the Notch or BMP pathways were inhibited. It should be noted that the BMP pathway under the inhibitor Numb of the Hedgehog pathway was not studied due to the significant cytotoxicity and apoptosis upregulation caused by the Numb inhibitor (also confirmed by us).[391] First, the

Notch pathway was inhibited using Hes6. This resulted in a major drop to BMP signaling (via Smad 1/5/8) for the peptide SGTQDSMVGWNK. The other peptide, VHVPLHRGAVSA experienced only a minor drop in BMP signaling indicating less of a reliance on synergy with Notch signaling. The condition VHVPLHRGAVSA also maintained higher levels of BMP signaling than the control groups even when Notch signaling was disrupted. Additionally, when the BMP pathway was inhibited, the peptides still maintained an advantage in BMP signaling over the control conditions, indicating some degree of robustness for the peptides to upregulate BMP pathway. Therefore, the BMP pathway is an important synergystic acting pathway for the peptides, and the peptide VHVPLHRGAVSA has the greatest advantage in BMP signaling.

Lastly, the Notch pathway was examined while the Notch or BMP pathways were inhibited. It has already been shown that without inhibitors, there is an equal upregulation of Notch signaling for all phage film conditions over other controls (Figure 20 and Figure 22). Hes6 is a notch pathway inhibitor that acts to inhibit Hes1.[376-377] When the Notch pathway was inhibited using Hes6, the level of the Noth signaling marker (Hes1) was dramatically lowered for the no peptide group (wild type phage film) (Figure 22). The level of Hes1 was also lowered for the peptide-displaying phage groups, but still obviously higher than that for the no peptide and other control conditions (Figure 22). This indicates that peptide-enabled BMP and Hedgehog pathways have synergy with the Notch pathway for the peptide-displaying phage groups; when the Hes6 was intended to inhbit the Notch pathway, the synergy reduced the

level of such inhibition. Hence, next, the Notch pathway was examined when the BMP pathway was inhibited with dorsomorphin. For the no peptide group (wild type phage), the Notch signaling by the phage substrates was reduced dramatically. The peptide groups also had decreased Notch signaling when the BMP pathway was inhibited. These results further indicate the synergy between the Notch signaling (via phage film topography) and BMP pathway (via peptides). Namely, inhibiting Notch signaling of the phage film topography became less favored for no peptide group (just wild type phages) than for peptide group (peptide-dispplaying phages) due to the synergy. When the Notch signling was inhibited, the level of inhibition was higher for the peptide SGTQDSMVGWNK group than for another peptide VHVPLHRGAVSA. Both peptides still maintained higher Notch signaling than the controls or wild type condition, indicating less dependence on the other two signaling pathways than (wild type) phage topography mediated notch signaling. In summary, the Notch signaling upregulation under all phage film conditions is likely a result of biophysical cues from the topography of the phage film which is approximately equivalent for all phage film conditions. This further confirms that the two peptides mainly signal through Hedgehog and BMP pathways.

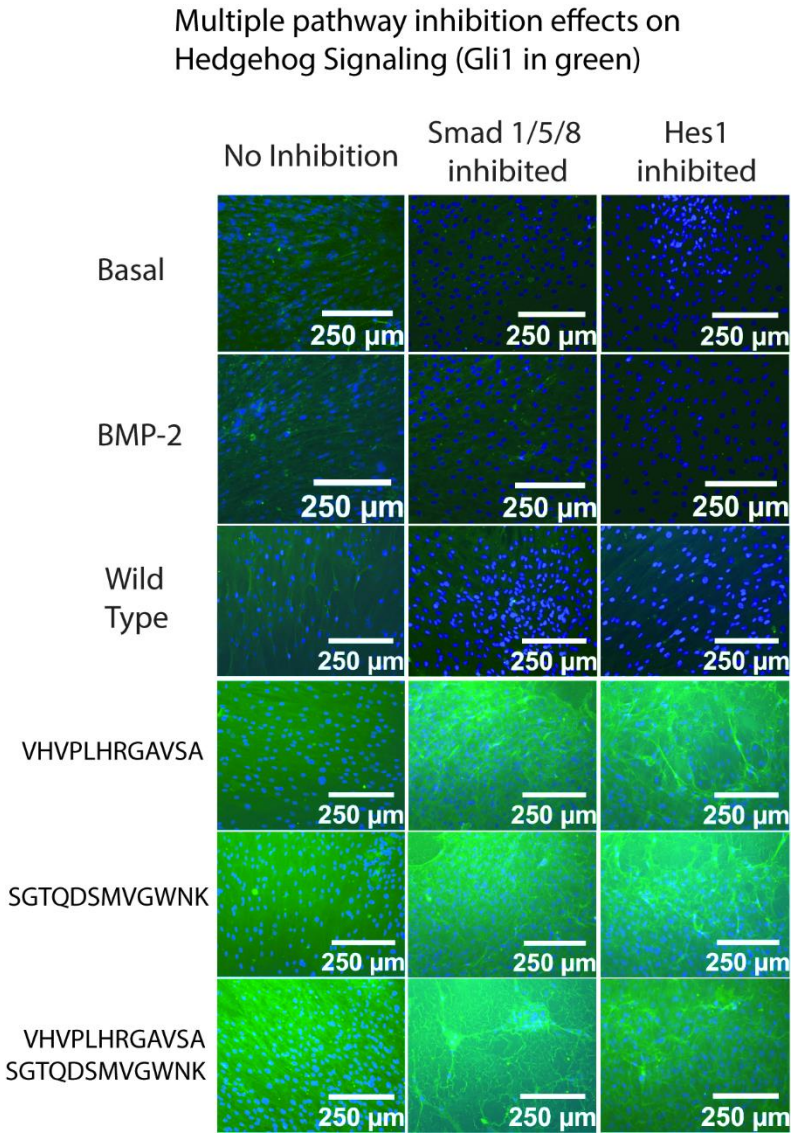


Figure 21. The effects of inhibiting Smad 1/5/8 (BMP pathway) and Hes1 (Notch pathway) on Gli1 (Hedgehog pathway) protein levels. Dorsomorphin was used to inhibit the phosphorylation of Smad 1/5/8 by the BMP receptor complex at a concentration of *1200 nM*, possibly causing a decrease in Smad 1/5/8 mRNA and protein levels[373]. Hes6 was used to inhibit Hes1 function[376] and possibly lower mRNA levels of Hes1[377]. Gli1 (Hedgehog pathway) levels are shown in green. Cell nuclei were stained using DAPI (blue). Without inhibitors, the peptides have a clear advantage in promoting Gli1 (Hedgehog pathway)

levels relative to wild type phage. Inhibiting the BMP and Notch pathways appeared to have little to no effect on the benefits of the peptides in the Hedgehog pathway as demonstrated through Gli1 protein levels. Therefore, the peptides have a considerably large effect on the Hedgehog signaling pathway independently of other signaling pathways.

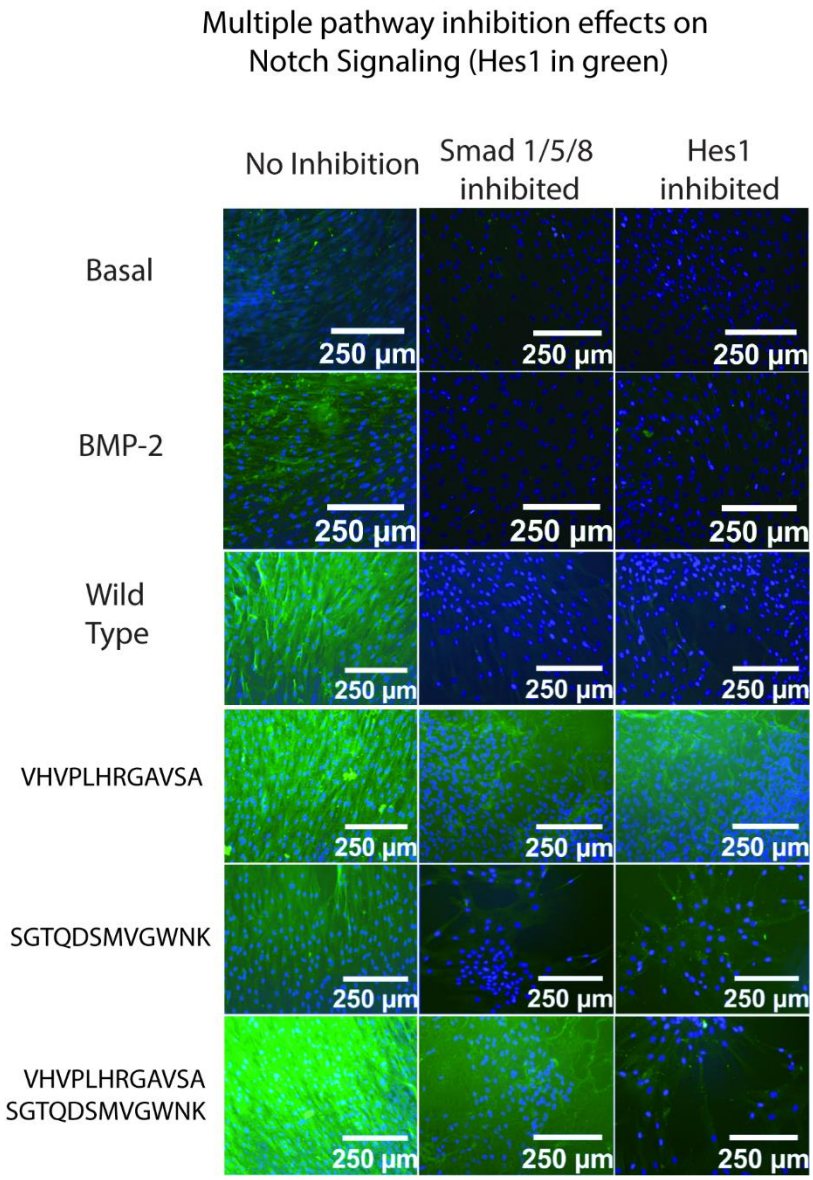


Figure 22. The effects of inhibiting Smad 1/5/8 (BMP pathway) and Hes1 (Notch pathway) on Hes1 (Notch pathway) protein levels. Dorsomorphin was used to inhibit the phosphorylation of Smad 1/5/8 by the BMP receptor complex at a concentration of *1200 nM*, possibly causing a decrease in Smad 1/5/8 mRNA and protein levels.[373].Hes6 was used to inhibit Hes1 function[376] and possibly lower mRNA levels of Hes1[377]. Hes1 (Notch signaling) is shown in green. Cell nuclei were stained using DAPI (blue). Without inhibitors, the

individual peptide-displaying phage films did not show an advantage over the wild type phage film, but all films showed an advantage over the control condition indicating that the Notch pathway may be an essential component of the ability of wild type phage films to differentiate hMSCs into osteoblasts. Wild type phage film Notch signaling was devastated by inhibition of either the BMP or Notch pathways as evidenced by a steep drop in Hes1 protein levels. This indicates that the natural ability of the topography of phage films to differentiate hMSCs into osteoblasts is likely dependent upon Notch signaling. However, the drop in wild type phage film Notch signaling upon preventing the phosphorylation of Smad 1/5/8 in the BMP pathway indicates some dependency of the Notch signaling on the BMP pathway being functional. It is likely from the data that wild type phage film upregulates the Notch pathway but still requires the BMP pathway to be functional for proper signaling to occur. Additionally, the peptide-displaying phage films showed a heavy drop in Notch signaling when either the Notch or BMP pathways were inhibited. However, they did not drop as far as the wild type phage film, indicating that the peptide-displaying phage mediated Notch signaling is less dependent on the other two signaling pathways than the wild type phage mediated Notch signaling. Additionally, the drop in Hes1 (notch pathway) levels caused by inhibiting Smad 1/5/8 (BMP pathway) indicates that the peptide-displaying phage films do benefit from BMP signaling. Taken with data from Figure 23 (the next figure), it is likely the additional boosts in peptide-based BMP signaling as well as

Hedgehog signaling are responsible for the increased levels of Notch signaling for peptides relative to wild type phage films under inhibiting conditions.

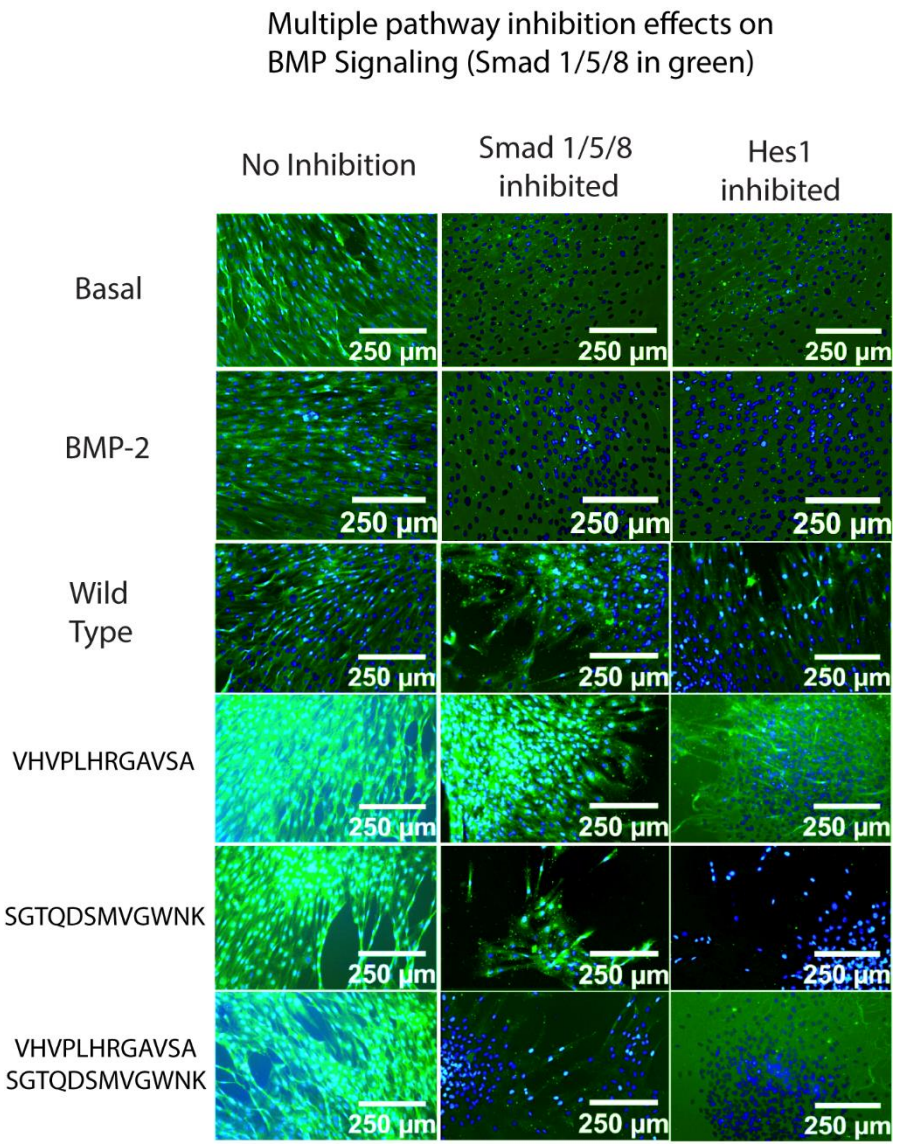


Figure 23. The effects of inhibiting Smad 1/5/8 (BMP pathway) and Hes1 (Notch pathway) on Smad 1/5/8 (BMP pathway) protein levels. Dorsomorphin was used to inhibit the phosphorylation of Smad 1/5/8 by the BMP receptor complex at a concentration of *1200 nM*, possibly causing a decrease in Smad 1/5/8 mRNA and protein levels[373]. Hes6 was used to inhibit Hes1 function[376]

and possibly lower mRNA levels of Hes1[377]. Smad 1/5/8 is shown in green. Cell nuclei were stained using DAPI (blue). With no inhibition, the peptides have a clear advantage in Smad 1/5/8 protein levels relative to wild type phages and controls. Inhibiting Hes1 (Notch pathway) caused a major drop in the peptide film BMP signaling for the peptide SGTQDSMVGWNK, but only a minor drop for the peptide VHVPLHRGAVSA.

4.4 Conclusion

Combining the results of the inhibition studies, the peptides VHVPLHRGAVSA and SGTQDSMVGWNK were demonstrated to signal through both the BMP and Hedgehod pathways. For the BMP pathway, we propose that the peptides bind to the BMPRs, which then initiate the phosphorylation of Smad 1/5/8 (Figure 24). Smad 1/5/8 is then complexed with Smad 4, which will lead to upregulated osteoblast differentiation genes. We also propose that the peptides upregulate the Hedgehog pathway by improving the production of the osteogenic transcription factor Gli1 independently of the BMP or Notch pathways. Lastly, we propose that the osteogenic capabilities of the phage film topography (i.e., not the peptides displayed on the film) can be attributed to increased Notch signaling but are not independent of BMP signaling synergy. Figure 24 gives an overview of the most important interactions discovered as described above. This figure was generated using protein database (PDB) structures[378-387, 392] and reported pathways.[125, 362, 364-375, 388-390]

The discovery of new osteogenic growth factor peptides serves as a proof of concept for our technique summarized in Figure 25. Phage display can identify a peptide binding to virtually any receptor for a given growth factor. By biopanning on the receptor targets of growth factors, we can produce a short peptide mimetic for those growth factors. Relative to recombinant proteins, these growth factor mimetic peptides are cheaper and less immunogenic. These short peptides can also be easily immobilized on substrates with greater control over their orientation, dispersal rate, and maintenance of functionality relative to recombinant protein growth factors.[321-322] We believe that our technique can be applied to find new short peptide growth factors capable of mimicking full protein growth factors for any known target. Once a peptide mimicking a growth factor is discovered, it can be integrated onto the scaffolds or implants for tissue repair and regeneration. Hence, our strategy opens up a new avenue to the discovery of a short peptide that can perform the same functions as growth factors.

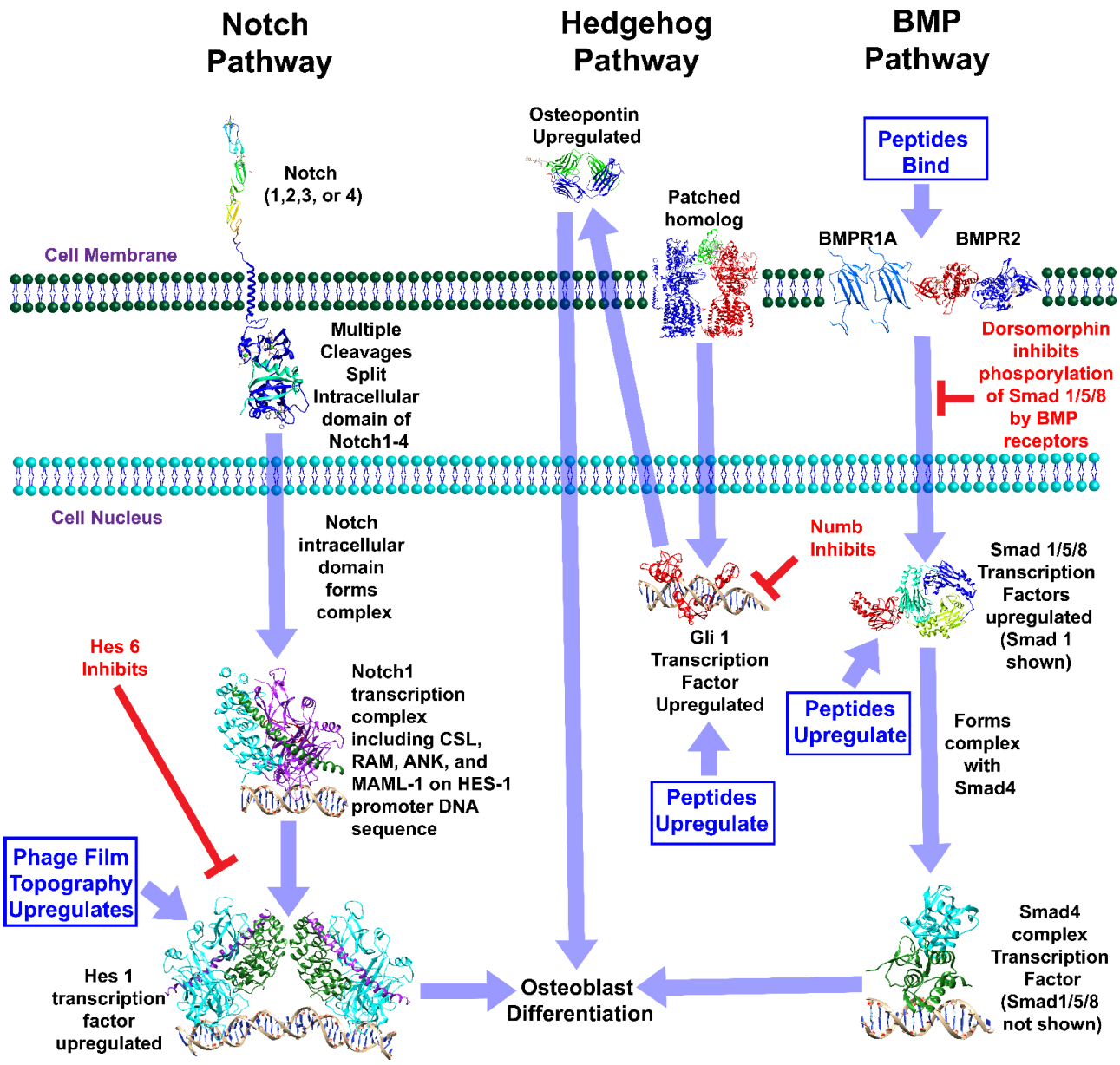


Figure 24. The possible signaling pathway targets of the osteogenic peptides and phage films. The pathways have been greatly simplified to show the known points affected by the peptides or film topography. The peptides signal through the BMP pathway and upregulate Smad 1/5/8. The peptides also upregulate Gli1 in the Hedgehog pathway through a mechanism independent of the BMP or Notch pathways. The phage film topography causes an upregulation of Hes1

in the Notch pathway. The abbreviations are as follows: CSL (CBF1, Suppressor of Hairless, Lag-1), RAM (RBP-Jkappa-associated module domain), ANK (Ankyrin repeats), MAML-1 (Mastermind-like), Hes (hairyenhancer of split), Gli1 (glioma-associated oncogene 1), Smad (Small Mothers Against Decapentaplegic), BMPR1A (BMP receptor type 1A), BMPR2 (BMP receptor type 2). Synergy exists between all pathways but is not shown. A great number of other factors exist within each pathway and are not shown for simplicity. Blue arrows indicate upregulation of an osteogenic pathway. Red arrows indicate inhibition targets for the studied points of each pathway. The structures of different proteins shown in this figure are obtained from the PDB according to their identities (Patched homolog 1: 6E1H; Gli1: 2GLI; Osteopontin: 3CXD; BMPR2: 3G2F; BMPR1A: 2K3G; Smad 1: 1KHU; Complex with Smad4: 5MEZ; Notch1: 4CUF, 5KZO, 3I08; Notch1 transcription complex: 3V79; Hes1: 3NBN).

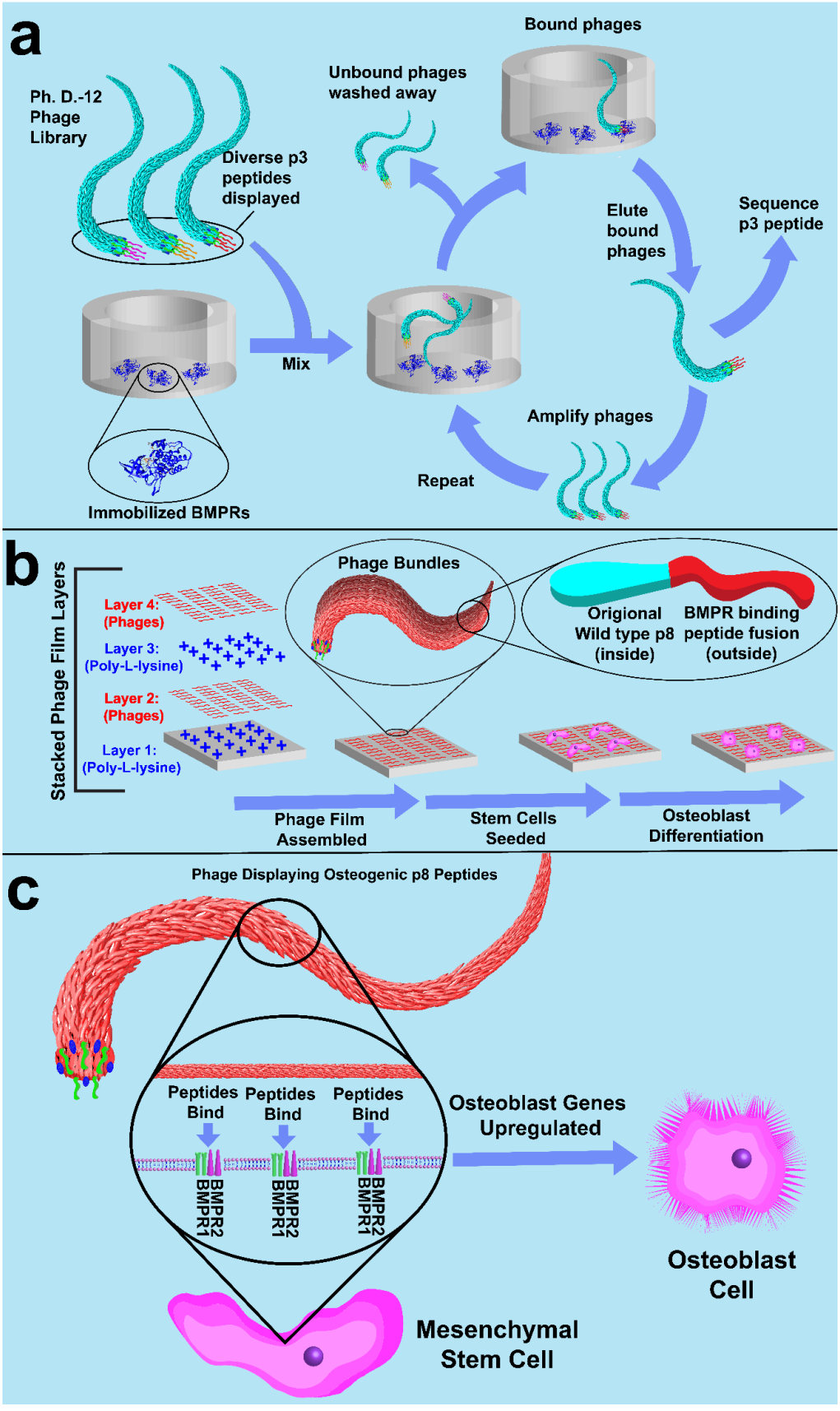

a
Ph. D.-12
Phage
Library
Diverse p3
peptides
displayed
Unbound phages
washed away
Bound phages
Elute
bound
phages
Sequence
p3 peptide
Mix
Amplify phages
Repeat
Immobilized BMPRs
b
Stacked Phage Film Layers
Layer 4:
(Phages)
Layer 3:
(Poly-L-lysine)
Layer 2:
(Phages)
Layer 1:
(Poly-L-lysine)
Phage Bundles
Origional
Wild type p8
(inside)
BMPR binding
peptide fusion
(outside)
Phage Film
Assembled
Stem Cells
Seeded
Osteoblast
Differentiation
c
Phage Displaying Osteogenic p8 Peptides
Peptides
Bind
Peptides
Bind
Peptides
Bind
BMPR2
BMPR1
BMPR2
BMPR1
BMPR2
BMPR1
Osteoblast Genes
Upregulated
Osteoblast
Cell
Mesenchymal
Stem Cell

Figure 25. In vitro work summary of the use of phages displaying BMPR-binding peptides to induce the differentiation of hMSCs into osteoblast cells. (a) In vitro biopanning against BMPRs to screen BMPR-binding peptides out of a phage-displayed random peptide library. Two types of BMPRs are used as biopanning targets, including BMPRI and BMPRII. (b) Assembly of M13 phage nanofibers displaying the BMPR-binding peptides into a film and culturing of MSCs on the resultant film to induce the osteogenic differentiation of MSCs. (c) Possible mechanism by which M13 phage nanofibers displaying the BMPR-binding peptides interact with the BMPR on the MSCs to trigger the osteogenic differentiation. The BMPR-binding peptides bind to BMP receptors and can upregulate osteoblast gene expression in addition to the unique topography of the phage film.

Chapter 5: Development of hybrid bone regenerative materials: A combination of 3D printing, phage display, and freeze casting

5.1 Introduction

5.1.1 Personalized 3D printed bone regenerative scaffolds

There is a pressing need for bone regenerative procedures due to skeletal deformities, removal of bone tumors, non-unions (failure of healing broken bone), avascular necrosis, and osteoporotic fractures.[393-399] Repairing large bone defects in load-bearing sites poses a major challenge as replacement implants need to have the appropriate mechanical strength and biocompatibility.[262, 400-402] 3D printing is a versatile approach since implants can be customized to fit any patient-specific complex defect within its resolution capabilities (16 µm resolution is achievable).[402-413] This is done by first using MicroCT to image a patient's defect and generate a computer model. A 3D printer then generates a custom implant to fit the defect.[414-415] For bone defects, titanium (Ti) and its alloys, the materials clinically used for bone implants due to their excellent mechanical properties,[416] are a desirable choice for generating porous implants by 3D printing to overcome the weaker mechanical properties of materials such as ceramics and polymers. 3D printing with titanium alloys is currently being clinically investigated for use in cranial and jaw implants, but could be applied universally for all types of bone defects clinically.[417] Compared to alternate 3D-printed bone materials, titanium alloys have the major advantage of being

mechanically strong enough for load bearing sites.[418] Titanium alloys are also inherently bioinert, making them an ideal implantable material.[418] However, there are several major issues in the field of bone implants which can be improved upon.[419] Specifically, the resultant implants still lack the capability of efficiently inducing bone formation to achieve excellent integration with the surrounding bone tissues.[419] Therefore, improving regenerative capabilities of 3D printed titanium alloy implants is still a great challenge in repairing bone defects in load-bearing sites. Bone implants need to closely mimic the native extracellular matrix (ECM) which can lead to improved cell adhesion, differentiation, proliferation, and tissue regeneration.[419] These qualities are essential for the bone implant to be in harmony with the native environment, ensuring that the defect area can be replaced with functional, healthy tissue having little or no reparative scar formation.[419] Additionally, microscale features that allow for cell penetration, nutrients diffusion, vascularization, cellular differentiation, and spatial organization of cellular growth are essential.[419] Here, we propose fine tuning the microscale features of implantable 3D printed titanium by coating it in a precisely aligned bone-mimetic structure made up of M13 phages. M13 phages are a human-safe filamentous virus measuring roughly 1000 nm in length. To align these phages into a bone-mimetic lamellar structure, a process called freeze casting can be used. This process uses the directional growth of ice crystals to push solid materials (phages in this case) into lamellar structures. When this process is utilized on phages, the resulting filamentous lamellar structures resemble that of collagen matrices in natural bone.[420-423] This allows for precise

control over mimicking the natural environment of bone-regenerative osteoblast cells. Additionally, phages have the benefit of being able to display short growth factor mimetic peptides. We have recently discovered the peptides VHVPLHRGAVSA and SGTQDSMVGWNK which have been demonstrated to induce human mesenchymal stem cells (hMSCs) to differentiate into osteoblasts. By combining personalized 3D printing, precise microenvironment structural control, and growth factor mimetic peptides, we have developed a new technique to improve bone regeneration. This technique could potentially be extended to coat any material with phages bearing growth factor mimetic peptides specific to the desired tissue type.

5.1.2 Freeze casting organized bone-mimetic lamellar structures

Freeze casting is a process in which the directional growth of ice crystals can push solid materials dissolved in an aqueous solution into an organized pattern. Upon being completely frozen, the ice can be removed through sublimation during which the sample is put under vacuum. When the directionality of the ice crystal growth is controlled by precise manipulations of the temperatures on all sides of the liquid suspension, complex, ordered structures can be formed.[424-425]When ice crystals are either grown directionally from the bottom up, top down, or a combination of these two, a lamellar structure can be obtained. A lamellar structure closely mimics the natural structure of bone.[426] Thus, lamellar structures are preferred to help provide a biophysical environmental cue for bone regeneration.

5.2 Materials and Experiments

5.2.1 Materials

Calcium nitrate tetrahydrate, carbon dioxide gas, ethanol, 1-ethyl-3-(3 dimethylaminopropyl) carbodiimide hydrochloride, isoflurane, Lidocaine, linoleic acid, octadecylamine, oxygen gas, paraformaldehyde, polyethylene glycol–8000, sodium hydroxide, sodium phosphate.

5.2.2 3D printing titanium alloy

3D printed titanium implants were created using a biocompatible metal alloy consisting of titanium, aluminum, and vanadium (Ti-6Al-4V, 6:4:90, Al: V: Ti, wt%) which is among the most commonly used titanium alloys for biomedical implants.[427-428] Specifically, a design of the desired porous scaffold was created in the digital format known as an STL (Stereo Lithography) file using a computer-aided design (CAD) software. Then commercial Ti-6Al-4V alloy powder (Sandvik, Sweden) was printed into an implant in pure Ar gas according to the STL file, by means of selective laser melting (SLM) through a commercial laser-based 3D printer (Concept LASER M2) specialized for printing metallic powder. The 3D printer was equipped with a Yb-FaserLaser with a focus beam diameter of 50 µm. The SLM parameters during 3D printing included a laser power of 100 W, a scan speed of 650 mm/s, a scan spacing of 70 µm, and a layer thickness of 30 µm. The scaffolds were cylindrical in shape with a height of 8 mm and a diameter of 5 mm. The pores within the scaffold measured ~200 µm in diameter.

5.2.3 Creating a double-sided freeze casting machine

A double-sided freeze casting machine was built loosely based on a published design.[429]A double sided freeze casting system allows for greater control over generating constant solidification velocities and can produce nearly constant lamellae spacing over a longer sample height relative to a one-sided freeze casting system.[429]Two Omega temperature controllers were integrated into the double sided freeze casting system to allow for a temperature control system. The controllers were programmed to either be able to allow for drops of 3 ºC / minute for both the top and bottom copper rods or for a drop of 3 ºC / minute for just the bottom rod while maintaining the top rod at 0 ºC (typically done unless otherwise stated). The final temperature was -135ºC. Reservoirs of liquid nitrogen were held in contact with the top and bottom copper rods to provide a cold source. Any liquid suspension to be freeze casted could fit in various sizes of containers which all fit in between the two copper rods. The containers consisted of top and bottom copper pieces which perfectly fit against the copper rods and a plastic cylindrical container that goes between them. The cylindrical container is open on both ends.

5.2.4 HAP nanorod synthesis, TEM imaging of HAP, and powder X-Ray diffraction of HAP

Hydrophobic hydroxyapatite (HAP) nanorods were synthesized according to a published protocol.[430] After synthesizing, the HAP nanorods were pelleted by centrifugation and washed with ethanol, pelleted in a centrifuge again, resuspended in water, frozen at -80 *ºC*, and freeze dried overnight. The nanorods were then ball milled overnight to obtain a fine HAP

powder. For TEM imaging, 10 *μL* HAP nanorods suspended in water were pipetted onto a formvar-coated TEM grid. After 3 minutes, any extra liquid was wicked away using a filter paper and the grid was dried using a hair dryer. The HAP nanorods were then imaged on a Jeol 2000 TEM at 200KV and 100K Magnification. Additionally, X-Ray diffraction was done on the ball-milled HAP powder.

5.2.5 Generating bone mimetic lamellar structures of combination of phage, hydroxyapatite, and collagen through freeze casting, cross linking, and sintering processes

Various solutions for freeze casting were optimized and their components are listed in the table below. Each solution was freeze casted using the constructed double-sided freeze casting machine with a temperature drop of 3 ºC/minute and a final temperature of -135 ºC. The frozen solutions were then freeze dried overnight. Images of the unprocessed scaffolds were taken by SEM after sputter coating with gold/ palladium. Additional processes were also done to strengthen composite scaffolds.

For the phage + collagen + HAP scaffold, crosslinking with 1-ethyl-3-(3 dimethylaminopropyl) carbodiimide hydrochloride (EDC) was done. Briefly, the scaffold was dropped into a solution of 200 *mM* EDC in ethanol. After incubating for 12 hours, the scaffold was placed in 0.1 *M* sodium phosphate for 2 hours to hydrolyze any unreacted o-isoacylurea intermediate. The scaffold was then soaked in PBS (pH 7.4) for 2 hours. To image this scaffold, the scaffold was dehydrated in a series of ethanol solutions (20%, 50%, 70%, 80%,

90%, 95%, 100%) incubating at each step for 20 minutes followed by critical point drying. The scaffold was then sputter coated with gold/palladium before SEM imaging.

For the pure HAP scaffolds, sintering was done after the freeze-drying process. For the first phase of sintering, the temperature was raised from 25 *ºC* to 550 *ºC* linearly over a time span of 2 hours and 55 minutes. The temperature was then held at 550 *ºC* for 2 hours. The temperature was then raised to 950 ºC linearly over 2 hours and 13 minutes. The temperature was held at 950 ºC for 5 minutes followed by linear cooling to 25 *ºC* over 5 hours and 8 minutes. For imaging, the scaffold was then gold/palladium sputter coated and imaged by SEM.

Table 10. Biodegradable freeze casting recipes.

Type of scaffold	M13 phage Amount	Rat tail collagen type 1 amount	Hydroxyapatite nanorod amount	PEG-8000
Pure Phage	1 *mL* of $9x10^{13}$ phages/mL	None	None	None
Phage + Collagen + HAP	1 *mL* of $9x10^{13}$ *phages/mL*	100 *µL* of 9.87 mg/mL	25 *mg*	None

HAP	None	None	50 *mg* in 1 *mL* of H_2O	20.8 *mg*

5.2.6 Freeze casting M13 phages onto 3D printed titanium

The titanium alloy scaffolds (cylindrical measuring 8 mm in height and 5 mm in diameter) were rinsed 3 times in distilled water followed by autoclaving. The scaffolds were then coated in poly-L-lysine by soaking in 2.5 *mL* of poly-L-lysine per 5 scaffolds in a 24-well cell culture plate for 30 minutes. The poly-L-lysine was then discarded, and the scaffolds were allowed to dry in a sterile hood overnight. In a sterile biological safety cabinet, 2 scaffolds were loaded into the sterile freeze casting holder (sterilized by autoclaving). 2 *mL* of sterile, filtered phage solution ($3.0x10^{13}$ *phages/mL*) was pipetted into the casting holder and directly into the pores of the titanium scaffolds. The solution was allowed to incubate at room temperature for 30 minutes so that phages could stick better to the scaffold. The scaffolds and phage solution were then freeze casted in the double-sided freeze casting machine with a temperature drop of 3 *ºC/minute* on the lower contact point and a constant 0 *ºC* on the upper contact point. The final temperature for the lower contact point was -135 *ºC*. The frozen scaffold and solution was then freeze dried overnight. For cell seeding, the scaffold was then soaked overnight in cell medium followed by seeding $3.6x10^4$ hMSCs onto the scaffold the next day in new medium. After 1 day of culturing, the scaffolds were implanted into the rat radial bone defect model.

5.2.7 Scanning electron microscopy, EDS, and cell attachment to scaffolds

After the freeze casting or cell seeding protocols for the titanium scaffolds, the scaffolds were fixed in 4% paraformaldehyde solution for 10 minutes. The scaffolds were then washed 5 times in PBS (pH 7.4). The scaffolds were then dehydrated in a series of ethanol dilutions (20%, 50%, 70%, 80%, 90%, 95%, 100%) incubating at each step for 20 minutes followed by critical point drying. The scaffold was then sputter coated with gold/ palladium before SEM or energy-dispersive X-ray spectroscopy (EDS) imaging.

5.2.8 Mechanical strength testing

Compression tests were done to determine the mechanical properties of the titanium scaffolds. The tests were performed using a Test Resources mechanical tester (800LE4AT30). The load cell value was 12.5 *kN* at room temperature. The cross-head speed was set to 0.008 mm/min. The elastic

$$Stress = \sigma = \frac{F}{\pi r^2}$$

$$Strain = \epsilon = \frac{\delta}{H}$$

F = Force (N)
R= radius of cylindrical sample
H = height of sample (mm)
δ = displacement (mm)

modulus was calculated from the linear region of the stress-strain curve using the 0.2% offset method. For the compression tests, the following equations were used to generate the stress strain curve.

For the healthy bone samples, a three-point bending test was done. The tests were also carried out using a Test Resources mechanical tester (800LE4AT30). The load cell value was 12.5 *kN* and the cross-head speed was set to 0.005 *mm/min*. The cross-head speed was set to 0.008 *mm/min*. The elastic modulus was calculated from the linear region of the stress-strain curve using the 0.2% offset method. For three-point bending, the following equations were used to generate the stress strain curve.

$$\text{Stress} = \sigma = \text{F}\frac{Lc}{4I}$$

$$Strain = \epsilon = -\delta\frac{12c}{L^2}$$

$$I = 0.78(r_o^4 - r_i^4)$$

$\text{I} = moment\ of\ inertia\ about\ a\ bending\ axis\ of\ a\ hollow\ cylinder$
$\text{F} = \text{Force (N)}$
$\text{c} = \text{outside radius of bone (mm)}$
$\text{L} = \text{length of beam (mm)}$
$\delta = \text{displacement (mm)}$

5.2.9 Generating a rat radial bone defect model

A rat radial bone defect model (removal of an 8 mm section of the radius bone) was generated for evaluating the bone regeneration potentials of these 3D printed titanium scaffolds. The animals were anesthetized by inhalation of 4% isoflurane/oxygen (*v/v*) mixture using an anesthesia machine (VT-110 small animal anesthesia machine) and then with 2% isoflurane (*v/v*) during the surgical operation with a non-rebreathing system. A radial defect of 8 *mm* was created using a rongeur unit (bone cutter). The defect was thoroughly rinsed with isotonic saline and any bone fragments were removed. After implanting the scaffold, the incision was closed with 5-0 sized silk sutures. A subcutaneous injection of 2% Lidocaine (*w/v*) was administered immediately directly into the surgical area under the skin after closure of the incision to relieve pain. At the end of the surgery, the animal was administered a subcutaneous injection of sterile saline at a dose of *10 mL/kg per surgery hour* and provided pure oxygen by a non-rebreathing system until it awakened from the isoflurane anesthesia. A dose of carprofen (anti-inflammatory drug) solution was subcutaneously given (4 *mg/kg*) every 12 hours for 7 days.

5.2.10 Preparation and fixation of harvested bone defect tissues

After 4 weeks and 12 weeks, Animals (N=5) were euthanized by CO_2 asphyxiation. The sections of the arms containing the implant (at the radius bone) were then cut way from the rest of the animal using bone cutters. The 4-

week implant samples were fixed in 10% *(w/v*) neutral formalin solution for 4 days. The 12-week samples were fixed in 4% paraformaldehyde for 4 days. Paraformaldehyde was used as it can produce better CD31 vascularization stains relative to fixing with formalin. The samples were then placed in a solution of 70% ethanol to 30% water (*v/v*).

5.2.11 Hematoxylin and Eosin Tissue Staining

The equipment necessary for sectioning titanium is very rare and expensive. I would like to thank Dr. Khandaker (University of Central Oklahoma) and his student, Sadegh (Univeristy of Central Oklahoma) for their help during the sectioning process.

The tissue sections were deparaffinized and hydrated with distilled water. Hematoxylin was applied to the sample with enough volume to cover the tissue section followed by incubation for 5 minutes. The mounted tissue slide was then rinsed in 2 changes of distilled water (sections were allowed to soak for 15 seconds on each exchange of water). Enough Bluing Reagent was then added to the tissue section to completely cover it followed by incubation for 10-15 seconds. The slides were then rinsed again in 2 changes of distilled water allowing 15 seconds of contact with the water each time. The slides were then dipped in 100% ethanol for 10 seconds. The excess ethanol was blotted off. Enough Eosin Y Solution was then added to completely cover the tissue section followed by incubation for 2-3 minutes. The slides were then rinsed in 100% ethanol for 10 seconds. Next, the slides were dehydrated in 3 changes of

100% ethanol allowing 1-2 minute incubation times at each exchange of ethanol. The sections were then cleared and cover slipped.

5.2.12 Von Kossa tissue Staining

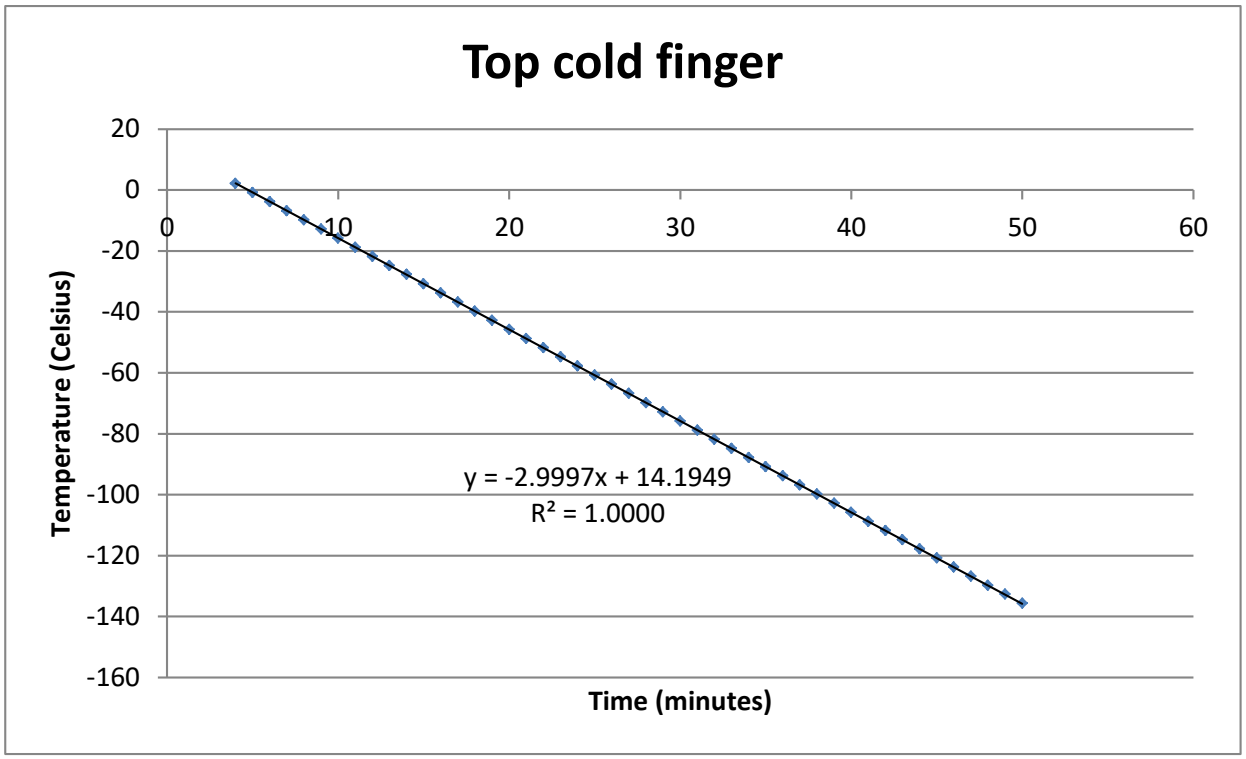
The sections were deparaffinized and hydrated in distilled water. The slides were then incubated in Silver Nitrate Solution (5%) for 30-60 minutes while exposed to an ultraviolet light. The slides were then rinsed in 3 changes of distilled water. The slides were then incubated in Sodium Thiosulfate Solution (5%) for 2-3 minutes. The slides were then rinsed for 2 minutes in running tap water followed by two changes of distilled water. The slides were then incubated in Nuclear Fast Red Solution for a duration of 5 minutes. Next, the slides were rinsed for 2 minutes in running tap water followed by 2 changes of distilled water. The samples were then dehydrated rapidly in 3 changes of fresh 100 proof ethanol. The slides were then cleared and mounted in synthetic resin.

5.3 Results and Discussion

5.3.1 Freeze casting machine performance

The double-sided freeze casting machine allowed for greater control over the linearity of the cooling rate of samples as shown in the figures below. Additionally, the top cold finger allows for control over the heat flux of the top of the sample. Another side benefit is that the sample can be completely sealed in a sterile container during the freeze casting when both a top and cold finger are

used. Overall, the double-sided freeze casting system is superior to the single-sided system.


Top cold finger
20
0
-20
-40
-60
-80
-100
-120
-140
-160
0
10
20
30
40
50
60
Temperature (Celsius)
Time (minutes)
y = -2.9997x + 14.1949
R² = 1.0000

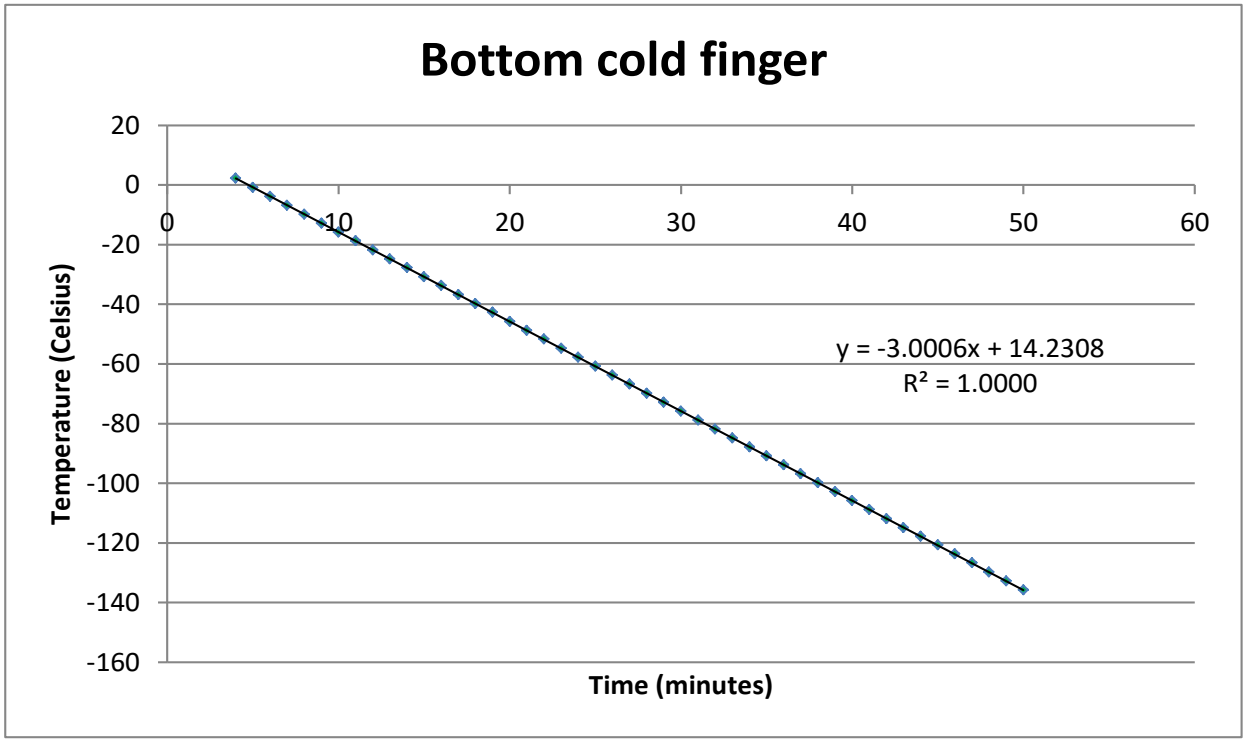

Bottom cold finger
20
0
-20
-40
-60
-80
-100
-120
-140
-160
0
10
20
30
40
50
60
Temperature (Celsius)
Time (minutes)
y = -3.0006x + 14.2308
R² = 1.0000

Figure 26. Double Sided Freeze Casting rates for the top cold finger (top) and bottom cold finger (bottom). The double-sided freeze casting system cooled at a very steady rate of 3 degrees Celsius per minute.

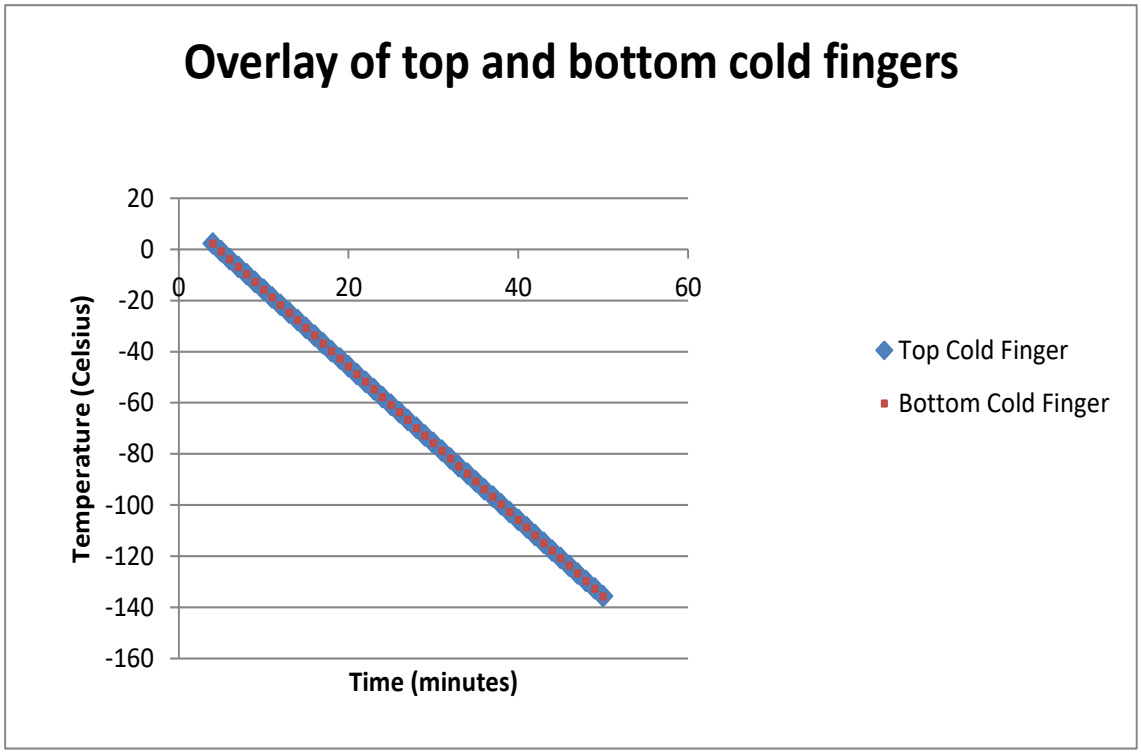


Figure 27. An overlay of the top and bottom cold fingers freeze casting rates. The two fingers showed very precise synchronization for temperature dropping rates.

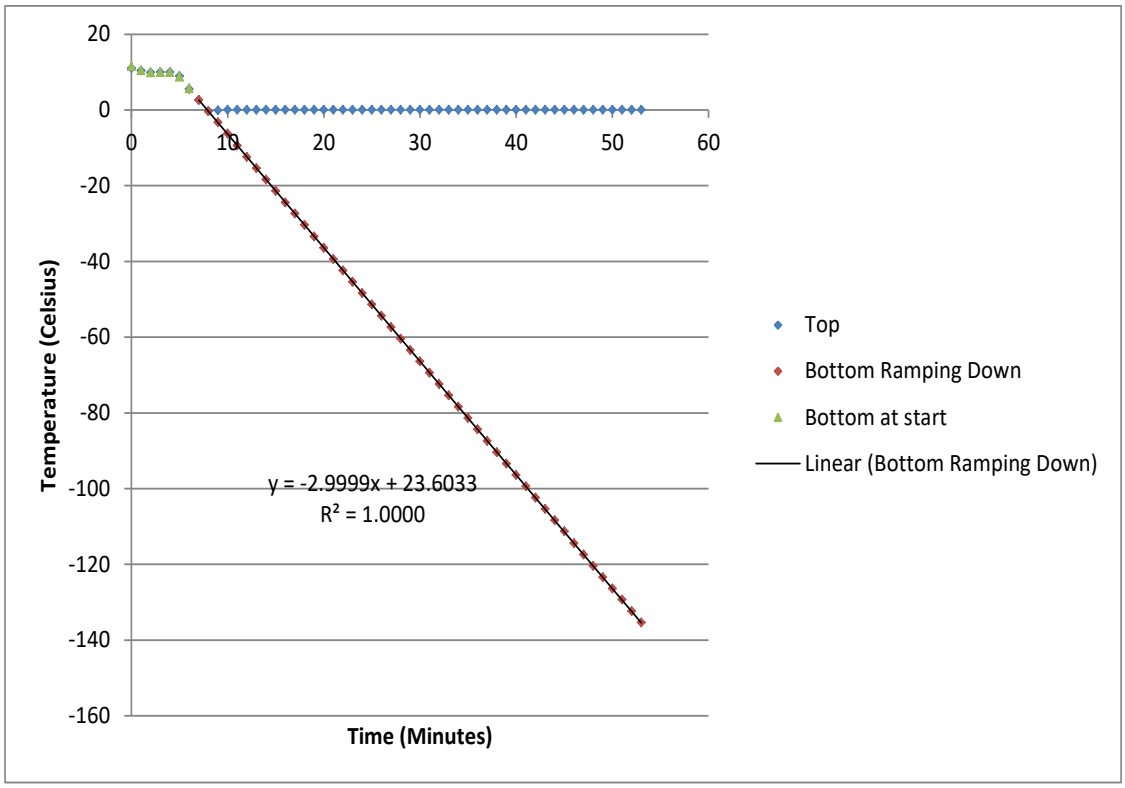


Figure 28. Temperature rates of the top (blue) and bottom (red) cold fingers in the double-sided freeze casting setup. In this run, the top cold finger was held at 0 ℃ while the bottom cold finger dropped at 3 ℃ / *minute*. The green shows the period of time where the cold fingers were adjusted and synchronized before reaching 0℃.

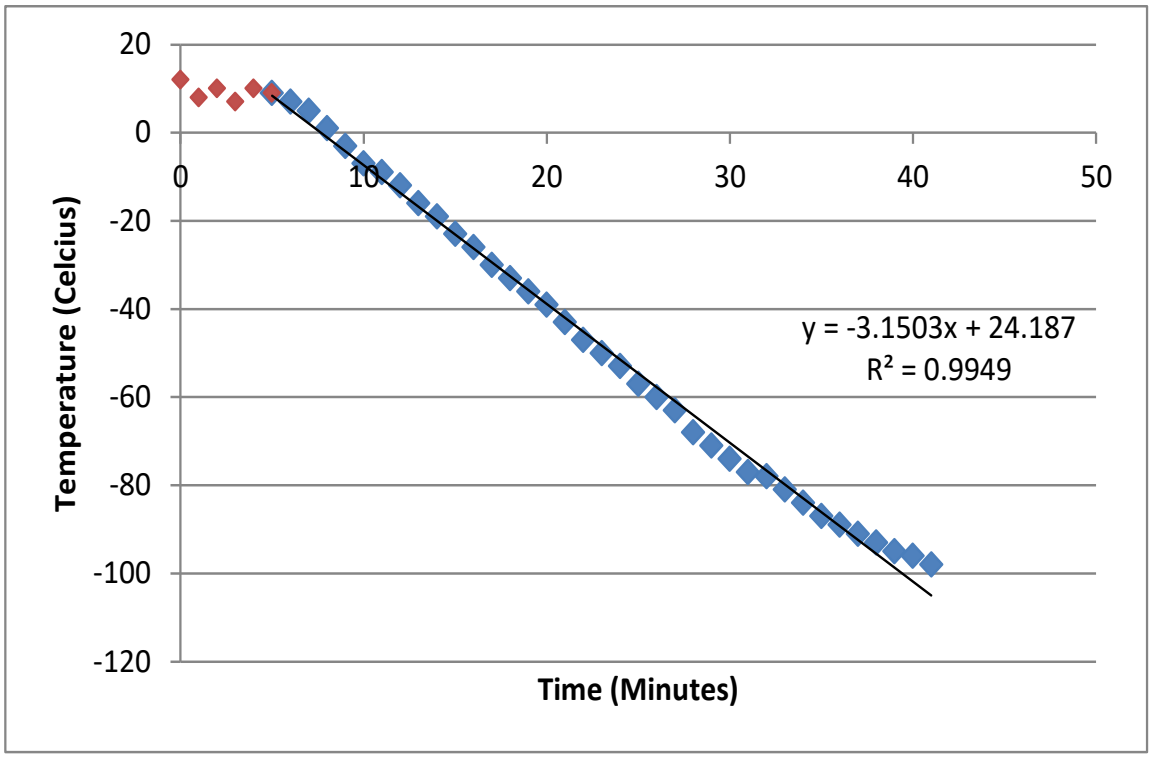
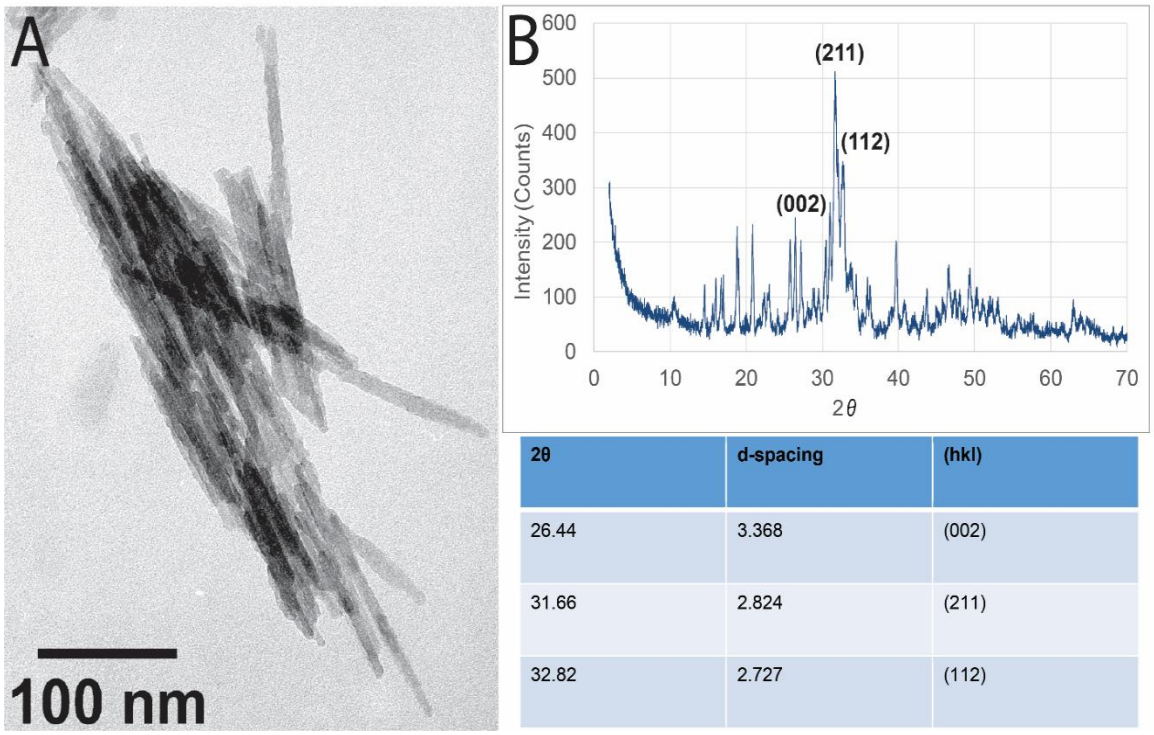


Figure 29. The temperature drop rate of a single-sided freeze casting system is shown. The system does not cool as linearly as the double-sided system and lacks a top cold finger to control the heat flux over the sample's top surface.

5.3.2 Hydroxyapatite powder X-Ray diffraction and TEM confirms synthesis of HAP nanorods

Hydroxyapatite nanorods were synthesized to be later used in freeze casting applications for bone regenerative scaffolds. Figure 30 shows the synthesized nanorods' morphology. X-ray diffraction was also done on the nanorods which confirmed that the nanorods were composed of hydroxyapatite according to the (hkl) values shown in Figure 30.



2θ	d-spacing	(hkl)
26.44	3.368	(002)
31.66	2.824	(211)
32.82	2.727	(112)

Figure 30. Hydroxyapatite $Ca_5(PO_4)_3(OH)$ nanorods. The nanorods were synthesized, imaged by TEM (A), and characterized by powder x-ray diffraction (B).

5.3.3 Just Phage and phage + hydroxyapatite characterization after freeze casting

Using the double-sided freeze casting machine built, several different lamellar scaffold structures could be created for their intended use in bone regeneration. Figure 31 shows the resulting lamellar structures. A close up of the scaffold containing just phage shows the fiber-like structure of M13 phages which form bundles within the scaffold. The pure phage scaffold was highly organized into a lamellar structure. However, pure phage scaffolds are rather weak to handle and will fall apart if not moved very carefully. They are not ideal

for load-bearing site bone regeneration. Additionally, the pure phage scaffolds will dissolve in water within minutes making them unsuitable for cell culture or cross-linking through EDC. When pure phage scaffolds are combined with HAP nanorods, the structure collapses and the scaffolds are too weak to visualize. Therefore, an additional component, rat tail collagen type 1 was added in parts C-F of Figure 32. Upon the addition of collagen, the scaffolds were stronger and could handle being combined with HAP as shown in C and D of Figure 31. However, these scaffolds were still easily degraded if not handled carefully and their durability in water was ~2 days. Therefore, additional strengthening was necessary which was provided by crosslinking in EDC. The cross-linked samples are shown in parts E and F of Figure 31. After crosslinking, the samples were stable in water or cell culture medium for greater than 2 weeks. However, their ability to regenerate bone in a load-bearing site was not possible as they had the consistency of a marshmallow. Due to the poor mechanical strength of this method, more mechanically strong methods were later pursued. However, this data does show that phages can be organized into a lamellar bone-like 3D structure using double-sided freeze casting. Additionally, upon strengthening the phages were semi-stable in water indicating some potential *in vitro* for 3D cell culture applications. These results were later used to develop a method in which phages could be used to coat materials.

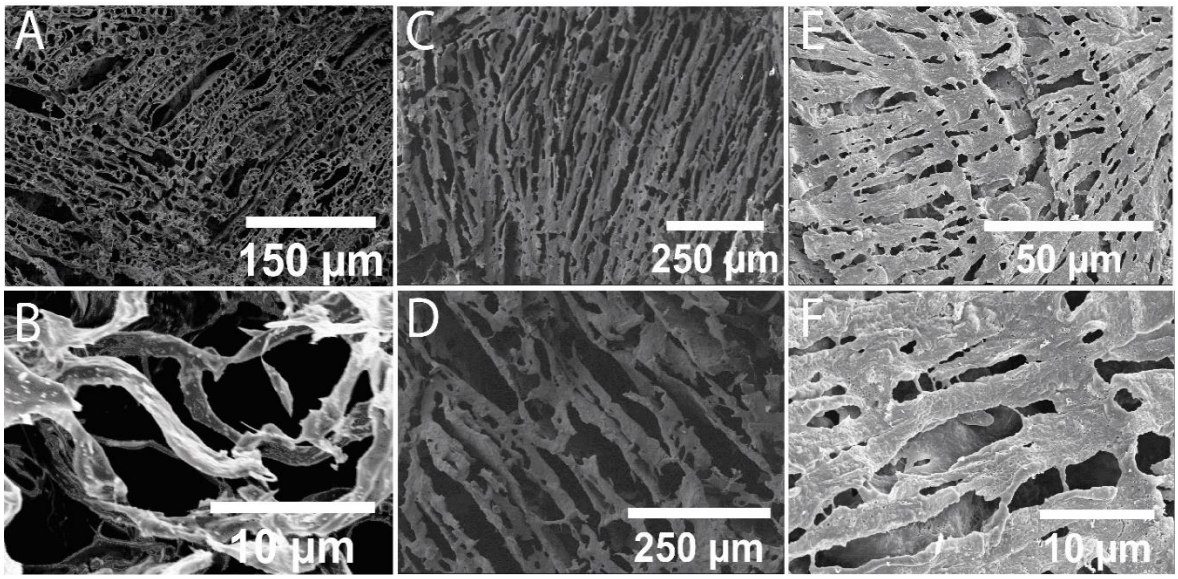


Figure 31. M13 phage scaffolds arranged through freeze casting and imaged by SEM. Pure M13 phage scaffolds at different magnifications (A and B). M13 phages combined with collagen and hydroxyapatite nanorods at different magnifications (C and D). M13 phages mixed with collagen and hydroxyapatite which were cross-linked using EDC.

The double-sided freeze casting system was also used to generate hydroxyapatite scaffolds held together with an organic binder, PEG-8000. These scaffolds showed excellent lamellar structures as shown in Figure 32. However, these scaffolds easily dissolved in water and had a stiffness comparable to a marshmallow which is not close to ideal for load bearing applications. Therefore, the scaffolds were sintered. This process also served to burn off the PEG-8000 leaving only pure HAP left in the scaffolds. The resulting structures are shown in Figure 33. While the sintered HAP scaffold appears to be a bit shriveled relative to the un-sintered scaffold, the highly organized lamellar structure was maintained. Additionally, the scaffolds were

now more durable and hard in nature. However, the scaffolds were still not considered strong enough for load-bearing sites as they could be broken with a very modest amount of pressure. Therefore, this route is not recommended. However, these data do demonstrate the power of the double-sided freeze casting system for organizing bone regenerative materials into a lamellar structure which could have potential *in vitro* for 3D cell culturing.

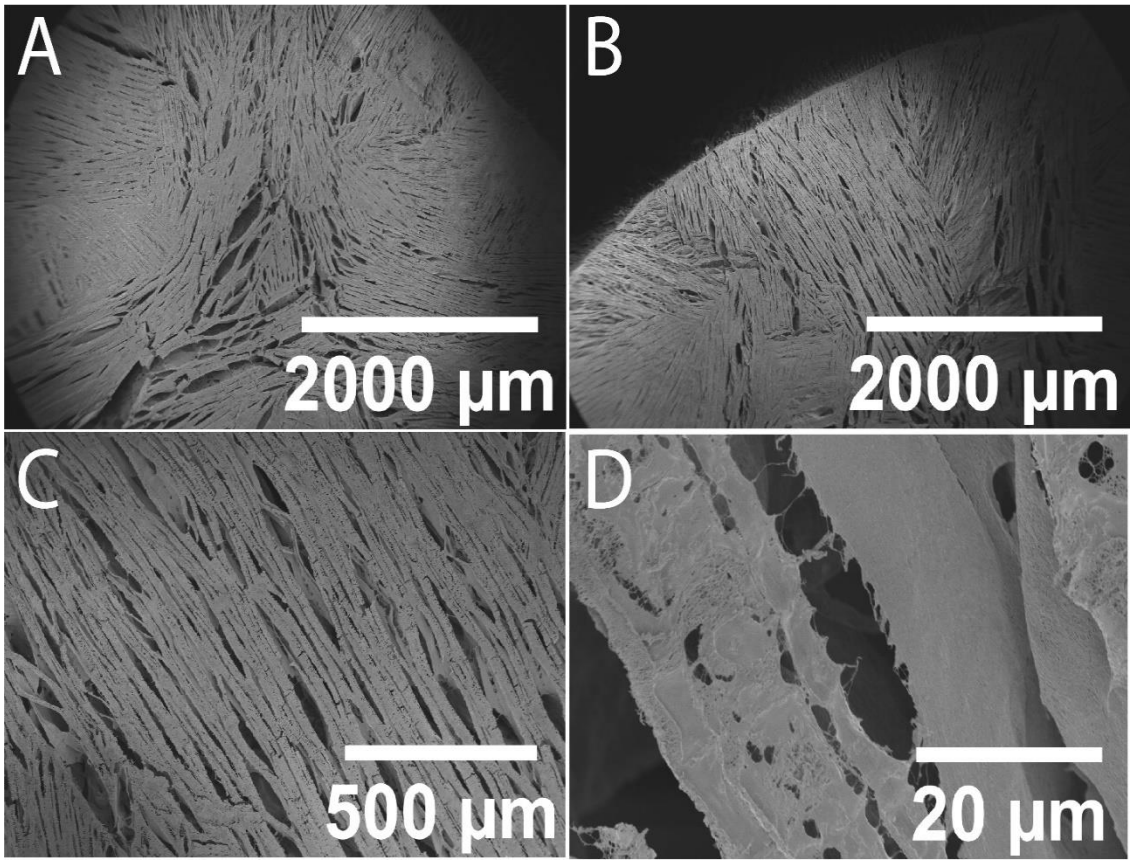


Figure 32. Freeze-casted HAP. (A) Center top view of scaffold; (B) Edge top view of scaffold; (C) zoomed in view of lamellar structure; (D) high magnification view of a chasm of the lamellar structure.

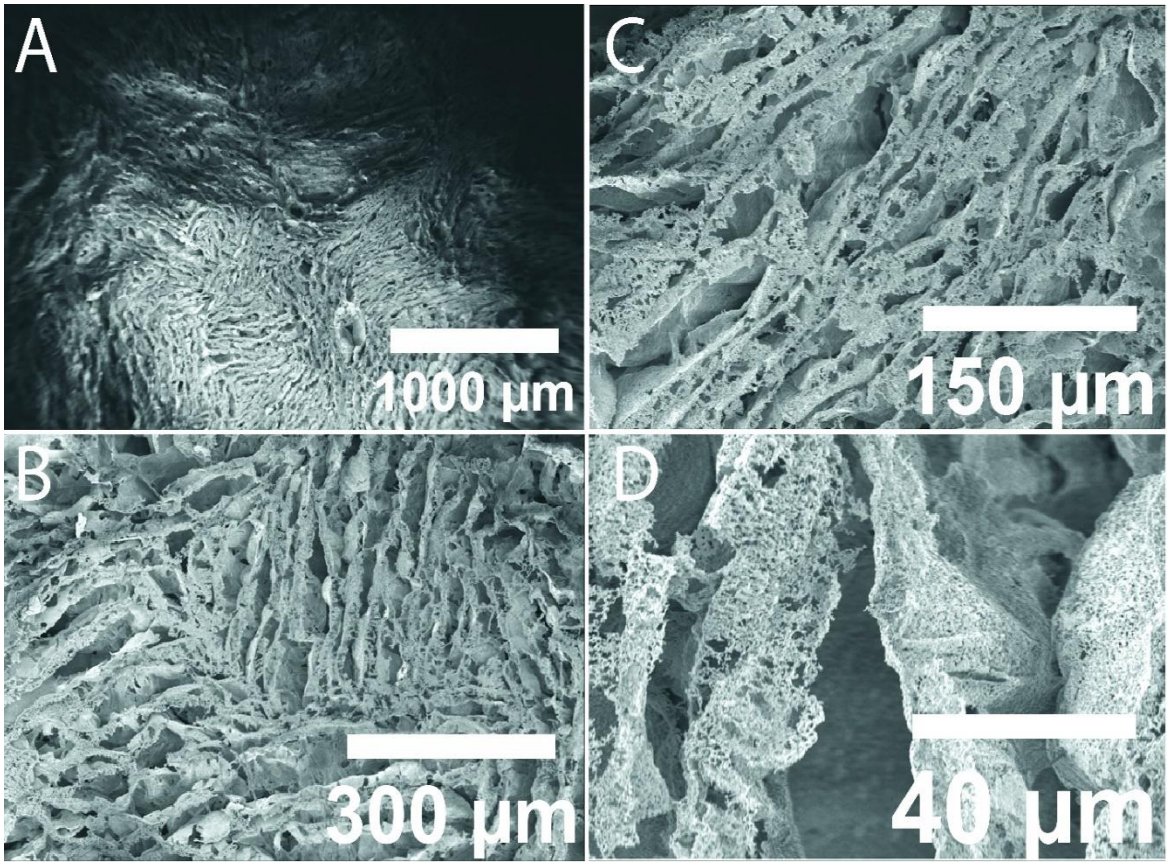


Figure 33. Freeze casted HAP which has been sintered. (A) Center top view; (B-D) top view at increasing magnification. The lamellar structure can be seen.

5.3.4 A combination of 3D printing, freeze casting, and growth factor mimetics to tune the microenvironment of implants

3D printed titanium implants were created using a biocompatible metal alloy consisting of titanium, aluminum, and vanadium (Ti-6Al-4V, 6:4:90, Al: V: Ti, wt%) which is among the most commonly used titanium alloys for biomedical implants.[427-428] Specifically, a design of the desired porous scaffold was created in the digital format known as an STL (Stereo Lithography) file

using a computer-aided design (CAD) software. Then commercial Ti-6Al-4V alloy powder was printed into an implant in pure Ar gas according to the STL file, by means of selective laser melting (SLM) through a commercial laser-based 3D printer (Concept LASER M2) specialized for printing metallic powder. The 3D printer was equipped with a Yb-FaserLaser with a focus beam diameter of 50 μm. The SLM parameters during 3D printing included a laser power of 100 W, a scan speed of 650 mm/s, a scan spacing of 70 μm, and a layer thickness of 30 μm. The scaffolds were cylindrical in shape with a height of 8 mm and a diameter of 5 mm (Figure 34). The pores within the scaffold measured ~200 μm in diameter which is important for cell penetration and the diffusion of nutrients throughout the scaffold (Fig. 2). When human mesenchymal stem cells (hMSCs) were cultured on these scaffolds they spread to cover both the top (Fig. 2Ac) and sides (Fig. 2Ad) of the scaffolds. Using EDS, the carbon contained in the cells could be visualized to show the locations of the cells (Fig 2Ac-d).

To control the microenvironment on the scaffolds, M13 phage structures were assembled using freeze casting to generate similar lamellar structures to collagen in natural bone (cite) (Fig. 2Ba-b). This process was done by directionally freezing water from the bottom of the scaffold to the top at a cooling rate of 3 ℃ /min while maintaining a constant temperature of 0 ℃ on the top (Fig 1?). As the ice crystals form, they push the M13 phages into the lamellar spaces in between the ice. When the ice is removed through sublimation under a vacuum, highly lamellar fibrous phage structures are

leftover (Fig. 2Ba-b). The direction of the freezing controls the direction of the lamellar structures, and therefore the sides of the scaffolds are where the lamellar structures occur (Fig. 2Ba-b). After coating with phages, the scaffolds were seeded with hMSCs which can be seen from the top view (Fig. 2Bc) and side view (Fig. 2Bd). The cell structures can be clearly seen from the top view, (Fig. 2Bc) and the carbon in them creates a contrast against the titanium background. The amount of phages deposited are heavier on the sides of the scaffold (Fig. 2Ba-b and d) due to the freeze casting process. The cells can still be seen on the side view of the phage coated scaffolds (Fig. 2Bd), but both phages and cells have carbon and are thus both colored green by EDS. An additional control mechanism over the microenvironment of the cells was the introduction of the growth factor mimetic peptides VHVPLHRGAVSA and SGTQDSMVGWNK. These peptides were displayed on the major coat protein of the filamentous M13 phages allowing for optimal surface area exposure. The display of these peptides on the phages does not alter the lamellar structures created through freeze casting. By combining the precise structural control mechanisms of 3D printing and freeze casting with the power of phages bearing growth factor mimetic peptides, we have created a new method for improving tissue regenerative implants.

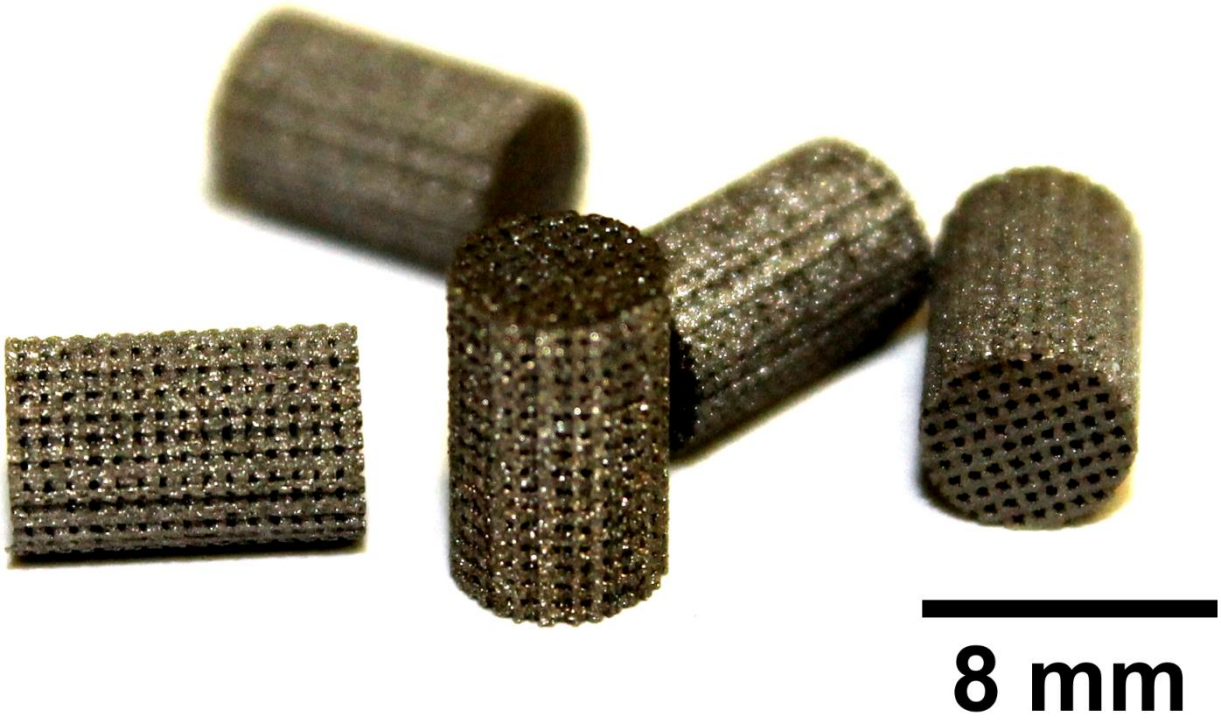


Figure 34. 3D printed titanium scaffolds.

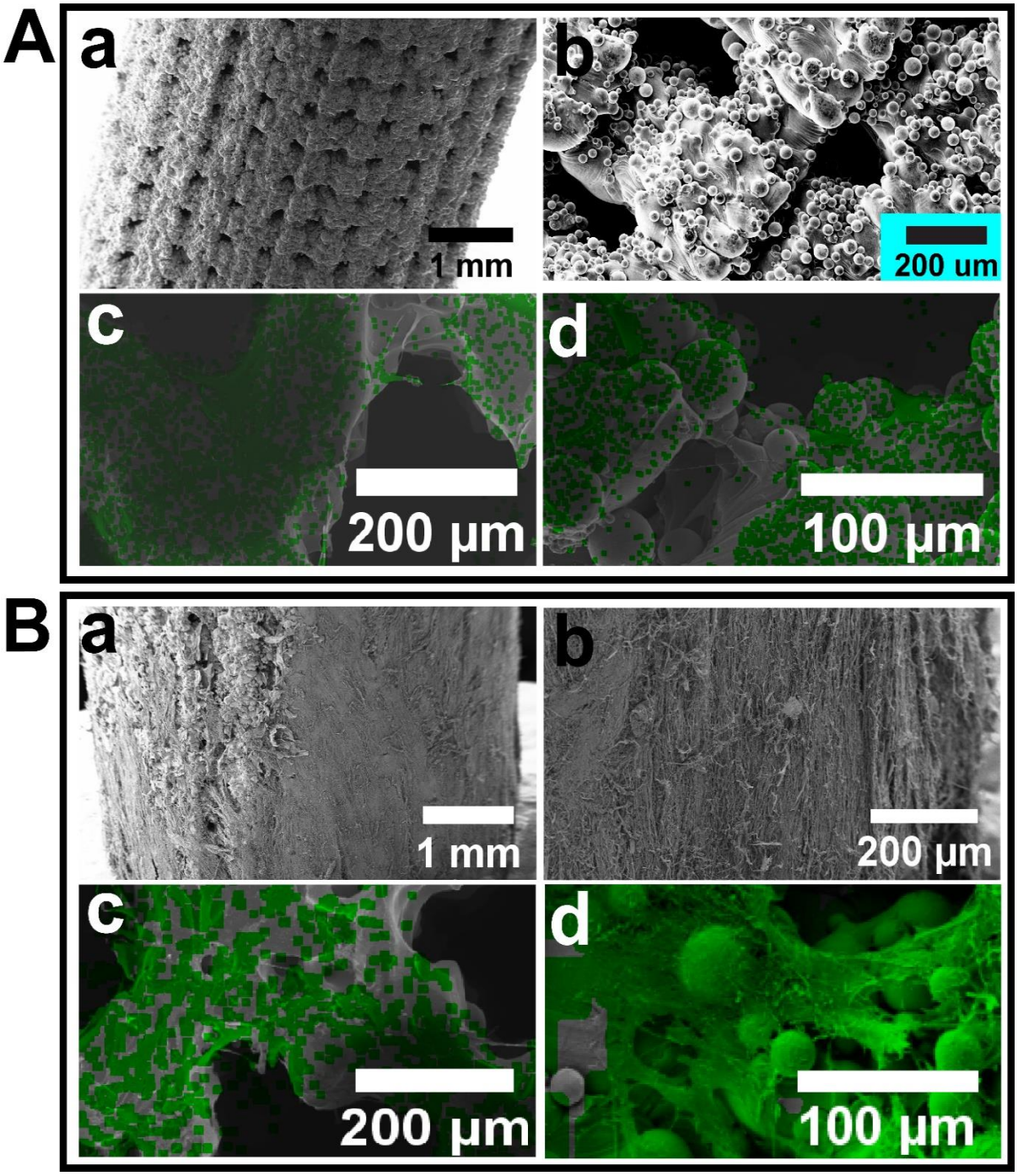


Figure 35. 3D printed titanium scaffold coating results. Green represents carbon imaged by energy-dispersive x-ray spectroscopy (EDS). (A) The scaffolds without phages are shown (a and b). The scaffolds without phages

were seeded with cells which can be seen from the top view (c) and side view (d). (B) The scaffolds were coated by freeze casting with phages (a and b) creating an aligned lamellar pattern. The phage-coated scaffolds were then seeded with cells which can be seen from the top view (c) and side view (d) of the scaffolds. This data shows that the phage coating procedure can create lamellar bone-mimetic structures that support cell growth. The carbon in both cells and phages (green) clearly shows a contrast between the titanium and biological material.

5.3.5 Mechanical strength properties of titanium-phage hybrid scaffolds show ideal bone-like properties in vivo

The mechanical properties of natural bone can have major effects on the health of the bone.[431] Therefore, our 3D printed scaffolds were designed to mimic the properties of natural bone. To evaluate these mechanical properties, stress strain curves for 3D printed scaffolds and healthy bone samples were created. The average Young's modulus for titanium scaffolds before implantation into rats was $3.7917 \pm 1.1284\ GPa$. The average Young's modulus for titanium scaffolds implanted for 4 weeks was $3.8436 \pm 0.7260\ GPa$. The Young's moduli of the titanium scaffolds before and after implantation were not statistically different indicating no degradation of the titanium. The average Young's modulus for healthy bone (4-week-old SD rats) was $10.1099 \pm 5.1366\ GPa$. No statistical difference was found between the Young's modulus for the titanium scaffolds and healthy bone. This data shows that the Young's moduli of the titanium scaffolds and healthy bone are

comparable. The average maximum stresses before failure of the titanium scaffolds before implantation, implanted 4 weeks, and healthy bone (4 week old SD rats) were $305.9027 \pm 14.2514\ GPa$, $278.1823 \pm 20.9649\ GPa$, and $229.1154 \pm 79.8224\ GPa$ respectively. There was no statistical difference between the maximum stress before failure for any of the conditions. This data demonstrates that the titanium alloy scaffolds are mechanically very similar to healthy bone.

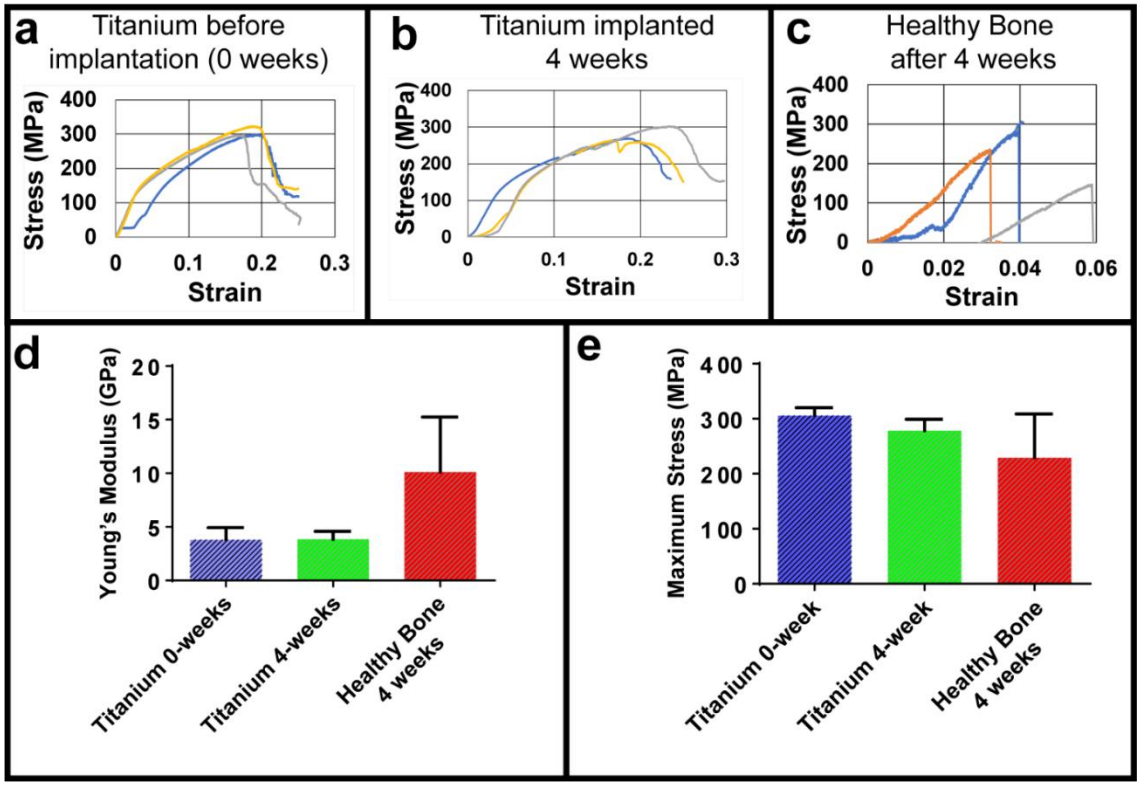


Figure 36. The mechanical properties of implanted scaffolds. (a-c) Replicate (n=3) stress strain curves for titanium scaffolds before implantation (a), for titanium scaffolds implanted 4 weeks (b), and for healthy bone after 4 weeks

(c). The young's moduli for each sample were not significantly different (d). The maximum stress was also not significantly different (e). This data indicates that the titanium scaffolds do not degrade over time and are highly similar to natural healthy bone in terms of mechanical properties. All data represent the mean ± standard deviation with n=3 repeats.

5.3.6 Histological staining shows tissue and calcium deposits in scaffolds

The 3D printed titanium scaffolds under each condition were harvested after 4 weeks of implantation in rats. The implants were fixed in 10% *(w/v*) neutral formalin solution followed by dehydration in a graded series of ethanol. The scaffolds were then embedded in a technovit resin followed by sectioning. H&E staining as well as Von Kossa staining were done from sections originating near the middle of the scaffolds. From the H&E staining, cells were able to penetrate deeply into the sample. The peptide conditions VHVPLHRGAVSA, SGTQDSMVGWNK, and the combination of these two peptides appeared to enhance the amount of tissue formation (Fig. 4). A Von Kossa stain indirectly stains for calcium by reacting silver ions with phosphates.[432] This turns areas of intense calcium deposition black and lighter areas gray. The Von Kossa staining reveals that bone formation around some of the conditions as well as calcium deposition did occur (Fig. 5). In particular, the peptides VHVPLHRGAVSA, SGTQDSMVGWNK, and the combination of these two peptides demonstrated greater bone regeneration than the control groups. This demonstrates that our technique for coating scaffolds with growth factor mimetic peptides helped with bone regeneration.

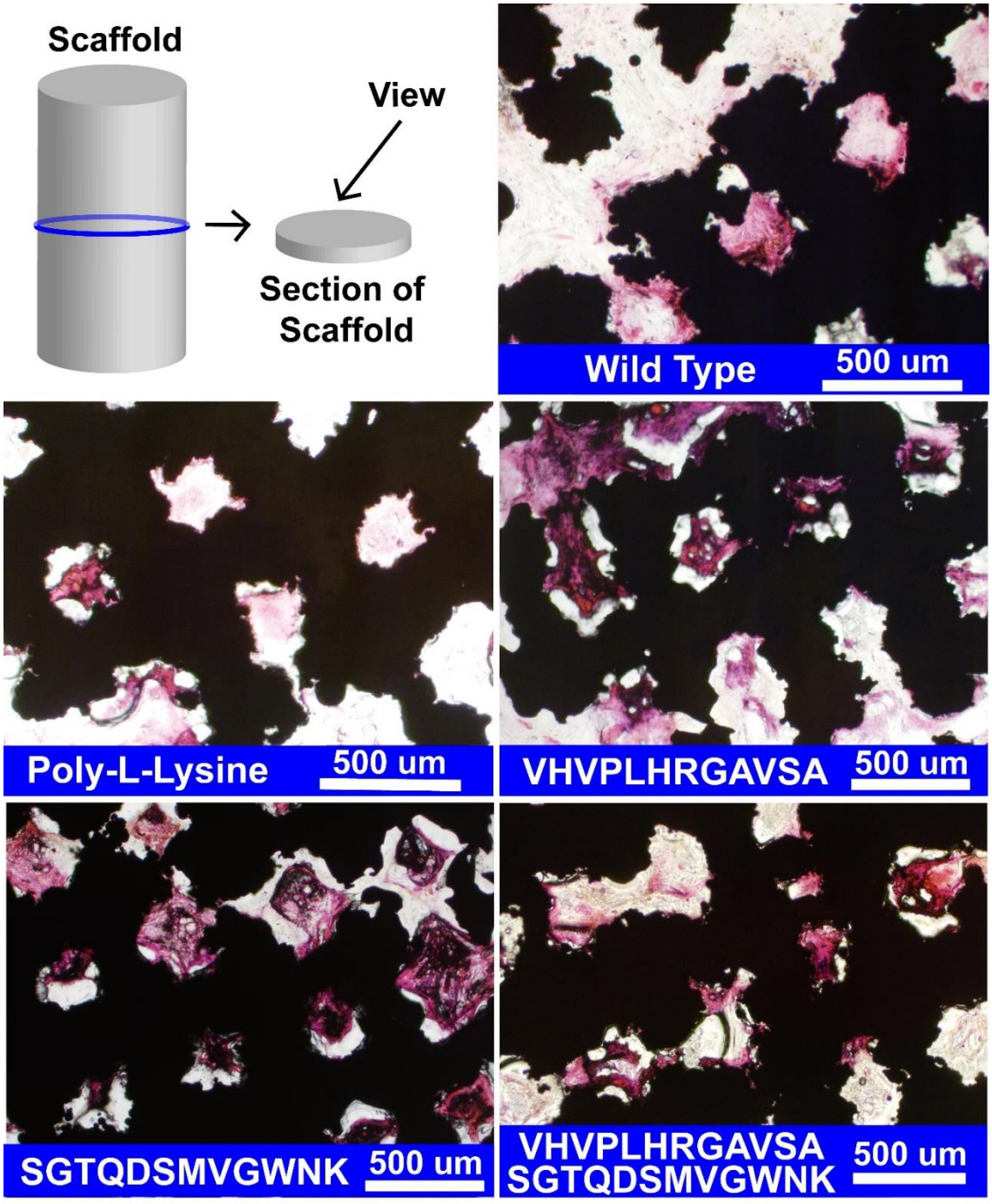


Figure 37. Top down view of a section of each cylindrical-shaped implant condition stained with H&E after being implanted 4 weeks. The section was taken from the middle of the scaffold. The dark black grids are the titanium and

the cells can be seen in purple/pink. The scaffolds supported the penetration and growth of cells even to the deepest regions of the scaffolds. The peptide-bearing phage samples VHVPLHRGAVSA, SGTQDSMVGWNK, and the combination of these two peptides appear to have more tissue growth within the scaffolds than the control conditions but are not different from each other.

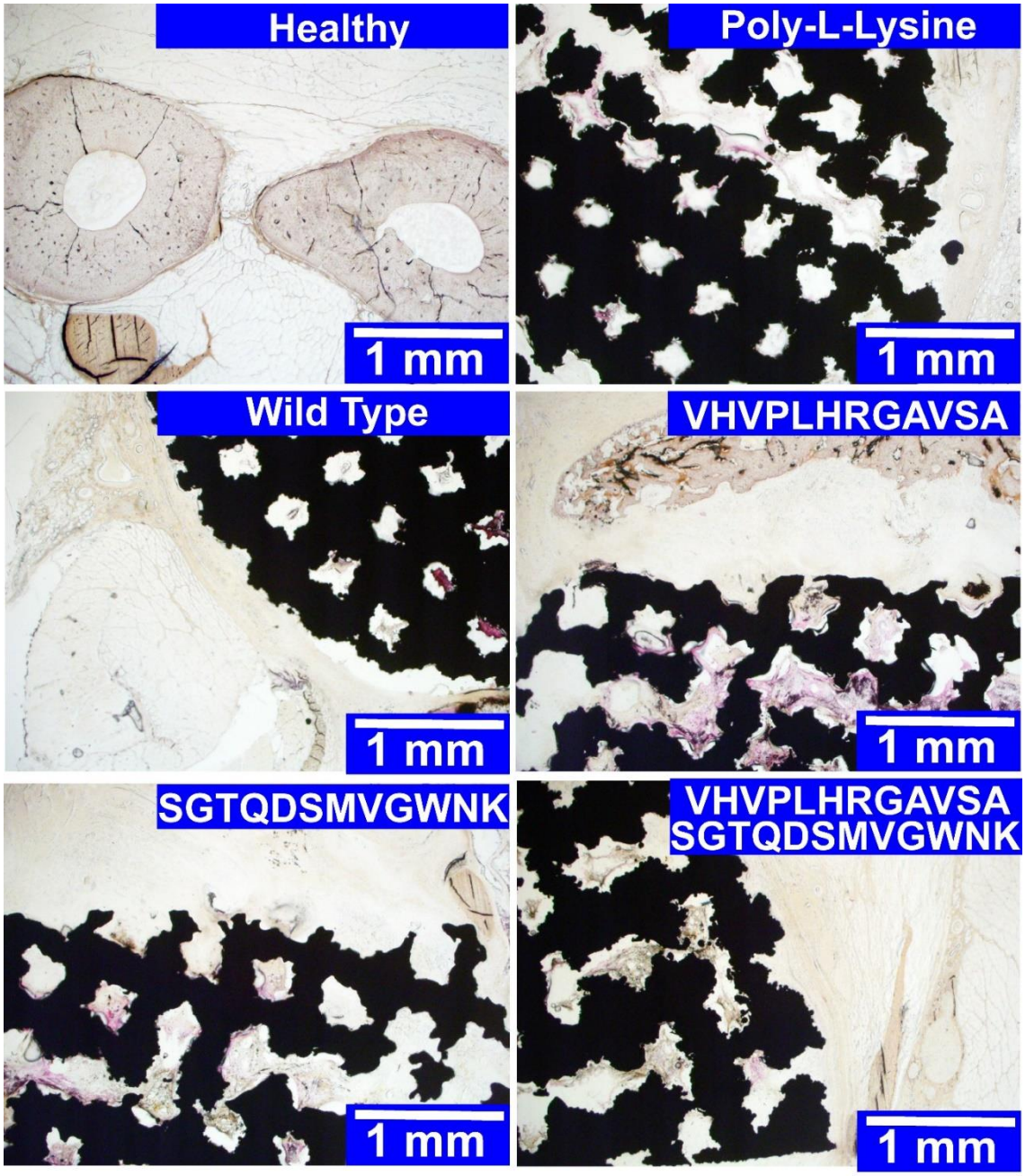


Figure 38. Von Kossa stains of 4-week implants in rat radial defect bone models viewed from the top down of the cylindrical scaffolds. The section was taken from the middle of the scaffold. The dark black grids are titanium. Other black areas are heavy calcium deposits. Gray areas indicate lighter calcium deposits. The lightly colored pink/purple are cells. The peptides

VHVPLHRGAVSA, SGTQDSMVGWNK, and the combination of these peptides appear to have more calcium deposition within and around the scaffolds.

5.4 Conclusion

Phage-based scaffolds were created with lamellar structures resembling natural bone. However, the biodegradable phage scaffolds created from pure phage, phage and collagen, or additions of hydroxyapatite with phage were not suitable for load bearing site bone tissue repair due to poor mechanical strength. The strategy was adapted to coat 3D printed titanium implants with mechanical strengths much closer to that of natural bone. Each phage coating was genetically engineered to have osteogenic peptides displayed. The phage coatings were aligned in lamellar structures through freeze casting onto the titanium. In a rat radial bone defect model, bone regeneration was discovered in the areas surrounding the implant. Cell penetration deep into the implants was observed through H&E staining. New calcium deposits were found within and around the scaffolds resembling natural bone via a Von Kossa stain. While this study was limited to a radial defect model, the process is relevant to coating any material. This work may become very useful for coating dental screws or any hardware implanted and integrated with bones.

References

1. Young, M.; Willits, D.; Uchida, M.; Douglas, T., Plant Viruses as Biotemplates for Materials and Their Use in Nanotechnology. *Annu. Rev. Phytopathol.* **2008,** *46* (1), 361-384.

2. Amy, W. N., Steinmetz, Design of virus-based nanomaterials for medicine, biotechnology, and energy. *Chem. Soc. Rev.* **2016,** *45*, 4074-4126

3. Culver, J. N.; Brown, A. D.; Zang, F.; Gnerlich, M.; Gerasopoulos, K.; Ghodssi, R., Plant virus directed fabrication of nanoscale materials and devices. *Virology* **2015,** *479-480* (Supplement C), 200-212.

4. Chen, Z.; Li, N.; Li, S.; Dharmarwardana, M.; Schlimme, A.; Gassensmith, J. J., Viral chemistry: the chemical functionalization of viral architectures to create new technology. *Wiley Interdiscip Rev Nanomed Nanobiotechnol* **2016,** *8* (4), 512-534.

5. Koudelka, K. J.; Pitek, A. S.; Manchester, M.; Steinmetz, N. F., Virus-Based Nanoparticles as Versatile Nanomachines. *Annu. Rev. Virol.* **2015,** *2* (1), 379-401.

6. Plchova, H.; Cerovska, N.; Vaculik, P.; Moravec, T., Plant viruses as scaffolds for the presentation of vaccine epitopes. *Biol. Plant.* **2017,** *61* (1), 1-12.

7. Berardi, A.; Evans, D. J.; Baldelli Bombelli, F.; Lomonossoff, G. P., Stability of plant virus-based nanocarriers in gastrointestinal fluids. *Nanoscale* **2018**, 1667-1679.

8. Wang, J.; Wang, L.; Yang, M.; Zhu, Y.; Tomsia, A.; Mao, C., Untangling the Effects of Peptide Sequences and Nanotopographies in a Biomimetic Niche for Directed Differentiation of iPSCs by Assemblies of Genetically Engineered Viral Nanofibers. *Nano Lett.* **2014,** *14* (12), 6850-6856.

9. Sawada, T., Filamentous virus-based soft materials based on controlled assembly through liquid crystalline formation. *Polym. J.* **2017,** *49*, 639.

10. Kim, W.-G.; Song, H.; Kim, C.; Moon, J.-S.; Kim, K.; Lee, S.-W.; Oh, J.-W., Biomimetic self-templating optical structures fabricated by genetically engineered M13 bacteriophage. *Biosens. Bioelectron.* **2016,** *85*, 853-859.

11. Zhou, K.; Eiben, S.; Wang, Q., Coassembly of Tobacco Mosaic Virus Coat Proteins into Nanotubes with Uniform Length and Improved Physical Stability. *ACS Appl. Mater. Interfaces* **2016,** *8* (21), 13192-13196.

12. Love, A. J.; Makarov, V. V.; Sinitsyna, O. V.; Shaw, J.; Yaminsky, I. V.; Kalinina, N. O.; Taliansky, M. E., A Genetically Modified Tobacco Mosaic Virus that can Produce Gold Nanoparticles from a Metal Salt Precursor. *Front Plant Sci* **2015,** *6*, 984.

13. Banik, S.; Mansour, A. A.; Suresh, R. V.; Wykoff-Clary, S.; Malik, M.; McCormick, A. A.; Bakshi, C. S., Development of a multivalent subunit vaccine against tularemia using tobacco mosaic virus (TMV) based delivery system. *PLoS One* **2015,** *10* (6), e0130858.

14. Wu, L.; Jiang, L.; Zhou, Z.; Fan, J.; Zhang, Q.; Zhu, H.; Han, Q.; Xu, Z., Expression of foot-and-mouth disease virus epitopes in tobacco by a tobacco mosaic virus-based vector. *Vaccine* **2003,** *21* (27–30), 4390-4398.

15. Koch, C.; Wabbel, K.; Eber, F. J.; Krolla-Sidenstein, P.; Azucena, C.; Gliemann, H.; Eiben, S.; Geiger, F.; Wege, C., Modified TMV Particles as Beneficial Scaffolds to Present Sensor Enzymes. *Front Plant Sci* **2015,** *6*, 1137.

16. Hommersom, C.; Matt, B.; van der Ham, A.; Cornelissen, J.; Katsonis, N., Versatile post-functionalization of the external shell of cowpea chlorotic mottle virus by using click chemistry. *Org. Biomol. Chem.* **2014,** *12* (24), 4065-4069.

17. Schoonen, L.; Pille, J.; Borrmann, A.; Nolte, R. J. M.; van Hest, J. C. M., Sortase A-Mediated N-Terminal Modification of Cowpea Chlorotic Mottle Virus for Highly Efficient Cargo Loading. *Bioconjug. Chem.* **2015,** *26* (12), 2429-2434.

18. Riekel, C.; Burghammer, M.; Snigirev, I.; Rosenthal, M., Microstructural metrology of tobacco mosaic virus nanorods during radial compression and heating. *Soft Matter* **2018,** *14* (2), 194-204.

19. Bruckman, M. A.; Randolph, L. N.; VanMeter, A.; Hern, S.; Shoffstall, A. J.; Taurog, R. E.; Steinmetz, N. F., Biodistribution, pharmacokinetics, and blood compatibility of native and PEGylated tobacco mosaic virus nano-rods and -spheres in mice. *Virology* **2014,** *449*, 163-173.

20. Kehoe, J. W.; Kay, B. K., Filamentous Phage Display in the New Millennium. *Chem. Rev.* **2005,** *105*, 4056-4072.

21. Lee, S.-Y.; Lim, J.-S.; Harris, M. T., Synthesis and application of virus-based hybrid nanomaterials. *Biotechnol. Bioeng.* **2012,** *109* (1), 16-30.

22. van Wezenbeek, P. M. G. F.; Hulsebos, T. J. M.; Schoenmakers, J. G. G., Nucleotide sequence of the filamentous bacteriophage M13 DNA genome: comparison with phage fd. *Gene* **1980,** *11* (1–2), 129-148.

23. Gray, B.; Brown, K., Combinatorial Peptide Libraries: Mining for Cell-Binding Peptides. *Chem. Rev.* **2013,** *114*, 1020-1081.

24. Endemann, H.; Model, P., Location of Filamentous Phage Minor Coat Proteins in Phage and in Infected Cells. *Am. J. Mol. Biol.* **1995,** *250* (4), 496-506.

25. Golmohammadi, R.; Valegård, K.; Fridborg, K.; Liljas, L., The Refined Structure of Bacteriophage MS2 at 2·8 Å Resolution. *J. Mol. Biol.* **1993,** *234* (3), 620-639.

26. Jiang, W.; Li, Z.; Zhang, Z.; Baker, M. L.; Prevelige, P. E.; Chiu, W., Coat protein fold and maturation transition of bacteriophage P22 seen at subnanometer resolutions. *Nat. Struct. Mol. Biol.* **2003,** *10* (2), 131-135.

27. Liang, L.; Zhao, H.; An, B.; Tang, L., High-resolution structure of podovirus tail adaptor suggests repositioning of an octad motif that mediates the sequential tail assembly. *Papillomavirus Research* **2018,** *115* (2), 313-318.

28. Namba, K.; Pattanayek, R.; Stubbs, G., Visualization of protein-nucleic acid interactions in a virus. *J. Mol. Biol.* **1989,** *208* (2), 307-325.

29. Scholthof, K.-B. G., Tobacco mosaic virus: a model system for plant biology. *Annu. Rev. Phytopathol.* **2004,** *42*, 13-34.

30. Speir, J. A.; Munshi, S.; Wang, G.; Baker, T. S.; Johnson, J. E., Structures of the native and swollen forms of cowpea chlorotic mottle virus determined by X-ray crystallography and cryo-electron microscopy. *Structure* **1995,** *3* (1), 63-78.

31. Belval, L.; Hemmer, C.; Sauter, C.; Reinbold, C.; Fauny, J.-D.; Berthold, F.; Ackerer, L.; Schmitt-Keichinger, C.; Lemaire, O.; Demangeat, G.; Ritzenthaler, C., Display of whole proteins on inner and outer surfaces of grapevine fanleaf virus-like particles. *Plant Biotechnol. J.* **2016,** *14*, 1-12.

32. Schellenberger, P.; Sauter, C.; Lorber, B.; Bron, P.; Trapani, S.; Bergdoll, M.; Marmonier, A.; Schmitt-Keichinger, C.; Lemaire, O.; Demangeat, G., Structural insights into viral determinants of nematode mediated Grapevine fanleaf virus transmission. *PLoS Pathog* **2011,** *7* (5), e1002034.

33. Lin, T.; Chen, Z.; Usha, R.; Stauffacher, C. V.; Dai, J.-B.; Schmidt, T.; Johnson, J. E., The Refined Crystal Structure of Cowpea Mosaic Virus at 2.8 Å Resolution. *Virology* **1999,** *265* (1), 20-34.

34. Hu, B.; Margolin, W.; Molineux, I. J.; Liu, J., The Bacteriophage T7 Virion Undergoes Extensive Structural Remodeling During Infection. *Science* **2013,** *339* (6119), 576-579.

35. Caspar, D. L. D., Assembly and Stability of the Tobacco Mosaic Virus Particle. In *Advances in Protein Chemistry*, C.B. Anfinsen, M. L. A.; John, T. E., Eds. Academic Press: San Diego, CA, 1964; Vol. Volume 18, pp 37-121.

36. Alonso, J. M.; Górzny, M. Ł.; Bittner, A. M., The physics of tobacco mosaic virus and virus-based devices in biotechnology. *Trends Biotechnol.* **2013,** *31* (9), 530-538.

37. Olofsson, L.; Ankarloo, J.; Andersson, P. O.; Nicholls, I. A., Filamentous bacteriophage stability in non-aqueous media. *J. Biol. Chem.* **2001,** *8* (7), 661-671.

38. Salivar, W. O.; Tzagoloff, H.; Pratt, D., Some physical-chemical and biological properties of the rod-shaped coliphage M13. *Virology* **1964,** *24* (3), 359-371.

39. Piggott, A. M.; Karuso, P., Identifying the cellular targets of natural products using T7 phage display. *Nat. Prod. Rep.* **2016,** *33* (5), 626-636.

40. Olga, K.; Farkhad, M.; Kenneth, A. M.; Valeri, B., TensorCalculator : exploring the evolution of mechanical stress in the CCMV capsid. *J. Phys. Condens. Matter* **2018,** *30* (4), 044006.

41. Schoenmakers, D. C.; Schoonen, L.; Rutten, M.; Nolte, R. J. M.; Rowan, A. E.; van Hest, J. C. M.; Kouwer, P. H. J., Virus-Like Particles as crosslinkers in fibrous biomimetic hydrogels: Approaches towards capsid rupture and gel repair. *Soft Matter* **2018**.

42. Lavelle, L.; Michel, J.-P.; Gingery, M., The disassembly, reassembly and stability of CCMV protein capsids. *J. Virol. Methods* **2007,** *146* (1–2), 311-316.

43. Fox, J. M.; Wang, G.; Speir, J. A.; Olson, N. H.; Johnson, J. E.; Baker, T. S.; Young, M. J., Comparison of the Native CCMV Virion within VitroAssembled CCMV Virions by Cryoelectron Microscopy and Image Reconstruction. *Virology* **1998,** *244* (1), 212-218.

44. Schoonen, L.; Maas, R. J. M.; Nolte, R. J. M.; van Hest, J. C. M., Expansion of the assembly of cowpea chlorotic mottle virus towards non-native and physiological conditions. *Tetrahedron* **2017,** *73* (33), 4968-4971.

45. Mateu, M. G., Virus engineering: functionalization and stabilization. *Protein Eng. Des. Sel.* **2011,** *24* (1-2), 53-63.

46. Sun, Y.; Yang, C.; Wu, B.; Wang, J.; Qu, S.; Weng, J.; Feng, B., Fabrication of nanostructured M13 bacteriophage films on titanium surfaces. *Mater. Lett.* **2016,** *182*, 39-42.

47. Shukla, S.; Myers, J. T.; Woods, S. E.; Gong, X.; Czapar, A. E.; Commandeur, U.; Huang, A. Y.; Levine, A. D.; Steinmetz, N. F., Plant viral nanoparticles-based HER2 vaccine: Immune response influenced by differential transport, localization and cellular interactions of particulate carriers. *Biomaterials* **2017,** *121*, 15-27.

48. Smith, L. L.; Buckley, R.; Lugar, P., Diagnostic Immunization with Bacteriophage ΦX 174 in Patients with Common Variable Immunodeficiency/Hypogammaglobulinemia. *Front. Immunol.* **2014,** *5* (410).

49. Steinmetz, N. F., Viral nanoparticles as platforms for next-generation therapeutics and imaging devices. *Nanomedicine* **2010,** *6* (5), 634-641.

50. Singh, P.; Prasuhn, D.; Yeh, R. M.; Destito, G.; Rae, C. S.; Osborn, K.; Finn, M. G.; Manchester, M., Bio-distribution, toxicity and pathology of cowpea mosaic virus nanoparticles in vivo. *J. Control. Release* **2007,** *120* (1–2), 41-50.

51. Kaiser, C. R.; Flenniken, M. L.; Gillitzer, E.; Harmsen, A. L.; Harmsen, A. G.; Jutila, M. A.; Douglas, T.; Young, M. J., Biodistribution studies of protein cage nanoparticles demonstrate broad tissue distribution and rapid clearance in vivo. *Int. J. Nanomed.* **2007,** *2* (4), 715.

52. Molenaar, T. J. M.; Michon, I.; de Haas, S. A. M.; van Berkel, T. J. C.; Kuiper, J.; Biessen, E. A. L., Uptake and Processing of Modified Bacteriophage M13 in Mice: Implications for Phage Display. *Virology* **2002,** *293* (1), 182-191.

53. Gulati, N. M.; Pitek, A. S.; Steinmetz, N. F.; Stewart, P. L., Cryo-electron tomography investigation of serum albumin-camouflaged tobacco mosaic virus nanoparticles. *Nanoscale* **2017,** *9* (10), 3408-3415.

54. M. Hooker, J.; P. O'Neil, J.; W. Romanini, D.; E. Taylor, S.; Francis, M. B., Genome-free Viral Capsids as Carriers for Positron Emission Tomography Radiolabels. *Mol Imaging Biol* **2008,** *10* (4), 182-191.

55. Yutin, N.; Makarova, K. S.; Gussow, A. B.; Krupovic, M.; Segall, A.; Edwards, R. A.; Koonin, E. V., Discovery of an expansive bacteriophage family that includes the most abundant viruses from the human gut. *Nat. Microbiol.* **2018,** *3* (1), 38-46.

56. Herelle, F. d., An invisible microbe that is antagonistic to the dysentery bacillus. *C. R. Acad Sci Paris* **1917,** *165*, 373-375.

57. Rohwer, F.; Segall, A. M., In retrospect: A century of phage lessons. *Nature* **2015,** *528* (7580), 46-48.

58. Matsuzaki, S.; Uchiyama, J.; Takemura-Uchiyama, I.; Daibata, M., Perspective: The age of the phage. *Nature* **2014,** *509* (7498), S9-S9.

59. Mao, C. B., Filamentous bacteriophages. In *Brenner's Encyclopedia of Genetics*, Stanley, M.; Kelly, H., Eds. Academic Press: San Diego, 2013; Vol. 1, pp 39-41.

60. Yosef, I.; Manor, M.; Kiro, R.; Qimron, U., Temperate and lytic bacteriophages programmed to sensitize and kill antibiotic-resistant bacteria. *Proc. Natl. Acad. Sci. U. S. A.* **2015,** *112* (23), 7267-7272.

61. Marraffini, L., Crispr-Cas, The Prokaryotic Adaptive Immune System. *FASEB J* **2016,** *30* (1 Supplement), 107.1.

62. Yosef, I.; Manor, M.; Qimron, U., Counteracting selection for antibiotic-resistant bacteria. *Bacteriophage* **2016,** *6* (1), e1096996.

63. Villion, M.; Moineau, S., Virology: Phages hijack a host's defence. *Nature* **2013,** *494* (7438), 433-434.

64. Verbeken, G.; Pirnay, J.; Lavigne, R.; Ceulemans, C.; De Vos, D., Viruses That Can Cure, When Antibiotics Fail…. *J. Microb. Biochem. Technol.* **2016,** *8*, 021-024.

65. Reardon, S., MICROBIOLOGY Phage therapy gets revitalized. *Nature* **2014,** *510* (7503), 15-16.

66. Agnès, K. H., Rock-Archer, A world first: Pherecydes Pharma launches multicenter clinical study of phage therapy in serious burn victims. In *For the first time, an industry-standard clinical trial is evaluating the tolerance and effectiveness of phages in fighting sensitive antibiotic-resistant infections*, Andrew Lloyd & Associates: 2015; pp 1-2.

67. Young, R.; Gill, J. J., Phage therapy redux—What is to be done? *Science* **2015,** *350* (6265), 1163-1164.

68. Sunderland, K.; Yang, M.; Mao, C., Phage-Enabled Nanomedicine: From Probes to Therapeutics in Precision Medicine. *Angew. Chem. Int. Ed.* **2016,** *56*, 1964-1992.

69. Krupovic, M.; Dutilh, B. E.; Adriaenssens, E. M.; Wittmann, J.; Vogensen, F. K.; Sullivan, M. B.; Rumnieks, J.; Prangishvili, D.; Lavigne, R.; Kropinski, A. M.; Klumpp, J.; Gillis, A.; Enault, F.; Edwards, R. A.; Duffy, S.; Clokie, M. R. C.; Barylski, J.; Ackermann, H.-W.; Kuhn, J. H., Taxonomy of prokaryotic viruses: update from the ICTV bacterial and archaeal viruses subcommittee. *Arch. Virol* **2016,** *161* (4), 1095-1099.

70. Kehoe, J. W.; Kay, B. K., Filamentous phage display in the new millennium. *Chemical reviews* **2005,** *105* (11), 4056-72.

71. Samoylova, T. I.; Morrison, N. E.; Globa, L. P.; Cox, N. R., Peptide Phage Display: Opportunities for Development of Personalized Anti-Cancer Strategies. *Anti-Cancer Agents Med. Chem.* **2006,** *6* (1), 9-17.

72. Brigati, J. R.; Samoylova, T. I.; Jayanna, P. K.; Petrenko, V. A., Phage display for generating peptide reagents. *Curr. Protoc. Protein Sci.* **2008,** *51*, 18.9:18.9.1–18.9.27.

73. Deutscher, S. L., Phage Display in Molecular Imaging and Diagnosis of Cancer. *Chem. Rev.* **2010,** *110* (5), 3196-3211.

74. Gray, B. P.; Brown, K. C., Combinatorial Peptide Libraries: Mining for Cell-Binding Peptides. *Chem. Rev.* **2014,** *114* (2), 1020-1081.

75. Sidhu, S. S.; Geyer, C. R., *Phage display in biotechnology and drug discovery*. 2 ed.; CRC Press: Boca Raton, Florida, 2015; Vol. 1.

76. Sagona, A. P.; Grigonyte, A. M.; MacDonald, P. R.; Jaramillo, A., Genetically modified bacteriophages. *Integr. Biol* **2016,** *8* (4), 465-474.

77. Karimi, M.; Mirshekari, H.; Basri, S. M. M.; Bahrami, S.; Moghoofei, M.; Hamblin, M. R., Bacteriophages and phage-inspired nanocarriers for targeted delivery of therapeutic cargos. *Adv. Drug Deliv. Rev* **2016,** *100*, 1-18.

78. Cao, B.; Yang, M.; Mao, C., Phage as a Genetically Modifiable Supramacromolecule in Chemistry, Materials and Medicine. *Acc. Chem. Res* **2016,** *49* (6), 1111-1120.

79. Lee, J.-w.; Song, J.; Hwang, M. P.; Lee, K. H., Nanoscale bacteriophage biosensors beyond phage display. *Int. J. Nanomed.* **2013,** *8*, 3917-3925.

80. Peltomaa, R.; López-Perolio, I.; Benito-Peña, E.; Barderas, R.; Moreno-Bondi, M. C., Application of bacteriophages in sensor development. *Anal. Bioanal. Chem.* **2015,** *408*, 1-24.

81. Huang, H.; Economopoulos, N. O.; Liu, B. A.; Uetrecht, A.; Gu, J.; Jarvik, N.; Nadeem, V.; Pawson, T.; Moffat, J.; Miersch, S.; Sidhu, S. S., Selection of recombinant anti-SH3 domain antibodies by high-throughput phage display. *Protein Sci.* **2015,** *24* (11), 1890-1900.

82. Hobbs, Z.; Abedon, S. T., Diversity of phage infection types and associated terminology: the problem with 'Lytic or lysogenic'. *FEMS Microbiol. Lett.* **2016,** *363* (7), doi.org/10.1093/femsle/fnw047.

83. Oppenheim, A. B.; Adhya, S. L., A new look at bacteriophage λ genetic networks. *J. Bacteriol.* **2007,** *189* (2), 298-304.

84. Hohn, T.; Katsura, I., Structure and Assembly of Bacteriophage Lambda. In *Curr. Top. Microbiol. Immunol.*, Arber, W.; Henle, W.; Hofschneider, P. H.; Humphrey, J. H.; Klein, J.; Koldovský, P.; Koprowski, H.; Maaløe, O.; Melchers, F.; Rott, R.; Schweiger, H. G.; Syruček, L.; Vogt, P. K., Eds. Springer Berlin Heidelberg: Berlin, 1977; Vol. 78, pp 69-110.

85. ACKERS, G. K.; JOHNSON, A. D.; SHEA, M. A., Quantitative model for gene regulation by lambda phage repressor. *Proc. Natl. Acad. Sci. U. S. A.* **1982,** *79*, 1129-1133.

86. Thattai, M.; van Oudenaarden, A., Intrinsic noise in gene regulatory networks. *Proc. Natl. Acad. Sci. U. S. A.* **2001,** *98* (15), 8614-8619.

87. Kobayashi, H.; Kærn, M.; Araki, M.; Chung, K.; Gardner, T. S.; Cantor, C. R.; Collins, J. J., Programmable cells: interfacing natural and engineered gene networks. *Proc. Natl. Acad. Sci. U. S. A.* **2004,** *101* (22), 8414-8419.

88. Reichardt, L. F., Control of bacteriophage lambda repressor synthesis after phage infection: The role of the N, cII, cIII and cro products. *Am. J. Mol. Biol.* **1975,** *93* (2), 267-288.

89. Leptihn, S.; Gottschalk, J.; Kuhn, A., T7 ejectosome assembly: A story unfolds. *Bacteriophage* **2016,** *6* (1), 1-5.

90. Cheng, X.; Zhang, X.; Pflugrath, J. W.; Studier, F. W., The structure of bacteriophage T7 lysozyme, a zinc amidase and an inhibitor of T7 RNA polymerase. *Proc. Natl. Acad. Sci. U. S. A.* **1994,** *91* (9), 4034-4038.

91. Heineman, R. H.; Bull, J. J., TESTING OPTIMALITY WITH EXPERIMENTAL EVOLUTION: LYSIS TIME IN A BACTERIOPHAGE. *Evolution* **2007,** *61* (7), 1695-1709.

92. Rakonjac; Bennett; Julian, Filamentous Bacteriophage: Biology, Phage Display. *Curr. Issues Mol. Biol.* **2011,** *13*, 51-76.

93. Lubkowski, J.; Hennecke, F.; Plückthun, A.; Wlodawer, A., Filamentous phage infection: crystal structure of g3p in complex with its coreceptor, the C-terminal domain of TolA. *Structure* **1999,** *7* (6), 711-722.

94. Russel, M., Filamentous phage assembly. *Mol. Microbiol.* **1991,** *5* (7), 1607-1613.

95. Hassan, F.; Kamruzzaman, M.; Mekalanos, J. J.; Faruque, S. M., Satellite phage TLCϕ enables toxigenic conversion by CTX phage through dif site alteration. *Nature* **2010,** *467*, 982-985.

96. Zenkin, N.; Naryshkina, T.; Kuznedelov, K.; Severinov, K., The mechanism of DNA replication primer synthesis by RNA polymerase. *Nature* **2006,** *439* (439), 617-620.

97. Allison, D.; Ganesan, A.; Olson, A.; Snyder, C.; Mitra, S., Electron microscopic studies of bacteriophage M13 DNA replication. *J. Virol.* **1977,** *24* (2), 673-684.

98. King, A. M.; Adams, M. J.; Lefkowitz, E. J., *Virus taxonomy: ninth report of the International Committee on Taxonomy of Viruses*. Elsevier: London, 2012; Vol. 9.

99. Wadia, J.; Eguchi, A.; Dowdy, S. F., DNA Delivery into Mammalian Cells Using Bacteriophage l Displaying the TAT Transduction Domain. *Cold Spring Harb Protoc* **2014,** *3*, 61-65.

100. Matsko, N.; Klinov, D.; Manykin, A.; Demin, V.; Klimenko, S., Atomic force microscopy analysis of bacteriophages φKZ and T4. *J. Electron Microsc.* **2001,** *50* (5), 417-422.

101. Korehei, R.; Kadla, J. F., Encapsulation of T4 bacteriophage in electrospun poly(ethylene oxide)/cellulose diacetate fibers. *Carbohydr. Polym.* **2014,** *100* (0), 150-157.

102. Hallewell, J.; Niu, Y.; Munns, K.; McAllister, T.; Johnson, R.; Ackermann, H.-W.; Thomas, J.; Stanford, K., Differing Populations of Endemic Bacteriophages in Cattle Shedding High and Low Numbers of Escherichia coli O157: H7 Bacteria in Feces. *Appl. Environ. Microbiol.* **2014,** *80* (13), 3819-3825.

103. Shabani, A.; Marquette, C.; Mandeville, R.; Lawrence, M., Magnetically-assisted impedimetric detection of bacteria using phage-modified carbon microarrays. *Talanta* **2013,** *116*, 1047–1053.

104. Mullaney, J. M.; Black, L. W., Bacteriophage T4 capsid packaging and unpackaging of DNA and proteins. *Methods Mol Biol* **2014,** *1108*, 69-85.

105. Tao, P.; Mahalingam, M.; Marasa, B. S.; Zhang, Z.; Chopra, A. K.; Rao, V. B., In vitro and in vivo delivery of genes and proteins using the bacteriophage T4 DNA packaging machine. *Proc. Natl. Acad. Sci. USA* **2013,** *110* (15), 5846-5851.

106. Serwer, P., Flattening and shrinkage of bacteriophage T7 after preparation for electron microscopy by negative staining. *J. Ultrastruct. Res.* **1977,** *58* (3), 235-243.

107. Zhang, H.; Xu, Y.; Huang, Q.; Yi, C.; Xiao, T.; Li, Q., Natural phage nanoparticle-mediated real-time immuno-PCR for ultrasensitive detection of protein marker. *Chem. Commun.* **2013,** *49* (36), 3778-3780.

108. Miller, S.; Samayoa, E.; Post, L.; Wright, C.; McKinley, G.; Wood, M.; Ching, J., Development and clinical evaluation of a novel fully automated qualitative PCR assay for the diagnosis of anogenital herpes simplex virus infection. *Diagn. Microbiol. Infect. Dis.* **2014,** *80* (0), 102-106.

109. Chen, J.; Alcaine, S. D.; Jiang, Z.; Rotello, V. M.; Nugen, S. R., Detection of Escherichia coli in drinking water using T7 bacteriophage-conjugated magnetic probe. *Anal. Chem.* **2015,** *87* (17), 8977-8984.

110. Zhou, X.; Cao, P.; Zhu, Y.; Lu, W.; Gu, N.; Mao, C., Phage-mediated counting by the naked eye of miRNA molecules at attomolar concentrations in a Petri dish. *Nat. Mater.* **2015,** *14*, 1058–1064.

111. Ackermann, H.-W., Chapter 1 - Bacteriophage Electron Microscopy. *Adv. Virus Res.* **2012,** *82*, 1-32.

112. Kale, A.; Bao, Y.; Zhou, Z.; Prevelige, P. E.; Gupta, A., Directed self-assembly of CdS quantum dots on bacteriophage P22 coat protein templates. *IOP Conf. Ser.: Mater. Sci. Eng.* **2013,** *24*, 1-7.

113. Murugesan, M.; Abbineni, G.; Nimmo, S. L.; Cao, B.; Mao, C., Virus-based Photo-Responsive Nanowires Formed By Linking Site-Directed Mutagenesis and Chemical Reaction. *Sci. Rep.* **2013,** *3*.

114. Mao, C.; Solis, D. J.; Reiss, B. D.; Kottmann, S. T.; Sweeney, R. Y.; Hayhurst, A.; Georgiou, G.; Brent, I.; Belcher, A. M., Virus-Based Toolkit for the Directed Synthesis of Magnetic and Semiconducting Nanowires. *Science* **2004,** *303*, 213-217.

115. Hyunjung, Y.; Debadyuti, G.; Moon-Ho, H.; Jifa, Q.; W., B. P.; S., S. M.; M, B. A., M13 Phage-Functionalized Single-Walled Carbon Nanotubes As Nanoprobes for Second Near-Infrared Window Fluorescence Imaging of Targeted Tumors. *Nano Lett.* **2012,** *12*, 1176−1183.

116. Sreeram, K. J.; Narayan, S.; Abbineni, G.; Hayhurst, A.; Mao, C. B., Architectonics of Phage-Liposome Nanowebs as Optimized Photosensitizer Vehicles for Photodynamic Cancer Therapy. *Mol Cancer Ther* **2010,** *9* (9), 2524-2535.

117. Bar, H.; Yacoby, I.; Benhar, I., Killing cancer cells by targeted drug-carrying phage nanomedicines. *BMC Biotechnol.* **2008,** *8*.

118. Bedi, D.; Musacchio, T.; Fagbohun, O. A.; Gillespie, J. W.; Deinnocentes, P.; Bird, R. C.; Bookbinder, L.; Torchilin, V. P.; Petrenko, V. A., Delivery of siRNA into breast cancer cells via phage fusion protein-targeted liposomes. *Nanomedicine* **2011,** *7*, 315–323.

119. Merzlyak, A.; Indrakanti, S.; Lee, S.-W., Genetically Engineered Nanofiber-Like Viruses For Tissue Regenerating Materials. *Nano Lett.* **2009,** *9* (2), 846-852.

120. Merzlyak, A.; Indrakanti, S.; Seung-Wuk, L., Genetically Engineered Nanofiber-Like Viruses For Tissue Regenerating Materials. *Nano Lett.* **2008,** *9*, 846-852.

121. Kovacs, E. W.; Hooker, J. M.; Romanini, D. W.; Holder, P. G.; Berry, K. E.; Francis, M. B., Dual-Surface-Modified Bacteriophage MS2 as an Ideal Scaffold for a Viral Capsid-Based Drug Delivery System. *Bioconjug. Chem.* **2007,** *18*, 1140-1147.

122. Capehart, S. L.; Coyle, M. P.; Glasgow, J. E.; Francis, M. B., Controlled integration of gold nanoparticles and organic fluorophores using synthetically modified MS2 viral capsids. *J. Am. Chem. Soc.* **2013,** *135* (8), 3011-3016.

123. Tong, G. J.; Hsiao, S. C.; Carrico, Z. M.; Francis, M. B., Viral Capsid DNA Aptamer Conjugates as Multivalent Cell Targeting Vehicles. *J. Am. Chem. Soc.* **2009,** *131* (31), 11174-11178.

124. Xiang, Y.; Morais, M. C.; Battisti, A. J.; Grimes, S.; Jardine, P. J.; Anderson, D. L.; Rossmann, M. G., Structural changes of bacteriophage ϕ29 upon DNA packaging and release. *EMBO J.* **2006,** *25* (21), 5229-5239.

125. Moon, J.-M.; Akin, D.; Xuan, Y.; Ye, P. D.; Guo, P.; Bashir, R., Capture and alignment of phi29 viral particles in sub-40 nanometer porous alumina membranes. *Biomed. Microdevices* **2009,** *11* (1), 135-142.

126. Butcher, S. J.; Bamford, D. H.; Fuller, S. D., DNA packaging orders the membrane of bacteriophage PRD1. *EMBO J.* **1995,** *14* (24), 6078.

127. Jalasvuori, M.; Friman, V.-P.; Nieminen, A.; Bamford, J. K. H.; Buckling, A., Bacteriophage selection against a plasmid-encoded sex apparatus leads to the loss of antibiotic-resistance plasmids. *Biol. Lett. (London, U. K.)* **2011,** *6*, 902–905.

128. Jemal, A.; Bray, F.; Center, M. M.; Ferlay, J.; Ward, E.; Forman, D., Global cancer statistics. *CA: a cancer journal for clinicians* **2011,** *61* (2), 69-90.

129. Siegel, R.; Naishadham, D.; Jemal, A., Cancer statistics, 2013. *CA: a cancer journal for clinicians* **2013,** *63* (1), 11-30.

130. Chen, W. Q.; Zeng, H. M.; Zheng, R. S.; Zhang, S. W.; He, J., Cancer incidence and mortality in china, 2007. *Chinese journal of cancer research = Chung-kuo yen cheng yen chiu* **2012,** *24* (1), 1-8.

131. Painter, J. A.; Hoekstra, R. M.; Ayers, T.; Tauxe, R. V.; Braden, C. R.; Angulo, F. J.; Griffin, P. M., Attribution of foodborne illnesses, hospitalizations, and deaths to food commodities by using outbreak data, United States, 1998–2008. *Emerg. Infect. Dis.* **2013,** *19* (3), 407-415.

132. Hoffmann, S.; Batz, M. B.; Morris Jr, J. G., Annual cost of illness and quality-adjusted life year losses in the United States due to 14 foodborne pathogens. *J. Food Prot.* **2012,** *75* (7), 1292-1302.

133. Nolen, L. D.; Osadebe, L.; Katomba, J.; Likofata, J.; Mukadi, D.; Monroe, B.; Doty, J.; Hughes, C. M.; Kabamba, J.; Malekani, J.; Bomponda, P. L.; Lokota, J. I.; Balilo, M. P.; Likafi, T.; Lushima, R. S.; Ilunga, B. K.; Nkawa, F.; Pukuta, E.; Karhemere, S.; Tamfum, J.-J. M.; Nguete, B.; Wemakoy, E. O.; McCollum, A. M.; Reynolds, M. G., Extended Human-to-Human Transmission during a Monkeypox Outbreak in the Democratic Republic of the Congo. *Emerg. Infect. Dis.* **2016,** *22* (6), 1014-1021.

134. Zhu, M.; Hu, Y.; Li, G.; Ou, W.; Mao, P.; Xin, S.; Wan, Y., Combining magnetic nanoparticle with biotinylated nanobodies for rapid and sensitive detection of influenza H3N2. *Nanoscale Res. Lett.* **2014,** *9* (1), 1-10.

135. Vemula, S. V.; Zhao, J.; Liu, J.; Wang, X.; Biswas, S.; Hewlett, I., Current Approaches for Diagnosis of Influenza Virus Infections in Humans. *Viruses* **2016,** *8* (4), 96-111.

136. McMullen, A. R.; Anderson, N. W.; Burnham, C.-A. D., Pathology Consultation on Influenza Diagnostics. *Am. J. Clin. Pathol.* **2016,** *145* (4), 440-448.

137. Zoni, A. C.; Catalá, L.; Ault, S. K., Schistosomiasis Prevalence and Intensity of Infection in Latin America and the Caribbean Countries, 1942-2014: A Systematic Review in the Context of a Regional Elimination Goal. *PLoS Negl. Trop. Dis.* **2016,** *10* (3), e0004493.

138. Meredith, R. F.; Bueschen, A. J.; Khazaeli, M. B.; Plott, W. E.; Grizzle, W. E.; Wheeler, R. H.; Schlom, J.; Russell, C. D.; Liu, T.; LoBuglio, A. F., Treatment of metastatic prostate carcinoma with radiolabeled antibody CC49. *Journal of nuclear medicine : official publication, Society of Nuclear Medicine* **1994,** *35* (6), 1017-22.

139. Eary, J. F.; Schroff, R. W.; Abrams, P. G.; Fritzberg, A. R.; Morgan, A. C.; Kasina, S.; Reno, J. M.; Srinivasan, A.; Woodhouse, C. S.; Wilbur, D. S.; et al., Successful imaging of malignant melanoma with technetium-99m-labeled monoclonal antibodies. *Journal of nuclear medicine : official publication, Society of Nuclear Medicine* **1989,** *30* (1), 25-32.

140. Wynant, G. E.; Murphy, G. P.; Horoszewicz, J. S.; Neal, C. E.; Collier, B. D.; Mitchell, E.; Purnell, G.; Tyson, I.; Heal, A.; Abdel-Nabi, H.; et al., Immunoscintigraphy of prostatic cancer: preliminary results with 111In-labeled monoclonal antibody 7E11-C5.3 (CYT-356). *The Prostate* **1991,** *18* (3), 229-41.

141. Goldenberg, D. M., Targeted therapy of cancer with radiolabeled antibodies. *Journal of nuclear medicine : official publication, Society of Nuclear Medicine* **2002,** *43* (5), 693-713.

142. Keefe, A. D.; Pai, S.; Ellington, A., Aptamers as therapeutics. *Nature reviews. Drug discovery* **2010,** *9* (7), 537-50.

143. Zhu, G.; Ye, M.; Donovan, M. J.; Song, E.; Zhao, Z.; Tan, W., Nucleic acid aptamers: an emerging frontier in cancer therapy. *Chem. Commun.* **2012,** *48* (85), 10472-80.

144. Zhang, Y.; Hong, H.; Cai, W., Tumor-targeted drug delivery with aptamers. *Curr. Med. Chem.* **2011,** *18* (27), 4185-94.

145. Yang, X.; Zhang, F.; Luo, J.; Pang, J.; Yan, S.; Luo, F.; Liu, J.; Wang, W.; Cui, Y.; Su, X., A new non-muscle-invasive bladder tumor-homing peptide identified by phage display in vivo. *Oncol. Rep.* **2016,** *36* (1), 79-89.

146. Kim, M. J.; Yu, J. H.; Oh, M. H.; Nam, Y. S.; Lee, D. Y., Development of fluorescence-conjugated islet-homing peptide using biopanning for targeted optical imaging of pancreatic islet. *J. Ind. Eng. Chem.* **2017,** *45*, 404-411.

147. Davidson, A. R., Virology: Phages make a group decision. *Nature* **2017,** *541*, 466–467.

148. Boerman, O. C.; Oyen, W. J.; Corstens, F. H., Radio-labeled receptor-binding peptides: a new class of radiopharmaceuticals. *Seminars in nuclear medicine* **2000,** *30* (3), 195-208.

149. Bolhassani, A., Potential efficacy of cell-penetrating peptides for nucleic acid and drug delivery in cancer. *Biochimica et biophysica acta* **2011,** *1816* (2), 232-46.

150. Behr, T. M.; Gotthardt, M.; Barth, A.; Behe, M., Imaging tumors with peptide-based radioligands. *The quarterly journal of nuclear medicine : official publication of the Italian Association of Nuclear Medicine* **2001,** *45* (2), 189-200.

151. Vives, E.; Schmidt, J.; Pelegrin, A., Cell-penetrating and cell-targeting peptides in drug delivery. *Biochimica et biophysica acta* **2008,** *1786* (2), 126-38.

152. Liu, R.; Li, X.; Xiao, W.; Lam, K. S., Tumor-targeting peptides from combinatorial libraries. *Adv. Drug Deliv. Rev.* **2016**, http://doi.org/10.1016/j.addr.2016.05.009.

153. Wang, Y.; Wang, Q.; Wu, A.-h.; Hao, Z.-p.; Liu, X.-j., Isolation of a peptide from Ph.D.-C7C phage display library for detection of Cry1Ab. *Anal. Biochem.* **2017,** *539*, 29-32.

154. Hart, S. L.; Knight, A. M.; Harbottle, R. P.; Mistry, A.; Hunger, H. D.; Cutler, D. F.; Williamson, R.; Coutelle, C., Cell binding and internalization by filamentous phage displaying a cyclic Arg-Gly-Asp-containing peptide. *J. Biol. Chem.* **1994,** *269* (17), 12468-74.

155. Beer, A. J.; Haubner, R.; Sarbia, M.; Goebel, M.; Luderschmidt, S.; Grosu, A. L.; Schnell, O.; Niemeyer, M.; Kessler, H.; Wester, H. J.; Weber, W. A.; Schwaiger, M., Positron emission tomography using [18F]Galacto-RGD identifies the level of integrin alpha(v)beta3 expression in man. *Clinical cancer research : an official journal of the American Association for Cancer Research* **2006,** *12* (13), 3942-9.

156. Pasqualini, R.; Koivunen, E.; Ruoslahti, E., Alpha v integrins as receptors for tumor targeting by circulating ligands. *Nature biotechnology* **1997,** *15* (6), 542-6.

157. Heckmann, D.; Kessler, H., Design and chemical synthesis of integrin ligands. *Methods in enzymology* **2007,** *426*, 463-503.

158. Wang, J.; Yang, M.; Zhu, Y.; Wang, L.; Tomsia, A. P.; Mao, C., Phage Nanofibers Induce Vascularized Osteogenesis in 3D Printed Bone Scaffolds. *Adv. Mater.* **2014,** *26* (29), 4961-4966.

159. Gehlsen, K. R.; Argraves, W. S.; Pierschbacher, M. D.; Ruoslahti, E., Inhibition of in vitro tumor cell invasion by Arg-Gly-Asp-containing synthetic peptides. *The Journal of cell biology* **1988,** *106* (3), 925-30.

160. Pierschbacher, M.; Hayman, E. G.; Ruoslahti, E., Synthetic peptide with cell attachment activity of fibronectin. *Proc. Natl. Acad. Sci. U.S.A.* **1983,** *80* (5), 1224-1227.

161. Garanger, E.; Boturyn, D.; Dumy, P., Tumor targeting with RGD peptide ligands-design of new molecular conjugates for imaging and therapy of cancers. *Anti-cancer agents in medicinal chemistry* **2007,** *7* (5), 552-8.

162. Hynes, R. O., Integrins: bidirectional, allosteric signaling machines. *Cell* **2002,** *110* (6), 673-87.

163. Choi, D. S.; Jin, H.-E.; Yoo, S. Y.; Lee, S.-W., Cyclic RGD Peptide Incorporation on Phage Major Coat Proteins for Improved Internalization by HeLa Cells. *Bioconjug. Chem.* **2014,** *25* (2), 216-223.

164. Kitagawa, T.; Kosuge, H.; Uchida, M.; Iida, Y.; Dalman, R. L.; Douglas, T.; McConnell, M. V., RGD targeting of human ferritin iron oxide nanoparticles enhances in vivo MRI of vascular inflammation and angiogenesis in experimental carotid disease and abdominal aortic aneurysm. *Magn. Reson. Imaging* **2017,** *45* (4), 1144-1153.

165. Smothers, J. F.; Henikoff, S.; Carter, P., Tech.Sight. Phage display. Affinity selection from biological libraries. *Science* **2002,** *298* (5593), 621-2.

166. Kehoe, J. W.; Kay, B. K., Filamentous phage display in the new millennium. *Chemical reviews* **2005,** *105* (11), 4056-72.

167. Dasa, S. S. K.; Seamen, M. E.; French, B. A.; Kelly, K. A., Targeted Delivery of Therapeutic Agents After Myocardial Infarction. *Circulation* **2014,** *130* (Suppl 2), A12105-A12105.

168. Arap, W.; Pasqualini, R.; Ruoslahti, E., Cancer Treatment by Targeted Drug Delivery to Tumor Vasculature in a Mouse Model. *Science* **1998,** *279* (5349), 377-380.

169. Gilmer, D. B.; Schmitz, J. E.; Thandar, M.; Euler, C. W.; Fischetti, V. A., The Phage Lysin PlySs2 Decolonizes Streptococcus suis from Murine Intranasal Mucosa. *PLoS One* **2017,** *12* (1), e0169180.

170. Adhikari, P.; Wen, A. M.; French, R. H.; Parsegian, V. A.; Steinmetz, N. F.; Podgornik, R.; Ching, W.-Y., Electronic structure, dielectric response, and surface charge distribution of RGD (1FUV) peptide. *Sci. Rep.* **2014,** *4*, 5605-5612.

171. Arap, W.; Kolonin, M. G.; Trepel, M.; Lahdenranta, J.; Cardó-Vila, M.; Giordano, R. J.; Mintz, P. J.; Ardelt, P. U.; Yao, V. J.; Vidal, C. I., Steps toward mapping the human vasculature by phage display. *Nature Med.* **2002,** *8* (2), 121-127.

172. Oliner, J.; Min, H.; Leal, J.; Yu, D.; Rao, S.; You, E.; Tang, X.; Kim, H.; Meyer, S.; Han, S. J.; Hawkins, N.; Rosenfeld, R.; Davy, E.; Graham, K.; Jacobsen, F.; Stevenson, S.; Ho, J.; Chen, Q.; Hartmann, T.; Michaels, M.; Kelley, M.; Li, L.; Sitney, K.; Martin, F.; Sun, J.-R.; Zhang, N.; Lu, J.; Estrada, J.; Kumar, R.; Coxon, A.; Kaufman, S.; Pretorius, J.; Scully, S.; Cattley, R.; Payton, M.; Coats, S.; Nguyen, L.; Desilva, B.; Ndifor, A.; Hayward, I.; Radinsky, R.; Boone, T.; Kendall, R., Suppression of angiogenesis and tumor growth by selective inhibition of angiopoietin-2. *Cancer Cell* **2004,** *6* (5), 507-516.

173. Bishop-Hurley, S. L.; Strachan, K. A.; Sutherland, I. A., The application of phage-displayed peptide libraries to ligand detection in eggs and larvae of Rhipicephalus (Boophilus) microplus. *Vet. Parasitol.* **2010,** *173* (1–2), 173-177.

174. Ghosh, A. K.; Ribolla, P. E. M.; Jacobs-Lorena, M., Targeting Plasmodium ligands on mosquito salivary glands and midgut with a phage display peptide library. *Proc. Natl. Acad. Sci. U.S.A.* **2001,** *98* (23), 13278-13281.

175. Liu, Y.; Brindley, P. J.; Zeng, Q.; Li, Y.; Zhou, J.; Chen, Y.; Yang, S.; Zhang, Z.; Liu, B.; Cai, L.; McManus, D. P., Identification of phage display

peptides with affinity for the tegument of Schistosoma japonicum schistosomula. *Mol. Biochem. Parasitol.* **2011,** *180* (2), 86-98.

176. Rhaiem, R. B.; Houimel, M., Targeting Leishmania major parasite with peptides derived from a combinatorial phage display library. *Acta. Trop.* **2016,** *159*, 11-19.

177. Anandakumar, S.; Boosi, K. N.; Bugatha, H.; Padmanabhan, B.; Sadhale, P. P., Phage displayed short peptides against cells of Candida albicans demonstrate presence of species, morphology and region specific carbohydrate epitopes. *PloS One* **2011,** *6* (2), e16868.

178. Wang, Y.; Ju, Z.; Cao, B.; Gao, X.; Zhu, Y.; Qiu, P.; Xu, H.; Pan, P.; Bao, H.; Wang, L.; Mao, C., Ultrasensitive Rapid Detection of Human Serum Antibody Biomarkers by Biomarker-Capturing Viral Nanofibers. *ACS Nano.* **2015,** *9* (4), 4475-4483.

179. Ghadjari, A.; Matthews, R. C.; Burnie, J. P., Epitope mapping Candida albicans proteinase (SAP 2). *FEMS Immunol. Med. Microbiol.* **1997,** *19* (2), 115-123.

180. Kioshima, E. S.; Aliperti, F.; Maricato, J. T.; Mortara, R. A.; Bagagli, E.; Mariano, M.; Lopes, J. D., A synthetic peptide selectively kills only virulent Paracoccidioides brasiliensis yeasts. *Microb. Infect.* **2011,** *13* (3), 251-260.

181. Zhu, M.; Gong, X.; Hu, Y.; Ou, W.; Wan, Y., Streptavidin-biotin-based directional double Nanobody sandwich ELISA for clinical rapid and sensitive detection of influenza H5N1. *J. Transl. Med.* **2014,** *12* (1), 1-10.

182. Gong, X.; Zhu, M.; Li, G.; Lu, X.; Wan, Y., Specific determination of influenza H7N2 virus based on biotinylated single-domain antibody from a phage-displayed library. *Anal. Biochem.* **2016,** *500*, 66-72.

183. Miller, L.; Michel, J.; Vogt, G.; Döllinger, J.; Stern, D.; Piesker, J.; Nitsche, A., Identification and characterization of a phage display-derived peptide for orthopoxvirus detection. *Anal. Bioanal. Chem.* **2014,** *406* (29), 7611-7621.

184. Wang, Q.; Chang, C.-s.; Pennini, M.; Pelletier, M.; Rajan, S.; Zha, J.; Chen, Y.; Cvitkovic, R.; Sadowska, A.; Thompson, J. H.; Lin, H. Y.; Barnes, A.; Rickert, K.; Wilson, S.; Stover, C. K.; Dall'Acqua, W. F.; Chowdhury, P. S.; Xiao, X., Target Agnostic Identification of Functional Monoclonal Antibodies against Klebsiella pneumoniae Multimeric MrkA Fimbrial Subunit. *J. Infect. Dis.* **2016,** *11*, 1-26.

185. Tu, Z.; Chen, Q.; Li, Y.; Xiong, Y.; Xu, Y.; Hu, N.; Tao, Y., Identification and characterization of species-specific nanobodies for the detection of Listeria monocytogenes in milk. *Anal. Biochem.* **2016,** *493*, 1-7.

186. Morton, J.; Karoonuthaisiri, N.; Stewart, L.; Oplatowska, M.; Elliott, C.; Grant, I., Production and evaluation of the utility of novel phage display-derived peptide ligands to Salmonella spp. for magnetic separation. *J. Appl. Microbiol.* **2013,** *115* (1), 271-281.

187. Rao, S. S.; Mohan, K. V. K.; Gao, Y.; Atreya, C. D., Identification and evaluation of a novel peptide binding to the cell surface of Staphylococcus aureus. *Microbiol. Res.* **2013,** *168* (2), 106-112.

188. Ferdosian, M.; Khatami, M. R.; Malekshahi, Z. V.; Mohammadi, A.; Kashani, H. H.; Shooshtari, M. B., Identification of Immunotopes against Mycobacterium leprae as Immune Targets Using PhDTm-12mer Phage Display Peptide Library. *Trop. J. Pharm. Res.* **2015,** *14* (7), 1153-1159.

189. Yang, H.; Sha, W.; Song, P.; Liu, Z.; Qin, L.; Huang, X.; Lu, J.; Wang, J.; Duthie, M. S.; Xiao, H.; Hu, Z., Screening and identification of immunoactive peptide mimotopes for the enhanced serodiagnosis of tuberculosis. *Appl. Microbiol. Biotechnol.* **2016,** *100* (5), 2279-2287.

190. Abbineni, G.; Modali, S.; Safiejko-Mroczka, B.; Petrenko, V. A.; Mao, C., Evolutionary selection of new breast cancer cell-targeting peptides and phages with the cell-targeting peptides fully displayed on the major coat and their effects on actin dynamics during cell internalization. *Molecular pharmaceutics* **2010,** *7* (5), 1629-42.

191. Bartolini, A.; Cardaci, S.; Lamba, S.; Oddo, D.; Marchiò, C.; Cassoni, P.; Amoreo, C. A.; Corti, G.; Testori, A.; Bussolino, F., BCAM and LAMA5 Mediate the Recognition between Tumor Cells and the Endothelium in the Metastatic Spreading of KRAS-Mutant Colorectal Cancer. *Clinical cancer research : an official journal of the American Association for Cancer Research* **2016,** *22* (19), 4923-4933.

192. Zhang, Z.-F.; Shan, X.; Wang, Y.-X.; Wang, W.; Feng, S.-Y.; Cui, Y.-B., Screening and selection of peptides specific for esophageal cancer cells from a phage display peptide library. *J. Cardiothorac. Surg.* **2014,** *9* (1), 1-7.

193. Wang, J.; Liu, Y.; Teesalu, T.; Sugahara, K. N.; Kotamrajua, V. R.; Adams, J. D.; Ferguson, B. S.; Gong, Q.; Oh, S. S.; Csordas, A. T.; Cho, M.; Ruoslahti, E.; Xiao, Y.; Soh, H. T., Selection of phage-displayed peptides on live adherent cells in microfluidic channels. *Proc. Natl. Acad. Sci. U.S.A.* **2011,** *108* (17), 6909-14.

194. Yeh, C.-Y.; Hsiao, J.-K.; Wang, Y.-P.; Lan, C.-H.; Wu, H.-C., Peptide-conjugated nanoparticles for targeted imaging and therapy of prostate cancer. *Biomaterials* **2016,** *99*, 1-15.

195. Zhang, Y.; Chen, J.; Zhang, Y.; Hu, Z.; Hu, D.; Pan, Y.; Ou, S.; Liu, G.; Yin, X.; Zhao, J., Panning and identification of a colon tumor binding peptide from a phage display peptide library. *J. Biomol. Screen.* **2007,** *12* (3), 429-435.

196. Wu, C.; Lo, S. L.; Boulaire, J.; Hong, M. L.; Beh, H. M.; Leung, D. S.; Wang, S., A peptide-based carrier for intracellular delivery of proteins into malignant glial cells in vitro. *Journal of controlled release : official journal of the Controlled Release Society* **2008,** *130* (2), 140-5.

197. Du, B.; Han, H.; Wang, Z.; Kuang, L.; Wang, L.; Yu, L.; Wu, M.; Zhou, Z.; Qian, M., targeted drug delivery to hepatocarcinoma in vivo by phage-displayed specific binding peptide. *Molecular cancer research : MCR* **2010,** *8* (2), 135-44.

198. Robinson, P.; Stuber, D.; Deryckere, F.; Tedbury, P.; Lagrange, M.; Orfanoudakis, G., Identification using phage display of peptides promoting targeting and internalization into HPV-transformed cell lines. *J. Mol. Recogn.* **2005,** *18* (2), 175-82.

199. Rasmussen, U. B.; Schreiber, V.; Schultz, H.; Mischler, F.; Schughart, K., Tumor cell-targeting by phage-displayed peptides. *Cancer gene therapy* **2002,** *9* (7), 606-12.

200. Rittner, K.; Schreiber, V.; Erbs, P.; Lusky, M., Targeting of adenovirus vectors carrying a tumor cell-specific peptide: in vitro and in vivo studies. *Cancer gene therapy* **2007,** *14* (5), 509-18.

201. Askoxylakis, V.; Zitzmann, S.; Mier, W.; Graham, K.; Kramer, S.; von Wegner, F.; Fink, R. H.; Schwab, M.; Eisenhut, M.; Haberkorn, U., Preclinical evaluation of the breast cancer cell-binding peptide, p160. *Clinical cancer research : an official journal of the American Association for Cancer Research* **2005,** *11* (18), 6705-12.

202. Askoxylakis, V.; Mier, W.; Zitzmann, S.; Ehemann, V.; Zhang, J.; Kramer, S.; Beck, C.; Schwab, M.; Eisenhut, M.; Haberkorn, U., Characterization and development of a peptide (p160) with affinity for neuroblastoma cells. *Journal of nuclear medicine : official publication, Society of Nuclear Medicine* **2006,** *47* (6), 981-8.

203. Michelfelder, S.; Lee, M.-K.; deLima-Hahn, E.; Wilmes, T.; Kaul, F.; Müller, O.; Kleinschmidt, J. A.; Trepel, M., Vectors selected from adeno-associated viral display

peptide libraries for leukemia cell–targeted cytotoxic gene therapy. *Exp. Hematol.* **2007,** *35* (12), 1766-1776.

204. Wang, L.; Hu, Y.; Li, W.; Wang, F.; Lu, X.; Han, X.; Lv, J.; Chen, J., Identification of a peptide specifically targeting ovarian cancer by the screening of a phage display peptide library. *Oncol. Lett.* **2016,** *11* (6), 4022-4026.

205. Kang, J.; Zhao, G.; Lin, T.; Tang, S.; Xu, G.; Hu, S.; Bi, Q.; Guo, C.; Sun, L.; Han, S.; Xu, Q.; Nie, Y.; Wang, B.; Liang, S.; Ding, J.; Wu, K., A peptide derived from phage display library exhibits anti-tumor activity by targeting GRP78 in gastric cancer multidrug resistance cells. *Cancer Lett.* **2013,** *339* (2), 247-259.

206. Han, J.; Gao, X.; Duan, W.; Lin, F.; Nie, G.; Xue, Q.; Huang, Y.; Duan, Y.; Wang, Q.; Hou, Y., The further characterization of the peptide specifically binding to gastric cancer. *Mol. Cell Probes* **2016,** *30* (3), 125-131.

207. Zhou, C.; Kang, J.; Wang, X.; Wei, W.; Jiang, W., Phage display screening identifies a novel peptide to suppress ovarian cancer cells in vitro and in vivo in mouse models. *BMC Cancer* **2015,** *15* (1), 1-12.

208. Gross, A. L.; Gillespie, J. W.; Petrenko, V. A., Promiscuous tumor targeting phage proteins. *Protein Eng.* **2016,** *29* (3), 93-103.

209. Lu, S.; Xu, X.; Zhao, W.; Wu, W.; Yuan, H.; Shen, H.; Zhou, C.; Li, L. S.; Ma, L., Targeting of embryonic stem cells by peptide-conjugated quantum dots. *PLoS One* **2010,** *5* (8), e12075.

210. Shao, Z.; Zhang, X.; Pi, Y.; Wang, X.; Jia, Z.; Zhu, J.; Dai, L.; Chen, W.; Yin, L.; Chen, H.; Zhou, C.; Ao, Y., Polycaprolactone electrospun mesh conjugated with an MSC affinity peptide for MSC homing in vivo. *Biomaterials* **2012,** *33* (12), 3375-87.

211. Bignone, P. A.; Krupa, R. A.; West, M. D.; Larocca, D., Selection of Phage Display Peptides Targeting Human Pluripotent Stem Cell-Derived Progenitor Cell Lines. In *Induced Pluripotent Stem (iPS) Cells: Methods and Protocols*, Turksen, K.; Nagy, A., Eds. Springer New York: New York, NY, 2016; Vol. 1, pp 269-283.

212. Caprini, A.; Silva, D.; Zanoni, I.; Cunha, C.; Volontè, C.; Vescovi, A.; Gelain, F., A novel bioactive peptide: assessing its activity over murine neural stem cells and its potential for neural tissue engineering. *N. Biotechnol.* **2013,** *30* (5), 552-562.

213. Bignone, P. A.; Krupa, R. A.; Sternberg, H.; Funk, W. D.; Snyder, E. Y.; West, M. D.; Larocca, D., Identification of human embryonic progenitor cell targeting peptides using phage display. *PLoS One* **2013,** *8* (3), 1-12.

214. Akerman, M. E.; Chan, W. C.; Laakkonen, P.; Bhatia, S. N.; Ruoslahti, E., Nanocrystal targeting in vivo. *Proc. Natl. Acad. Sci. U.S.A.* **2002,** *99* (20), 12617-21.

215. Paasonen, L.; Sharma, S.; Braun, G. B.; Kotamraju, V. R.; Chung, T. D.; She, Z. G.; Sugahara, K. N.; Yliperttula, M.; Wu, B.; Pellecchia, M., New

p32/gC1qR Ligands for Targeted Tumor Drug Delivery. *ChemBioChem* **2016,** *17* (7), 570-575.

216. Zhang, W. J.; Sui, Y. X.; Budha, A.; Zheng, J. B.; Sun, X. J.; Hou, Y. C.; Wang, T. D.; Lu, S. Y., Affinity peptide developed by phage display selection for targeting gastric cancer. *World journal of gastroenterology : WJG* **2012,** *18* (17), 2053-60.

217. Lee, S. M.; Lee, E. J.; Hong, H. Y.; Kwon, M. K.; Kwon, T. H.; Choi, J. Y.; Park, R. W.; Kwon, T. G.; Yoo, E. S.; Yoon, G. S.; Kim, I. S.; Ruoslahti, E.; Lee, B. H., Targeting bladder tumor cells in vivo and in the urine with a peptide identified by phage display. *Molecular cancer research : MCR* **2007,** *5* (1), 11-9.

218. Zhi, M.; Wu, K. C.; Dong, L.; Hao, Z. M.; Deng, T. Z.; Hong, L.; Liang, S. H.; Zhao, P. T.; Qiao, T. D.; Wang, Y.; Xu, X.; Fan, D. M., Characterization of a specific phage-displayed Peptide binding to vasculature of human gastric cancer. *Cancer biology & therapy* **2004,** *3* (12), 1232-5.

219. Lee, K. J.; Lee, J. H.; Chung, H. K.; Ju, E. J.; Song, S. Y.; Jeong, S.-Y.; Choi, E. K., Application of peptide displaying phage as a novel diagnostic probe for human lung adenocarcinoma. *Amino Acids* **2016,** *48*, 1079-1086.

220. Lee, K. J.; Lee, J. H.; Chung, H. K.; Choi, J.; Park, J.; Park, S. S.; Ju, E. J.; Park, J.; Shin, S. H.; Park, H. J.; Ko, E. J.; Suh, N.; Kim, I.; Hwang, J. J.; Song, S. Y.; Jeong, S.-Y.; Choi, E. K., Novel peptides functionally targeting in vivo human lung cancer discovered by in vivo peptide displayed phage screening. *Amino Acids* **2015,** *47* (2), 281-289.

221. Azhdarinia, A.; Daquinag, A. C.; Tseng, C.; Ghosh, S. C.; Ghosh, P.; Amaya-Manzanares, F.; Sevick-Muraca, E.; Kolonin, M. G., A peptide probe for targeted brown adipose tissue imaging. *Nature communications* **2013,** *4*, 2472.

222. Essler, M.; Ruoslahti, E., Molecular specialization of breast vasculature: a breast-homing phage-displayed peptide binds to aminopeptidase P in breast vasculature. *Proc. Natl. Acad. Sci. U.S.A.* **2002,** *99* (4), 2252-7.

223. Hong, H. Y.; Choi, J. S.; Kim, Y. J.; Lee, H. Y.; Kwak, W.; Yoo, J.; Lee, J. T.; Kwon, T. H.; Kim, I. S.; Han, H. S.; Lee, B. H., Detection of apoptosis in a rat model of focal cerebral ischemia using a homing peptide selected from in vivo phage display. *Journal of controlled release : official journal of the Controlled Release Society* **2008,** *131* (3), 167-72.

224. Korbelin, J.; Sieber, T.; Michelfelder, S.; Lunding, L.; Spies, E.; Hunger, A.; Alawi, M.; Rapti, K.; Indenbirken, D.; Muller, O. J.; Pasqualini, R.; Arap, W.; Kleinschmidt, J. A.; Trepel, M., Pulmonary Targeting of Adeno-associated Viral Vectors by Next-generation Sequencing-guided Screening of Random Capsid Displayed Peptide Libraries. *Mol. Ther.* **2016,** *24*, 1-12.

225. Kurabi, A.; Pak, K. K.; Bernhardt, M.; Baird, A.; Ryan, A. F., Discovery of a Biological Mechanism of Active Transport through the Tympanic Membrane to the Middle Ear. *Sci. Rep.* **2016,** *6*, 1-11.

226. Körbelin, J.; Dogbevia, G.; Michelfelder, S.; Ridder, D. A.; Hunger, A.; Wenzel, J.; Seismann, H.; Lampe, M.; Bannach, J.; Pasparakis, M.; Kleinschmidt, J. A.; Schwaninger, M.; Trepel, M., A brain microvasculature endothelial cell-specific viral vector with the potential to treat neurovascular and neurological diseases. *EMBO Mol. Med.* **2016,** *8* (6), 609-625.

227. Choudhury, S. R.; Fitzpatrick, Z.; Harris, A. F.; Maitland, S. A.; Ferreira, J. S.; Zhang, Y.; Ma, S.; Sharma, R. B.; Gray-Edwards, H. L.; Johnson, J. A.; Johnson, A. K.; Alonso, L. C.; Punzo, C.; Wagner, K. R.; Maguire, C. A.; Kotin, R. M.; Martin, D. R.; Sena-Esteves, M., In Vivo Selection Yields AAV-B1 Capsid for Central Nervous System and Muscle Gene Therapy. *Mol. Ther.* **2016,** *24*, 1-11.

228. Ngweniform, P.; Abbineni, G.; Cao, B. R.; Mao, C. B., Self-Assembly of Drug-Loaded Liposomes on Genetically Engineered Target-Recognizing M13 Phage: A Novel Nanocarrier for Targeted Drug Delivery. *Small* **2009,** *5* (17), 1963-1969.

229. Sergeeva, A.; Kolonin, M. G.; Molldrem, J. J.; Pasqualini, R.; Arap, W., Display technologies: Application for the discovery of drug and gene delivery agents. *Adv. Drug Deliv. Rev.* **2006,** *58* (15), 1622-1654.

230. Chung, W.-J.; Kwon, K.-Y.; Song, J.; Lee, S.-W., Evolutionary Screening of Collagen-like Peptides That Nucleate Hydroxyapatite Crystals. *Langmuir* **2011,** *27* (12), 7620-7628.

231. Irving, M. B.; Pan, O.; Scott, J. K., Random-peptide libraries and antigen-fragment libraries for epitope mapping and the development of vaccines and diagnostics. *Current opinion in chemical biology* **2001,** *5* (3), 314-24.

232. Yang, S. H.; Chung, W.-J.; McFarland, S.; Lee, S.-W., Assembly of Bacteriophage into Functional Materials. *Chem. Rec.* **2013,** *13* (1), 43-59.

233. Smith, G. P.; Petrenko, V. A., Phage display. *Chem. Rev.* **1997,** *97* (2), 391-410.

234. Barbas, C. F.; Burton, D. R.; Scott, J. K.; Silverman, G. J., *Phage display: a laboratory manual*. Cold Spring Harbor Laboritory Press: New York, 2001; Vol. 1, p 1-736.

235. Danner, S.; Belasco, J. G., T7 phage display: a novel genetic selection system for cloning RNA-binding proteins from cDNA libraries. *Proc. Natl. Acad. Sci. U.S.A.* **2001,** *98* (23), 12954-9.

236. Willats, W. G., Phage display: practicalities and prospects. *Plant. Mol. Biol.* **2002,** *50* (6), 837-854.

237. Zhou, X.; Cao, P.; Zhu, Y.; Lu, W.; Gu, N.; Mao, C., Phage-mediated counting by the naked eye of miRNA molecules at attomolar concentrations in a Petri dish. *Nat. Mater.* **2015,** *14* (10), 1058-1064.

238. Smith, G. P., Filamentous fusion phage: novel expression vectors that display cloned antigens on the virion surface. *Science* **1985,** *228* (4705), 1315-1317.

239. Yin, L.; Luo, Y.; Liang, B.; Wang, F.; Du, M.; Petrenko, V. A.; Qiu, H.-J.; Liu, A., Specific ligands for classical swine fever virus screened from landscape phage display library. *Antiviral Res.* **2014,** *109*, 68-71.

240. Liu, Y.; Adams, J. D.; Turner, K.; Cochran, F. V.; Gambhir, S. S.; Soh, H. T., Controlling the selection stringency of phage display using a microfluidic device. *Lab on a chip* **2009,** *9* (8), 1033-6.

241. Cung, K.; Slater, R. L.; Cui, Y.; Jones, S. E.; Ahmad, H.; Naik, R. R.; McAlpine, M. C., Rapid, multiplexed microfluidic phage display. *Lab on a chip* **2012,** *12* (3), 562-5.

242. Brinton, L. T.; Bauknight, D. K.; Dasa, S. S. K.; Kelly, K. A., PHASTpep: analysis software for discovery of cell-selective peptides via phage display and next-generation sequencing. *PloS One* **2016,** *11* (5), e0155244.

243. Caberoy, N. B.; Zhou, Y.; Jiang, X.; Alvarado, G.; Li, W., Efficient Identification of Tubby-Binding Proteins by an Improved System of T7 Phage Display. *J. Mol. Recogn.* **2010,** *23* (1), 74–83.

244. Cao, B.; Mao, C., Identification of microtubule-binding domains on microtubule-associated proteins by major coat phage display technique. *Biomacromolecules* **2009,** *10* (3), 555-64.

245. Lee, S. W.; Mao, C.; Flynn, C. E.; Belcher, A. M., Ordering of quantum dots using genetically engineered viruses. *Science* **2002,** *296* (5569), 892-5.

246. McGuire, M. J.; Li, S.; Brown, K. C., Biopanning of phage displayed peptide libraries for the isolation of cell-specific ligands. *Methods Mol Biol* **2009,** *504*, 291-321.

247. Brigati, J. R.; Samoylova, T. I.; Jayanna, P. K.; Petrenko, V. A., Phage display for generating peptide reagents. *Current protocols in protein science / editorial board, John E. Coligan ... [et al.]* **2008,** *51*, 18.9:18.9.1–18.9.27.

248. Dasa, S. S. K.; Xu, Y.; Seaman, M. E.; French, B. A.; Kelly, K. A., Development of Targeted Drug Delivery Agents for Cardiac Regeneration. *Circulation* **2013,** *128* (Suppl 22), A15171-A15171.

249. Gelain, F.; Cigognini, D.; Caprini, A.; Silva, D.; Colleoni, B.; Donega, M.; Antonini, S.; Cohen, B.; Vescovi, A., New bioactive motifs and their use in functionalized self-assembling peptides for NSC differentiation and neural tissue engineering. *Nanoscale* **2012,** *4* (9), 2946-2957.

250. Nadim, M. K.; DiNorcia, J.; Ji, L.; Groshen, S.; Levitsky, J.; Sung, R. S.; Kim, W. R.; Andreoni, K.; Mulligan, D.; Genyk, Y. S., Inequity in organ allocation for patients awaiting liver transplantation: Rationale for uncapping the model for end-stage liver disease. *J. Hepatol.* **2017,** *67*, https://doi.org/10.1016/j.jhep.2017.04.022.

251. Alver, S. K.; Lorenz, D. J.; Washburn, K.; Marvin, M. R.; Brock, G. N., Comparison of two equivalent MELD scores for hepatocellular carcinoma patients using data from the United Network for Organ Sharing liver transplant waiting list registry. *Transpl. Int.* **2017,** *30*, 1098-1109.

252. Peng, D. M.; Qu, Q.; McDonald, N.; Hollander, S. A.; Bernstein, D.; Maeda, K.; Kaufman, B. D.; Rosenthal, D. N.; McElhinney, D. B.; Almond, C. S., Impact of the 18th birthday on waitlist outcomes among young adults listed for heart transplant: A regression discontinuity analysis. *J. Heart Lung Transplant.* **2017,** *36*, https://doi.org/10.1016/j.healun.2017.05.018.

253. Talamantes, E.; Norris, K. C.; Mangione, C. M.; Moreno, G.; Waterman, A. D.; Peipert, J. D.; Bunnapradist, S.; Huang, E., Linguistic Isolation and Access to the Active Kidney Transplant Waiting List in the United States. *Clin. J. Am. Soc. Nephrol.* **2017**, doi: 10.2215/CJN.07150716.

254. Saldaña, R. S.; Schrem, H.; Barthold, M.; Kaltenborn, A., Prognostic Abilities and Quality Assessment of Models for the Prediction of 90-Day Mortality in Liver Transplant Waiting List Patients. *PloS one* **2017,** *12* (1), e0170499.

255. Formica, R. N., Opportunities to Increase Availability of Deceased Donor Kidneys. *Clin. J. Am. Soc. Nephrol.* **2017,** *6*, 974-982.

256. Manook, M.; Koeser, L.; Ahmed, Z.; Robb, M.; Johnson, R.; Shaw, O.; Kessaris, N.; Dorling, A.; Mamode, N., Post-listing survival for highly sensitised patients on the UK kidney transplant waiting list: a matched cohort analysis. *Lancet* **2017,** *389* (10070), 727-734.

257. Mironov, V.; Visconti, R. P.; Kasyanov, V.; Forgacs, G.; Drake, C. J.; Markwald, R. R., Organ printing: Tissue spheroids as building blocks. *Biomaterials* **2009,** *30* (12), 2164-2174.

258. Zhang, Y. S.; Yue, K.; Aleman, J.; Mollazadeh-Moghaddam, K.; Bakht, S. M.; Yang, J.; Jia, W.; Dell'Erba, V.; Assawes, P.; Shin, S. R.; Dokmeci, M. R.; Oklu, R.; Khademhosseini, A., 3D Bioprinting for Tissue and Organ Fabrication. *Ann. Biomed. Eng.* **2017,** *45* (1), 148-163.

259. Pati, F.; Gantelius, J.; Svahn, H. A., 3D bioprinting of tissue/organ models. *Angew. Chem. Int. Ed.* **2016,** *55* (15), 4650-4665.

260. Jang, J.; Park, H.-J.; Kim, S.-W.; Kim, H.; Park, J. Y.; Na, S. J.; Kim, H. J.; Park, M. N.; Choi, S. H.; Park, S. H.; Kim, S. W.; Kwon, S.-M.; Kim, P.-J.; Cho, D.-W., 3D printed complex tissue construct using stem cell-laden decellularized extracellular matrix bioinks for cardiac repair. *Biomaterials* **2017,** *112*, 264-274.

261. Jung, J. W.; Lee, J.-S.; Cho, D.-W., Computer-aided multiple-head 3D printing system for printing of heterogeneous organ/tissue constructs. *Sci. Rep.* **2016,** *6*, 21685.

262. Zhang, W.; Feng, C.; Yang, G.; Li, G.; Ding, X.; Wang, S.; Dou, Y.; Zhang, Z.; Chang, J.; Wu, C.; Jiang, X., 3D-printed scaffolds with synergistic effect of hollow-pipe structure and bioactive ions for vascularized bone regeneration. *Biomaterials* **2017,** *135*, 85-95.

263. Park, J. Y.; Shim, J.-H.; Choi, S.-A.; Jang, J.; Kim, M.; Lee, S. H.; Cho, D.-W., 3D printing technology to control BMP-2 and VEGF delivery spatially and temporally to promote large-volume bone regeneration. *J. Mater. Chem. B* **2015,** *3* (27), 5415-5425.

264. Markstedt, K.; Mantas, A.; Tournier, I.; Martínez Ávila, H.; Hägg, D.; Gatenholm, P., 3D Bioprinting Human Chondrocytes with Nanocellulose–Alginate Bioink for Cartilage Tissue Engineering Applications. *Biomacromolecules* **2015,** *16* (5), 1489-1496.

265. Pati, F.; Jang, J.; Ha, D.-H.; Kim, S. W.; Rhie, J.-W.; Shim, J.-H.; Kim, D.-H.; Cho, D.-W., Printing three-dimensional tissue analogues with decellularized extracellular matrix bioink. *Nature communications* **2014,** *5*, doi:10.1038/ncomms4935.

266. Nakayama, Y.; Takewa, Y.; Sumikura, H.; Yamanami, M.; Matsui, Y.; Oie, T.; Kishimoto, Y.; Arakawa, M.; Ohmuma, K.; Tajikawa, T.; Kanda, K.; Tatsumi, E., In-body tissue-engineered aortic valve (Biovalve type VII) architecture based on 3D printer molding. *J. Biomed. Mater. Res. B Appl. Biomater.* **2015,** *103* (1), 1-11.

267. Pati, F.; Ha, D.-H.; Jang, J.; Han, H. H.; Rhie, J.-W.; Cho, D.-W., Biomimetic 3D tissue printing for soft tissue regeneration. *Biomaterials* **2015,** *62*, 164-175.

268. Lozano, R.; Stevens, L.; Thompson, B. C.; Gilmore, K. J.; Gorkin Iii, R.; Stewart, E. M.; in het Panhuis, M.; Romero-Ortega, M.; Wallace, G. G., 3D printing of layered brain-like structures using peptide modified gellan gum substrates. *Biomaterials* **2015,** *67*, 264-273.

269. Lee, H.; Han, W.; Kim, H.; Ha, D.-H.; Jang, J.; Kim, B. S.; Cho, D.-W., Development of Liver Decellularized Extracellular Matrix Bioink for Three-Dimensional Cell Printing-Based Liver Tissue Engineering. *Biomacromolecules* **2017,** *18* (4), 1229-1237.

270. Zhao, Y.; Yao, R.; Ouyang, L.; Ding, H.; Zhang, T.; Zhang, K.; Cheng, S.; Sun, W., Three-dimensional printing of Hela cells for cervical tumor model in vitro. *Biofabrication* **2014,** *6* (3), 035001.

271. Wang, X.; Li, T.; Ma, H.; Zhai, D.; Jiang, C.; Chang, J.; Wang, J.; Wu, C., A 3D-printed scaffold with MoS2 nanosheets for tumor therapy and tissue regeneration. *NPG Asia Mater.* **2017,** *9*, e376.

272. Laronda, M. M.; Rutz, A. L.; Xiao, S.; Whelan, K. A.; Duncan, F. E.; Roth, E. W.; Woodruff, T. K.; Shah, R. N., A bioprosthetic ovary created using 3D printed microporous scaffolds restores ovarian function in sterilized mice. *Nature communications* **2017,** *8*, 15261.

273. Gross, B. C.; Erkal, J. L.; Lockwood, S. Y.; Chen, C.; Spence, D. M., Evaluation of 3D Printing and Its Potential Impact on Biotechnology and the Chemical Sciences. *Anal. Chem.* **2014,** *86* (7), 3240-3253.

274. Seyed Farid Seyed, S.; Samira, G.; Mehdi, M.; Hooman, Y.; Hendrik Simon Cornelis, M.; Nahrizul Adib, K.; Noor Azuan Abu, O., A review on powder-based additive manufacturing for tissue engineering: selective laser sintering and inkjet 3D printing. *Sci. Technol. Adv. Mater.* **2015,** *16* (3), 033502.

275. Truby, R. L.; Lewis, J. A., Printing soft matter in three dimensions. *Nature* **2016,** *540* (7633), 371-378.

276. Barner-Kowollik, C.; Bastemeyer, M.; Blasco, E.; Patrick, M.; Delaittre, G.; Richter, B.; Wegener, M., 3D Laser Micro- and Nano-Printing: Challenges for Chemistry. *Angew. Chem. Int. Ed.* **2017,** *56*, 15828-15845.

277. Au, A. K.; Huynh, W.; Horowitz, L. F.; Folch, A., 3D-Printed Microfluidics. *Angew. Chem. Int. Ed.* **2016,** *55* (12), 3862-3881.

278. Serra, T.; Planell, J. A.; Navarro, M., High-resolution PLA-based composite scaffolds via 3-D printing technology. *Acta Biomater.* **2013,** *9* (3), 5521-5530.

279. Ripley, B.; Kelil, T.; Cheezum, M. K.; Goncalves, A.; Di Carli, M. F.; Rybicki, F. J.; Steigner, M.; Mitsouras, D.; Blankstein, R., 3D printing based on

cardiac CT assists anatomic visualization prior to transcatheter aortic valve replacement. *J. Cardiovasc. Comput. Tomogr.* **2016,** *10* (1), 28-36.

280. Interactive presurgical simulation applying advanced 3D imaging and modeling techniques for skull base and deep tumors. *J. Neurosurg.* **2013,** *119* (1), 94-105.

281. Gulati, K.; Prideaux, M.; Kogawa, M.; Lima-Marques, L.; Atkins, G. J.; Findlay, D. M.; Losic, D., Anodized 3D–printed titanium implants with dual micro- and nano-scale topography promote interaction with human osteoblasts and osteocyte-like cells. *J. Tissue. Eng. Regen. Med.* **2016**, 10.1002/term.2239.

282. Bose, S.; Vahabzadeh, S.; Bandyopadhyay, A., Bone tissue engineering using 3D printing. *Mater. Today* **2013,** *16* (12), 496-504.

283. Murphy, S. V.; Skardal, A.; Atala, A., Evaluation of hydrogels for bio-printing applications. *J. Biomed Mater Res A* **2013,** *101A* (1), 272-284.

284. Jabbari, E., Bioconjugation of hydrogels for tissue engineering. *Curr. Opin. Biotechnol.* **2011,** *22* (5), 655-660.

285. Stanton, M.; Samitier, J.; Sánchez, S., Bioprinting of 3D hydrogels. *Lab on a chip* **2015,** *15* (15), 3111-3115.

286. Pataky, K.; Braschler, T.; Negro, A.; Renaud, P.; Lutolf, M. P.; Brugger, J., Microdrop Printing of Hydrogel Bioinks into 3D Tissue-Like Geometries. *Adv. Mater.* **2012,** *24* (3), 391-396.

287. Yan, J.; Huang, Y.; Chrisey, D. B., Laser-assisted printing of alginate long tubes and annular constructs. *Biofabrication* **2012,** *5* (1), 015002.

288. Pourchet, L. J.; Thepot, A.; Albouy, M.; Courtial, E. J.; Boher, A.; Blum, L. J.; Marquette, C. A., Human Skin 3D Bioprinting Using Scaffold-Free Approach. *Adv. Healthc. Mater.* **2017,** *6* (4), 1601101-n/a.

289. Tan, Y.; Richards, D. J.; Trusk, T. C.; Visconti, R. P.; Yost, M. J.; Kindy, M. S.; Drake, C. J.; Argraves, W. S.; Markwald, R. R.; Mei, Y., 3D printing facilitated scaffold-free tissue unit fabrication. *Biofabrication* **2014,** *6* (2), 024111.

290. Abbadessa, A.; Blokzijl, M. M.; Mouser, V. H. M.; Marica, P.; Malda, J.; Hennink, W. E.; Vermonden, T., A thermo-responsive and photo-polymerizable chondroitin sulfate-based hydrogel for 3D printing applications. *Carbohydr. Polym.* **2016,** *149*, 163-174.

291. Rezende, R.; Pereira, F.; Kasyanov, V.; Kemmoku, D.; Maia, I.; Da Silva, J.; Mironov, V., Scalable biofabrication of tissue spheroids for organ printing. *Procedia CIRP* **2013,** *5*, 276-281.

292. Rutz, A. L.; Hyland, K. E.; Jakus, A. E.; Burghardt, W. R.; Shah, R. N., A Multimaterial Bioink Method for 3D Printing Tunable, Cell-Compatible Hydrogels. *Adv. Mater.* **2015,** *27* (9), 1607-1614.

293. Chimene, D.; Lennox, K. K.; Kaunas, R. R.; Gaharwar, A. K., Advanced Bioinks for 3D Printing: A Materials Science Perspective. *Ann. Biomed. Eng.* **2016,** *44* (6), 2090-2102.

294. Ouyang, L.; Highley, C. B.; Rodell, C. B.; Sun, W.; Burdick, J. A., 3D Printing of Shear-Thinning Hyaluronic Acid Hydrogels with Secondary Cross-Linking. *ACS Biomater. Sci. Eng.* **2016,** *2* (10), 1743-1751.

295. Highley, C. B.; Prestwich, G. D.; Burdick, J. A., Recent advances in hyaluronic acid hydrogels for biomedical applications. *Curr. Opin. Biotechnol.* **2016,** *40*, 35-40.

296. Hamlet, S. M.; Vaquette, C.; Shah, A.; Hutmacher, D. W.; Ivanovski, S., 3-Dimensional functionalized polycaprolactone-hyaluronic acid hydrogel constructs for bone tissue engineering. *J. Clin. Periodontol.* **2017,** *44* (4), 428-437.

297. Lee, D.-Y.; Lee, H.; Kim, Y.; Yoo, S. Y.; Chung, W.-J.; Kim, G., Phage as versatile nanoink for printing 3-D cell-laden scaffolds. *Acta Biomater.* **2016,** *29*, 112-124.

298. Yang, M.; Sunderland, K.; Mao, C., Virus-Derived Peptides for Clinical Applications. *Chem. Rev.* **2017,** *117* (15), 10377-10402.

299. Sunderland, K. S.; Yang, M.; Mao, C., Phage-Enabled Nanomedicine: From Probes to Therapeutics in Precision Medicine. *Angew. Chem. Int. Ed.* **2017,** *56* (8), 1964-1992.

300. Ursan, I. D.; Chiu, L.; Pierce, A., Three-dimensional drug printing: A structured review. *J. Am. Pharm. Assoc.* **2013,** *53* (2), 136-144.

301. Sandler, N.; Salmela, I.; Fallarero, A.; Rosling, A.; Khajeheian, M.; Kolakovic, R.; Genina, N.; Nyman, J.; Vuorela, P., Towards fabrication of 3D printed medical devices to prevent biofilm formation. *Int. J. Pharm.* **2014,** *459* (1–2), 62-64.

302. Kaully, T.; Kaufman-Francis, K.; Lesman, A.; Levenberg, S., Vascularization—the conduit to viable engineered tissues. *Tissue Eng. Part B Rev.* **2009,** *15* (2), 159-169.

303. Zhao, X.; Liu, L.; Wang, J.; Xu, Y.; Zhang, W.; Khang, G.; Wang, X., In vitro vascularization of a combined system based on a 3D printing technique. *J. Tissue Eng. Regen. Med.* **2016,** *10* (10), 833-842.

304. Wu, W.; DeConinck, A.; Lewis, J. A., Omnidirectional Printing of 3D Microvascular Networks. *Adv. Mater.* **2011,** *23* (24), H178-H183.

305. Xu, C.; Chai, W.; Huang, Y.; Markwald, R. R., Scaffold-free inkjet printing of three-dimensional zigzag cellular tubes. *Biotechnol. Bioeng.* **2012,** *109* (12), 3152-3160.

306. Lee, V. K.; Lanzi, A. M.; Ngo, H.; Yoo, S.-S.; Vincent, P. A.; Dai, G., Generation of Multi-scale Vascular Network System Within 3D Hydrogel Using 3D Bio-printing Technology. *Cell Mol Bioeng* **2014,** *7* (3), 460-472.

307. Zhao, L.; Lee, V. K.; Yoo, S.-S.; Dai, G.; Intes, X., The integration of 3-D cell printing and mesoscopic fluorescence molecular tomography of vascular constructs within thick hydrogel scaffolds. *Biomaterials* **2012,** *33* (21), 5325-5332.

308. Kolesky, D. B.; Truby, R. L.; Gladman, A. S.; Busbee, T. A.; Homan, K. A.; Lewis, J. A., 3D Bioprinting of Vascularized, Heterogeneous Cell-Laden Tissue Constructs. *Adv. Mater.* **2014,** *26* (19), 3124-3130.

309. Lee, V. K.; Kim, D. Y.; Ngo, H.; Lee, Y.; Seo, L.; Yoo, S.-S.; Vincent, P. A.; Dai, G., Creating perfused functional vascular channels using 3D bio-printing technology. *Biomaterials* **2014,** *35* (28), 8092-8102.

310. Heintz, K. A.; Bregenzer, M. E.; Mantle, J. L.; Lee, K. H.; West, J. L.; Slater, J. H., Fabrication of 3D Biomimetic Microfluidic Networks in Hydrogels. *Adv. Healthc. Mater.* **2016,** *5* (17), 2153-2160.

311. Wray, L. S.; Tsioris, K.; Gi, E. S.; Omenetto, F. G.; Kaplan, D. L., Slowly degradable porous silk microfabricated scaffolds for vascularized tissue formation. *Adv. Funct. Mater.* **2013,** *23* (27), 3404-3412.

312. Li, H.; Xue, K.; Kong, N.; Liu, K.; Chang, J., Silicate bioceramics enhanced vascularization and osteogenesis through stimulating interactions between endothelia cells and bone marrow stromal cells. *Biomaterials* **2014,** *35* (12), 3803-3818.

313. Li, H.; Chang, J., Bioactive silicate materials stimulate angiogenesis in fibroblast and endothelial cell co-culture system through paracrine effect. *Acta Biomater.* **2013,** *9* (6), 6981-6991.

314. He, D.; Zhuang, C.; Chen, C.; Xu, S.; Yang, X.; Yao, C.; Ye, J.; Gao, C.; Gou, Z., Rational Design and Fabrication of Porous Calcium–Magnesium Silicate Constructs That Enhance Angiogenesis and Improve Orbital Implantation. *ACS Biomaterials Science & Engineering* **2016,** *2* (9), 1519-1527.

315. Poniatowski; #x141; A., u.; Wojdasiewicz, P.; Gasik, R.; Szukiewicz, D., Transforming Growth Factor Beta Family: Insight into the Role of Growth

Factors in Regulation of Fracture Healing Biology and Potential Clinical Applications. *Mediators Inflamm.* **2015,** *2015*, 17.

316. Martino, M. M.; Briquez, P. S.; Güç, E.; Tortelli, F.; Kilarski, W. W.; Metzger, S.; Rice, J. J.; Kuhn, G. A.; Müller, R.; Swartz, M. A.; Hubbell, J. A., Growth Factors Engineered for Super-Affinity to the Extracellular Matrix Enhance Tissue Healing. *Science* **2014,** *343* (6173), 885-888.

317. Crispim, J. F.; Fu, S. C.; Lee, Y. W.; Fernandes, H. A. M.; Jonkheijm, P.; Yung, P. S. H.; Saris, D. B. F., Bioactive Tape With BMP-2 Binding Peptides Captures Endogenous Growth Factors and Accelerates Healing After Anterior Cruciate Ligament Reconstruction. *Am. J. Sports Med.* **2018,** *46* (12), 2905-2914.

318. Porta, G. D.; Nguyen, B.-N. B.; Campardelli, R.; Reverchon, E.; Fisher, J. P., Synergistic effect of sustained release of growth factors and dynamic culture on osteoblastic differentiation of mesenchymal stem cells. *J. Biomed. Mater. Res. B* **2015,** *103* (6), 2161-2171.

319. Yang, Y.-Q.; Tan, Y.-Y.; Wong, R.; Wenden, A.; Zhang, L.-K.; Rabie, A. B. M., The role of vascular endothelial growth factor in ossification. *Int J Oral Sci* **2012,** *4* (2), 64-68.

320. Nieto-Estévez, V.; Defterali, Ç.; Vicario-Abejón, C., IGF-I: A Key Growth Factor that Regulates Neurogenesis and Synaptogenesis from Embryonic to Adult Stages of the Brain. *Front Neurosci* **2016,** *10* (52).

321. Lee, K.; Silva, E. A.; Mooney, D. J., Growth factor delivery-based tissue engineering: general approaches and a review of recent developments. *J. Royal Soc. Interface* **2011,** *8* (55), 153.

322. Kim, S. E.; Song, S.-H.; Yun, Y. P.; Choi, B.-J.; Kwon, I. K.; Bae, M. S.; Moon, H.-J.; Kwon, Y.-D., The effect of immobilization of heparin and bone morphogenic protein-2 (BMP-2) to titanium surfaces on inflammation and osteoblast function. *Biomaterials* **2011,** *32* (2), 366-373.

323. Poynton, A. R.; Lane, J. M., Safety Profile for the Clinical Use of Bone Morphogenetic Proteins in the Spine. *Spine* **2002,** *27* (16S), S40-S48.

324. Boerman, O. C.; Oyen, W. J.; Corstens, F. H., Radio-labeled receptor-binding peptides: a new class of radiopharmaceuticals. *Seminars in nuclear medicine* **2000,** *30* (3), 195-208.

325. Bolhassani, A., Potential efficacy of cell-penetrating peptides for nucleic acid and drug delivery in cancer. *Biochimica et Biophysica Acta* **2011,** *1816* (2), 232-46.

326. Behr, T. M.; Gotthardt, M.; Barth, A.; Behe, M., Imaging tumors with peptide-based radioligands. *The quarterly journal of nuclear medicine : official publication of the Italian Association of Nuclear Medicine* **2001,** *45* (2), 189-200.

327. Vives, E.; Schmidt, J.; Pelegrin, A., Cell-penetrating and cell-targeting peptides in drug delivery. *Biochimica et Biophysica Acta* **2008,** *1786* (2), 126-38.

328. Liu, R.; Li, X.; Xiao, W.; Lam, K. S., Tumor-targeting peptides from combinatorial libraries. *Advanced Drug Delivery Reviews* **2016**, 13-37.

329. Wang, Y.; Wang, Q.; Wu, A.-h.; Hao, Z.-p.; Liu, X.-j., Isolation of a peptide from Ph.D.-C7C phage display library for detection of Cry1Ab. *Analytical Biochemistry* **2017**, 30113-30116.

330. Yang, M.; Sunderland, K.; Mao, C., Virus-Derived Peptides for Clinical Applications. *Chemical Reviews* **2017,** *117* (15), 10377-10402.

331. Shields, L. B. E.; Raque, G. H.; Glassman, S. D.; Campbell, M.; Vitaz, T.; Harpring, J.; Shields, C. B., Adverse Effects Associated With High-Dose Recombinant Human Bone Morphogenetic Protein-2 Use in Anterior Cervical Spine Fusion. *Spine* **2006,** *31* (5), 542-547.

332. Bragdon, B.; Moseychuk, O.; Saldanha, S.; King, D.; Julian, J.; Nohe, A., Bone Morphogenetic Proteins: A critical review. *Cell. Signal.* **2011,** *23* (4), 609-620.

333. Harth, S.; Kotzsch, A.; Hu, J. L.; Sebald, W.; Mueller, T. D., A Selection Fit Mechanism in BMP Receptor IA as a Possible Source for BMP Ligand-Receptor Promiscuity. *Plos One* **2010,** *5* (9).

334. Heinecke, K.; Seher, A.; Schmitz, W.; Mueller, T. D.; Sebald, W.; Nickel, J., Receptor oligomerization and beyond: a case study in bone morphogenetic proteins. *Bmc Biol* **2009,** *7*, 59.

335. Lavery, K.; Swain, P.; Falb, D.; Alaoui-Ismaili, M. H., BMP-2/4 and BMP-6/7 differentially utilize cell surface receptors to induce osteoblastic differentiation of human bone marrow-derived mesenchymal stem cells. *J. Biol. Chem.* **2008,** *283* (30), 20948-20958.

336. Lowery, J. W.; Pazin, D.; Intini, G.; Kokabu, S.; Chappuis, V.; Capelo, L. P.; Rosen, V., The Role of BMP2 Signaling in the Skeleton. *Crit Rev Eukar Gene* **2011,** *21* (2), 177-185.

337. Knippenberg, M.; Helder, M. N.; Doulabi, B. Z.; Wuisman, P. I. J. M.; Klein-Nulend, J., Osteogenisis versus chondrogenesis by BMP-2 and BMP-7 in adipose stem cells. *Biochem. Biophys. Res. Commun.* **2006,** *342*, 902-908.

338. Saito, A.; Suzuki, Y.; Ogata, S.-i.; Ohtsuki, C.; Tanihar, M., Activation of osteo-progenitor cells by a novel synthetic peptide derived from the bone morphogenetic protein-2 knuckle epitope. *Biochimica et biophysica acta* **2003,** *1651*, 60-67.

339. Bose, S.; Tarafder, S.; Bandyopadhyay, A., Effect of Chemistry on Osteogenesis and Angiogenesis Towards Bone Tissue Engineering Using 3D Printed Scaffolds. *Ann. Biomed. Eng.* **2017,** *45* (1), 261-272.

340. Chen, G. Q.; Deng, C. X.; Li, Y. P., TGF-beta and BMP Signaling in Osteoblast Differentiation and Bone Formation. *Int. J. Biol. Sci.* **2012,** *8* (2), 272-288.

341. Petrenko, V. A.; Smith, G. P.; Gong, X.; Quinn, T., A library of organic landscapes on filamentous phage. *Protein Eng.* **1996,** *9* (9), 797-801.

342. Smith, G. P.; Petrenko, V. A., Phage display. *Chemical Reviews* **1997,** *97* (2), 391-410.

343. Verheust, C.; Pauwels, K.; Mahillon, J.; Helinski, D. R.; Herman, P., Contained use of Bacteriophages: Risk Assessment and Biosafety Recommendations. *Applied Biosafety* **2010,** *15* (1), 32-44.

344. Cao, B. R.; Mao, C. B., Identification of microtubule-binding domains on microtubule-associated proteins by major coat phage display technique. *Biomacromolecules* **2009,** *10* (3), 555-564.

345. Ma, K.; Wang, D. D.; Lin, Y. Y.; Wang, J. L.; Petrenko, V.; Mao, C. B., Synergetic targeted delivery of Sleeping-Beauty transposon system to mesenchymal stem cells using LPD nanoparticles modified with a phage-displayed targeting peptide. *Adv. Funct. Mater.* **2013,** *23* (9), 1172-1181.

346. Whaley, S. R.; English, D. S.; Hu, E. L.; Barbara, P. F.; Belcher, A. M., Selection of peptides with semiconductor binding specificity for directed nanocrystal assembly. *Nature* **2000,** *405* (6787), 665-668.

347. Ahmad, G.; Dickerson, M. B.; Cai, Y.; Jones, S. E.; Ernst, E. M.; Vernon, J. P.; Haluska, M. S.; Fang, Y.; Wang, J.; Subrarnanyarn, G.; Naik, R. R.; Sandhage, K. H., Rapid bioenabled formation of ferroelectric BaTiO3 at room temperature from an aqueous salt solution at near neutral pH. *J. Am. Chem. Soc.* **2008,** *130* (1), 4-5.

348. Lee, J. Y.; Choo, J. E.; Choi, Y. S.; Suh, J. S.; Lee, S. J.; Chung, C. P.; Park, Y. J., Osteoblastic differentiation of human bone marrow stromal cells in self-assembled BMP-2 receptor-binding peptide-amphiphiles. *Biomaterials* **2009,** *30* (21), 3532-3541.

349. Ng, S.; Jafari, M. R.; Derda, R., Bacteriophages and Viruses as a Support for Organic Synthesis and Combinatorial Chemistry. *ACS Chem. Biol.* **2012,** *7* (1), 123-138.

350. Nam, K. T.; Peelle, B. R.; Lee, S.-W.; Belcher, A. M., Genetically Driven Assembly of Nanorings Based on the M13 Virus. *Nano Lett.* **2004,** *4* (1), 23-27.

351. Alberts, E.; Warner, C.; Barnes, E.; Pilkiewicz, K.; Perkins, E.; Poda, A., Genetically tunable M13 phage films utilizing evaporating droplets. *Colloids Surf B Biointerfaces* **2018,** *161*, 210-218.

352. Lee, B. Y.; Zhang, J.; Zueger, C.; Chung, W.-J.; Yoo, S. Y.; Wang, E.; Meyer, J.; Ramesh, R.; Lee, S.-W., Virus-based piezoelectric energy generation. *Nat Nano* **2012,** *7* (6), 351-356.

353. Zhu, H.; Cao, B.; Zhen, Z.; Laxmi, A. A.; Li, D.; Liu, S.; Mao, C., Controlled growth and differentiation of MSCs on grooved films assembled from monodisperse biological nanofibers with genetically tunable surface chemistries. *Biomaterials* **2011,** *32* (21), 4744-4752.

354. Courchesne, N. M. D.; Klug, M. T.; Chen, P. Y.; Kooi, S. E.; Yun, D. S.; Hong, N.; Fang, N. X.; Belcher, A. M.; Hammond, P. T., Assembly of a Bacteriophage-Based Template for the Organization of Materials into Nanoporous Networks. *Adv. Mater.* **2014,** *26* (21), 3398-3404.

355. Tom, S.; Jin, H.-E.; Heo, K.; Lee, S.-W., Engineered phage films as scaffolds for CaCO3 biomineralization. *Nanoscale* **2016,** *8* (34), 15696-15701.

356. Huang, W.; Yang, S.; Shao, J.; Li, Y.-P., Signaling and transcriptional regulation in osteoblast commitment and differentiation. *Front. Biosci.* **2007,** *12*, 3068-3092.

357. Pittenger, M. F.; Mackay, A. M.; Beck, S. C.; Jaiswal, R. K.; Douglas, R.; Mosca, J. D.; Moorman, M. A.; Simonetti, D. W.; Craig, S.; Marshak, D. R., Multilineage Potential of Adult Human Mesenchymal Stem Cells. *Science* **1999,** *284* (5411), 143-147.

358. Chung, W.-J.; Oh, J.-W.; Kwak, K.; Lee, B. Y.; Meyer, J.; Wang, E.; Hexemer, A.; Lee, S.-W., Biomimetic self-templating supramolecular structures. *Nature* **2011,** *478*, 364.

359. Wang, J.; Wang, L.; Yang, M.; Zhu, Y.; Tomsia, A.; Mao, C., Untangling the Effects of Peptide Sequences and Nanotopographies in a Biomimetic Niche for Directed Differentiation of iPSCs by Assemblies of Genetically Engineered Viral Nanofibers. *Nano Letters* **2014,** *14* (12), 6850-6856.

360. Li, C.-J.; Madhu, V.; Balian, G.; Dighe, A. S.; Cui, Q., Cross-Talk Between VEGF and BMP-6 Pathways Accelerates Osteogenic Differentiation of Human Adipose-Derived Stem Cells. *J. Cell. Physiol.* **2015**, 2671-2682.

361. Miyazono, K.; Maeda, S.; Imamura, T., BMP receptor signaling: Transcriptional targets, regulation of signals, and signaling cross-talk. *Cytokine Growth Factor Rev.* **2005,** *16* (3), 251-263.

362. Honda, Y.; Ding, X.; Mussano, F.; Wiberg, A.; Ho, C.-m.; Nishimura, I., Guiding the osteogenic fate of mouse and human mesenchymal stem cells through feedback system control. *Sci. Rep.* **2013,** *3*, 3420.

363. Lin, G. L.; Hankenson, K. D., Integration of BMP, Wnt, and Notch signaling pathways in osteoblast differentiation. *J. Cell. Biochem.* **2011,** *112* (12), 3491-3501.

364. Neelam, J.; E., H. S.; I., C. A.; P., B. S., Osteogenic differentiation of purified, culture expanded human mesenchymal stem cells in vitro. *J. Cell. Biochem.* **1997,** *64* (2), 295-312.

365. Goentoro, L.; Kirschner, M. W., Evidence that Fold-Change, and Not Absolute Level, of β-Catenin Dictates Wnt Signaling. *Mol. Cell* **2009,** *36* (5), 872-884.

366. Wang, Y.; Zhang, X.; Shao, J.; Liu, H.; Liu, X.; Luo, E., Adiponectin regulates BMSC osteogenic differentiation and osteogenesis through the Wnt/β-catenin pathway. *Sci. Rep.* **2017,** *7* (1), 3652.

367. Fujita, K.-i.; Janz, S., Attenuation of WNT signaling by DKK-1 and -2 regulates BMP2-induced osteoblast differentiation and expression of OPG, RANKL and M-CSF. *Mol. Cancer* **2007,** *6* (1), 71.

368. Anja, H.; Sabrina, v. E.; K., S. G.; Anja, B.; Matthias, Z.; Michael, S.; Peter, H.; Petra, K.; Elisabeth, S., The pro-form of BMP-2 interferes with BMP-2 signalling by competing with BMP-2 for IA receptor binding. *FASEB J* **2009,** *276* (21), 6386-6398.

369. Marcus, J.; Johannes, F.; Wiebke, D.; Xinning, L.; C., A. D.; Akos, C.; Christian, P. W.; Sabine, L. H.; Rüdiger, K., Dexamethasone modulates BMP-2 effects on mesenchymal stem cells in vitro. *J. Orthop. Res.* **2008,** *26* (11), 1440-1448.

370. Lysdahl, H. B., Anette ; Foldager, Bindzus; Bünger, Cody, Preconditioning Human Mesenchymal Stem Cells with a Low Concentration of BMP2 Stimulates Proliferation and Osteogenic Differentiation In Vitro. *BioResearch* **2014,** *3* (6).

371. Hironori, H. S., Ohba; Fumiko, Yano; Taku, Saito; Toshiyuki, Ikeda; Keiji, Nakajima; Yuske, Komiyama; Naomi, Nakagata; Kentaro, Suzuki; Tsuyoshi,Takato; Hiroshi, Kawaguchi; Ung-il, Chung, Gli1 Protein Participates in Hedgehog-mediated Specification of Osteoblast Lineage during Endochondral Ossification. *J. Biol. Chem.* **2012,** *287*, 17860-17869.

372. Jong-Seo, L.; M, T. D.; Gabriel, G.; A, C. S.; Shin-ichi, Y.; W, H. P., HES1 Cooperates With pRb to Activate RUNX2-Dependent Transcription. *J. Bone Miner. Res.* **2006,** *21* (6), 921-933.

373. Amy, T.; Melissa, S.; Aaron, B.; Brandon, H.; Julia, D.; An, Z.; Lieve, U.; D., J. E.; Raj, G.; C., M. K., Smad1/5 and Smad4 Expression Are Important for Osteoclast Differentiation. *J. Cell. Biochem.* **2015,** *116* (7), 1350-1360.

374. Chang, S.-F.; Chang, C. A.; Lee, D.-Y.; Lee, P.-L.; Yeh, Y.-M.; Yeh, C.-R.; Cheng, C.-K.; Chien, S.; Chiu, J.-J., Tumor cell cycle arrest induced by shear stress: Roles of integrins and Smad. *Proc. Natl. Acad. Sci. U.S.A.* **2008,** *105* (10), 3927-3932.

375. Kim, J. H.; Liu, X.; Wang, J.; Chen, X.; Zhang, H.; Kim, S. H.; Cui, J.; Li, R.; Zhang, W.; Kong, Y.; Zhang, J.; Shui, W.; Lamplot, J.; Rogers, M. R.; Zhao, C.; Wang, N.; Rajan, P.; Tomal, J.; Statz, J.; Wu, N.; Luu, H. H.; Haydon, R. C.; He, T.-C., Wnt signaling in bone formation and its therapeutic potential for bone diseases. *Ther. Adv. Musculoskelet. Dis.* **2013,** *5* (1), 13-31.

376. Bae, S.; Bessho, Y.; Hojo, M.; Kageyama, R., The bHLH gene Hes6, an inhibitor of Hes1, promotes neuronal differentiation. *Development* **2000,** *127* (13), 2933-2943.

377. Ball, A. J.; Abrahamsson, A. E.; Tyrberg, B.; Itkin-Ansari, P.; Levine, F., HES6 reverses nuclear reprogramming of insulin-producing cells following cell fusion. *Biochem. Biophys. Res. Commun.* **2007,** *355* (2), 331-337.

378. Deatherage, C. L.; Lu, Z.; Kroncke, B. M.; Ma, S.; Smith, J. A.; Voehler, M. W.; McFeeters, R. L.; Sanders, C. R., Structural and biochemical differences between the Notch and the amyloid precursor protein transmembrane domains. *Sci. Adv.* **2017,** *3* (4), e1602794.

379. Gordon, W. R.; Vardar-Ulu, D.; L'Heureux, S.; Ashworth, T.; Malecki, M. J.; Sanchez-Irizarry, C.; McArthur, D. G.; Histen, G.; Mitchell, J. L.; Aster, J. C.; Blacklow, S. C., Effects of S1 Cleavage on the Structure, Surface Export, and Signaling Activity of Human Notch1 and Notch2. *PLoS ONE* **2009,** *4* (8), e6613.

380. Choi, S. H.; Wales, T. E.; Nam, Y.; O'Donovan, D.; Sliz, P.; Engen, J. R.; Blacklow, S. C., Conformational locking upon cooperative assembly of Notch transcription complexes. *Structure(London, England:1993)* **2012,** *20* (2), 340-349.

381. Arnett, K. L.; Hass, M.; McArthur, D. G.; Ilagan, M. X. G.; Aster, J. C.; Kopan, R.; Blacklow, S. C., Structural and Mechanistic Insights into Cooperative Assembly of Dimeric Notch Transcription Complexes. *Nat. Struct. Mol. Biol.* **2010,** *17* (11), 1312-1317.

382. Qi, X.; Schmiege, P.; Coutavas, E.; Li, X., Two Patched molecules engage distinct sites on Hedgehog yielding a signaling-competent complex. *Science* **2018**.

383. Pavletich, N.; Pabo, C., Crystal structure of a five-finger GLI-DNA complex: new perspectives on zinc fingers. *Science* **1993,** *261* (5129), 1701-1707.

384. Du, J.; Hou, S.; Zhong, C.; Lai, Z.; Yang, H.; Dai, J.; Zhang, D.; Wang, H.; Guo, Y.; Ding, J., Molecular Basis of Recognition of Human Osteopontin by 23C3, a Potential Therapeutic Antibody for Treatment of Rheumatoid Arthritis. *J. Mol. Biol.* **2008,** *382* (4), 835-842.

385. Kotzsch, A.; Nickel, J.; Seher, A.; Heinecke, K.; van Geersdaele, L.; Herrmann, T.; Sebald, W.; Mueller, T. D., Structure Analysis of Bone Morphogenetic Protein-2 Type I Receptor Complexes Reveals a Mechanism of Receptor Inactivation in Juvenile Polyposis Syndrome. *J. Biol. Chem.* **2008,** *283* (9), 5876-5887.

386. Qin, B. Y.; Chacko, B. M.; Lam, S. S.; de Caestecker, M. P.; Correia, J. J.; Lin, K., Structural Basis of Smad1 Activation by Receptor Kinase Phosphorylation. *Mol. Cell* **2001,** *8* (6), 1303-1312.

387. Martin-Malpartida, P.; Batet, M.; Kaczmarska, Z.; Freier, R.; Gomes, T.; Aragón, E.; Zou, Y.; Wang, Q.; Xi, Q.; Ruiz, L.; Vea, A.; Márquez, J. A.; Massagué, J.; Macias, M. J., Structural basis for genome wide recognition of 5-bp GC motifs by SMAD transcription factors. *Nature communications* **2017,** *8*, 2070.

388. Pursglove, S. E.; Mackay, J. P., CSL: A notch above the rest. *Int. J. Biochem. Cell Biol.* **2005,** *37* (12), 2472-2477.

389. Yoon, J. W.; Kita, Y.; Frank, D. J.; Majewski, R. R.; Konicek, B. A.; Nobrega, M. A.; Jacob, H.; Walterhouse, D.; Iannaccone, P., Gene Expression Profiling Leads to Identification of GLI1-binding Elements in Target Genes and a Role for Multiple Downstream Pathways in GLI1-induced Cell Transformation. *J. Biol. Chem.* **2002,** *277* (7), 5548-5555.

390. Suresh, S.; Irvine, A. E., The NOTCH signaling pathway in normal and malignant blood cell production. *Cell Commun. Signal.* **2015,** *9* (1), 5-13.

391. Yanmeng, K. M., Ding; Guangyan, Tianp; Haisheng, Guo; Yunyan, Wan; Zhouhong, Yao; Bin, Li; Dianjie, Lin, Overexpression of Numb suppresses

tumor cell growth and enhances sensitivity to cisplatin in epithelioid malignant pleural mesothelioma. *Oncol. Rep.* **2013,** *30* (1), 313-319.

392. Klages, J.; Kotzsch, A.; Coles, M.; Sebald, W.; Nickel, J.; Müller, T.; Kessler, H., The Solution Structure of BMPR-IA Reveals a Local Disorder-to-Order Transition upon BMP-2 Binding. *Biochemistry* **2008,** *47* (46), 11930-11939.

393. Robey, P. G.; Kuznetsov, S. A.; Ren, J.; Klein, H. G.; Sabatino, M.; Stroncek, D. F., Generation of clinical grade human bone marrow stromal cells for use in bone regeneration. *Bone* **2015,** *70* (0), 87-92.

394. Jones, A.; Aarvold, A.; New, A.; Dunlop, D.; Oreffo, R., The treatement of avascular necrosis of the femoral head using impaction bone grafting and skeletal stem cells. *Journal of Bone & Joint Surgery, British Volume* **2012,** *94* (SUPP XVIII), 26-26.

395. Guadilla, J.; Fiz, N.; Andia, I.; Sánchez, M., Arthroscopic management and platelet-rich plasma therapy for avascular necrosis of the hip. *Knee Surgery, Sports Traumatology, Arthroscopy* **2012,** *20* (2), 393-398.

396. Banks, L. N.; Trail, I. A., Local Vascular Bone Graft Reconstruction. In *Disorders of the Hand*, Springer: 2015; pp 153-160.

397. Euler, S. A.; Hengg, C.; Wambacher, M.; Spiegl, U. J.; Kralinger, F., Allogenic bone grafting for augmentation in two-part proximal humeral fracture fixation in a high-risk patient population. *Archives of Orthopaedic and Trauma Surgery* **2015,** *135* (1), 79-87.

398. Health, U. D. o.; Services, H., Bone health and osteoporosis: a report of the Surgeon General. Rockville, MD: US Department of Health and Human Services, Office of the Surgeon General: 2004.

399. Sandler, H., *Inactivity: physiological effects*. Elsevier: 2012.

400. Kaully, T.; Kaufman-Francis, K.; Lesman, A.; Levenberg, S., Vascularization—the conduit to viable engineered tissues. *Tissue Engineering Part B* **2009,** *15* (2), 159-169.

401. Zhao, X.; Liu, L.; Wang, J.; Xu, Y.; Zhang, W.; Khang, G.; Wang, X., In vitro vascularization of a combined system based on a 3D printing technique. *Journal of Tissue Engineering and Regenerative Medicine* **2016,** *10* (10), 833-842.

402. Park, J. Y.; Shim, J.-H.; Choi, S.-A.; Jang, J.; Kim, M.; Lee, S. H.; Cho, D.-W., 3D printing technology to control BMP-2 and VEGF delivery spatially and temporally to promote large-volume bone regeneration. *Journal of Materials Chemistry B* **2015,** *3* (27), 5415-5425.

403. Trombetta, R.; Inzana, J. A.; Schwarz, E. M.; Kates, S. L.; Awad, H. A., 3D Printing of Calcium Phosphate Ceramics for Bone Tissue Engineering and Drug Delivery. *Annals of Biomedical Engineering* **2017,** *45* (1), 23-44.

404. Park, S. A.; Lee, S. H.; Kim, W. D., Fabrication of porous polycaprolactone/hydroxyapatite (PCL/HA) blend scaffolds using a 3D plotting system for bone tissue engineering. *Bioprocess and Biosystems Engineering* **2011,** *34* (4), 505-513.

405. Shim, J.-H.; Lee, J.-S.; Kim, J. Y.; Cho, D.-W., Bioprinting of a mechanically enhanced three-dimensional dual cell-laden construct for osteochondral tissue engineering using a multi-head tissue/organ building system. *Journal of Micromechanics and Microengineering* **2012,** *22* (8), 085014.

406. Meseguer-Olmo, L.; Vicente-Ortega, V.; Alcaraz-Baños, M.; Calvo-Guirado, J. L.; Vallet-Regí, M.; Arcos, D.; Baeza, A., In-vivo behavior of Si-hydroxyapatite/polycaprolactone/DMB scaffolds fabricated by 3D printing. *Journal of Biomedical Materials Research Part A* **2013,** *101A* (7), 2038-2048.

407. Bose, S.; Tarafder, S.; Bandyopadhyay, A., Effect of Chemistry on Osteogenesis and Angiogenesis Towards Bone Tissue Engineering Using 3D Printed Scaffolds. *Annals of Biomedical Engineering* **2017,** *45* (1), 261-272.

408. Chong, W.; Qilong, Z.; Min, W., Cryogenic 3D printing for producing hierarchical porous and rhBMP-2-loaded Ca-P/PLLA nanocomposite scaffolds for bone tissue engineering. *Biofabrication* **2017,** *9* (2), 025031.

409. Rindone, A. N.; Nyberg, E.; Grayson, W. L., 3D-Printing Composite Polycaprolactone-Decellularized Bone Matrix Scaffolds for Bone Tissue Engineering Applications. Walker, J. M., Ed. Humana Press: Totowa, NJ, 2017; Vol. 10.1007/7651_2017_37, pp 1-18.

410. Huifeng, S.; Xiurong, K.; An, L.; Miao, S.; Yong, H.; Xianyan, Y.; Jianzhong, F.; Yanming, L.; Lei, Z.; Guojing, Y.; Sanzhong, X.; Zhongru, G., Bone regeneration in 3D printing bioactive ceramic scaffolds with improved tissue/material interface pore architecture in thin-wall bone defect. *Biofabrication* **2017,** *9* (2), 025003.

411. Wong, K. V.; Hernandez, A., A review of additive manufacturing. *ISRN Mechanical Engineering* **2012,** *2012*, Article ID 208760.

412. Li, J. P.; Habibovic, P.; van den Doel, M.; Wilson, C. E.; de Wijn, J. R.; van Blitterswijk, C. A.; de Groot, K., Bone ingrowth in porous titanium implants produced by 3D fiber deposition. *Biomaterials* **2007,** *28* (18), 2810-2820.

413. Wang, J.; Yang, M.; Zhu, Y.; Wang, L.; Tomsia, A. P.; Mao, C. B., Phage nanofibers induce vascularized osteogenesis in 3D printed bone scaffolds. *Advanced Materials* **2014**, 4961–4966.

414. Verrier, S.; Alini, M.; Alsberg, E.; Buchman, S.; Kelly, D.; Laschke, M.; Menger, M.; Murphy, W.; Stegemann, J.; Schütz, M., Tissue engineering and regenerative approaches to improving the healing of large bone defects. *Eur Cell Mater* **2016,** *32*, 87-110.

415. Minoda, Y.; Yoshida, T.; Sugimoto, K.; Baba, S.; Ikebuchi, M.; Nakamura, H., Detection of Small Periprosthetic Bone Defects after Total Knee Arthroplasty. *J. Arthroplasty* **2014,** *29* (12), 2280-2284.

416. Clark, P. A.; Rodriguez, A.; Sumner, D. R.; Hussain, M. A.; Mao, J. J., Modulation of bone ingrowth of rabbit femur titanium implants by in vivo axial micromechanical loading. *Journal of Applied Physiology* **2005,** *98* (5), 1922.

417. Ma, L.; Zhou, Y.; Zhu, Y.; Lin, Z.; Chen, L.; Zhang, Y.; Xia, H.; Mao, C., 3D printed personalized titanium plates improve clinical outcome in microwave ablation of bone tumors around the knee. *Sci. Rep.* **2017,** *7* (1), 7626.

418. Maleksaeedi, S.; Wang, J. K.; El-Hajje, A.; Harb, L.; Guneta, V.; He, Z.; Wiria, F. E.; Choong, C.; Ruys, A. J., Toward 3D Printed Bioactive Titanium Scaffolds with Bimodal Pore Size Distribution for Bone Ingrowth. *Procedia CIRP* **2013,** *5* (Supplement C), 158-163.

419. Asa; #x; ad, F.; Pagni, G.; Pilipchuk, S. P.; Giann; #xec; , A. B.; Giannobile, W. V.; Rasperini, G., 3D-Printed Scaffolds and Biomaterials: Review of Alveolar Bone Augmentation and Periodontal Regeneration Applications. *Int. J. Dent.* **2016,** *2016*, 15.

420. Wingender, B.; Bradley, P.; Saxena, N.; Ruberti, J. W.; Gower, L., Biomimetic organization of collagen matrices to template bone-like microstructures. *Matrix Biol.* **2016,** *52-54*, 384-396.

421. Boyde, A.; Hobdell, M. H., Scanning electron microscopy of lamellar bone. *Z Zellforsch Mikrosk Anat* **1968,** *93* (2), 213-231.

422. Alexander, B.; Daulton, T. L.; Genin, G. M.; Lipner, J.; Pasteris, J. D.; Wopenka, B.; Thomopoulos, S., The nanometre-scale physiology of bone: steric modelling and scanning transmission electron microscopy of collagen–mineral structure. *J. Royal Soc. Interface* **2012**.

423. Lee, J. Y.; Chung, J.; Chung, W.-J.; Kim, G., Fabrication and in vitro biocompatibilities of fibrous biocomposites consisting of PCL and M13 bacteriophage-conjugated alginate for bone tissue engineering. *J. Mater. Chem. B* **2016,** *4* (4), 656-665.

424. Deville, S.; Saiz, E.; Tomsia, A. P., Freeze casting of hydroxyapatite scaffolds for bone tissue engineering. *Biomaterials* **2006,** *27* (32), 5480-5489.

425. Tang, Y.; Zhao, K.; Hu, L.; Wu, Z., Two-step freeze casting fabrication of hydroxyapatite porous scaffolds with bionic bone graded structure. *Ceram. Int.* **2013,** *39* (8), 9703-9707.

426. Weiner, S.; Traub, W.; Wagner, H. D., Lamellar Bone: Structure–Function Relations. *J. Struct. Biol.* **1999,** *126* (3), 241-255.

427. Deligianni, D. D.; Katsala, N.; Ladas, S.; Sotiropoulou, D.; Amedee, J.; Missirlis, Y. F., Effect of surface roughness of the titanium alloy Ti–6Al–4V on human bone marrow cell response and on protein adsorption. *Biomaterials* **2001,** *22* (11), 1241-1251.

428. Heinl, P.; Müller, L.; Körner, C.; Singer, R. F.; Müller, F. A., Cellular Ti–6Al–4V structures with interconnected macro porosity for bone implants fabricated by selective electron beam melting. *Acta Biomater.* **2008,** *4* (5), 1536-1544.

429. Waschkies, T.; Oberacker, R.; Hoffmann, M. J., Investigation of structure formation during freeze-casting from very slow to very fast solidification velocities. *Acta Mater.* **2011,** *59* (13), 5135-5145.

430. X., W.; J., Z.; Q., P.; D., L. Y., Liquid–Solid–Solution Synthesis of Biomedical Hydroxyapatite Nanorods. *Adv Mater* **2006,** *18* (15), 2031-2034.

431. Morgan, E. F.; Unnikrisnan, G. U.; Hussein, A. I., Bone Mechanical Properties in Healthy and Diseased States. *Annu. Rev. Biomed. Eng.* **2018,** *20* (1), 119-143.

432. Rungby, J.; Kassem, M.; Eriksen, E. F.; Danscher, G., The von Kossa reaction for calcium deposits: silver lactate staining increases sensitivity and reduces background. *Histochem. J.* **1993,** *25* (6), 446-451.

Appendix: List of Copyrights and Permissions

JOHN WILEY AND SONS LICENSE TERMS AND CONDITIONS

Sep 19, 2018

This Agreement between Kegan S Sunderland ("You") and John Wiley and Sons ("John Wiley and Sons") consists of your license details and the terms and conditions provided by John Wiley and Sons and Copyright Clearance Center.

License Number	4432560234317
License date	Sep 19, 2018
Licensed Content Publisher	John Wiley and Sons
Licensed Content Publication	Angewandte Chemie International Edition
Licensed Content Title	Phage-Enabled Nanomedicine: From Probes to Therapeutics in Precision Medicine
Licensed Content Author	Kegan S. Sunderland, Mingying Yang, Chuanbin Mao
Licensed Content Date	Jan 24, 2017
Licensed Content Volume	56
Licensed Content Issue	8
Licensed Content Pages	29
Type of Use	Dissertation/Thesis
Requestor type	Author of this Wiley article
Format	Print and electronic
Portion	Full article
Will you be translating?	No
Title of your thesis / dissertation	VIRUS-SELECTED OSTEOGENESIS-INDUCING PEPTIDES FOR ENHANCED BONE REGENERATION IN 3D PRINTED TITANIUM ALLOY IMPLANTS
Expected completion date	Dec 2018
Expected size (number of pages)	200

Requestor Location	Kegan S Sunderland 101 Stephenson Parkway, Room 3310 Norman, OK 73019-5300 NORMAN, OK 73019 United States Attn: Kegan S Sunderland
Publisher Tax ID	EU826007151
Total	**0.00 USD**

Terms and Conditions

TERMS AND CONDITIONS

This copyrighted material is owned by or exclusively licensed to John Wiley & Sons, Inc. or one of its group companies (each a"Wiley Company") or handled on behalf of a society with which a Wiley Company has exclusive publishing rights in relation to a particular work (collectively "WILEY"). By clicking "accept" in connection with completing this licensing transaction, you agree that the following terms and conditions apply to this transaction (along with the billing and payment terms and conditions established by the Copyright Clearance Center Inc., ("CCC's Billing and Payment terms and conditions"), at the time that you opened your RightsLink account (these are available at any time at http://myaccount.copyright.com).

Terms and Conditions

- The materials you have requested permission to reproduce or reuse (the "Wiley Materials") are protected by copyright.

- You are hereby granted a personal, non-exclusive, non-sub licensable (on a stand-alone basis), non-transferable, worldwide, limited license to reproduce the Wiley Materials for the purpose specified in the licensing process. This license, **and any CONTENT (PDF or image file) purchased as part of your order,** is for a one-time use only and limited to any maximum distribution number specified in the license. The first instance of republication or reuse granted by this license must be completed within two years of the date of the grant of this license (although copies prepared before the end date may be distributed thereafter). The Wiley Materials shall not be used in any other manner or for any other purpose, beyond what is granted in the license. Permission is granted subject to an appropriate acknowledgement given to the author, title of the material/book/journal and the publisher. You shall also duplicate the copyright notice that appears in the Wiley publication in your use of the Wiley Material. Permission is also granted on the understanding that nowhere in the text is a previously published source acknowledged for all or part of this Wiley Material. Any third party content is expressly excluded from this permission.

- With respect to the Wiley Materials, all rights are reserved. Except as expressly granted by the terms of the license, no part of the Wiley Materials may be copied, modified, adapted (except for minor reformatting required by the new Publication), translated, reproduced, transferred or distributed, in any form or by any means, and no derivative works may be made based on the Wiley Materials without the prior permission of the respective copyright owner.**For STM Signatory Publishers clearing permission under the terms of the STM Permissions Guidelines only, the terms of the license are extended to include subsequent editions and for editions in other languages, provided such editions are for the work as a whole in situ and does not involve the separate exploitation of the permitted figures or extracts,** You may not alter, remove or suppress in any manner any copyright, trademark or other notices displayed by the Wiley Materials. You may not license, rent, sell, loan, lease, pledge, offer as security, transfer or assign the Wiley Materials on a stand-alone basis, or any of the rights granted to you hereunder to any other person.

- The Wiley Materials and all of the intellectual property rights therein shall at all times remain the exclusive property of John Wiley & Sons Inc, the Wiley Companies, or their respective licensors, and your interest therein is only that of having possession of and the right to reproduce the Wiley Materials pursuant to Section 2 herein during the continuance of this Agreement. You agree that you

own no right, title or interest in or to the Wiley Materials or any of the intellectual property rights therein. You shall have no rights hereunder other than the license as provided for above in Section 2. No right, license or interest to any trademark, trade name, service mark or other branding ("Marks") of WILEY or its licensors is granted hereunder, and you agree that you shall not assert any such right, license or interest with respect thereto

- NEITHER WILEY NOR ITS LICENSORS MAKES ANY WARRANTY OR REPRESENTATION OF ANY KIND TO YOU OR ANY THIRD PARTY, EXPRESS, IMPLIED OR STATUTORY, WITH RESPECT TO THE MATERIALS OR THE ACCURACY OF ANY INFORMATION CONTAINED IN THE MATERIALS, INCLUDING, WITHOUT LIMITATION, ANY IMPLIED WARRANTY OF MERCHANTABILITY, ACCURACY, SATISFACTORY QUALITY, FITNESS FOR A PARTICULAR PURPOSE, USABILITY, INTEGRATION OR NON-INFRINGEMENT AND ALL SUCH WARRANTIES ARE HEREBY EXCLUDED BY WILEY AND ITS LICENSORS AND WAIVED BY YOU.

- WILEY shall have the right to terminate this Agreement immediately upon breach of this Agreement by you.

- You shall indemnify, defend and hold harmless WILEY, its Licensors and their respective directors, officers, agents and employees, from and against any actual or threatened claims, demands, causes of action or proceedings arising from any breach of this Agreement by you.

- IN NO EVENT SHALL WILEY OR ITS LICENSORS BE LIABLE TO YOU OR ANY OTHER PARTY OR ANY OTHER PERSON OR ENTITY FOR ANY SPECIAL, CONSEQUENTIAL, INCIDENTAL, INDIRECT, EXEMPLARY OR PUNITIVE DAMAGES, HOWEVER CAUSED, ARISING OUT OF OR IN CONNECTION WITH THE DOWNLOADING, PROVISIONING, VIEWING OR USE OF THE MATERIALS REGARDLESS OF THE FORM OF ACTION, WHETHER FOR BREACH OF CONTRACT, BREACH OF WARRANTY, TORT, NEGLIGENCE, INFRINGEMENT OR OTHERWISE (INCLUDING, WITHOUT LIMITATION, DAMAGES BASED ON LOSS OF PROFITS, DATA, FILES, USE, BUSINESS OPPORTUNITY OR CLAIMS OF THIRD PARTIES), AND WHETHER OR NOT THE PARTY HAS BEEN ADVISED OF THE POSSIBILITY OF SUCH DAMAGES. THIS LIMITATION SHALL APPLY NOTWITHSTANDING ANY FAILURE OF ESSENTIAL PURPOSE OF ANY LIMITED REMEDY PROVIDED HEREIN.

- Should any provision of this Agreement be held by a court of competent jurisdiction to be illegal, invalid, or unenforceable, that provision shall be deemed amended to achieve as nearly as possible the same economic effect as the original provision, and the legality, validity and enforceability of the remaining provisions of this Agreement shall not be affected or impaired thereby.

- The failure of either party to enforce any term or condition of this Agreement shall not constitute a waiver of either party's right to enforce each and every term and condition of this Agreement. No breach under this agreement shall be deemed waived or excused by either party unless such waiver or consent is in writing signed by the party granting such waiver or consent. The waiver by or consent of a party to a breach of any provision of this Agreement shall not operate or be construed as a waiver of or consent to any other or subsequent breach by such other party.

- This Agreement may not be assigned (including by operation of law or otherwise) by you without WILEY's prior written consent.

- Any fee required for this permission shall be non-refundable after thirty (30) days from receipt by the CCC.

- These terms and conditions together with CCC's Billing and Payment terms and conditions (which are incorporated herein) form the entire agreement between you and WILEY concerning this licensing transaction and (in the absence of fraud) supersedes all prior agreements and representations of the parties, oral or written. This Agreement may not be amended except in writing

signed by both parties. This Agreement shall be binding upon and inure to the benefit of the parties' successors, legal representatives, and authorized assigns.

- In the event of any conflict between your obligations established by these terms and conditions and those established by CCC's Billing and Payment terms and conditions, these terms and conditions shall prevail.

- WILEY expressly reserves all rights not specifically granted in the combination of (i) the license details provided by you and accepted in the course of this licensing transaction, (ii) these terms and conditions and (iii) CCC's Billing and Payment terms and conditions.

- This Agreement will be void if the Type of Use, Format, Circulation, or Requestor Type was misrepresented during the licensing process.

- This Agreement shall be governed by and construed in accordance with the laws of the State of New York, USA, without regards to such state's conflict of law rules. Any legal action, suit or proceeding arising out of or relating to these Terms and Conditions or the breach thereof shall be instituted in a court of competent jurisdiction in New York County in the State of New York in the United States of America and each party hereby consents and submits to the personal jurisdiction of such court, waives any objection to venue in such court and consents to service of process by registered or certified mail, return receipt requested, at the last known address of such party.

WILEY OPEN ACCESS TERMS AND CONDITIONS

Wiley Publishes Open Access Articles in fully Open Access Journals and in Subscription journals offering Online Open. Although most of the fully Open Access journals publish open access articles under the terms of the Creative Commons Attribution (CC BY) License only, the subscription journals and a few of the Open Access Journals offer a choice of Creative Commons Licenses. The license type is clearly identified on the article.

The Creative Commons Attribution License

The Creative Commons Attribution License (CC-BY) allows users to copy, distribute and transmit an article, adapt the article and make commercial use of the article. The CC-BY license permits commercial and non-

Creative Commons Attribution Non-Commercial License

The Creative Commons Attribution Non-Commercial (CC-BY-NC)License permits use, distribution and reproduction in any medium, provided the original work is properly cited and is not used for commercial purposes.(see below)

Creative Commons Attribution-Non-Commercial-NoDerivs License

The Creative Commons Attribution Non-Commercial-NoDerivs License (CC-BY-NC-ND) permits use, distribution and reproduction in any medium, provided the original work is properly cited, is not used for commercial purposes and no modifications or adaptations are made. (see below)

Use by commercial "for-profit" organizations

Use of Wiley Open Access articles for commercial, promotional, or marketing purposes requires further explicit permission from Wiley and will be subject to a fee.

Further details can be found on Wiley Online Library http://olabout.wiley.com/WileyCDA/Section/id-410895.html

Other Terms and Conditions:

v1.10 Last updated September 2015

Questions? customercare@copyright.com or +1-855-239-3415 (toll free in the US) or +1-978-646-2777.



PERMISSION/LICENSE IS GRANTED FOR YOUR ORDER AT NO CHARGE

This type of permission/license, instead of the standard Terms & Conditions, is sent to you because no fee is being charged for your order. Please note the following:

- Permission is granted for your request in both print and electronic formats, and translations.
- If figures and/or tables were requested, they may be adapted or used in part.
- Please print this page for your records and send a copy of it to your publisher/graduate school.
- Appropriate credit for the requested material should be given as follows: "Reprinted (adapted) with permission from (COMPLETE REFERENCE CITATION). Copyright (YEAR) American Chemical Society." Insert appropriate information in place of the capitalized words.
- One-time permission is granted only for the use specified in your request. No additional uses are granted (such as derivative works or other editions). For any other uses, please submit a new request.

BACK CLOSE WINDOW

Copyright © 2018 Copyright Clearance Center, Inc. All Rights Reserved. Privacy statement. Terms and Conditions.
Comments? We would like to hear from you. E-mail us at customercare@copyright.com

IACUC Approval

The University of Oklahoma

INSTITUTIONAL ANIMAL CARE AND USE COMMITTEE

August 24, 2017

Dr. Chuanbin Mao
University of Oklahoma
Department of Chemistry and Biochemistry

Dear Dr. Mao,

Your IACUC protocol entitled **"Bone Regeneration by Bionanofiber-based Bone Substitutes"** has been approved by Institutional Animal Care and Use Committee. This protocol has been assigned tracking number **R17-028**. Please refer to this number in all correspondence related to this protocol. The protocol is approved for a period the three years and expires **24 August, 2020**. You will need to provide an annual report within 60 days of the first and second anniversaries of this approval. Prior to those due dates, my office will send a reminder and a copy of the annual report form. If you have any changes to this protocol in research personnel, type of number of animals used, methods that may cause pain or distress, or methods of anesthesia, analgesia or euthanasia, please submit a request for a protocol amendment prior to implementing these changes. The amendment form is available on the website www.iacuc.ou.edu.

The University of Oklahoma has an Animal Welfare Assurance on file with the Office of Laboratory Animal Welfare under assurance number: D16-00153 (A3240-01), which is in effect through 30 June, 2021; and the institution is registered as a research facility with USDA (Certificate Number 73-R-0100) through March 2019.

Sincerely,

Dr. Eli S. Bridge
Chair, Institutional Animal Care and Use Committee

Cc: Glen S. Krutz (Institutional Officer)
LAR office
Jennie Parker (Office of Research Services)

Oklahoma Biological Survey, 111 E. Chesapeake Street, Norman, Oklahoma 73019-6121 PHONE: (405) 325-2658 FAX: (405) 325-7702

Supplemental Data

1 way ANOVA for BMPR1A				
Number of families	1			
Number of comparisons per family	21			
Alpha	0.05			
Tukey's multiple comparisons test	Mean Diff.	95% CI of diff.	Significant?	Summary
VHVPLHRGAVSA vs. SGTQDSMVGWNK	0.02425	-0.1237 to 0.1722	No	ns
VHVPLHRGAVSA vs. Wild Type	0.3808	0.2328 to 0.5287	Yes	****
VHVPLHRGAVSA vs. TAKYLPMRPGPL	0.1243	-0.02371 to 0.2722	No	ns
VHVPLHRGAVSA vs. DYHDPSLPTLRK	0.287	0.1390 to 0.4350	Yes	****
VHVPLHRGAVSA vs. GNNPLHVHHDKR	0.3803	0.2323 to 0.5282	Yes	****
VHVPLHRGAVSA vs. NAKYPTMRPGPL	0.3	0.1520 to 0.4480	Yes	****
SGTQDSMVGWNK vs. Wild Type	0.3565	0.2085 to 0.5045	Yes	****
SGTQDSMVGWNK vs. TAKYLPMRPGPL	0.1	-0.04796 to 0.2480	No	ns
SGTQDSMVGWNK vs. DYHDPSLPTLRK	0.2628	0.1148 to 0.4107	Yes	***
SGTQDSMVGWNK vs. GNNPLHVHHDKR	0.356	0.2080 to 0.5040	Yes	****
SGTQDSMVGWNK vs. NAKYPTMRPGPL	0.2758	0.1278 to 0.4237	Yes	****
Wild Type vs. TAKYLPMRPGPL	-0.2565	-0.4045 to -0.1085	Yes	***
Wild Type vs. DYHDPSLPTLRK	-0.09375	-0.2417 to 0.05421	No	ns
Wild Type vs. GNNPLHVHHDKR	-0.0005	-0.1485 to 0.1475	No	ns
Wild Type vs. NAKYPTMRPGPL	-0.08075	-0.2287 to 0.06721	No	ns
TAKYLPMRPGPL vs. DYHDPSLPTLRK	0.1628	0.01479 to 0.3107	Yes	*
TAKYLPMRPGPL vs. GNNPLHVHHDKR	0.256	0.1080 to 0.4040	Yes	***
TAKYLPMRPGPL vs. NAKYPTMRPGPL	0.1758	0.02779 to 0.3237	Yes	*
DYHDPSLPTLRK vs. GNNPLHVHHDKR	0.09325	-0.05471 to 0.2412	No	ns
DYHDPSLPTLRK vs. NAKYPTMRPGPL	0.013	-0.1350 to 0.1610	No	ns
GNNPLHVHHDKR vs. NAKYPTMRPGPL	-0.08025	-0.2282 to 0.06771	No	ns

1 way ANOVA for BMPR2				
Number of families	1			
Number of comparisons per family	3			
Alpha	0.05			
Tukey's multiple comparisons test	Mean Diff.	95% CI of diff.	Significant?	Summary
RDYHPRDHTATW vs. SGTQDSMVGWNK	-0.00125	-0.1749 to 0.1724	No	ns
RDYHPRDHTATW vs. Wild Type	0.3325	0.1589 to 0.5061	Yes	**
SGTQDSMVGWNK vs. Wild Type	0.3338	0.1601 to 0.5074	Yes	**

Supplementary Table 11. ANOVA statistical significance report corresponding to the ELISA data in Figure 10 (n=4 for all samples). The calculations were done using Prism software.

1 way ANOVA for Alamar Blue 41 Hours

Number of families	1			
Number of comparisons per family	21			
Alpha	0.05			
Tukey's multiple comparisons test	Mean Diff.	95% CI of diff.	Significant?	Summary
Positive Control vs. KRTGQYKLGSKTGPGQK	0.09536	0.02471 to 0.1660	Yes	**
Positive Control vs. VHVPLHRGAVSA	0.09931	0.02866 to 0.1700	Yes	**
Positive Control vs. RDYHPRDHTATW	0.1825	0.1119 to 0.2532	Yes	****
Positive Control vs. SGTQDSMVGWNK	0.09692	0.02627 to 0.1676	Yes	**
Positive Control vs. TAKYLPMRPGPL	0.1589	0.08829 to 0.2296	Yes	****
Positive Control vs. Wild Type	0.1748	0.1042 to 0.2455	Yes	****
KRTGQYKLGSKTGPGQK vs. VHVPLHRGAVSA	0.003948	-0.06670 to 0.07460	No	ns
KRTGQYKLGSKTGPGQK vs. RDYHPRDHTATW	0.08718	0.01653 to 0.1578	Yes	**
KRTGQYKLGSKTGPGQK vs. SGTQDSMVGWNK	0.00156	-0.06909 to 0.07221	No	ns
KRTGQYKLGSKTGPGQK vs. TAKYLPMRPGPL	0.06358	-0.007073 to 0.1342	No	ns
KRTGQYKLGSKTGPGQK vs. Wild Type	0.07946	0.008811 to 0.1501	Yes	*
VHVPLHRGAVSA vs. RDYHPRDHTATW	0.08324	0.01259 to 0.1539	Yes	*
VHVPLHRGAVSA vs. SGTQDSMVGWNK	-0.002387	-0.07304 to 0.06826	No	ns
VHVPLHRGAVSA vs. TAKYLPMRPGPL	0.05963	-0.01102 to 0.1303	No	ns
VHVPLHRGAVSA vs. Wild Type	0.07551	0.004864 to 0.1462	Yes	*
RDYHPRDHTATW vs. SGTQDSMVGWNK	-0.08562	-0.1563 to -0.01497	Yes	*
RDYHPRDHTATW vs. TAKYLPMRPGPL	-0.02361	-0.09426 to 0.04704	No	ns
RDYHPRDHTATW vs. Wild Type	-0.007722	-0.07837 to 0.06293	No	ns
SGTQDSMVGWNK vs. TAKYLPMRPGPL	0.06202	-0.008634 to 0.1327	No	ns
SGTQDSMVGWNK vs. Wild Type	0.0779	0.007251 to 0.1486	Yes	*
TAKYLPMRPGPL vs. Wild Type	0.01588	-0.05477 to 0.08654	No	ns

1 way ANOVA for Alamar Blue 71 Hours

Number of families	1			
Number of comparisons per family	21			
Alpha	0.05			
Tukey's multiple comparisons test	Mean Diff.	95% CI of diff.	Significant?	Summary
Positive Control vs. KRTGQYKLGSKTGPGQK	0.2476	0.1282 to 0.3670	Yes	****
Positive Control vs. VHVPLHRGAVSA	0.2424	0.1229 to 0.3618	Yes	****
Positive Control vs. RDYHPRDHTATW	0.4322	0.3128 to 0.5517	Yes	****
Positive Control vs. SGTQDSMVGWNK	0.2782	0.1588 to 0.3977	Yes	****
Positive Control vs. TAKYLPMRPGPL	0.3489	0.2295 to 0.4684	Yes	****
Positive Control vs. Wild Type	0.437	0.3176 to 0.5564	Yes	****
KRTGQYKLGSKTGPGQK vs. VHVPLHRGAVSA	-0.005231	-0.1247 to 0.1142	No	ns
KRTGQYKLGSKTGPGQK vs. RDYHPRDHTATW	0.1846	0.06519 to 0.3041	Yes	***
KRTGQYKLGSKTGPGQK vs. SGTQDSMVGWNK	0.03064	-0.08880 to 0.1501	No	ns
KRTGQYKLGSKTGPGQK vs. TAKYLPMRPGPL	0.1013	-0.01809 to 0.2208	No	ns
KRTGQYKLGSKTGPGQK vs. Wild Type	0.1894	0.06998 to 0.3089	Yes	***
VHVPLHRGAVSA vs. RDYHPRDHTATW	0.1899	0.07042 to 0.3093	Yes	***
VHVPLHRGAVSA vs. SGTQDSMVGWNK	0.03587	-0.08357 to 0.1553	No	ns
VHVPLHRGAVSA vs. TAKYLPMRPGPL	0.1066	-0.01286 to 0.2260	No	ns
VHVPLHRGAVSA vs. Wild Type	0.1946	0.07521 to 0.3141	Yes	***
RDYHPRDHTATW vs. SGTQDSMVGWNK	-0.154	-0.2734 to -0.03455	Yes	**
RDYHPRDHTATW vs. TAKYLPMRPGPL	-0.08328	-0.2027 to 0.03616	No	ns
RDYHPRDHTATW vs. Wild Type	0.00479	-0.1146 to 0.1242	No	ns
SGTQDSMVGWNK vs. TAKYLPMRPGPL	0.07071	-0.04873 to 0.1901	No	ns
SGTQDSMVGWNK vs. Wild Type	0.1588	0.03934 to 0.2782	Yes	**
TAKYLPMRPGPL vs. Wild Type	0.08807	-0.03137 to 0.2075	No	ns

Supplementary Table 12. ANOVA details for alamar blue cell proliferation data.